UNIVERSITY OF
SOUTHAMPTON

Holographic Laser Resonators

Jason Mark Hendricks

Submitted for the degree of Doctor of Philosophy

Faculty of Science
Department of Physics

March 5, 2002

UNIVERSITY OF SOUTHAMPTON

ABSTRACT

Faculty of Science
Department of Physics

Doctor of Philosophy

Holographic Laser Resonators

By Jason Mark Hendricks

The work presented within this thesis details the development and characterisation of a CW solid-state adaptive resonator that uses phase-conjugation to actively correct for phase distortions present within the resonator loop. It is shown that the phase-conjugate of a given beam can be produced by the process of degenerate four-wave mixing inside a gain medium. In this scheme two mutually coherent beams overlap within a population inverted region of a laser amplifier and the subsequent interference pattern between them spatially hole burns a grating into the gain. The diffraction efficiency of such gain-gratings is studied both theoretically and experimentally and it is shown that, due to the stored inversion, CW phase-conjugate reflectivities of greater than 100 can be achieved in Nd:YVO_4. Using this gain four-wave mixing scheme an adaptive resonator is built that is capable of oscillating with a phase-conjugate mode. The ability of the volume gain-grating to encode and react dynamically to phase distortions present within the resonator loop ensures that the phase-conjugate output beam from the resonator always remains a faithful reproduction of the beam used to seed the resonator. The interactions occurring within the resonator are modelled and a resonator capable of producing an 11.6 W near-diffraction limited output is demonstrated. The power-scaling capabilities of such lasers is then considered and it is shown that the output power can be increased whilst maintaining phase-conjugate oscillation. It is shown that a phase-conjugate output of 6 W can be scaled to 11.7 W with the addition of a power amplifier placed into the existing setup.

”I don’t understand you,” said Alice. ”It’s dreadfully confusing!”
”That’s the effect of living backwards,” the Queen said kindly: ”it always makes one a little giddy at first–”
”Living backwards!” Alice repeated in great astonishment. ”I never heard of such a thing!”
”– but there’s one great advantage in it, that one’s memory works both ways.”
”I’m sure mine only works one way,” Alice remarked. ”I can’t remember things before they happen.”
”It’s a poor sort of memory that only works backwards,” the Queen remarked.

Lewis Carroll, from the book *Through the Looking Glass.*

Acknowledgements

During my time at the Optoelectronics Research Centre I have had the opportunity to work and interact with many talented people and now the time has come to thank them for all the help and encouragement they have given me throughout.

Firstly the biggest thanks must go to my supervisor, Prof. Rob Eason, who, throughout the last three years has offered support, encouragement as well as the many varied ideas and useful discussion to keep me on track - Rob you are probably the most optimistic guy I (the most pessimistic student) will ever meet! - thanks for all your help. I am also grateful to Dr Dave Shepherd, Dr Mike Damzen and Dr Graham Crofts for all the help and advice they gave me throughout and also to Spectron lasers Inc. for the CASE studentship and useful discussions. Thanks must also go to others who worked with me - Simon 'if you can draw it I can make it' Butler for making sense of my scribbles, Dave 'if you can make it I can break it' Hillier for pointing out the weaknesses in my equipment and Sakelaris 'it is cold in this lab - no?' Mailis for showing me the ropes.

A big thanks also goes out to my friends who kept me smiling when the lab got me frowning. Steve, Malcolm, Sak, Tim, Simon, Denis, Ian and everyone else who I begged, borrowed and stole equipment from.

Finally a special thanks to all the 'non-laser' people - my family and friends who now know the ins and outs of adaptive lasers resonators but couldn't care less! And most importantly (my woman) Nerissa who has put up with me for the last seven years.

Contents

Glossary

ASE	Amplified spontaneous emission
BP	Backward pump
BS	Beam splitter
CW	Continuous-wave
DFWM	Degenerate four-wave mixing
ESA	Excited state absorption
ETU	Energy transfer upconversion
FP	Forward pump
FWM	Four-wave mixing
FSR	Free spectral range
NPPPCM	Non-polarisation preserving phase-conjugate mirror
NRTE	Non-reciprocal transmission element
OPC	Optical phase-conjugation
PA	Power amplifier
PC	Phase-conjugate
PCM	Phase-conjugate mirror
PCO	Phase-conjugate oscillator
PPPCM	Polarisation preserving phase-conjugate mirror
RIG	Refractive index grating
S	Signal
SBS	Stimulated Brillouin scattering
SLM	Single longitudinal mode
SSSP	Small signal single pass

Chapter 1

Introduction

1.1 Power scaling of solid-state lasers

Diode pumping of solid-state lasers has been the subject of intense research in recent years as a way of producing high-power, high brightness outputs in a relatively cheap, compact device. The continuous-wave power output from commercial diode bars can now exceed 60 W [1] whilst the stacking of several such bars can produce devices capable of delivering a continuous-wave output of up to 4000 W [2]. A major drawback however, of using such high pump power densities to pump a crystal is that a correspondingly higher fraction of heat energy is deposited into the crystal lattice leading to degradation in the spatial quality of the laser output.

This thesis is concerned with the study and development of a particular class of diode-pumped solid-state laser that uses holographic phase-conjugate techniques to actively correct for phase distortions introduced into the oscillating cavity modes due to, for example, thermal effects within the amplifier crystal. This first chapter is intended as a basic introduction to the causes of heat generation within an amplifier crystal as well as some of the more popular methods used to overcome, or at least limit the negative effects associated with the buildup of heat energy.

The chapter begins with an overview of the main effects that contribute

to the heating of the laser crystal and describes problems that are introduced by this rise in temperature. In section 1.1.2 some of the more effective solutions devised so far to increase the output power and combat the detrimental heating effects within diode-pumped solid-state lasers are reviewed. Section 1.3 describes what is meant by a phase-conjugate wave, giving mathematical descriptions of their distortion correcting abilities and how this can be put to use in the power-scaling of laser resonators. In Section 1.4 a brief description is given of the more popular methods used to produce phase-conjugate waves and their relative advantages and disadvantages over phase-conjugation via saturable gain four-wave mixing. Finally in section 1.6 an overview is presented of this thesis and its logical progression.

1.1.1 Heat generation in diode-pumped crystals

As stated above, the generation of heat inside the lattice of a laser crystal can degrade both the power and quality of the oscillating mode leading to a corresponding degradation in brightness of the laser output. The majority of heat generated within the crystal is caused primarily through quantum defect heating [3, 4]. The energy is created via non-radiative decay from the pump band to the upper laser level and from the lower laser level to the ground-state, the excess being given up to the crystal lattice as thermal vibrations. The percentage of absorbed pump power within the crystal lattice that adds to the heating of the crystal in this way is known as the quantum defect and is defined as the difference in energy between the pump and laser photons over the energy of the pump photons (see equation 1.1). For example, a Nd:YVO_4 amplifier with a laser wavelength of 1064 nm and pump wavelength of 808 nm the percentage of pump-beam energy that is converted into heat energy within the crystal is

$$quantum\,defect = \frac{E_{pump} - E_{laser}}{E_{pump}} = 1 - \frac{\lambda_{pump}}{\lambda_{laser}} = 0.24 \qquad (1.1)$$

that is 24% of the pump power absorbed in a Nd:YVO_4 crystal is converted into heat energy due to the process of quantum defect heating alone[2].

Other processes, such as energy transfer upconversion (ETU) [5], excited state absorption (ESA) [6,7] and cross relaxation [5], can also occur within excited Nd ions in the crystal lattice that also act to increase the thermal loading. Figure 1.1 shows the first of these three effects in schematic form.

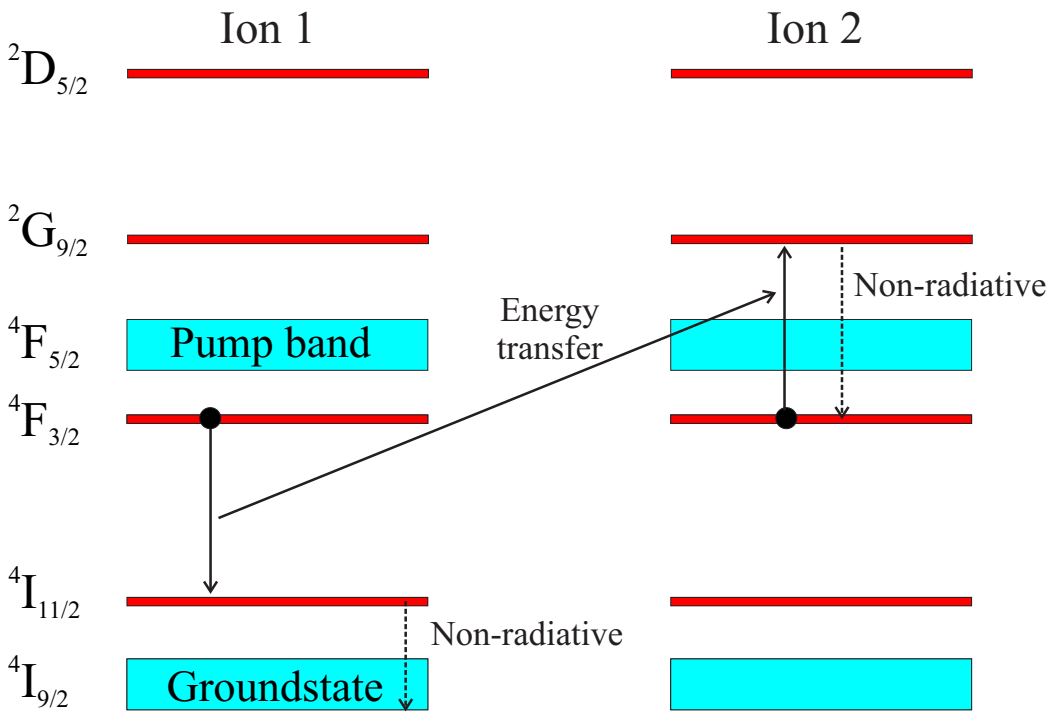

Figure 1.1: Energy transfer upconversion in Nd.

Energy transfer upconversion (shown in figure 1.1), also known as Auger upconversion, occurs when a Nd ion, initially in the $^4F_{3/2}$ upper laser level, drops to the ground-state and transfers its energy to a neighboring exited ion which is thereby excited to a higher energy state. This ion subsequently relaxes, via non-radiative decay, back down to the $^4F_{3/2}$ laser level, resulting in the energy of one of the excited ions being converted to heat energy within the lattice and a corresponding reduction in the overall gain of the amplifier.

The second of these effects, excited state absorption, is shown in figure 1.2. An ion is excited into the $^4F_{3/2}$ level from the ground-state by a pump photon. Whilst in this metastable level another pump photon is absorbed exciting the ion to a higher level. The ion then decays back to the $^4F_{3/2}$ level, via non-radiative decay, which, again, adds to the thermal loading of the crystal lattice.

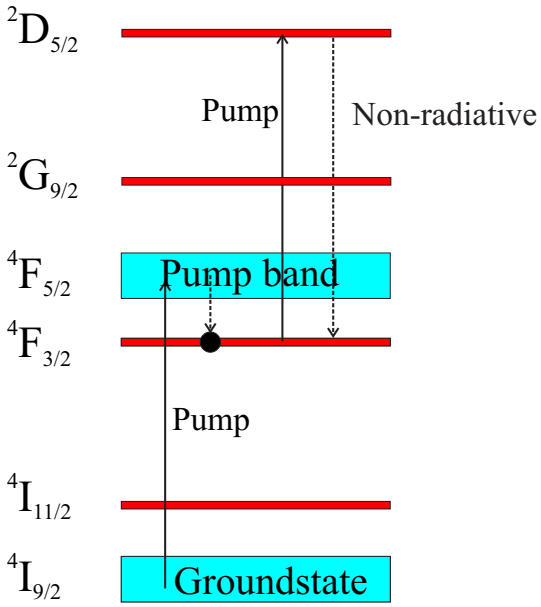

Figure 1.2: Excited state absorption in Nd.

The final effect, shown in figure 1.3, is cross relaxation. Ion 1, initially in the $^4F_{3/2}$ level drops to some intermediate level and transfers its energy to a neighboring ion 2 exciting it from the ground-state to the same intermediate level. Both ions then decay non-radiatively to the ground-state, depositing their energy into the crystal lattice in the process.

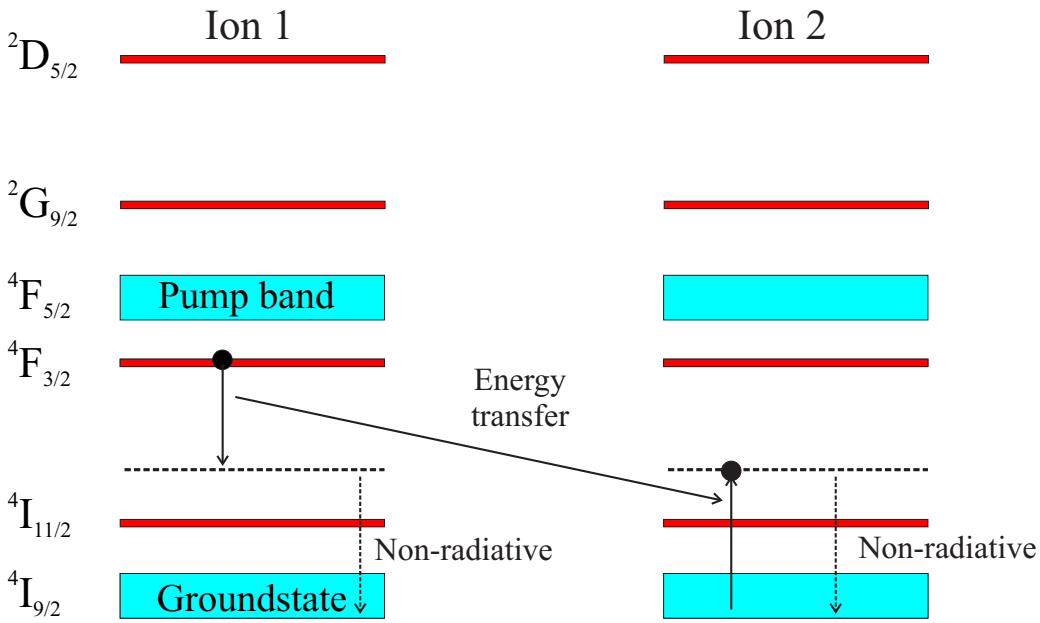

Figure 1.3: Cross relaxation in Nd.

These heating effects are detrimental to the lasing process in several ways.

First of all, the refractive index of the crystal is a function of its temperature so as more heat is deposited the local change in refractive index can cause aberrations in the transverse-mode of the cavity affecting the laser beam spatial quality and laser stability [8]. Secondly, the temperature rise in the crystal induces stress in the lattice which can manifest itself as either stress-induced birefringence, causing the polarisation state of the cavity beam to change resulting in losses due to polarisation elements and misalignment within the laser cavity [9], the physical bulging of the end face causing a lensing effect [8] or more catastrophically damage or fracture of the laser crystal [10].

1.1.2 Methods of power-scaling

Much of the ongoing work of others now concerns itself with scaling the output power from diode-pumped solid-state lasers whilst simultaneously reducing the thermal effects so that high-power near diffraction-limited outputs and hence high brightness beams are produced. The approach to this problem is twofold: firstly, reduce the thermal loading of the laser crystal by, for example, use of more efficient cooling schemes or by directly pumping into the upper laser level [11], and secondly, by reducing the effects that are *caused* by thermal loading.

One solution is to use the tightly-folded resonator geometry shown in figure 1.4 [12]. In this system a fibre lensed diode bar is proximity coupled to the amplifier crystal. The crystal is HR coated for the laser wavelength on the pump-face and the side opposite the pump-face (apart from a small region which is AR coated so that the laser beam can enter/exit the crystal). The TEM_{00} mode is then aligned so that as it bounces between the HR coated faces the mode is made to overlap with each single emitter of the multi-stripe diode. This allows good matching of the mode with the gain inverted regions. Thermal effects are also minimised in this configuration due to the side-pumped slab geometry whereby the pump power is distributed over a larger area. However, this geometry is very alignment sensitive over so many bounces.

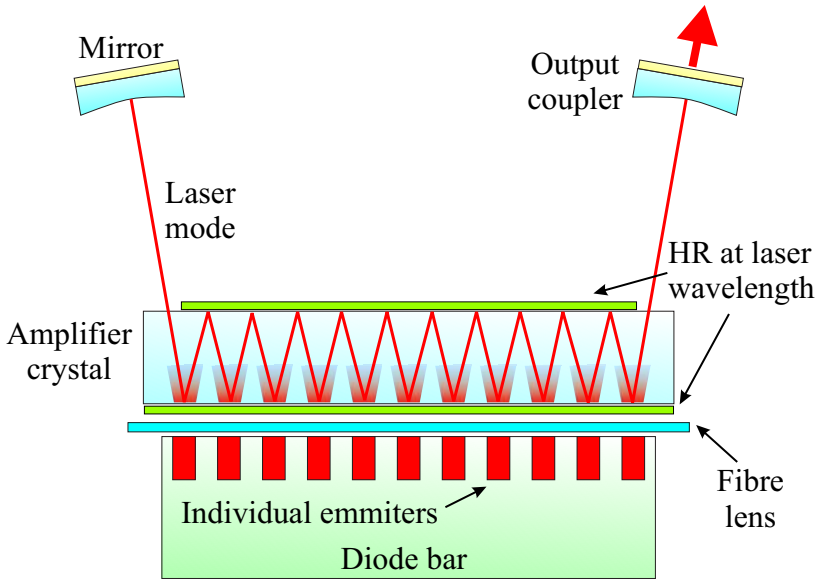

Figure 1.4: Tightly folded resonator.

One of the more promising techniques developed to date for power-scaling solid-state lasers is the thin-disk laser shown in figure 1.5 [13]. In this arrangement the amplifier consists of a thin crystal mounted onto a heat-sink in order to obtain an axial heat gradient within the crystal and hence reduce thermal lensing effects associated with radial heat extraction. The laser mode is formed perpendicular to the plane of the disk along the axial heat flow. However, the thickness of the disk is much less than the pump absorption length of the amplifier crystal. In order to achieve maximum pump absorption a complex system of mirrors needs to be used to multi-pass the pump beam. This both increases the cost of the system and limits the effective minimum thickness of the amplifier crystal. Typically these systems have been operating on a TEM_{00} mode (M^2 = 1.2) with up to 97 Watts of CW output power (pumped with 247 Watts) in a 240 μm thick Yb:YAG laser amplifier [14].

Another technique worthy of mention is the use of waveguide geometries to reduce thermal effects. Figure 1.6 shows a typical geometry of a double-clad fibre laser. The single mode doped core of the fibre offers confinement of the laser made. The diode pump light can be shaped into a convenient size, ready for coupling into the fibre, by various diode beam-shaping techniques [15]. The pump is then launched into the large ra-

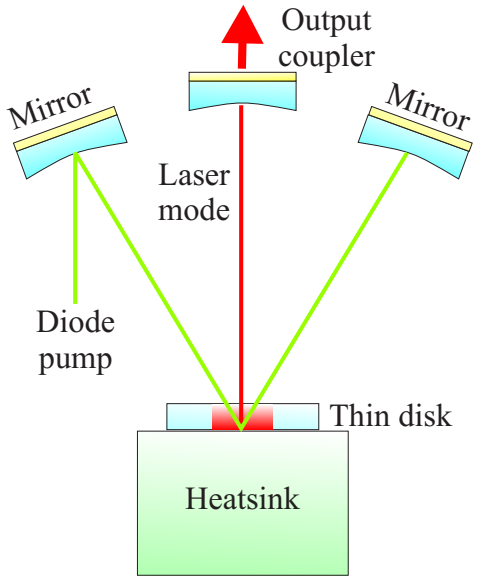

Figure 1.5: Thin disk laser.

dius inner-cladding of the fibre where it is absorbed within the doped core as it is guided down the fibre by the cladding. Effective cooling of the double-clad fibre can be achieved due to the large surface to volume ratio of a cylindrical geometry. Using this method continuous-wave near diffraction-limited output powers of 110 W using a pump power of around 180 W have been achieved in Yb doped double-clad fibres [16].

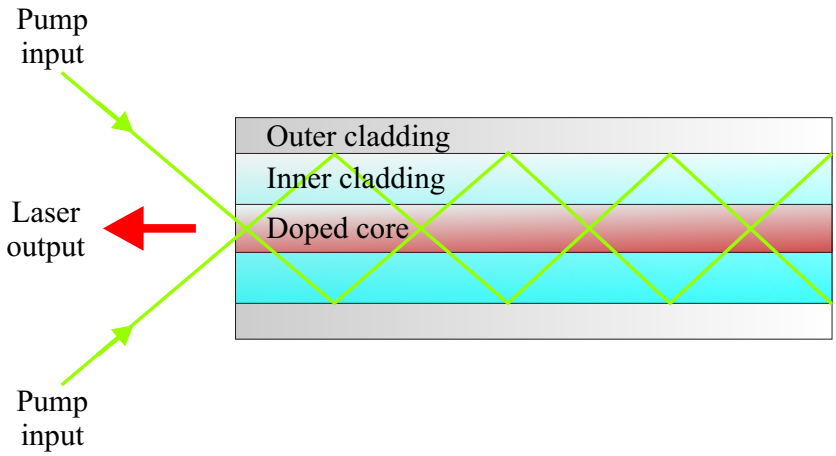

Figure 1.6: Double clad fibre laser.

1.2 History and uses of phase-conjugation

Another method that can be used to scale the output power from lasers is that of optical phase-conjugation (OPC). OPC is a technique used to exactly reverse the direction and total phase of any arbitrary wavefront. It was first demonstrated by Zel'dovich *et al* [17] in 1972. Light from a pulsed ruby laser was directed towards a capillary tube containing high pressure methane gas to investigate stimulated Brillouin scattering (SBS) within the gas. A highly distorting (ground glass) phase-plate was placed between the ruby laser and the SBS cell producing a highly distorted laser beam. The SBS cell acted like a conventional mirror, reflecting some of the incident laser light back towards the distorting phase-plate. However, unlike a conventional mirror the distorted beam upon passing back through the phase-plate had been corrected of any distortions thereby reproducing the initial high quality input. The wave reflected from the SBS cell was the phase-conjugate (PC) of the incident wave and so the cell could be viewed as a phase-conjugate mirror (PCM).

Five years after the discovery by Zel'dovich a new scheme was suggested by Hellwarth that could produce PC waves within almost any medium whose non-linear response to an optical field caused a refractive index change that was a function of the intensity of the optical field [18]. This scheme, known as four-wave mixing (FWM), required two mutually coherent beams to interfere within the non-linear medium and hence form a volume refractive index grating. A third beam, Bragg matched to one of the grating writing beams could then read this grating producing a phase-conjugate wave of the other writing beam. This standard FWM geometry is shown in figure 1.7.

In this configuration a reference beam defined as the forward-pump (FP) interferes with the beam that is to be phase-conjugated which is known as the signal (S). This interference pattern then modulates some[1] property of

[1] any property of the medium which can produce an intensity dependent refractive index change. For example the non-linear Kerr effect, $n(I) = n_l + n_{nl}I$, produces an intensity dependent refractive index n(I) where n_l is the usual linear refractive index and n_{nl} is the non-linear refractive index

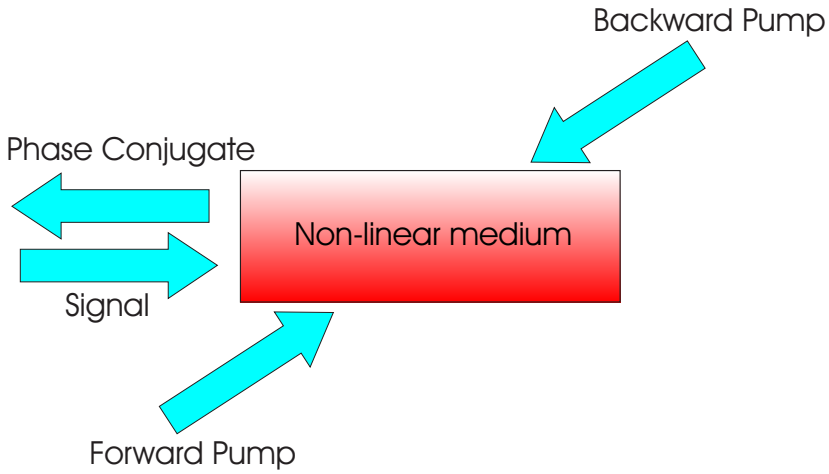

Figure 1.7: Standard four-wave mixing geometry.

the medium to produce a volume refractive index grating. A third beam known as the backward-pump (BP), which ideally is the phase-conjugate of the FP reference beam, is then directed towards the grating. This BP beam then produces a fourth wave, via diffraction from the grating, that is the PC of the S beam. In this sense FWM can be viewed as a holographic reconstruction process (see section 2.5). However, unlike conventional holography where the grating is fixed, the grating written within the non-linear medium can change in response to changes within the signal beam. This means that the phase-conjugate of the signal beam can be produced in real-time and can dynamically react to changes in the phase of the signal beam, assuming that the time scale on which the changes to the signal beam occur are greater than the response time of the particular non-linear effect used.

In the FWM configuration shown in figure 1.7, the grating, written by the interference between the FP and the S beam is known as a *transmission* grating and is read out by the BP. However, because the BP,FP and S beams are all present at the same time within the non-linear material other gratings can be formed (this is discussed further in section 2.6). One other grating in particular can also contribute to the formation of the PC wave. A *reflection* grating is written by the interference pattern produced by the BP and the S beams. This is then read out by the FP (which is the PC of the BP and therefore Bragg matched to the grating). The first order diffraction

of the FP by the reflection grating also produces the PC of the S beam and so the PC beam consists of contributions from both a transmission and reflection grating.

Subsequently, many applications for the use of phase-conjugate waves produced by SBS and FWM were suggested and demonstrated, ranging from the tracking of moving objects, focussing of high intensity laser beams in laser fusion systems to lensless imaging systems (photolithography) [19]. Probably the most important application developed was the use of phase-conjugate mirrors in place of a conventional mirror inside a laser cavity [20]. The distortion correcting abilities of the PCM could then be used to compensate for distortions in the cavity mode due to imperfect cavity design, the use of poor quality optics and dynamic thermal and mechanical instabilities. It was shown that the modes of a PC resonator were highly stable [21] and that the resonator was able to actively correct for severe phase-distortions placed into the cavity. In one demonstration Feinberg *et al* produced a PC laser cavity that used a metal kitchen spatula in place of one of its mirrors [22]. Since these early days interest in the topic has continued to grow, spurred mainly by the use of phase-conjugate waves to correct for distortions within laser resonators and the field has been the subject of several review papers [19, 23–25] and books [26–28].

1.3 Properties of phase-conjugate waves

The process of phase-conjugation can be best explained in terms of plane waves incident on a plane mirror. An initial plane wave, with wave vector

$$\mathrm{k}_{inc} = k_x\widehat{x} + k_y\widehat{y} + k_z\widehat{z} \tag{1.2}$$

is incident on a conventional plane mirror. The incident beam is reflected from the mirror to give a new wave vector

$$\mathrm{k}_{ref} = k_x\widehat{x} + k_y\widehat{y} - k_z\widehat{z} \tag{1.3}$$

The mirror only changes the component of the incident wave k-vector that is normal to the mirror. This allows us to redirect the wave in any arbitrary

direction by simply tilting the mirror. A phase-conjugate mirror (PCM) on the over hand reverses the complete wave vector of the incident wave i.e. $k_{ref} = -k_{inc}$, so that the reflected wave exactly retraces the path of the incident plane wave in the reverse direction for all angles. It follows therefore that the reflected beam can no longer be steered by this PCM as the reflected beam will always travel back to the point of origin of the incident beam as is illustrated in figure 1.8.

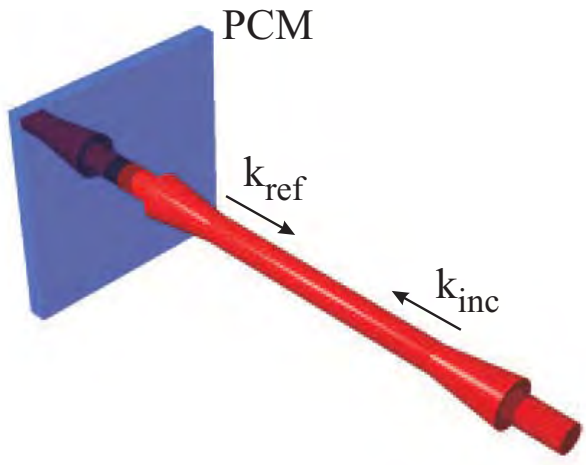

Figure 1.8: The incident beam is directed towards the phase-conjugate mirror where its k-vector is completely reversed so that the reflected phase-conjugate wave retraces the incident beam path.

An extension of this shows that any arbitrary wavefront, which can be viewed as a superposition of many plane-waves, retraces its incident path exactly upon reflection from the PCM remaining, at all points, the phase-conjugate of the incident wave. An incident converging beam would be reflected to produce a diverging beam and vice versa as this is shown schematically in figure 1.9. This remarkable property of phase-conjugate waves have lead some people to refer to them as 'time reversed waves' [29]. It is as if after reflection from the phase-conjugate mirror, time has now been reversed and the incident wave is retracing its steps back through time.

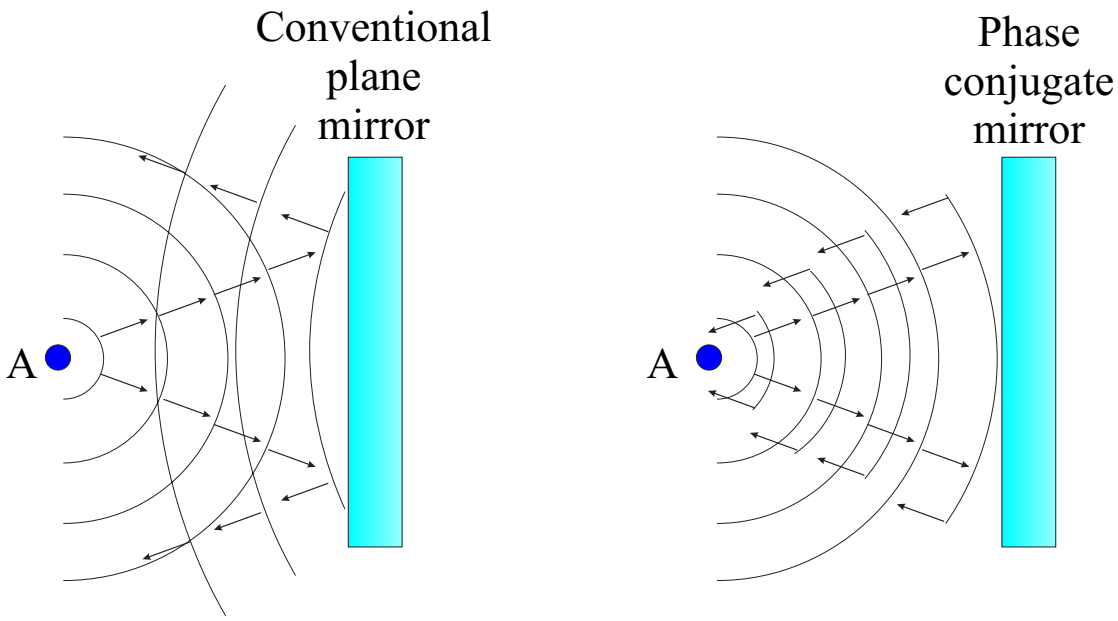

Figure 1.9: When a diverging beam emanating from a point source at A is incident on a conventional mirror only the k-vector that is normal to the mirror is reversed and the wave continues to diverge on reflection. In a phase-conjugate mirror the entire k-vector is reversed and so the reflected wave converges back to the point source at A.

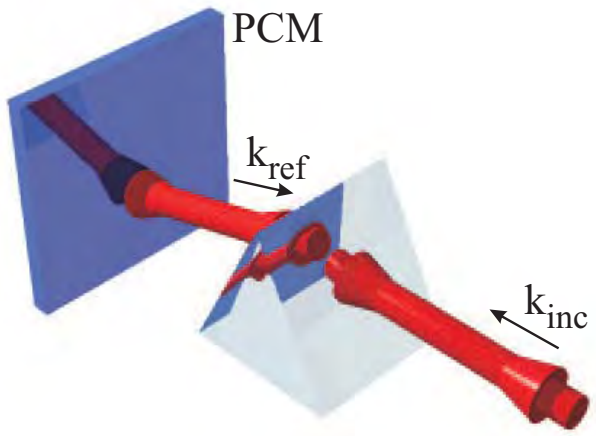

Figure 1.10: A glass prism placed into the path of the beam deflects it downwards. The phase-conjugate beam still retraces the incident beam's path back to the same point.

1.3.1 Distortion correction theorem

If a glass wedge is now placed into the path of the beam incident on the phase-conjugate mirror as shown in figure 1.10, the beam is deflected downwards on its path towards the PCM. Upon reflection the phase-conjugate wave retraces the path of the original incident beam back towards the same point on the wedge, where it is deflected back towards the original light source. The point to note here is that the reflected beam is not at all affected by the presence of the wedge in its path. The final returned beam has the same position, direction, size and phase-front as the beam that would have been returned had the wedge not been there. This can be extended to any large number of randomly orientated wedges and hence any distortion, figure 1.11, as long as the distorted beam is still captured by the PCM.

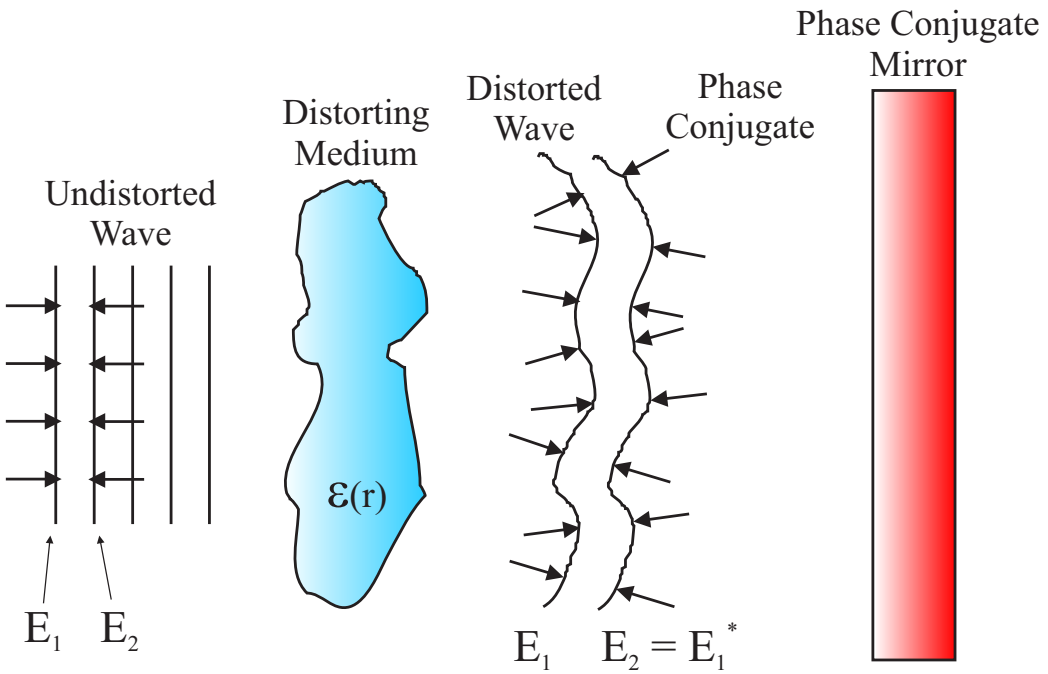

Figure 1.11: The undistorted incident field travelling from left to right is distorted as it passes through the phase-aberrating medium. The reflected phase-conjugate beam experiences the distortion in reverse and is healed of any distortions

The distortion correction theorem can be expressed mathematically using the proof first presented by Yariv [30]. The wave travelling from left to

right in figure 1.11 is described by

$$E_1 = \psi_1(r)\, e^{i(\omega t - kz)} \tag{1.4}$$

where ω is the angular frequency of the wave, k is its wavenumber and $\psi_1(r) = A(r)\, e^{-\phi(r)}$ is the complex amplitude describing the transverse amplitude, $A(r)$, and phase variations, $\phi(r)$, from that of a plane wave. Substituting E_1 in to the wave-equation to gives

$$\begin{aligned} \nabla^2 E_1 - \mu\varepsilon(r)\frac{\partial E_1}{\partial t^2} &= 0 \\ \nabla^2 E_1 + \omega^2 \mu\varepsilon(r) E_1 &= 0 \end{aligned} \tag{1.5}$$

where $\varepsilon(r)$ describes the spatially varying dielectric constant representing a spatially varying refractive index - the phase-distortion in figure 1.11. Substituting the second derivative (wrt x, y and z) of equation 1.4 into the wave equation and applying the slowly varying envelope approximation (SVEA) yields

$$\nabla_\perp^2 \psi_1 + \left[\omega^2 \mu\varepsilon(r) - k^2\right]\psi_1 - 2ik\frac{\partial \psi_1}{\partial z} = 0 \tag{1.6}$$

where $\nabla_\perp^2 = \frac{\partial^2}{\partial x^2} + \frac{\partial^2}{\partial y^2}$ is the Laplacian of the transverse field components and where it is assumed that $\left|\frac{\partial^2 \psi_1}{\partial z^2}\right| \ll \left|2k\frac{\partial \psi_1}{\partial z}\right|$ i.e. the envelope modulating the complex amplitude of the wave (due to for example loss or gain) varies slowly with respect to one optical cycle of the wave. The complex conjugate of equation 1.6 is given by

$$\nabla_\perp^2 \psi_1^* + \left[\omega^2 \mu\varepsilon(r) - k^2\right]\psi_1^* + 2ik\frac{\partial \psi_1^*}{\partial z} = 0 \tag{1.7}$$

A solution to equation 1.7 is

$$E_2 = \psi_1^*(r)\, e^{i(\omega t + kz)} = Phase\ Conjugate\ of\ E_1 \tag{1.8}$$

which has a complex amplitude that is the phase-conjugate of the complex amplitude of the field travelling from left to right (field 1) and travels in

the opposite direction i.e. from right to left. Both fields obey the same wave equation and because of the uniqueness property of this type of differential equation, if field 1 is known for all x and y at a certain plane z = z_0 then the field can be found at every other point x,y and z [24]. This means that if the phase-conjugate of field 1, E_2, can be generated by a PCM at the same plane z = z_0 then as it propagates from right to left it will remain the phase-conjugate of field 1 at every point, implying that field 2 will become a plane wave upon re-traversing the distortion so that it remains the phase-conjugate of field 1.

Phase-conjugation can therefore be used to correct for aberrations within a system. Even more attractive is the fact that the phase-conjugate mirror in, for example, a gain-saturation four-wave mixing configuration can react dynamically to changes in the phase of the initial incident beam and have reflectivities of greater than unity producing a distortion correcting mirror *with gain*.

1.3.2 Resonators with phase-conjugate mirrors

At this stage it is useful to look at the stability of a laser resonator with a phase-conjugate mirror in place of a standard mirror as shown in figure 1.12. Following the analysis presented in [20, 21] the ray-transfer matrix for one round trip of the system, starting with a reflection from the conventional curved mirror, is given by

$$\begin{aligned} M_{round\,trip} &= M_{dist}M_{pcm}M_{dist}M_{mirror} \\ &= \begin{pmatrix} 1 & d \\ 0 & 1 \end{pmatrix}\begin{pmatrix} 1 & 0 \\ 0 & -1 \end{pmatrix}\begin{pmatrix} 1 & d \\ 0 & 1 \end{pmatrix}\begin{pmatrix} 1 & 0 \\ \frac{2}{R} & 1 \end{pmatrix} \\ &= \begin{pmatrix} 1 & 0 \\ -\frac{2}{R} & -1 \end{pmatrix} \end{aligned} \tag{1.9}$$

where M_{dist} is the transfer matrix for a distance d, M_{mirror} is the transfer matrix for a mirror of radius of curvature, R, and M_{pcm} is the transfer ma-

trix for a PCM. The transfer matrix for a double-pass though the system can then given by

$$M_{double\ pass} = M_{round\ trip} M_{round\ trip} = \begin{pmatrix} 1 & 0 \\ 0 & 1 \end{pmatrix} \tag{1.10}$$

The stability condition of the resonator requires that the trace of the transfer-matrix divided by two is less than or equal to one [31]. The double-pass transfer matrix shown in 1.10 is always equal to one and is completely independent of the distance between the two mirrors and the radius of curvature of the spherical mirror. A more general proof is given in [20] where it is shown that a resonator with a PCM is always stable regardless of the number of (passive) intracavity optical elements present which can be represented by an overall ABCD matrix.

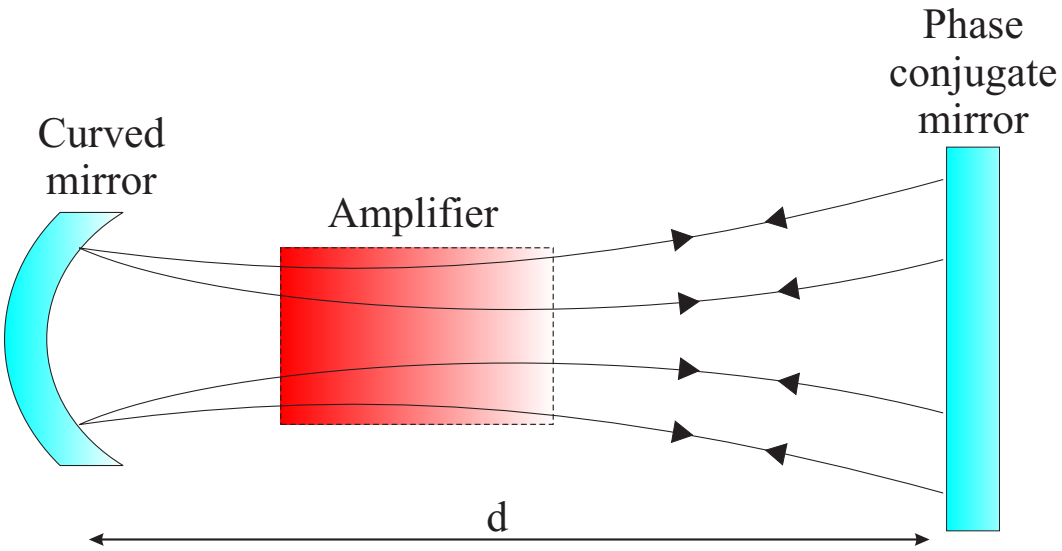

Figure 1.12: After a double round-trip though the phase-conjugate resonator a stable mode is produced.

It is this inherent stability that makes the use of a PCM inside a laser cavity an attractive option for laser design. For example, by adjusting the cavity length, d, in figure 1.12 its mode size can be altered to match that of the gain region of the laser amplifier leading to more efficient extraction of the power and providing discrimination between transverse cavity modes. This results in low order cavity modes that can oscillate with large mode sizes inside the PC resonator, giving all the benefits of having

the large controllable mode volumes and subsequent efficient power extraction characteristic of unstable resonators [32, 33] but with the added advantage of a stable cavity.

1.4 Other methods of phase-conjugation

In this section a brief introduction to two of the more popular methods of producing the phase-conjugate of any arbitrary wavefront is given. The physical process governing the production of the phase-conjugate wave is described and a brief overview is given of typical phase-conjugate reflectivities that have so far been achieved.

1.4.1 Stimulated Brillouin scattering

Probably the most commonly used method of producing phase-conjugate waves is that of stimulated Brillouin scattering (SBS). In fact it has featured in the only commercial laser system to date to use phase-conjugation for correction of internal aberrations (Coherent - Infinity laser). In its most basic form SBS consists of an incident laser beam with an angular frequency ω_{inc} scattering from a moving refractive index grating, caused by acoustic phonon waves, of angular frequency Ω, travelling in the same direction as the k-vector of the incident laser beam as shown in figure 1.13.

The incident light scattered from the refractive index grating is down-shifted in frequency (typically by around 10 GHz [34]) to the Stokes frequency $\omega_{ref} = \omega_{inc} - \Omega$. The reflected Stokes wave interferes with the incident laser beam to produce an interference pattern that has a frequency component which is equal to the frequency difference between the incident laser field and the Stokes reflected wave. This, of course, is the frequency of the acoustic phonon wave, Ω, in the material, and thus the interference tends to reinforce the original acoustic phonon wave that caused the scattering via the electrostrictive effect. The electrostrictive effect is a process whereby the Brillouin material becomes compressed in regions of

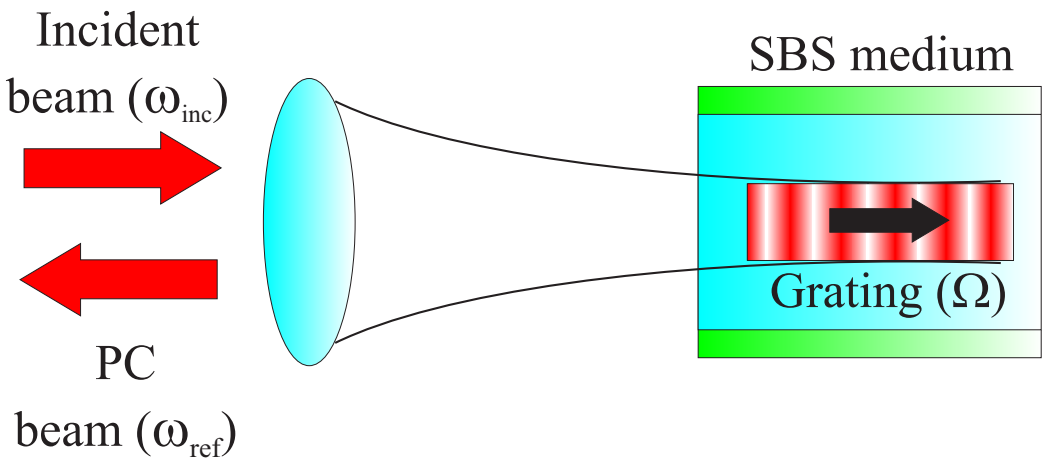

Figure 1.13: Phase-conjugation via stimulated Brillouin scattering.

high electric fields causing periodic density variations and hence periodic refractive index variations in the material which act as gratings to couple the incident wave into the reflected Stokes wave. This causes a positive feedback mechanism, whereby the scattering of the laser beam from the now stronger grating increases the Stokes wave amplitude, and the interference between the laser beam and the Stokes field tends to reinforce the acoustic phonon wave producing reflectivities of greater than 90% [35]. The Stokes reflected wave from the Brillouin medium was shown by Zel'dovich [17] to be the phase-conjugate of the incident wave since it had a gain factor over twice that of any other back scattered wave and so the system could be viewed as a phase-conjugate mirror.

The main disadvantage of phase-conjugation via SBS is the high intensities (typically $10^6\ Wcm^{-2}$) needed to reach the SBS threshold within bulk media. It is for this reason that the majority of the work in this field has concentrated on the pulsed regime where these high threshold intensities can be easily achieved. Work in the CW regime requires very high power lasers to achieve even modest PC reflectivities. Recent work however has shown that high CW PC reflectivities can be achieved by using optical fibres as the SBS medium, whereby a combination of very long interaction lengths and small core sizes can significantly reduce the CW SBS threshold. Using this method CW PC reflectivities of greater than 70% have been achieved within a 4.23 km length of 50 μm core multimode fibre for an in-

put power of only 250 mW [36].

SBS in its basic form described above is capable of, as already stated, producing PC reflectivities of typically up to 90%. Other Brillouin geometries do exist, however, that can produce greater than unity reflectivities based upon the four-wave mixing geometries described earlier [37] although a description of this process is beyond the scope of this thesis.

1.4.2 Photorefractive phase-conjugation

Another method commonly used to produce the phase-conjugate of a given wave is phase-conjugation via the photorefractive effect [24]. This effect is caused by the formation of refractive index gratings (RIG) inside a suitable electro-optic material when a modulated intensity pattern is present within that medium. What follows is a brief overview of the effect; for a more detailed analysis see [24]. Figure 1.14 shows how the RIG is formed. Two mutually coherent waves, E_1 and E_2, interfere within the electro-optic material to produce the spatially varying intensity pattern (interference pattern), I(Z), shown in (a). The high optical intensity at the antinodes of the interference pattern cause mobile charge carriers (electrons or holes) to be excited from occupied donor states into the conduction band. These mobile carriers are now free to diffuse through the material until they are trapped by empty donors. The resultant space charge density, $\rho(Z)$, shown in (b) where it can be seen that the regions at the nodes of the interference pattern have acquired an excess amount of mobile carriers whilst those at the anti-nodes have lost the mobile carriers (in the case of figure 1.14 the mobiles carriers are electrons leaving an excess amount of holes at the antinodes of the interference pattern).

Plot (c) shows the resulting electric field, E(Z), produced within the material due to the new charge distribution. It is this electric field which, via the electro-optic effect, produces the spatial variation of refractive index, $\Delta n(Z)$, within the material according to $\Delta n(Z) = -\frac{1}{2}n^3 r E(Z)$ where r is the electro-optic coefficient for the interaction and n is the normal refractive index of the material.

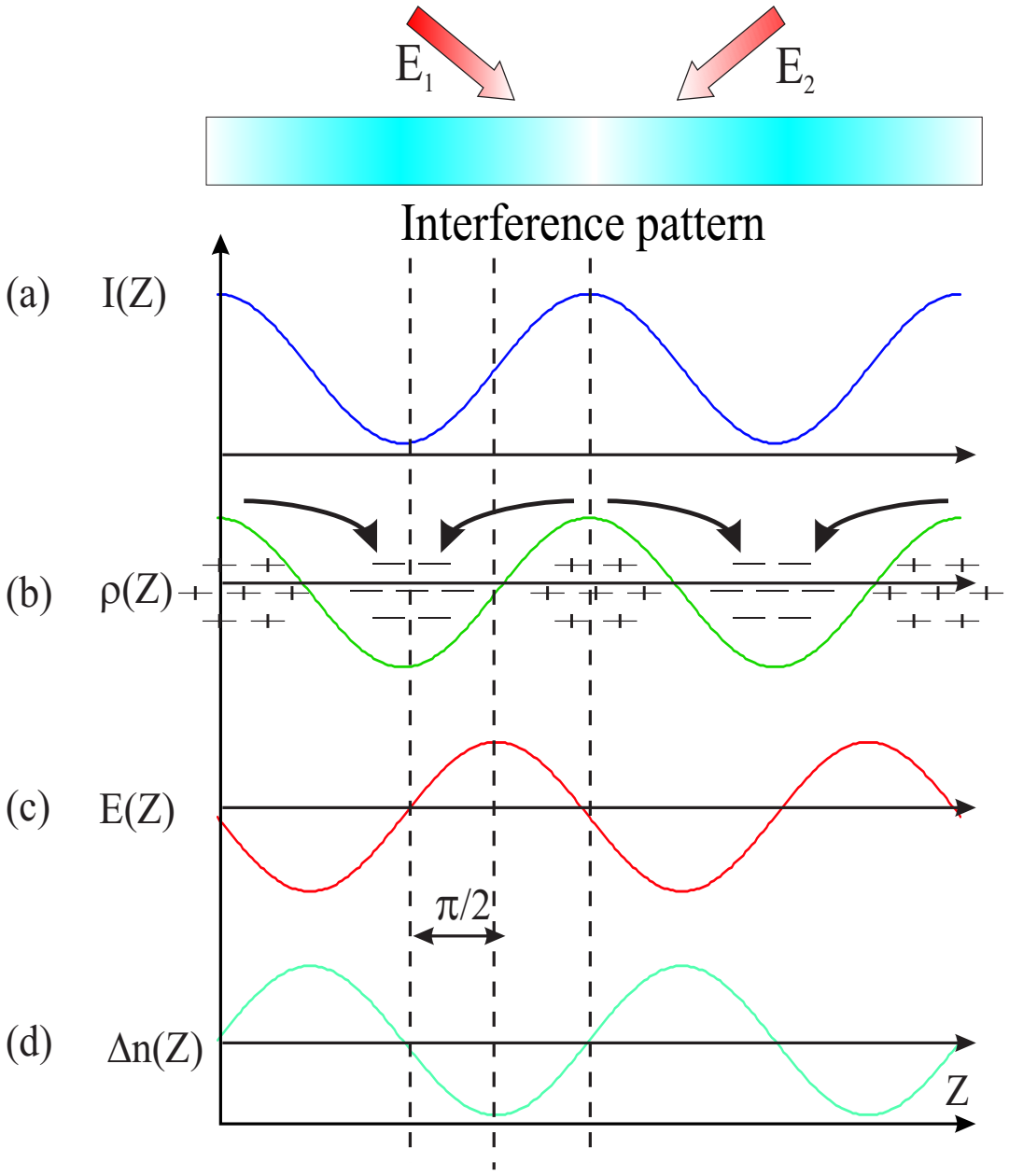

Figure 1.14: Formation of a refractive index grating via the photorefractive effect.

The photorefractive material can now be used as the medium in which a four-wave mixing interaction can take place, the dynamic interference pattern being stored as a refractive index grating within the material. The phase-conjugate wave of one of the inputs can then be produced depending on the specific geometry [38]. Although photorefraction can be used to produce phase-conjugate waves quite readily its uses are limited by the intensity dependent response time of the gratings to a change in the signal beam (from anywhere around a few μs in, for example, GaAs [39] up to a few hours in $BaTiO_3$ [39]). This means any laser cavity built using a photorefractive PCM cannot correct for dynamic distortions that change with a rate faster than the response time of the photorefractive crystal, although in other applications of phase-conjugation, such as holographic memory, this ability to store the gratings over an extended period can be beneficial.

1.5 The neodymium ion

The solid-state laser crystal used in the experimental work reported in this thesis is 1.1 at.% doped neodymium doped yttrium ortho-vanadate (Nd:YVO_4) and so a brief summary of its main characteristics is required (see table 1.1). This crystal was primarily chosen because of its high stimulated emission cross-section at the main lasing transition of 1064 nm (9 times that of the Nd:YAG laser medium for light polarised parallel to crystal c-axis) and high absorption coefficient (4.5 times that of Nd:YAG for light polarised parallel to crystal c-axis) over a broad range of wavelengths centred around the main pump wavelength of 808 nm. This large coefficient, resulting in a small pump absorption depth (around 320 μm), when combined with intense pumping such as that available from laser diodes can lead to high inversion densities producing the very high gain-coefficients required in gain-saturation four-wave mixing [40].

Another advantage of using Nd:YVO_4 is its uniaxial tetragonal crystal structure leading to a high natural birefringence and hence polarised laser emission. This renders the effects of any thermally induced birefringence negligible when compared to the natural birefringence. This is in stark

Parameter	Nd:YVO_4	Nd:YAG
Stim. emiss. cross sect. @ 1064 nm	25x10^{-19} cm^{-2}	2.8x10^{-19} cm^{-2}
Absorption coefficient @ 808 nm	31.4 cm^{-1}	7.1 cm^{-1}
Fluorescence lifetime	90 μs	230 μs
Gain bandwidth @ 1064 nm	0.96 nm (254 Ghz)	0.6 nm (160 Ghz)
absorption bandwidth @ 808 nm	12 nm	2.5 nm
Intrinsic loss @ 1064 nm	0.001 cm^{-1}	0.003 cm^{-1}
Thermal conductivity ‖c-axis	5.23 $Wm^{-1}K^{-1}$	14 $Wm^{-1}K^{-1}$
Thermal conductivity ⊥c-axis	5.10 $Wm^{-1}K^{-1}$	14 $Wm^{-1}K^{-1}$
Structure	Tetragonal	Cubic
Naturally birefringent	Yes	No

Table 1.1: Comparison of the optical and mechanical properties of 1.1 at.% doped *a*-cut Nd:YVO_4 and Nd:YAG (values are for light polarised ‖ to *c*-axis).

contrast to the Nd:YAG crystal whose cubic crystal structure has no naturally occurring birefringence and is therefore susceptible to the effects of thermally induced birefringence. The two refractive index values, the ordinary index, n_o, for light polarised perpendicular to the crystal c-axis and the extraordinary index, n_e, for light polarised parallel to it have values of 1.96 and 2.17 respectively for 1064 nm light in Nd:YVO_4 giving a birefringence of $n_e - n_o = 0.21$.

Figure 1.15 shows the energy level scheme for the trivalent Nd^{3+} rare-earth ion. The main pump transition is between the ${}^4I_{9/2} \rightarrow {}^4F_{5/2}$ levels and can be pumped via the conveniently placed 808 nm wavelength transition using commercially available semiconductor diode lasers. The Stark splitting of the ${}^4F_{5/2}$ pump level is smaller within Nd:YVO_4 than Nd:YAG and so the individual Stark levels are closer together. This leads to a much broader and less spiky absorption profile in Nd:YVO_4 making it less sensitive to changes in the wavelength of the pump diode due to temperature changes within the pump diodes [41].

The Nd^{3+} ion in a YVO_4 lattice has three main laser transitions lying at 920

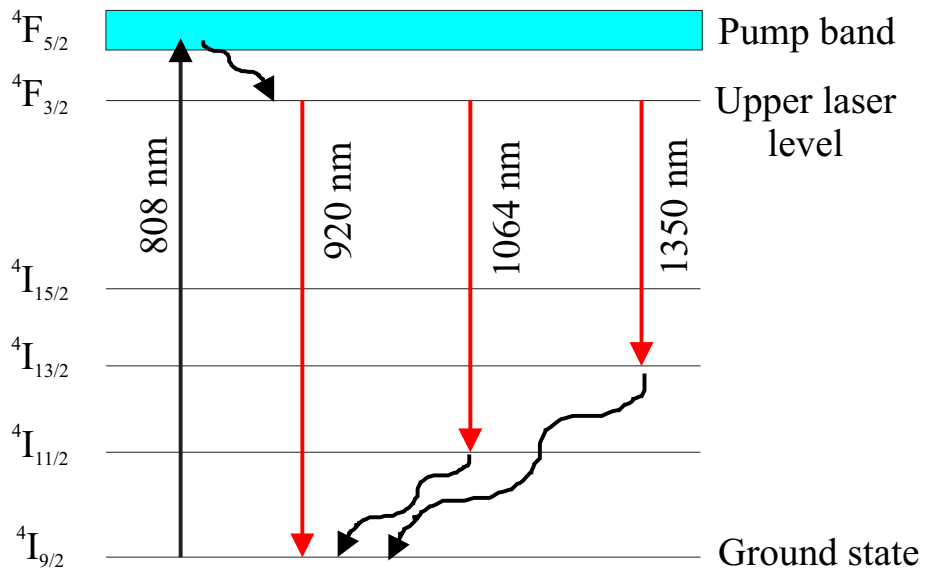

Figure 1.15: Energy level diagram showing the main laser transitions of the Nd^{3+} ion in YVO_4.

nm, 1064 nm and 1350 nm which correspond to transitions from the long lived upper laser level, $^4F_{3/2}$, which has a fluorescent lifetime of around 90 µs in 1.1 at.% doped YVO_4 , to the $^4I_{9/2}$, $^4I_{11/2}$ and $^4I_{13/2}$ levels respectively.

The use of Nd dopant ions within a YVO_4 crystal lattice is not without its problems. As already discussed in section 1.1.1, Nd:YVO_4 can suffer from a reduction in the available gain due to cross relaxation and upconversion between neighboring exited ions [42]. This occurs particularly when the crystal is doped with high concentrations of Nd limiting the effective dopant concentration to around 3 at.%. Another negative point, particularly for Q-switched operation of lasers, is the lower fluorescence lifetime of Nd:YVO_4 compared to Nd:YAG leading to a lower energy storage capability. Finally, the thermal conductivity of the Nd:YVO_4 crystal lattice is under half that of Nd:YAG making the removal of heat energy within the crystal lattice harder thereby increasing the risk of detrimental thermal effects as well as the risk of thermal fracture [10].

1.6 Thesis Outline

This thesis is concerned with the development of a novel CW self-adaptive phase-conjugate resonator using a diode pumped Nd:YVO_4 crystal for the amplifying medium. An attractive feature of this type of phase-conjugate oscillator (PCO) is its ability to correct for phase distortions placed within the resonator loop via phase-conjugation by gain FWM. This distortion correcting ability is then put to use in the power-scaling of the holographic resonator, whereby an additional amplifier is placed at various points around the phase-conjugate resonator in an attempt to increase the output power whilst maintaining SLM near diffraction limited operation.

In chapter 2 the theory behind FWM within a saturable gain material will be presented. Gain saturation FWM will be discussed in terms of a dynamic holographic process, the gain-gratings being formed within the population inversion of the amplifier. Theoretical investigations will show the form of the gain-gratings produced for different gain FWM regimes. Finally, details of an experimental scheme used to demonstrate gain FWM within a Nd:YVO_4 crystal will be presented showing that CW FWM reflectivities as high as 100 are possible.

In chapter 3 various resonator geometries are explored that utilize the high FWM reflectivities presented in chapter 2 to form an adaptive resonator capable of correcting phase distortions placed within the resonator loop. The operation of these adaptive resonators is broken down into stages in an attempt to analyze and explain features such as SLM and single transverse mode output. Finally, phase-conjugate resonators are demonstrated experimentally that are capable of running on a SLM near diffraction-limited mode with output powers of up to 11.6 W even when severe phase distortions are present within the resonator cavity.

In chapter 4 initial investigations into the scaling of the output power of the phase-conjugate resonators demonstrated in chapter 3 will be presented. The placement of additional power-amplifiers at various positions around the resonator loop is explored theoretically to give an indication as to where maximum power extraction, alignment etc. can be optimised.

Finally, it is shown that a phase-conjugate resonator operating with an output of around 6 W can be scaled in power to 11.7 W with the use of an additional power-amplifier within the output arm of the phase-conjugate resonator.

In chapter 5 some groundwork is set for the possibility of using multimode fibres as the gain element for saturable gain FWM. The use of phase-conjugation to correct for modal and polarisation scrambling within the fibre is explored and it is shown that not all the scrambled information need be phase-conjugated to produce the initial undistorted input wave. These results are then put to use in the demonstration of a novel two fibre device that shows amplitude non-reciprocity in a phase-conjugate configuration, a necessary part of any future fibre implementation of an adaptive resonator.

Finally in chapter 6 some future work is explored both for the bulk phase-conjugate resonator and a possible fibre implementation. The main numerical and experimental results presented within this thesis will be summarised. This will be followed by a discussion on the relative merits of adaptive holographic lasers compared to the conventional solid-state laser technology available today.

1.7 References

[1] Coherent Inc. `http://www.coherentinc.com/downloads/785_to_830_nm_Water_CooledDS.pdf`.

[2] Dilas Diodenlaser GmbH. `http://www.rofin.com/english/laser/macro/diode/df-high-tech.htm`.

[3] W. Koechner. Solid-state laser engineering. pages 393–451. Springer-Verlag, 1999.

[4] T. Y. Fan. Heat-generation in Nd:YAG and Yb:YAG. *IEEE Journal of Quantum Electronics*, 29(6):1457–1459, 1993.

[5] S. Guy, C. L. Bonner, D. P. Shepherd, D. C. Hanna, and A. C. Tropper. High-inversion densities in Nd:YAG: Upconversion and bleaching. *IEEE Journal of Quantum Electronics*, 34(5):900–909, 1998.

[6] Y. Guyot and R. Moncorge. Excited-state absorption in the infrared-emission domain of Nd^{3+} doped $Y_3Al_5O_{12}$, $YLiF_4$, and $LaMgAl_{11}O_{19}$. *Journal of Applied Physics*, 73(12):8526–8530, 1993.

[7] Y. F. Chen, L. J. Lee, T. M. Huang, and C. L. Wang. Study of high-power diode-end-pumped Nd:YVO_4 laser at 1.34 μm : influence of Auger upconversion. *Optics Communications*, 163:198–202, 1999.

[8] J. L. Blows, T. Omatsu, J. Dawes, H. Pask, and M. Tateda. Heat generation in Nd:YVO_4 with and without laser action. *IEEE Photonics Technology Letters*, 10(12):1727–1729, 1998.

[9] W. Koechner and D. K. Rice. Effect of birefringence on the performance of linearly polarized YAG:Nd lasers. *IEEE Journal of Quantum Electronics*, 6(9):557–566, 1970.

[10] Y. F. Chen. Design criteria for concentration optimization in scaling diode end-pumped lasers to high powers: Influence of thermal fracture. *IEEE Journal of Quantum Electronics*, 35(2):234–239, 1999.

[11] V. Lupei, N. Pavel, and T. Taira. Highly efficient laser emission in concentrated Nd:YVO_4 components under direct puping into the emitting level. *Optics Communications*, 201(1-2):431–435, 2002.

[12] T. M. Baer, D. F. Head, P. Gooding, G. J. Kintz, and S. Hutchison. Performance of diode-pumped Nd:YAG and Nd:YLF lasers in a tightly folded resonator configuration. *IEEE Journal of Quantum Electronics*, 28(4):1131–1138, 1992.

[13] A. Giesen, H. Hugel, A. Voss, K. Wittig, U. Brauch, and H. Opower. Scalable concept for diode-pumped high-power solid-state lasers. *Applied Physics B-Lasers and Optics*, 58(5):365–372, 1994.

[14] M. Karzewski, U. Brauch, K. Contag, A. Giesen, I. Johannsen, C. Stewen, and A. Voss. 100 W TEM operation of Yb:YAG thin disc

laser with high efficiency. In *Advanced Solid-State Lasers 1998 Technical Digest*, pages 82–84, 1998.

[15] W. A. Clarkson and D. C. Hanna. Two-mirror beam-shaping technique for high-power diode bars. *Optics Letters*, 21(6):375–377, 1996.

[16] V. Dominic, S. MacCormack, R. Waarts, S. Sanders, S. Bicknese, R. Dohle, E. Wolak, P. S. Yeh, and E. Zucker. 110 W fibre laser. *Electronics Letters*, 35(14):1158–1160, 1999.

[17] B. Ya. Zel'dovich, V.I. Popovichev, V.V. Ragul'skii, F.S. Faizullov, and P.N. Lebedev. Connection between the wave-fronts of the reflected and excited light in stimulated Mandel'shtam-Brillouin scattering. *Soviet Journal JEPT Letters*, 15(3):160, 1972.

[18] R. W. Hellwarth. Generation of time-reversed wave fronts by nonlinear refraction. *Journal of the Optical Society of America*, 67(1):1–3, 1977.

[19] B. J. Feldman, Irving J. B., Fisher R. A., Phipps C. R., Watkins D. E., and Thomos S. J. Through the looking glass with phase conjugation. *Los Alamos science*, 3(1):3–17, 1982.

[20] J. AuYeung, D. Fekete, D. M. Pepper, and A. Yariv. A theoretical and experimental investigation of the modes of optical resonators with phase-conjugate mirrors. *IEEE Journal of Quantum Electronics*, 15(10):1180–1188, 1979.

[21] Juan F. Lam and W. P. Brown. Optical resonators with phase-conjugate mirrors. *Optics Letters*, 5(2):61–63, 1980.

[22] R. A. Fisher. Optical phase conjugation. pages 435–437. Academic Press, 1983.

[23] D. A. Rockwell. A review of phase-conjugate solid-state lasers. *IEEE Journal of Quantum Electronics*, 24(6):1124–1140, 1988.

[24] P. Yeh. Photorefractive phase conjugators. *Proceedings of the IEEE*, 80(3):436–450, 1992.

[25] H. J. Eichler and O. Mehl. Phase conjugate mirrors. *Journal of Nonlinear Optical Physics and Materials*, 10(1):43–52, 2001.

[26] R. A. Fisher. Optical phase conjugation. Academic Press, 1983.

[27] B. Y. Zeldovich, Pilipetsky N. F., and Shkunov V. V. Principles of phase conjugation. Springer-Verlag, 1985.

[28] M. Gower and Proch D. Optical phase conjugation. Springer-Verlag, 1994.

[29] A. Yariv. Optical electronics in modern communications. page 640. Oxford University Press, 1997.

[30] A. Yariv. Compensation for atmospheric degradation of optical beam transmission by nonlinear optical mixing. *Optics Communications*, 21(1):49–50, 1977.

[31] H. Kogelnik and T. Li. Laser beams and resonators. *Proceedings of the IEEE*, 54(10):1312–1328, 1966.

[32] A. E. Siegman. Lasers. pages 858–890. University Science Books, 1986.

[33] D. R. Hall and P. E. Jackson. The physics and technology of laser resonators. pages 21–39. Institute of Physics publishing, 1992.

[34] G. P. Agrawal. Nonlinear fiber optics. page 355. Academic Press, 2001.

[35] Rainbow Photonics. `http://www.rainbowphotonics.com`.

[36] R. G. Harrison, V. I. Kovalev, W. P. Lu, and D. J. Yu. SBS self-phase conjugation of CW Nd:YAG laser radiation in an optical fibre. *Optics Communications*, 163(4-6):208–211, 1999.

[37] A. M. Scott and K. D. Ridley. A review of Brillouin-enhanced 4-wave mixing. *IEEE Journal of Quantum Electronics*, 25(3):438–459, 1989.

[38] J. Feinberg. Self-pumped, continuous-wave phase conjugator using internal reflection. *Optics Letters*, 7(10):486–488, 1982.

[39] A. M. Glass, A. M. Johnson, D. H. Olson, W. Simpson, and A. A. Ballman. 4-wave mixing in semi-insulating InP and GaAs using the photorefractive effect. *Applied Physics Letters*, 44(10):948–950, 1984.

[40] S. Mailis, J. Hendricks, D. P. Shepherd, A. C. Tropper, N. Moore, R. W. Eason, G. J. Crofts, M. Trew, and M. J. Damzen. High-phase-conjugate reflectivity ($>$ 800%) obtained by degenerate four-wave mixing in a continuous-wave diode-side- pumped Nd:YVO_4 amplifier. *Optics Letters*, 24(14):972–974, 1999.

[41] W. Koechner. Solid-state laser engineering. pages 63–65. Springer-Verlag, 1999.

[42] D. C. Brown. Heat, fluorescence, and stimulated-emission power densities and fractions in Nd:YAG. *IEEE Journal of Quantum Electronics*, 34(3):560–572, 1998.

Chapter 2

Saturable gain four-wave mixing

2.1 Overview

In this chapter saturable gain four-wave mixing is introduced as a method of producing phase-conjugate waves. Section 2.2 describes how the gain coefficient of a solid-state amplifier is saturated by increasing beam intensities. The concept of a modulated intensity pattern producing a modulation in the gain of an amplifier, giving rise to gain-gratings, is then presented. The basic idea of four-wave mixing is shown in section 2.5 by an analogy to the more familiar holographic wavefront reconstruction process and it is shown that the phase-conjugate reconstruction of an incident wave can be produced. The modelling of the four-wave mixing process is described in section 2.7 where the spatial evolution of the gain-gratings and their subsequent diffraction efficiency is shown. In section 2.8 the experimental scheme used to demonstrate saturable gain four-wave mixing is described and it is shown that a PCM with reflectivities of greater than unity can be produced. This makes possible the use of gain four-wave mixing phase-conjugate mirrors as distortion correcting gain elements inside adaptive phase-conjugate resonator geometries.

2.2 Gain saturation

The standard expression for the gain experienced by a signal beam of intensity, I, as it travels though an amplifier with a small signal *amplitude* gain coefficient, α_0, is given by [1]

$$\frac{dI}{dz} = 2\alpha_0 I \tag{2.1}$$

It is assumed that the signal beam is of sufficiently low intensity, thereby maintaining a constant population inversion density and hence gain coefficient as it propagates along the length of the amplifier. This is known as the small-signal condition. As the signal fields intensity grows further it starts to significantly deplete the population inversion causing a decrease in the local gain coefficient and so grows at a slower rate as it continues to travel through the amplifier. Equation 2.1 can be modified to show this saturation behavior giving [1]

$$\frac{dI}{dz} = 2\alpha_{sat} I \tag{2.2}$$

where α_{sat} is the homogenously broadened saturated gain coefficient and is given on resonance by [2]

$$\alpha_{sat} = \frac{\alpha_0}{1 + \frac{I}{I_{sat}}} \tag{2.3}$$

this equation describes how the small-signal (unsaturated) gain coefficient, α_0, is reduced as the signal field intensity, I, increases. I_{sat} is the saturation intensity, a property of the gain medium material, and is defined as the signal intensity required to reduce the gain coefficient to half of its small-signal value. The saturation intensity for a signal beam of angular frequency ω is [1]

$$I_{sat} = \frac{\hbar\omega}{\sigma_{se}\tau} \tag{2.4}$$

where σ_{se} is the stimulated emission cross section of the amplifier material and τ is its fluorescence lifetime ($I_{sat} = 0.83\ kW\ cm^{-2}$ for Nd:YVO_4) [3].

Substituting equation 2.4 into equation 2.2 and integrating from I_1 to I_2, at z_1 and z_2 respectively, the saturated gain equation is obtained [1]

$$\ln\left(\frac{I_1}{I_2}\right) + \frac{I_1 - I_2}{I_{sat}} = 2\alpha_0 z \tag{2.5}$$

where $z = z_2 - z_1$. The intensity at a distance, z, inside the amplifier for a given signal input intensity and small signal gain, α_0, can then be found by solving equation 2.5 numerically.

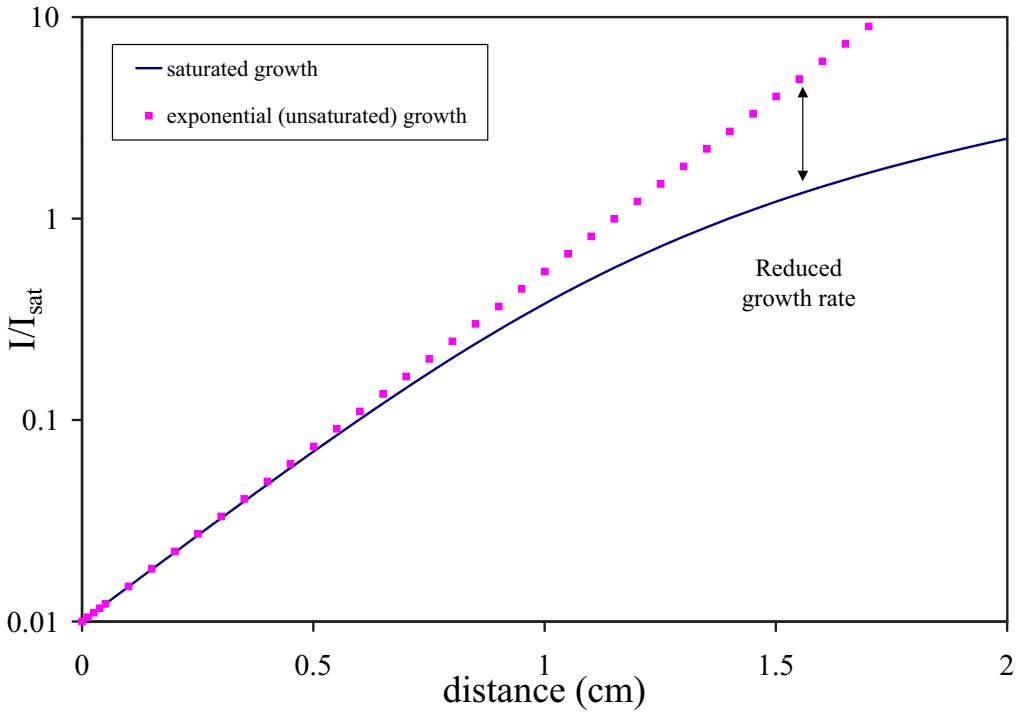

Figure 2.1: Plot of the intensity (normalised to I_{sat}) against distance within a single pass amplifier.

Figure 2.1 shows how an initial input intensity, $I_1 = 0.01\ kW\ cm^{-2}$, is amplified as it travels along an amplifier with a small-signal gain coefficient, $\alpha_0 = 2\ cm^{-1}$ and an $I_{sat} = 1\ kW\ cm^{-2}$. In the unsaturated case the growth is exponential and the gain coefficient is constant. In the saturated case the growth, at low intensities, is exponential and matches that of the unsaturated line. As the intensity is increased further the gain falls

resulting in reduced growth of the wave as it travels along the amplifier. Figure 2.2 shows how the saturated gain coefficient, α_{sat}, which has been normalised to α_0, evolves along the amplifier due to the growth of the field intensity as shown in figure 2.1. The important point to note here is

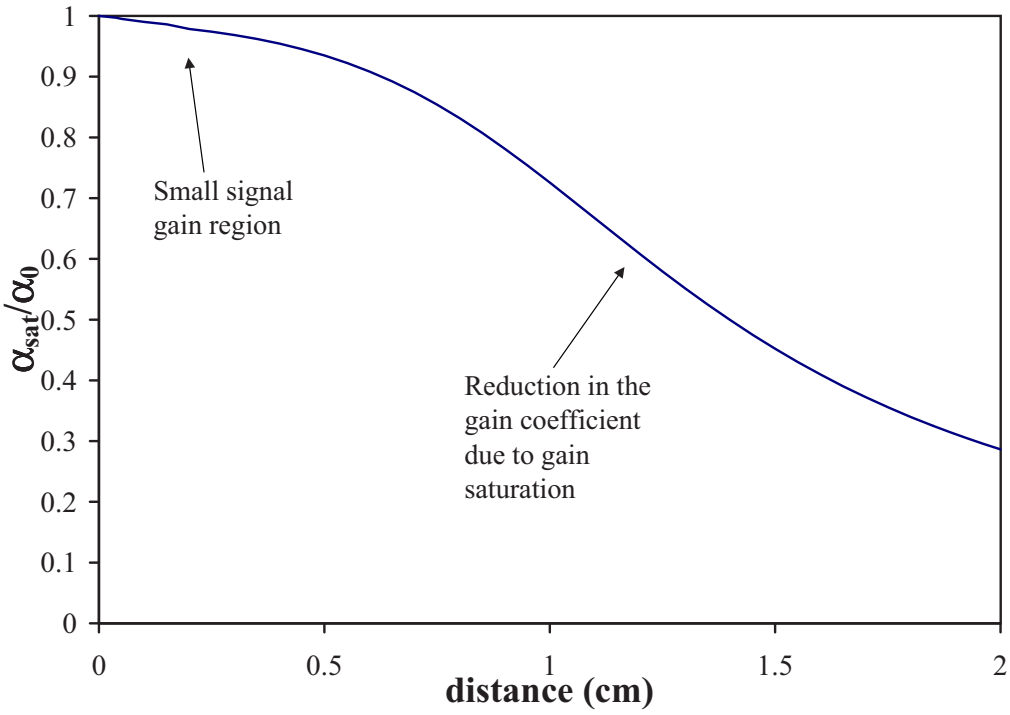

Figure 2.2: Plot of the gain coefficient, α_{sat}, (normalised to α_0) against distance within a single pass amplifier.

that a field with a spatially dependent intensity profile, incident within an amplifying medium will produce a locally varying gain coefficient in that medium. For example, the standing wave field profile produced within a linear laser cavity can significantly reduce the gain at the antinodes of the interference pattern whilst having little or no effect at the nodes thereby spatially burning holes in the gain. This can be problematic as other longitudinal modes of the linear cavity can start to oscillate by accessing the unused gain in the nodal areas of the first standing wave [4] and so resonators have to be engineered that avoid such problems [5].

2.3 Gain-gratings

The spatial hole burning of the amplifier gain described in section 2.2 is central to the operation of the phase-conjugate resonators presented later in this thesis. It was shown that the small signal gain, α_o, of an amplifier could be saturated by a field of intensity, I, according to

$$\alpha_{sat} = \frac{\alpha_o}{1 + \frac{I}{I_{sat}}} \tag{2.6}$$

Figure 2.3 shows graphically how a modulated intensity, produced for example within an interference pattern, can lead to a modulation in the local gain of an amplifier. The gain-grating is formed when the two fields E_1 and E_2 interfere within the amplifier (assuming the frequency of the fields lie within the gain-bandwidth of the medium). The high intensity antinodes of the interference pattern deplete the population inversion to a much larger extent than the low intensity nodes leading to a corresponding modulation in the local gain coefficient. This modulated gain can be viewed as a volume diffraction grating in which is stored all the information needed to reconstruct both the phase and amplitude of the two original beams. It can be seen from figure 2.3 that the grating has a π phase-shift with respect to the interference pattern, as the maximum of the modulated gain occurs for local minima within the interference pattern and vice-versa. This π phase-shift has important consequences for the design of any adaptive phase-conjugate resonators incorporating volume gain-gratings and is discussed further in section 3.6.

2.4 Grazing incidence amplifier

A major shortcoming in the side-pumping of solid-state lasers is the poor overlap between the laser mode and the pumped region, and this can result in poor utilisation of the gain available within the crystal. Another concern is the non-uniform gain seen by the laser mode as it travels through the inverted region [6]. The side of the beam nearest the pump

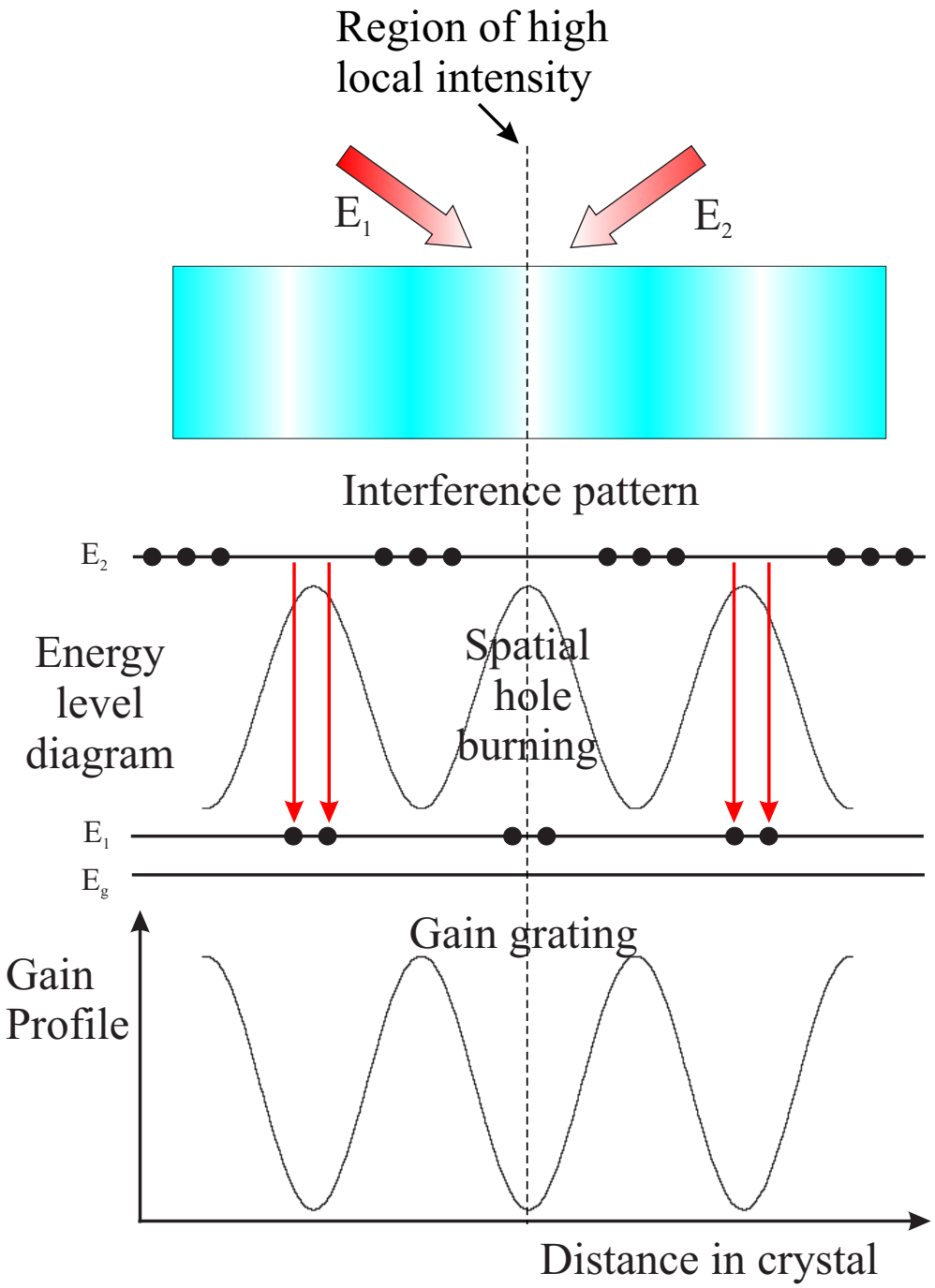

Figure 2.3: The interference between two mutually coherent fields that are resonant with the gain of the crystal burns holes in the population inversion. Regions of modulated gain can be viewed as a volume grating which is π out of phase with the interference pattern

face experiences more gain than the side furthest from it, a consequence of the fact that the population inversion experiences an exponential decrease as a function of distance within the crystal. End-pumping schemes, in general, do not suffer from this effect as the pumping-beam can be matched very effectively to the laser mode using beam-shaping techniques [7] or fibre pump delivery schemes. On the other hand, side pumping with a laser diode can be advantageous in that it tends to spread the thermal load over a larger area of the crystal reducing detrimental thermal effects such as those described in section 1.1.1.

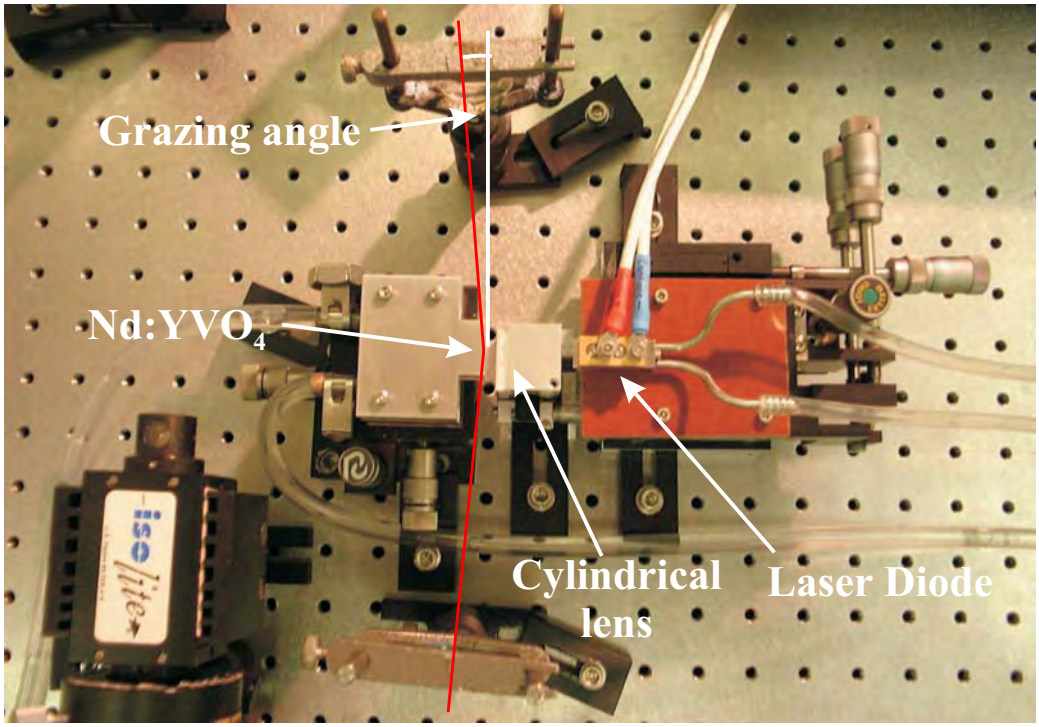

Figure 2.4: Bounce geometry diode pumped amplifier.

A side-pumping scheme that can, to some extent, overcome the problems mentioned above is the grazing incidence amplifier shown in figure 2.4 (after Bernard *et al* [6]). In this scheme the crystal is side-pumped by a laser-diode brought to a line focus using a cylindrical lens. A probe laser beam is then focussed into the crystal such that it makes a small grazing angle with the side-pumped face where it is subsequently totally internally reflected, the reflected beam then exits from the other side of the crystal (see figure 2.5). There are two major advantages to this scheme. Firstly, the probe beam travels into the region of highest inversion density, the

region closest to the pumped face, and hence can access the higher gain. Secondly, to a first approximation, the non-uniformity of the gain region is averaged out across the whole beam as it is reflected from the pumped face: this aspect will be explored further in section 2.4.3.

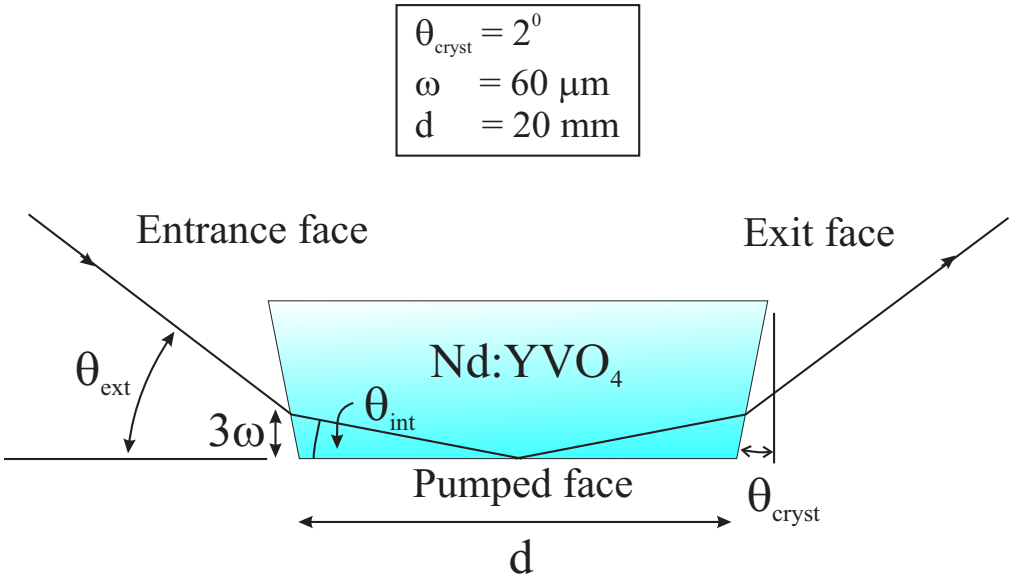

Figure 2.5: Bounce geometry inside the diode-pumped amplifier.

Figure 2.5 shows a schematic of the Nd:YVO_4 crystal used in the adaptive phase-conjugate resonator described in chapter 3. The crystal's faces were wedged with an angle, $\theta_{cryst} = 2^0$, reducing the effect of parasitic lasing occurring within the crystal thereby reducing the available gain. For the probe beam to access as much of the stored power within the crystal as possible it would have to enter the crystal very close to the pumped face at a small internal angle, θ_{int}. In order to reduce the diffraction loss of the probe beam as it enters the crystal the distance from the pumped face to the point of entry should be roughly 3ω, where ω is the spot size of the probe beam at the entrance face of the crystal. To achieve total internal reflection at the centre of the pump face the minimum internal angle, θ_{int}, is given by

$$\theta_{int} = \tan^{-1}\left(\frac{3\omega}{d/2}\right) \tag{2.7}$$

where d is the length of the crystal. For example, using a 20 mm long

crystal where the spot size of the probe at the entrance face is 60 μm , the minimum internal angle that can achieve reflection from the pumped crystal face without significant diffraction loss at the entrance face of the crystal is around 1^0. From geometrical consideration and the use of Snell's law, the external angle, θ_{ext}, required for a given internal angle, θ_{int}, is given by

$$\theta_{ext} = \sin^{-1}\left(n \sin\left(\theta_{int} + \theta_{cryst}\right)\right) - \theta_{cryst} \tag{2.8}$$

where n is the appropriate refractive index for Nd:YVO_4 . For a value of $\theta_{cryst} = 2^0$, a refractive index value n = 2.17 and a $\theta_{int} = 1^0$, the required external angle is approximately 4.5^0. The minimum external angle at which the probe beam can enter the crystal without suffering significant diffraction losses at the crystal entrance face is therefore around 4.5^0 with a point of entry, 3ω, which is 180 μm from the pumped face.

2.4.1 Diode pumping

An important parameter in the design of any diode-pumped solid state laser is the focussed spot size of the diode beam inside the amplifier crystal. Once this is known it will then be possible to engineer the spot size of the laser beam mode, via use of appropriate focal length lenses, such that the overlap between the mode and the pumped region of the crystal can be maximised, thereby extracting the maximum available power.

The diode laser bars used in all the experiments described in this thesis all had high power, highly divergent elliptical output beams making impossible the use of a commercial M^2 measuring device (such as a Coherent Modemaster). One way of determining the M^2 of the diode is to use the scanning slit technique [8] shown in figure 2.6.

Using this procedure the second moment of the vertical intensity distribution can be found by scanning a silicon photodiode with a horizontal slit arrangement (consisting of two razor blades spaced by around 100 μm) in the y direction and noting the intensity profile on an oscilloscope attached

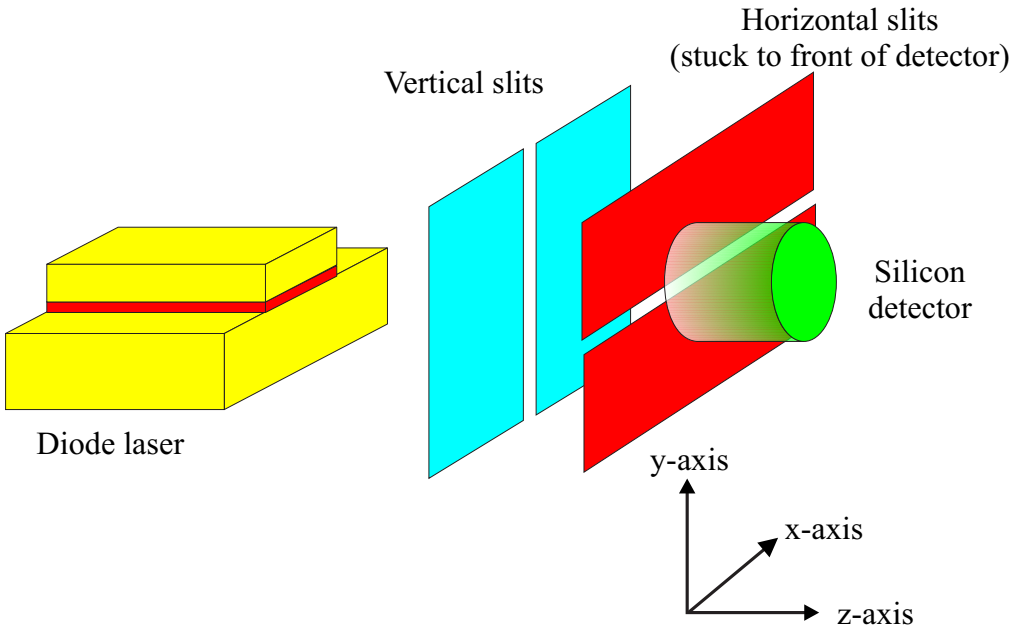

Figure 2.6: Apparatus used to measure spot size and M^2 of a diode laser.

to the silicon detector. The second moment of a beam (in rectangular coordinates) in the y direction, $\sigma_y^2(z)$, a distance z along the beam propagation axis is given by [9] (see appendix A for a derivation)

$$\sigma_y^2(z) = \frac{\int_{-\infty}^{\infty}\int_{-\infty}^{\infty}(y-\bar{y})^2 I(x,y,z)\,dxdy}{\int_{-\infty}^{\infty}\int_{-\infty}^{\infty} I(x,y,z)\,dxdy} \tag{2.9}$$

where $\bar{y}$ is the centroid (first moment) of the intensity distribution, $I(x,y,z)$. The beam spot size at position z along the beam propagation axis, $\omega_y(z)$, can then be found using (see appendix A)

$$\omega_y(z) = 2\sigma_y(z) \tag{2.10}$$

Following the analysis of Bonner [10] the procedure for experimentally finding the waist size is as follows

1. The vertical and horizontal slits are placed at a set position, z, along the beam propagation axis. The silicon detector and horizontal slits

arrangement is then scanned in the y direction and the intensity profile for each y position is obtained from the oscilloscope.

2. The centroid, $\bar{y}$, of the intensity profile is located.

3. The y axis data is then offset so that the centroid of the measured intensity profile lies at $y = 0$.

4. The area under the intensity profile is set to unity

$$I_{norm}(y) = \int_{-\infty}^{\infty} I(y)dA = 1 \tag{2.11}$$

5. The second moment (in its discrete form) is found using

$$\sigma_y^2(z) = \sum_{-\infty}^{\infty} y^2 I_{norm}(y) \tag{2.12}$$

6. Finally the beam spot size at position z, $\omega_y(z)$, can be found using equation 2.10.

The spot sizes are then recorded at several z positions along the diode beam propagation path. Knowing the spot size, $\omega_y(z)$, for each value of z, the far-field divergence half-angle, θ_{half} of the diode beam can be found using

$$\theta_{half} = \tan^{-1}\left(\frac{\omega_y(z)}{z}\right) \tag{2.13}$$

A value for the diode beam M^2 parameter can then be obtained using

$$M^2 = \frac{\pi\omega_0\theta_{half}}{\lambda} \tag{2.14}$$

Where ω_0 is the waist size of the diode beam and λ is its wavelength. Using the above method the M^2 parameter was found for both the 40 W and 60 W *fibre lensed* diodes used in this thesis yielding values of 5 and 5.5 respectively. Knowing this value it is now possible to calculate the spot

size, $\omega_{focussed}$, of the diode beam after passing through a lens of known focal length , f, using the formula

$$\omega_{focussed} = \frac{M^2 \lambda f}{\pi \omega_{lens}} \tag{2.15}$$

where ω_{lens} is the spot size of the beam at the lens. In the experiments described in this thesis two different focal length cylindrical lenses were used to launch the diode pump light into the Nd:YVO_4 crystal. The first (f = 12.7 mm) gives a focussed spot size, $\omega_{focussed}$, of 72 µm when placed into equation 2.15 (where M^2 = 5.5, λ = 808 nm and ω_{lens} = 250 µm). The second lens with a focal length, f, of 6.35 mm yielded a focussed spot size, $\omega_{focussed}$, of 36 µm .

2.4.2 Amplifier model

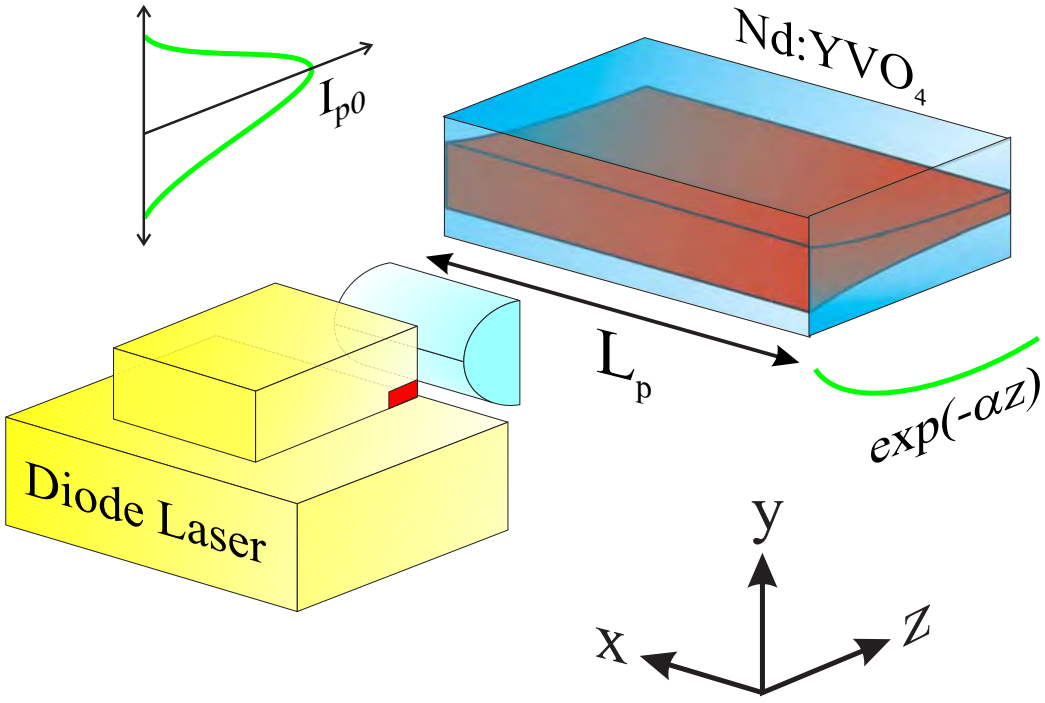

Figure 2.7: Schematic of the gain model geometry.

The intensity incident at any point in a laser gain medium, $I_P(x, y, z)$, due to the laser diode pump source shown in figure 2.7 is given by

$$I_P(x,y,z) = I_{P0}(0,0,0)\exp\left(-\frac{2y^2}{\omega_P^2(z)}\right)\exp(-\alpha z)\,tophat\left(\frac{x}{L_p}\right) \quad (2.16)$$

where it is assumed that the pump diode emits a beam with a Gaussian distribution (with a peak intensity $I_{P0}(0,0,0)$) in the fast-direction (y-axis) and a top-hat function in the slow-direction (x-axis) with a width of L_p. The Gaussian beam width, $\omega_P(z)$, of the pump beam varies as it propagates into the crystal. However, the Rayleigh range of the focussed pump beam

$$z_r = \frac{\pi\omega_0^2}{M^2\lambda} \quad (2.17)$$

for a pump wavelength, λ = 808 nm, with an M^2 of 5 focussed to a waist size of, ω_0 = 72 µm is 4 mm (or 8.8 mm when focussed into the Nd:YVO_4 crystal with refractive index of 2.2) which is much greater than the absorption depth of a 1.1 at.% doped Nd:YVO_4 crystal (320 µm for 1.1 atm% doped crystal) [11]. It is therefore assumed that ω_P is constant and hence any z-axis dependence of the focussed pump beam is lost. The total incident power from the diode pump source, P_{inc}, is given as

$$\begin{aligned}
P_{inc} &= \int_{Area} I_P(x,y,0)\,dA \\
P_{inc} &= \int_{y=-\infty}^{\infty}\int_{x=0}^{L_P} I_P(x,y,0)\,dxdy \\
P_{inc} &= 2L_P I_{P0}(0,0,0)\int_{y=0}^{\infty}\exp\left(-\frac{2y^2}{\omega_P^2(0)}\right)dy \\
P_{inc} &= I_{P0}(0,0,0)\,L_P\omega_P(0)\sqrt{\frac{\pi}{2}}
\end{aligned} \quad (2.18)$$

rearranging this in terms of $I_{P0}(0,0,0)$ and substituting into 2.16 gives

$$I_P(x,y,z) = \frac{P_{inc}}{L_P\omega_P(0)}\sqrt{\frac{2}{\pi}}\exp\left(-\frac{2y^2}{\omega_P^2(z)}\right)\exp(-\alpha z)\,tophat\left(\frac{x}{L_p}\right) \quad (2.19)$$

This equation describes the pump intensity distribution at every point inside the crystal given in terms of the diode laser total power output, P_{inc}, and the geometry of the pump beam.

To find the rate per unit volume, R_P, at which the crystal (with a pump absorption coefficient α) is pumped at a specific point equation 2.16 can be substituted into

$$R_P = \frac{\alpha I_P(x,y,z)}{h\nu_P} \tag{2.20}$$

giving

$$R_P(x,y,z) = \frac{\alpha}{h\nu_P}\frac{P_{inc}}{L_P\omega_P(0)}\sqrt{\frac{2}{\pi}}\exp\left(-\frac{2y^2}{\omega_P^2(z)}\right)\exp(-\alpha z)\,tophat\left(\frac{x}{L_P}\right) \tag{2.21}$$

The steady-state four-level rate equation for the crystal without a lasing field present is given by

$$\frac{dN_0(x,y,z)}{dt} = R_P(x,y,z) - \frac{N_0(x,y,z)}{\tau} = 0 \tag{2.22}$$

where $N_0(x,y,z)$ is the unsaturated inverted population density of the upper laser level per unit volume and τ is the fluorescence lifetime of that level. Rearranging 2.22 and substituting 2.21 gives

$$\begin{aligned} N_0(x,y,z) &= R_P(x,y,z)\,\tau \qquad (2.23)\\ &= \frac{\alpha}{h\nu_P}\frac{P_{inc}\tau}{L_P\omega_P(0)}\sqrt{\frac{2}{\pi}}\exp\left(-\frac{2y^2}{\omega_P^2(z)}\right)\exp(-\alpha z)\,tophat\left(\frac{x}{L_P}\right) \end{aligned}$$

and this equation then describes the unsaturated population at any point in the crystal in terms of the pump power, the pump geometry and the crystal properties. However, at the high levels of pumping intensities used throughout this thesis, effects such as ETU are expected to play a role in reducing the gain available for amplification of a laser beam. This can be

included into the rate equation 2.22 with the addition of a term describing the rate per unit volume at which ETU processes occur from the upper laser level

$$\frac{dN_0(x,y,z)}{dt} = R_P(x,y,z) - \frac{N_0(x,y,z)}{\tau} - WN_0^2(x,y,z) \tag{2.24}$$

where W is the upconversion parameter which for Nd:YVO_4 has a value of $4 \times 10^{-22}\ m^3 s^{-1}$ [12]. At steady-state, equation 2.24 can be expressed as a quadratic equation

$$WN_0^2(x,y,z) + \frac{N_0(x,y,z)}{\tau} - R_P(x,y,z) = 0 \tag{2.25}$$

with the solution

$$N_0(x,y,z) = \frac{-\tau^{-1} + \sqrt{\tau^{-2} + 4WR_P(x,y,z)}}{2W} \tag{2.26}$$

The steady-state inversion (including ETU) at any point in the crystal can now be found by substituting equation 2.21 in to equation 2.26.

The unsaturated gain per unit length at any point in the crystal is given as $g_0(x,y,z) = \sigma_{se} N_0(x,y,z)$ where σ_{se} is the stimulated emission cross-section for the laser transition. The saturated gain per unit length is found using

$$g_{sat}(x,y,z) = \frac{g_0(x,y,z)}{1 + \frac{I_{las}(x,y,z)}{I_{sat}}} = \frac{\sigma_{se} N_0(x,y,z)}{1 + \frac{I_{las}(x,y,z)}{I_{sat}}} \tag{2.27}$$

The differential equation describing the growth of the laser beam, $I_{las}(x,y,z)$, as it travels through a pumped region of gain, $g_{sat}(x,y,z)$, is

$$\begin{aligned} \frac{dI_{las}(x,y,z)}{dz} &= g_{sat}(x,y,z)\, I_{las}(x,y,z) \\ \frac{dI_{las}(x,y,z)}{dz} &= \frac{\sigma_{se} N_0(x,y,z)}{1 + \frac{I_{las}(x,y,z)}{I_{sat}}} I_{las}(x,y,z) \end{aligned} \tag{2.28}$$

The bounce geometry in the amplifier configuration requires equation 2.28 to be modified. Upon reflection from the pumped face of the crystal part of the signal beam will pass through a region of gain that contains part of the intensity from the same beam before reflection, as shown in region A of figure 2.8. As well as the self-saturation the reflected beam experiences due its own intensity it also experiences a cross-saturation from the beam before reflection. Taking this into account equation 2.28 now becomes

$$\frac{dI_{las}(x,y,z)}{dz} = \frac{\sigma_{se} N_0(x,y,z)}{1 + \frac{I_{total}(x,y,z)}{I_{sat}}} I_{las}(x,y,z) \tag{2.29}$$

where $I_{total}(x,y,z)$ is the total intensity at that point in the crystal from both the field before and the field after reflection from the pump face.

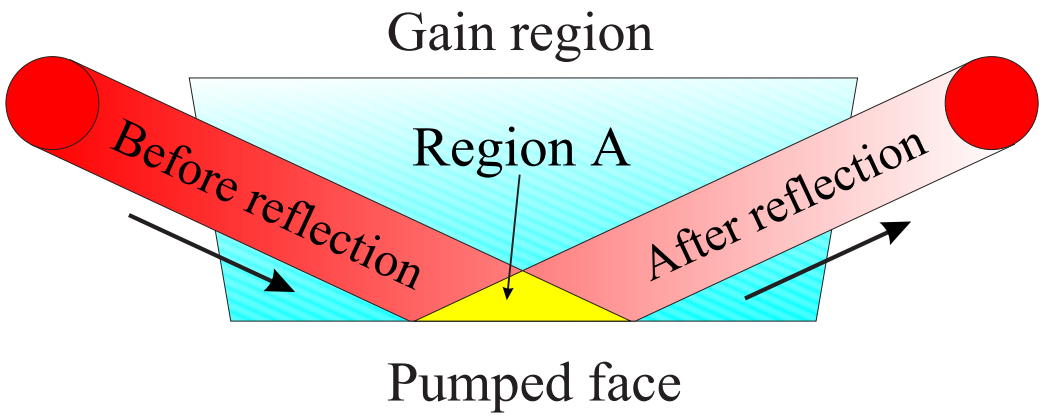

Figure 2.8: Self and cross saturation of the probe beam.

2.4.3 Numerical gain model

Equations 2.29 along with equation 2.23 were then solved numerically using a program written in Matlab code. The pump intensity distribution within the Nd:YVO_4 crystal shown in figure 2.7 is shown in figure 2.9. A diode pump spot size, ω_P, of 36 µm was used corresponding to a diode cylindrical focussing lens of 6.35 mm (see section 2.4.1) . In the y-direction the Gaussian pump beam has its maximum intensity at the centre of the crystal, either side of which the intensity is reduced. In the z-direction

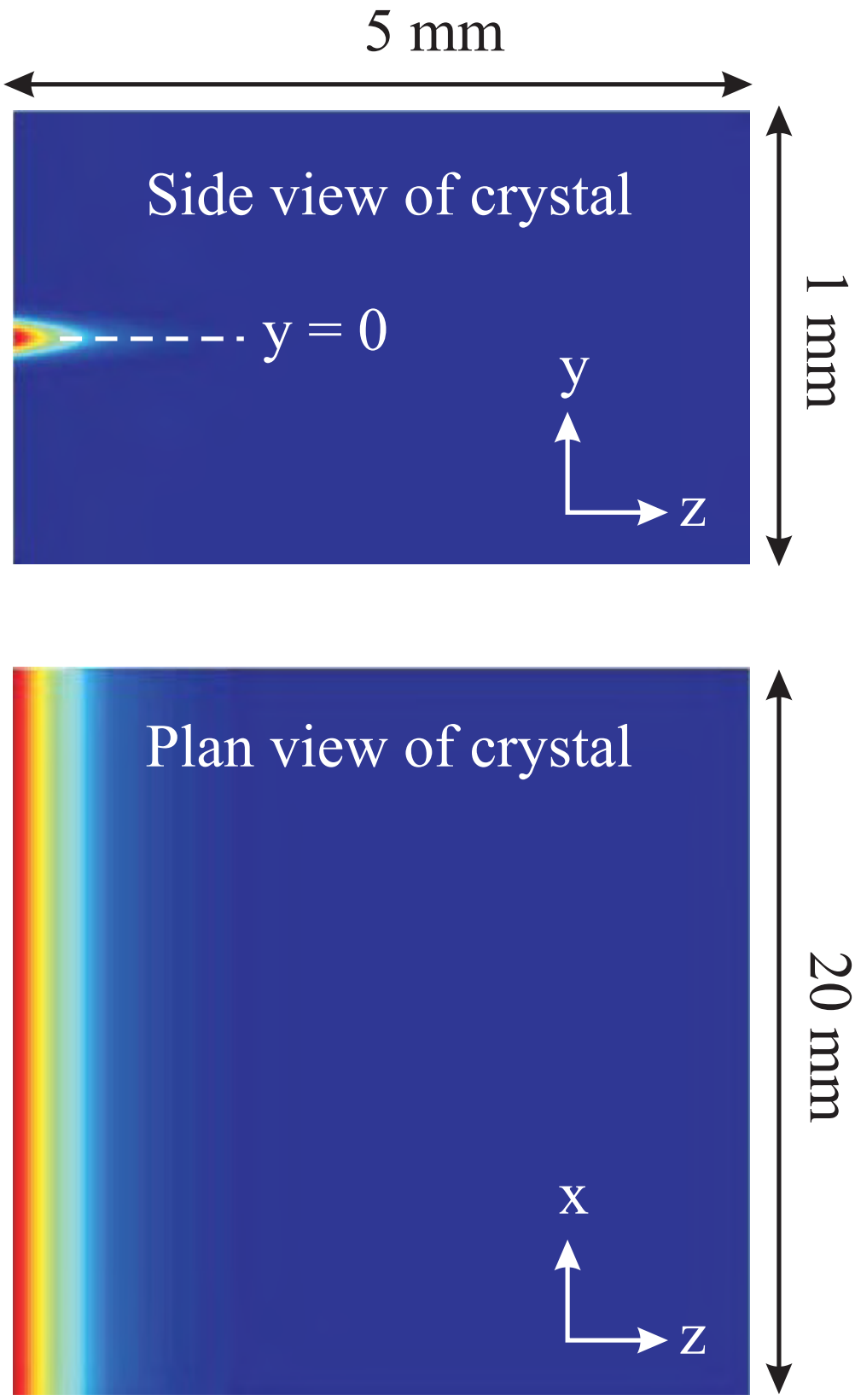

Figure 2.9: The modelled diode pump intensity distribution within the Nd:YVO_4 crystal.

the intensity decays exponentially with distance, resulting in the highest intensities being at the pumped face of the crystal.

A Gaussian input beam, shown in figure 2.10, with a spot size of 36 μm was then traced through the pumped crystal shown in figure 2.9. The Gaussian input beam was segmented into a 100 by 100 array and each individual element traced through the gain region, reflecting off the pumped face of the crystal to become the output.

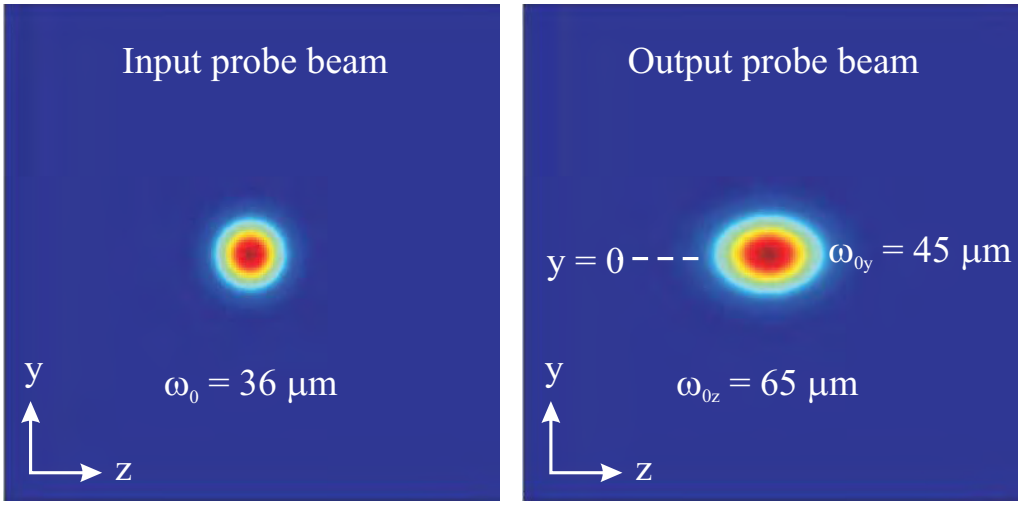

Figure 2.10: The modelled circular Gaussian input beam and reshaped output.

The amplified output beam, shown in figure 2.10, has been reshaped by the non-uniform gain distribution within the crystal. The spot-size of the output in the z-direction is seen to exceed that in the y-direction. This is due to the Gaussian pump distribution in the y-direction with its peak intensity, and hence peak gain, occurring at y = 0 (see figures 2.9 and 2.10) for other values of y the probe travels through the wings of the Gaussian pump distribution as so experiences less gain resulting in the elliptically shaped output [6, 13]. This gain model was then compared to the experimental results using the parameters shown in table 2.1.

A Gaussian probe beam of known power was used for the input and its single pass gain was measured. This was repeated for a number of different input probe beam powers and the results are shown in figure 2.11. The green line shows the modelling results for a diode spot size of 72 μm at the

Diode focussing lens	12.7 mm	6.35 mm
Diode pump spot size	72 µm	36 µm
Diode pump power	32 W	32 W
External probe beam angle	4 °	4 °
Probe beam spot size	36 µm	36 µm
Probe beam power range	1 mW - 300 mW	1 mW - 300 mW
Crystal dimensions	1 * 5 * 20 mm	1 * 5 * 20 mm

Table 2.1: Parameters used in model

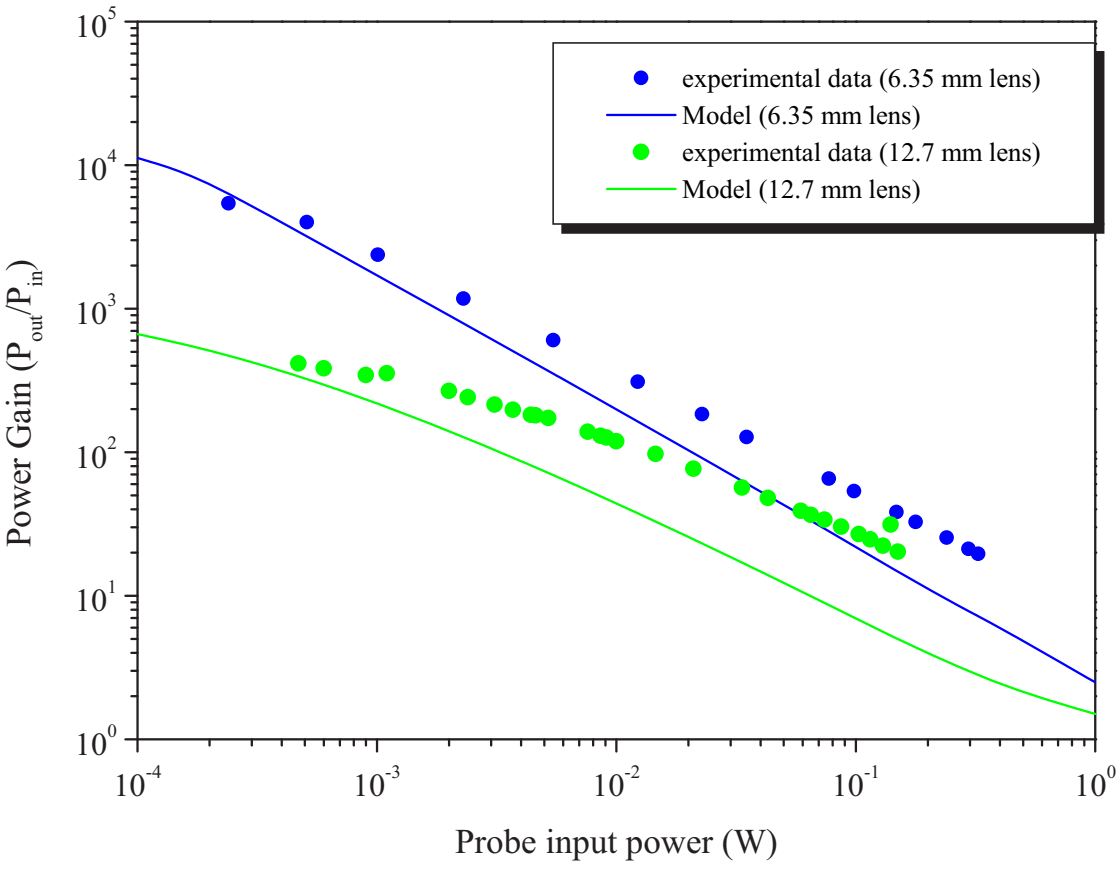

Figure 2.11: A graph comparing the modelled and experimental single pass gain data.

pumped face of the crystal and the green points show the experimental values obtained using a 12.7 mm focal length cylindrical diode focussing lens and the other parameters shown in table 2.1. The blue line and blue points show the modelling and experimental values, respectively, for the 6.35 mm focal length focussing lens, corresponding to a spot-size of 36 μm at the pumped face of the crystal. The model shows reasonable agreement with both sets of experimental data at low input probe powers predicting small-signal single pass (SSSP) gains of 1000 and 15000 (extrapolated from the graph) for the 12.7 mm lens and 6.35 mm lens respectively. At larger probe input powers the experimental data points shows that the gain saturates less than that predicted by the model. As a result the modelled gain is around a factor of 4 less than that found experimentally.

Using this bounce geometry in a Nd:YVO_4 crystal with 60 W of pump power experimental SSSP gains of greater than 15000 have been achieved. These extremely high gains, due to the high absorption coefficient, wide absorption bandwidth and large stimulated emission cross section of Nd:-YVO_4, allow gain-gratings of high contrast to be written within the amplifier with correspondingly high diffraction efficiency [14].

2.5 Holographic analogy of FWM

In the previous sections it was shown how the saturation of gain within an amplifier can lead to the formation of volume gain-gratings when an on-resonance modulated intensity is present. In this and the subsequent sections the use of these gain-gratings as dynamic diffractive elements is explored with values of diffraction efficiencies that can greatly exceed unity. It is shown that in certain four-wave mixing geometries a wave can be produced that is the amplified phase-conjugate of one of the interacting beams. A good way to grasp the general concept of gain saturation FWM is to compare it to the more familiar process of volume holography. Figure 2.12 shows the basic holographic technique. Two mutually coherent fields, the forward pump (FP) and signal beam (S) are described by $E_{FP} = \psi_{FP}(r)\, e^{i(\omega t - kz)}$ and $E_S = \psi_S(r)\, e^{i(\omega t - kz)}$ where ω is the angular frequency

of the fields, k is their wavenumber and $\psi_{FP,S}(r) = A_{FP,S}(r)\, e^{-\phi_{FP,S}(r)}$ is the complex amplitude describing the transverse amplitude, $A(r)$, and phase variations, $\phi(r)$, from that of a plane wave. The two fields are made to overlap within a suitable holographic material where they interfere and produce a volume holographic grating. This volume grating contains all the information needed to reconstruct the phase and amplitudes of either of the original interfering beams given the appropriate reading beam.

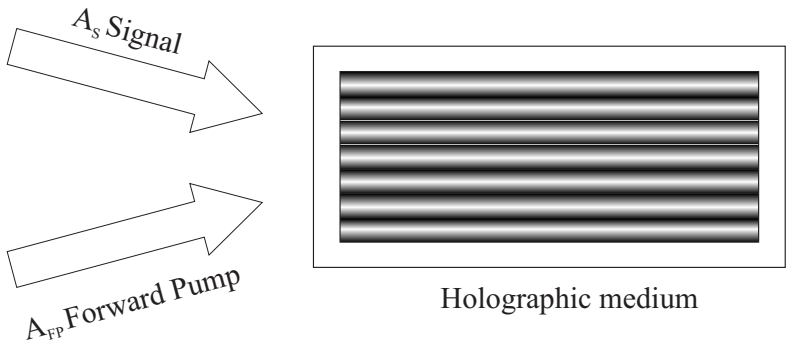

Figure 2.12: Formation of a diffraction grating by the interference of two writing beams (the forward pump and signal) inside a medium that is capable of recording the resultant interference pattern.

The intensity distribution recorded in the grating due to the interference of the two fields is given by

$$I = (E_{FP} + E_S)(E_{FP} + E_S)^* \tag{2.30}$$

which after expansion becomes

$$I = E_{FP}E_{FP}^* + E_S E_S^* + E_{FP}E_S^* + E_S E_{FP}^* \tag{2.31}$$

In conventional holography the grating writing beams are now turned off and the recording material is processed to produce a permanent grating or hologram. The signal field can then be reconstructed by redirecting the FP towards the hologram at the same angle and position as used for recording as shown in figure 2.13.

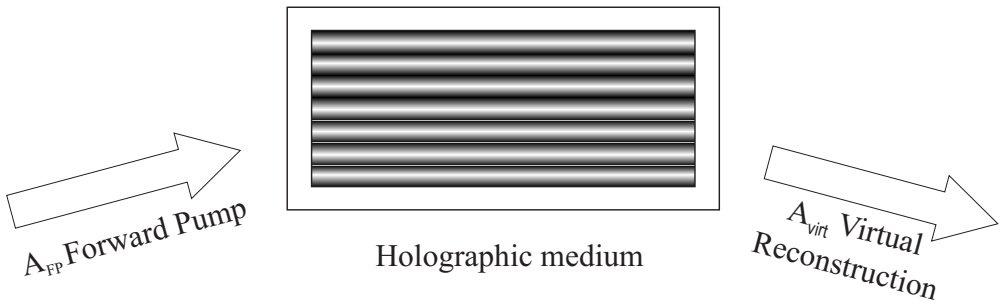

Figure 2.13: Reading the stored volume-hologram to produce a virtual reconstruction of the original signal beam.

The hologram is developed in such a way that the amplitude transmittance, t, of the hologram is linearly proportional to the intensity distribution of the interference pattern described by equation 2.31 [15].

$$t \propto I \tag{2.32}$$

The FP in figure 2.13 is diffracted by the volume hologram to form a virtual image of the signal field (the reconstructed hologram). The transmitted complex amplitude of this new field, E_{virt}, is the product of the amplitude transmittance, t, and E_{FP} and is given by

$$E_{virt} \propto tE_{FP} = \left(E_{FP}E_{FP}^{*} + E_{S}E_{S}^{*}\right)E_{FP} + E_{FP}E_{FP}E_{S}^{*} + E_{FP}E_{FP}^{*}E_{S} \tag{2.33}$$

or rewriting in terms of intensities

$$E_{virt} = \underbrace{\left(I_{FP} + I_{S}\right)E_{FP}}_{1} + \underbrace{E_{FP}^{2}E_{S}^{*}}_{2} + \underbrace{I_{FP}E_{S}}_{3} \tag{2.34}$$

The first term in equation 2.34 is just a proportional reconstruction of the FP which passes straight through the volume hologram (the zeroth order of the grating). The second term is not phased matched to the grating and will not radiate in a volume hologram where the Bragg condition needs to satisfied. The third term represents the proportional reconstruction of the signal wave and produces a virtual image of the original object (first order diffraction from the grating).

2.5.1 Producing the PC wave

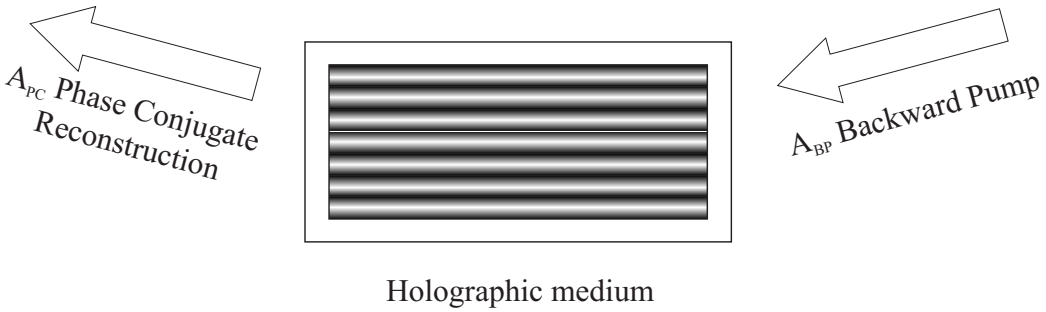

Figure 2.14: Reading off the volume-hologram using a backward pump which is the phase-conjugate of the forward pump. This configuration produces a phase-conjugate reconstruction of the original signal beam

A phase-conjugate reconstruction of the signal field can be produced by reading the hologram with a field that is the phase-conjugate of the FP. This new field, the backward pump (BP), is given by

$$E_{BP} = E^*_{FP} \tag{2.35}$$

Figure 2.14 shows the geometry used in the phase-conjugate reconstruction process. The reconstructed field, E_{PC}, produced when the grating is read by the BP is given by

$$E_{PC} \propto tE_{BP} = \left(E_{FP}E^*_{FP} + E_S E^*_S\right) E_{BP} + E_{BP}E_{FP}E^*_S + E_{BP}E^*_{FP}E_S \tag{2.36}$$

Substituting $E_{BP} = E^*_{FP}$ into equation 2.36 gives

$$E_{PC} \propto tE^*_{FP} = \left(E_{FP}E^*_{FP} + E_S E^*_S\right) E^*_{FP} + E^*_{FP}E_{FP}E^*_S + E^*_{FP}E^*_{FP}E_S \tag{2.37}$$

Again, rewriting in terms of intensities

$$E_{PC} \propto tE^*_{FP} = \underbrace{\left(I_{FP} + I_S\right) E^*_{FP}}_{1} + \underbrace{I_{FP}E^*_S}_{2} + \underbrace{\left(E^*_{FP}\right)^2 E_S}_{3} \tag{2.38}$$

The first term in equation 2.38 is just a proportional reconstruction of the BP (which is the phase-conjugate of the FP). The second term is the important term that represents the phase-conjugate holographic reconstruction of the signal field (E_S^* term). The third term is again not phased matched to the grating and will not radiate in a volume hologram.

2.6 Other gratings formed

In section 2.5 FWM was introduced by being compared to the more familiar process of *static* holography, a permanent grating was written inside a material that was processed in such a way as to store the interference pattern, once the writing beams had been removed. The grating was subsequently read out by a reading beam to produce a PC wave. The process of writing and reading the gratings in *static* holography is usually considered as two independent processes, whereas gain FWM is a *dynamic* interaction and the gain-grating will change in response to a change in the writing beams. All four FWM beams (the FP, BP, S and PC) are present at the same time within the *dynamic* gain medium and so interference can occur between all of the mutually coherent beams present and several other gratings are simultaneously formed within the gain medium.

In a four-wave mixing interaction the total electric field present in a saturable gain medium is given by

$$\underline{\varepsilon}_T(\underline{r},t) = \tfrac{1}{2}\underline{E}_T(\underline{r},t)\exp(i\omega t) + c.c. \tag{2.39}$$

where $\underline{E}_T$ is the total complex electric field amplitude for the four fields present and is given by

$$\underline{E}_T = \psi_1 e^{-i\underline{k}_1\cdot\underline{r}} + \psi_2 e^{-i\underline{k}_2\cdot\underline{r}} + \psi_3 e^{-i\underline{k}_3\cdot\underline{r}} + \psi_4 e^{-i\underline{k}_4\cdot\underline{r}} \tag{2.40}$$

where $\underline{k}_j$ is the wave vector of the jth field with magnitude $\left|\underline{k}_j\right| = k = 2\pi n/\lambda_0$ with λ_0 the wavelength of the interacting fields in free-space and

n the refractive index of the gain medium. The complex slowly varying amplitude, ψ_j , describes the amplitude and phase variations of the jth electric field and is written as

$$\underline{\psi}_j = A_j e^{\phi_j} \tag{2.41}$$

where A_j describes the amplitude and ϕ_j describes the phase structure in the transverse direction of the fields. The four interacting fields present in the saturable gain medium will now write a series of gain-gratings via the process of spatial hole burning. The total time averaged intensity within the medium is given by [16]

$$I_T = \tfrac{1}{2} n \varepsilon_0 c \underline{E}_T \underline{E}_T^* \tag{2.42}$$

inserting equation 2.40 into equation 2.42 and multiplying out the terms we get the following equation (normalised to $I_{sat} = \frac{1}{2} n \varepsilon_0 c A_{sat} A_{sat}^*$) describing the coherent interference pattern of the interacting fields

$$\begin{aligned}
\frac{I_T}{I_{sat}} = \frac{1}{A_{sat}^2} (&\psi_1\psi_1^* + \psi_2\psi_2^* + \psi_3\psi_3^* + \psi_4\psi_4^* \\
&+\psi_1\psi_2^* e^{i(\underline{k}_2 - \underline{k}_1)\cdot\underline{r}} + \psi_1\psi_3^* e^{i(\underline{k}_3 - \underline{k}_1)\cdot\underline{r}} + \psi_1\psi_4^* e^{i(\underline{k}_4 - \underline{k}_1)\cdot\underline{r}} \\
&+\psi_2\psi_1^* e^{i(\underline{k}_1 - \underline{k}_2)\cdot\underline{r}} + \psi_2\psi_3^* e^{i(\underline{k}_3 - \underline{k}_2)\cdot\underline{r}} + \psi_2\psi_4^* e^{i(\underline{k}_4 - \underline{k}_2)\cdot\underline{r}} \\
&+\psi_3\psi_1^* e^{i(\underline{k}_1 - \underline{k}_3)\cdot\underline{r}} + \psi_3\psi_2^* e^{i(\underline{k}_2 - \underline{k}_3)\cdot\underline{r}} + \psi_3\psi_4^* e^{i(\underline{k}_4 - \underline{k}_3)\cdot\underline{r}} \\
&+\psi_4\psi_1^* e^{i(\underline{k}_1 - \underline{k}_4)\cdot\underline{r}} + \psi_4\psi_2^* e^{i(\underline{k}_2 - \underline{k}_4)\cdot\underline{r}} + \psi_4\psi_3^* e^{i(\underline{k}_3 - \underline{k}_4)\cdot\underline{r}})
\end{aligned} \tag{2.43}$$

This gives us a D.C component to the interference pattern which describes the average background intensity given by

$$\sigma = \frac{1}{A_{sat}^2} \sum_{j=1}^{4} \psi_j(z,t)\, \psi_j^*(z,t) \tag{2.44}$$

and the grating writing terms that describe the interference between each of the four incident fields. Figure 2.15 shows the six gratings, described in equation 2.43, that can potentially occur.

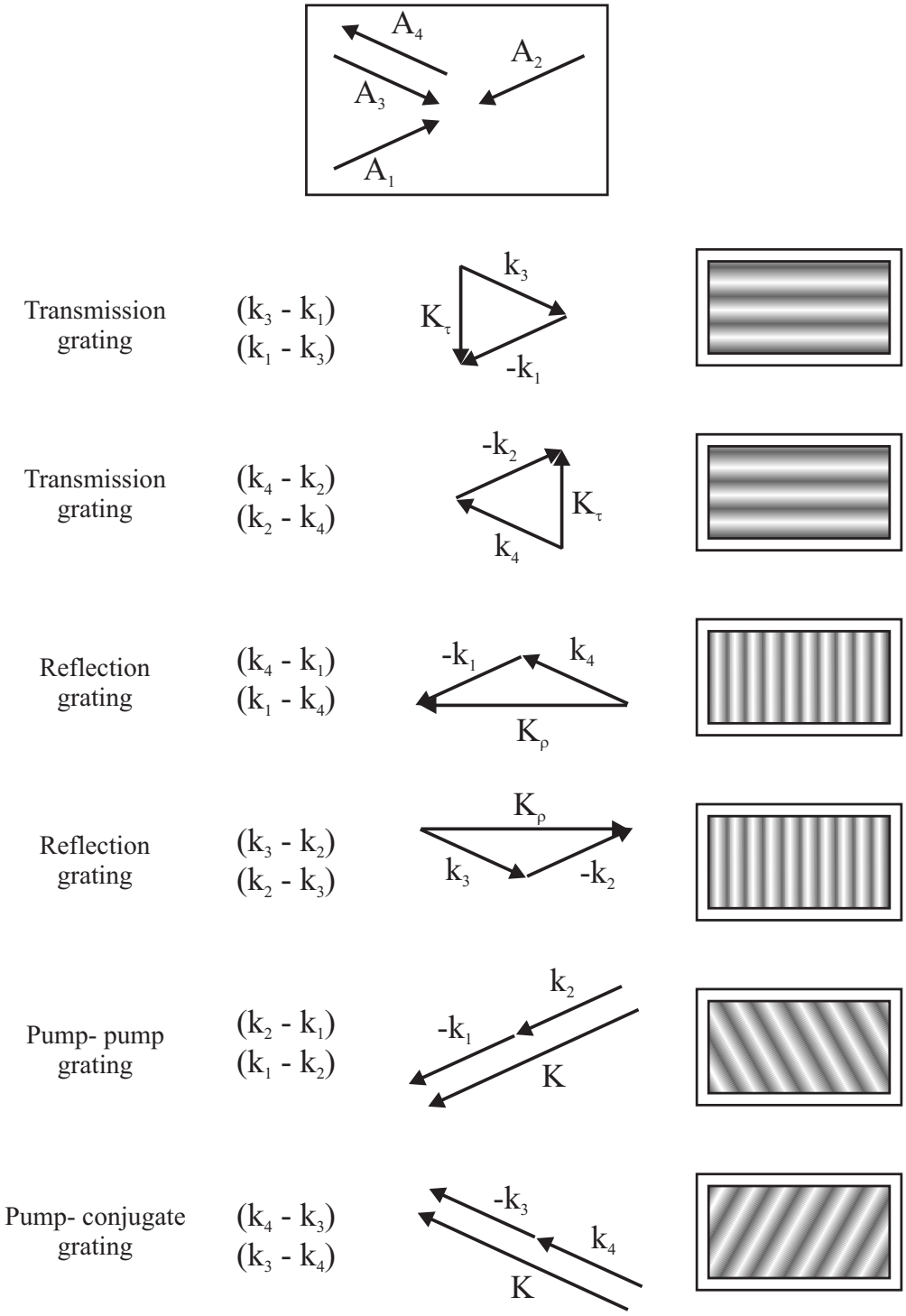

Figure 2.15: The six interference patterns produced due to the interaction between the four FWM beams.

2.7 Four-wave mixing modelling

The four-wave mixing interactions occurring inside saturable gain media have been modelled by co-workers on this project [17]. The interaction of the four waves inside the gain region leads to two sets of coupled differential equations that describe the evolution of the beams as they propagate the length of the FWM crystal. To greatly simplify the theory it is assumed that only a single transmission or a single reflection grating is produced within the FWM crystal at any one time unlike the experimental case where both gratings are present simultaneously (see section 2.6). The interactions producing both gratings are shown schematically in figure 2.16 where the transmission grating is formed through the interference of A_1 and A_3 and the reflection grating through interference of A_2 and A_3. The coupled equations describing the growth of the FWM fields for a single reflection grating are given by (see appendix B for a full derivation)

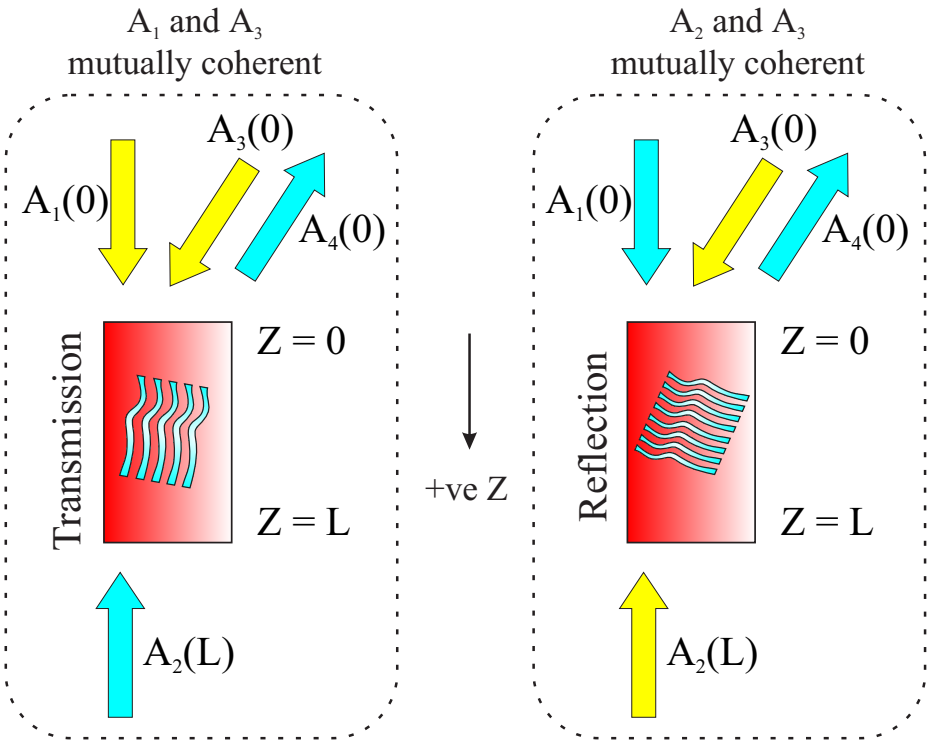

Figure 2.16: Geometry of the transmission and reflection gratings used in the FWM model.

$$
\begin{aligned}
+\frac{dA_1}{dz} &= \gamma_\rho A_1 + \kappa_\rho A_4 \\
-\frac{dA_2}{dz} &= \gamma_\rho A_2 + \kappa_\rho^* A_3 \\
+\frac{dA_3}{dz} &= \gamma_\rho A_3 + \kappa_\rho^* A_2 \\
-\frac{dA_4}{dz} &= \gamma_\rho A_4 + \kappa_\rho A_1
\end{aligned}
\tag{2.45}
$$

and for a single transmission grating are given by

$$
\begin{aligned}
+\frac{dA_1}{dz} &= \gamma_\tau A_1 + \kappa_\tau A_3 \\
-\frac{dA_2}{dz} &= \gamma_\tau A_2 + \kappa_\tau^* A_4 \\
+\frac{dA_3}{dz} &= \gamma_\tau A_3 + \kappa_\tau^* A_1 \\
-\frac{dA_4}{dz} &= \gamma_\tau A_4 + \kappa_\tau A_2
\end{aligned}
\tag{2.46}
$$

where γ_ρ and γ_τ are the self-coupling coefficients (for the reflection and transmission gratings respectively) and describe the average gain seen by the beam as it travels through the FWM region, and where κ_ρ and κ_τ are the diffractive coupling coefficients and are given by

$$
\begin{aligned}
\gamma_{\rho,\tau} &= \alpha_{\rho,\tau}^{(0)} \\
\kappa_{\rho,\tau} &= \frac{1}{2}\alpha_{\rho,\tau}^{(1)} \exp\left(i\phi_{\rho,\tau}\right)
\end{aligned}
\tag{2.47}
$$

A full description and derivation of these terms can be found in appendix B. Essentially the coupled equations of 2.45 and 2.46 describe the growth of each individual field amplitude, $A_{1,2,3,4}$, as it travels though the gain medium. This growth consists of two components. The first describes how each field is amplified by the average gain in the FWM region, $\alpha_{\rho,\tau}^{(0)}$, through the self-coupling coefficient, $\gamma_{\rho,\tau}$. The second describes how each field is amplified by the coupling of one of the other fields via diffraction from a gain-grating, mediated by the diffractive coupling coefficient , $\kappa_{\rho,\tau}$.

Equations 2.45 and 2.46 were solved using a numerical shooting routine for varying values of grating writing beam intensity. Figure 2.17 shows

the modelled diffraction efficiency, $\frac{I_4(0)}{I_1(0)}$, of a *reflection* gain-grating as a function of the grating writing beam intensity (normalised to the saturation intensity). The amplitude gain-length product, $\alpha_0 L$, for the model was set to 4 giving an intensity gain, $G = exp(2\alpha_0 L)$, of 2981. The graph shows that the gain-grating clearly has an optimum diffraction efficiency at a normalised writing beam intensity, $\frac{I_2(L)}{I_{sat}}$, of 0.01 either side of which the efficiency falls.

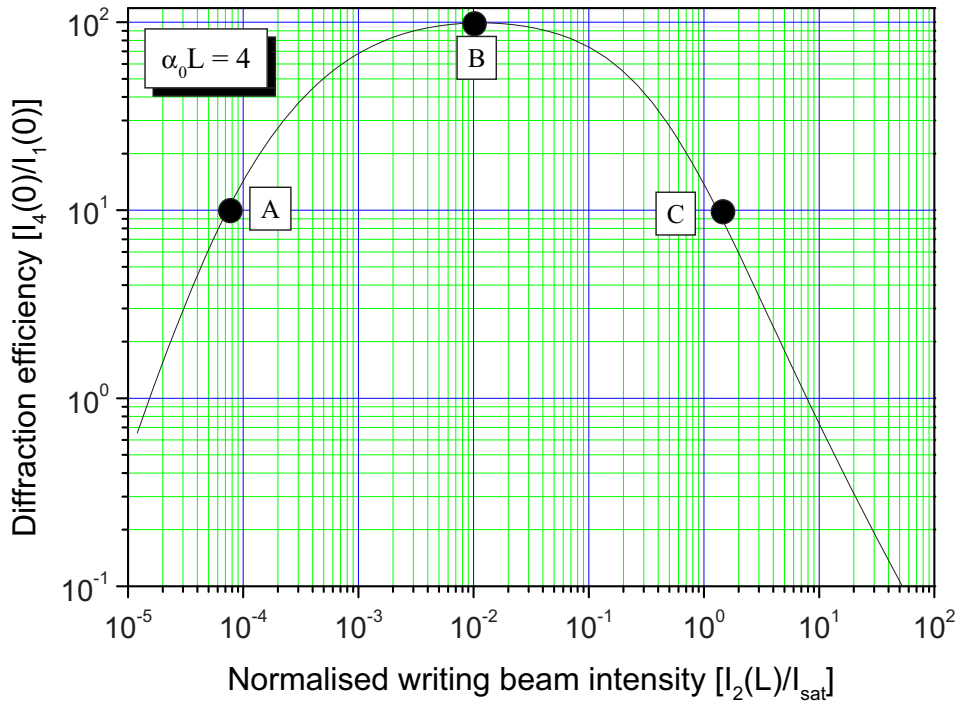

Figure 2.17: Plot of the diffraction efficiency of a reflection grating as a function of the normalised writing beam intensity for a small signal gain-length product of 4.

In their original paper [17] *Crofts et al* solved the coupled equations 2.45 and 2.46 to produce input-output plots like the one shown in figure 2.17. The model used, however, was limited in that it would produce an output at the end of the FWM crystal for a given input, giving no insight into the form of the gain-gratings existing within the crystal.

This model was subsequently refined with the inclusion of interference effects inside the gain-medium allowing the possibility of viewing the grat-

ing *evolution* along the crystal length (+ve Z direction in figure 2.16). Figure 2.18 shows both the interference pattern profile caused by the grating writing beams and the gain-grating that it writes, via spatial hole burning, within the FWM amplifier. The writing beam amplitude , $A_2(L)$ and $A_3(0)$, was set at point A in figure 2.17. From the graph it can be seen that the interference pattern intensity (blue line) is, on average, very low and is only weakly modulated along the length of the amplifier. This, in turn, means that the gain (green line) is, on average, only weakly saturated and has a small modulation. This causes the diffraction efficiency of the grating at point A (in figure 2.17) to be smaller than the optimum value.

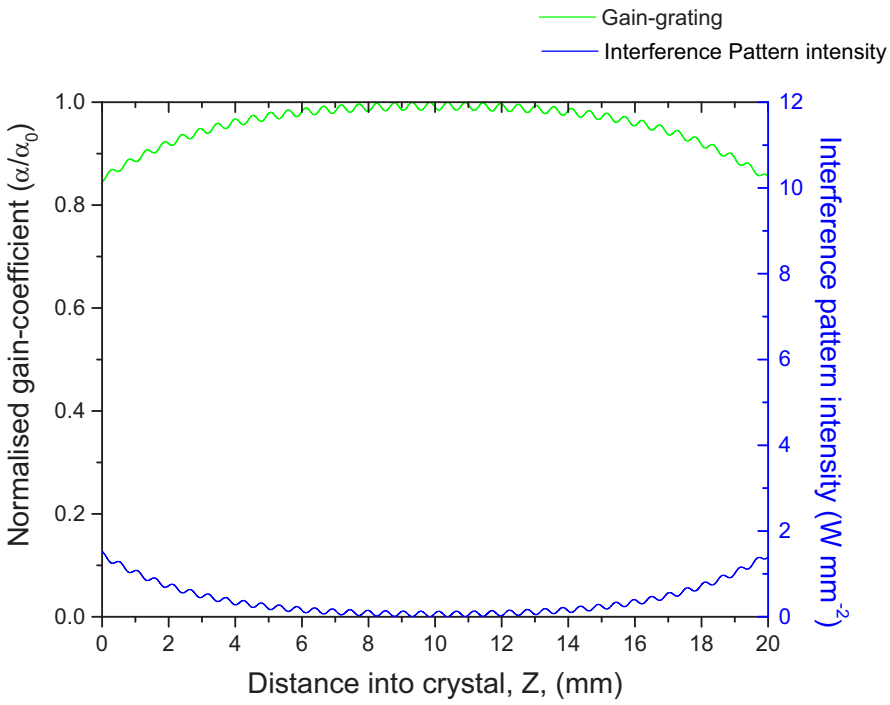

Figure 2.18: Cross-section of the normalised gain-coefficient throughout the crystal at point A in figure 2.17

A point to note regarding the interference fringes shown in figure 2.18 is that in reality the fringes are spaced roughly $\frac{\lambda_0}{2n} = 245$ nm apart, for clarity, however, the graph shows a much larger fringe spacing. This can be achieved by artificially changing the wavelength used in the model without affecting the results since the model is wavelength independent.

Figure 2.19 shows the interference pattern and subsequent gain-grating formed at point B in figure 2.17, which corresponds to the maximum diffraction efficiency. Here the interference between the grating writing beams has a much larger modulation and hence spatial hole burning produces a well defined grating in the gain of the FWM amplifier.

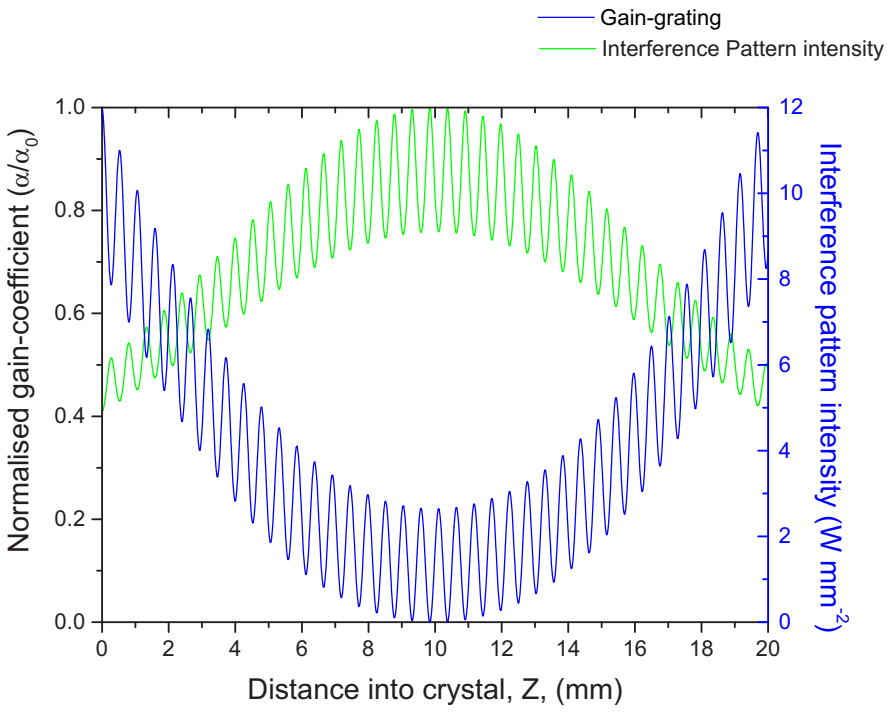

Figure 2.19: Cross section of normalised gain-coefficient throughout the crystal at point B in figure 2.17

Finally, figure 2.20 shows the interference pattern and gain-grating at point C in figure 2.17. At this stage the interference pattern is highly modulated due to the high and roughly equal intensities of the two writing beams as they pass through the crystal. This burns a highly modulated grating into the gain but at the expense of removing most of the power, effectively over-saturating the FWM amplifier. A read-out beam incident on this grating would see very little gain (since most has been removed) and hence the diffraction efficiency starts to fall.

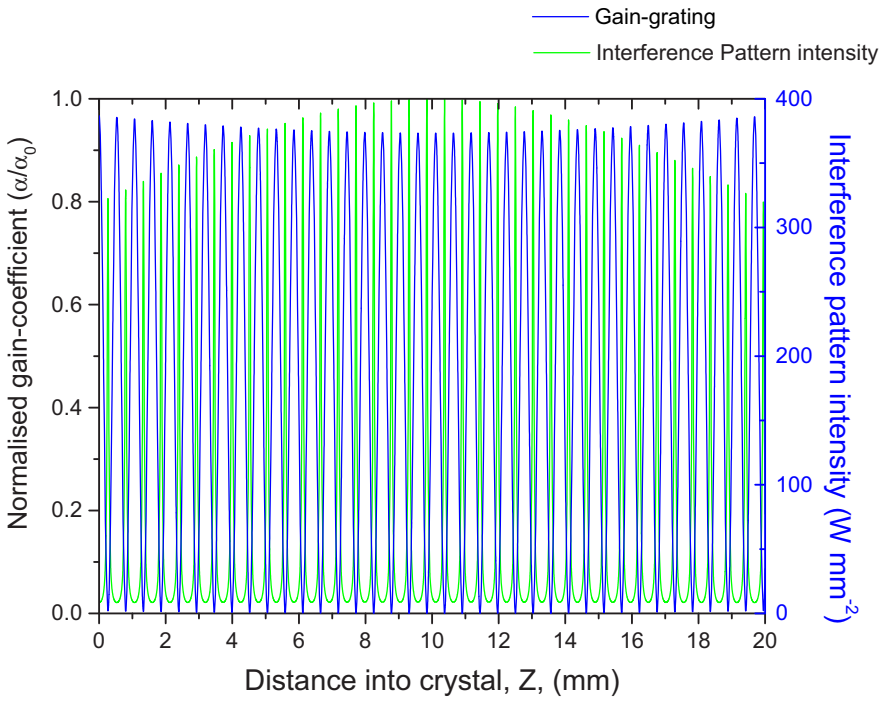

Figure 2.20: Cross section of normalised gain-coefficient throughout the crystal at point C in figure 2.17

Figure 2.21 shows the diffraction efficiency of a *transmission* gain-grating as a function of the grating normalised writing beam intensity. The amplitude gain-length product, $\alpha_0 L$, for the model was also set to 4.

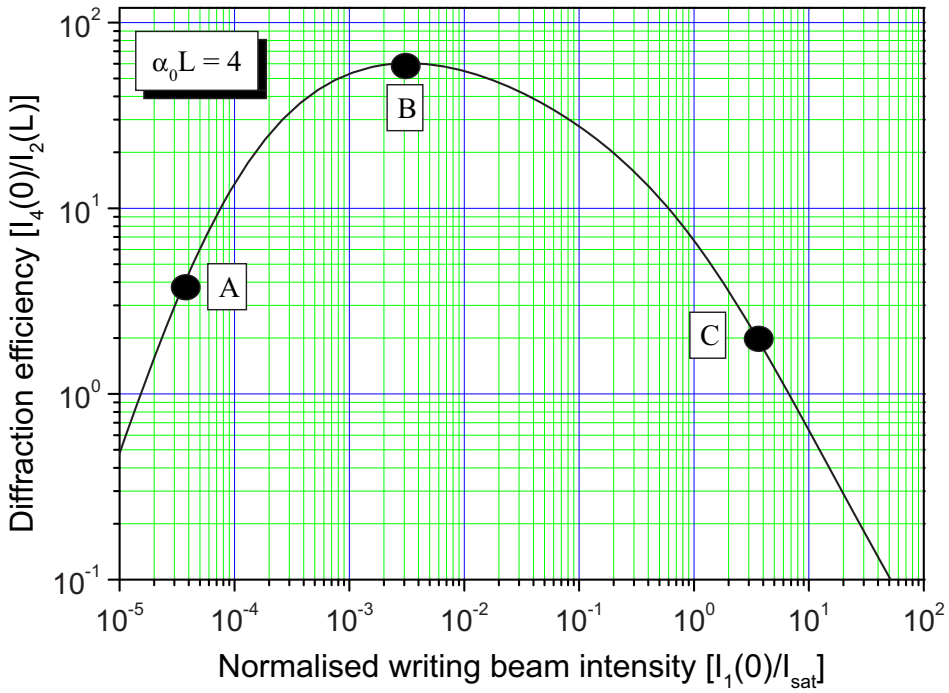

Figure 2.21: Plot of the diffraction efficiency of a transmission grating as a function of the normalised writing beam intensity for a small signal gain-length product of 4.

The *transmission* gratings formed at points A, B and C in figure 2.21 are shown in figures 2.22, 2.23 and 2.24 respectively. In figure 2.22, taken at point A, the grating is only weakly modulated (only two grating periods are shown for clarity). A reduction in the gain only becomes appreciable towards the end of the crystal (20 mm) giving a low diffraction efficiency at that point in figure 2.21.

As the writing beam intensity is increased towards point B the diffraction efficiency increases until it reaches its maximum value at point B. Figure 2.23 shows that the grating formed at this stage is modulated throughout the entire length of the crystal and is well defined.

A further increase in the writing beam intensities has a detrimental ef-

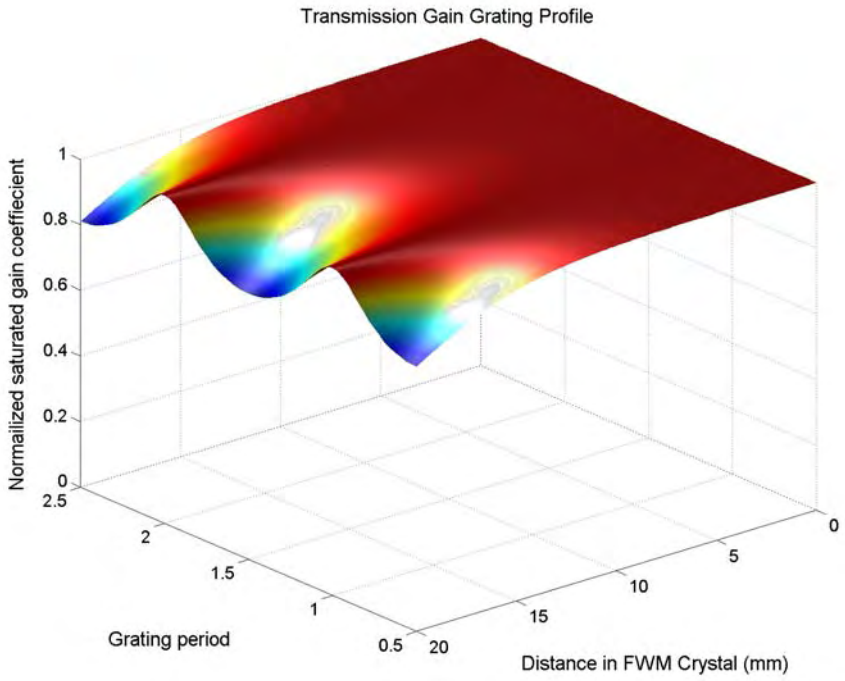

Figure 2.22: Under-saturated gain-grating corresponding to $\alpha_0 L = 4$ at $I_1(0)/I_{sat} = 4.5 \times 10^{-5}$

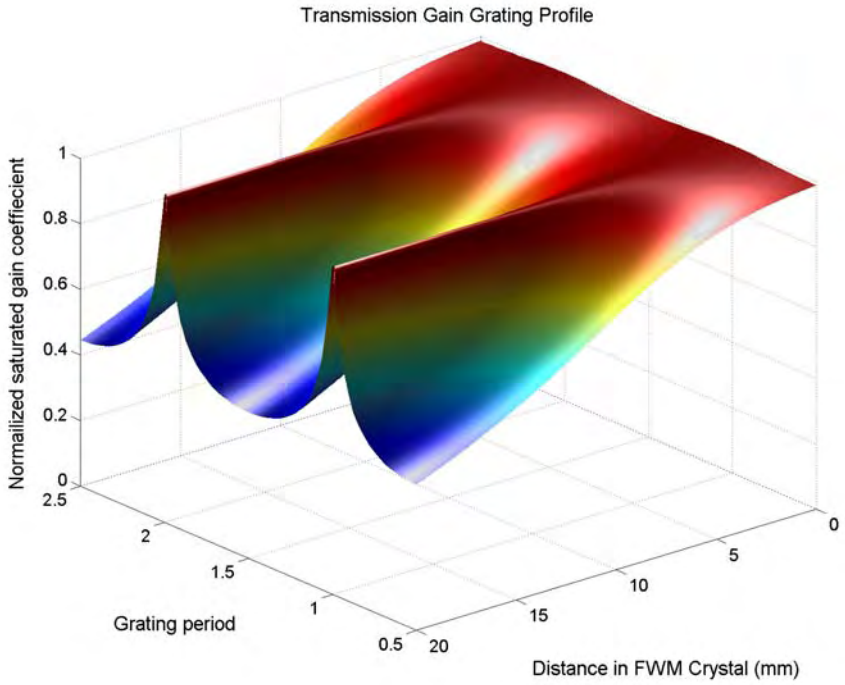

Figure 2.23: Maximum diffraction efficiency grating corresponding to $\alpha_0 L = 4$ at $I_1(0)/I_{sat} = 3 \times 10^{-3}$

fect on the diffraction efficiency of the gain-grating. Figure 2.24 shows the grating at point C. Here the large intensities of the grating writing beams cause the subsequent interference pattern to saturate a large amount of the gain, producing deeply modulated gratings but at the expense of removing most of the population inversion. Any subsequent grating reading beam would suffer low amplification and hence poor diffraction efficiency.

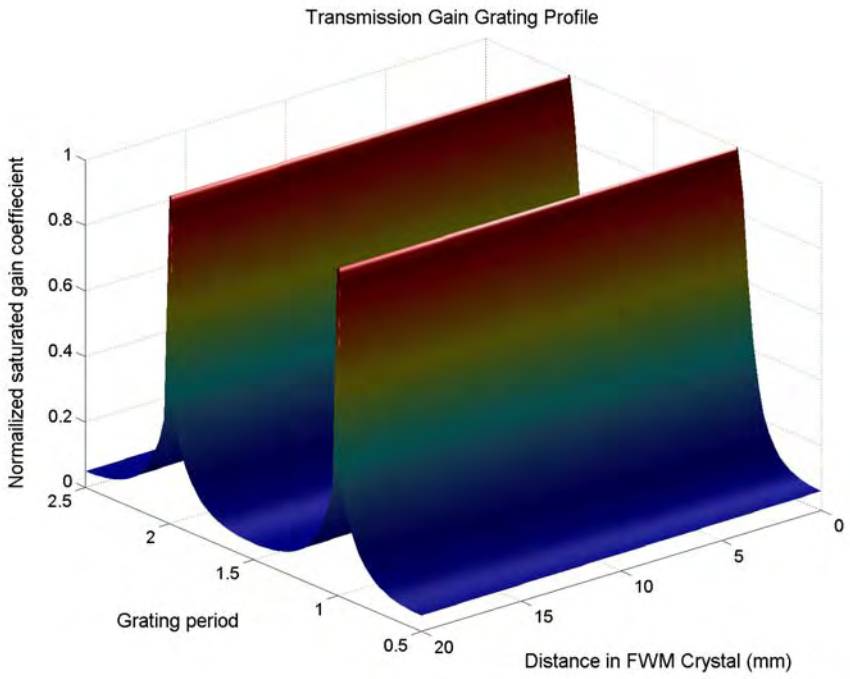

Figure 2.24: Over-saturated grating corresponding to $\alpha_0 L = 4$ at $I_1(0)/I_{sat} = 3.5$

2.7.1 Unequal writing beam intensities

The analysis of both the reflection and transmission gratings in the last section was performed for equal writing beam intensities at the input face of the crystal. For the reflection grating shown in figure 2.19 the two writing beams enter from opposite ends of the crystal. As the two beams counter-propagate along the length of the crystal both are amplified by equal amounts. This means that the only point at which the two beams equal each other in intensity is exactly half way along the crystal. The subsequent *interference* pattern at this point would have maximum contrast,

that is, a maximum intensity of four times the intensity of a single writing beam at the centre point of the crystal and a minimum intensity of zero. The gain-grating formed will then also have a maximum contrast.

However, for the transmission grating shown in figure 2.23 both writing beams co-propagate the length of the crystal i.e. both enter from the same end of the crystal. As the two beams travel along the amplifier both experience equal amounts of amplification and therefore have equal intensities along the entire crystal length. This means that the interference between the beams has a maximum contrast at every point. The minimum (nodes) of the interference pattern will be zero (only for equal intensity beams) and so the gain coefficients at these points remains unchanged.

In a real system, however, the gain experienced by each writing beam is different due to the non-uniform gain region and the different angle at which the beams enter the gain region. This could be compensated for, to some extent, by changing the relative intensities of the two input beams so that at some point within the crystal (say the centre) the beams are approximately equal and hence write a high contrast grating.

Figure 2.25 shows the effect of using unequal writing beam inputs on the diffraction efficiency of a single reflection grating. The first curve (black line) shows the diffraction efficiency, $I_4(0)/I_1(0)$, against normalised writing beam intensity, $I_2(L)/I_{sat}$, when both writing beams $A_2(L)$ and $A_3(0)$ are equal. This case has already been discussed in section 2.7. The second curve (blue line) shows the diffraction efficiency when one of the writing beams $A_3(0)$ is made three times smaller than the other $A_2(L)$. In this case the peak diffraction efficiency of the grating has fallen from nearly 100 (for equal beams) to around 17. The third curve (red line) shows the effects of a factor of ten difference between the writing beams.

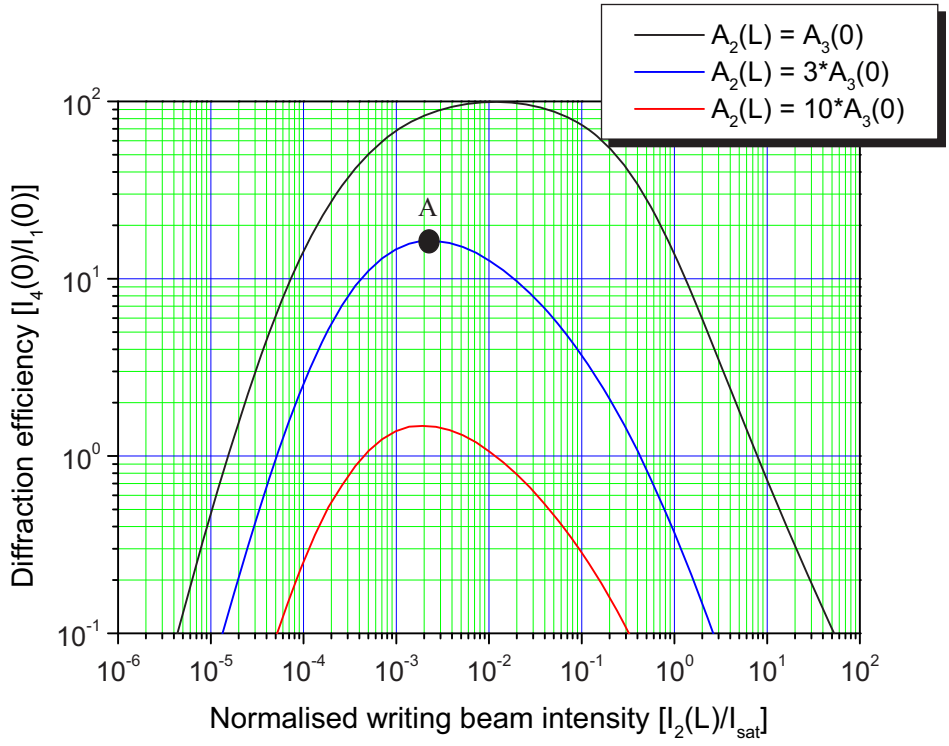

Figure 2.25: Diffraction efficiency characteristics of a single reflection grating for various writing beam ratios.

Figure 2.26 shows the form of the *reflection* gain-grating at point A in figure 2.25. Now the point at which the counter-propagating writing beams are equal is no longer at the centre of the crystal but is offset to one side. Here, because of the factor of three difference between the writing beams, the interference pattern shows weak modulation and hence the subsequent gain-grating shows a low diffraction efficiency.

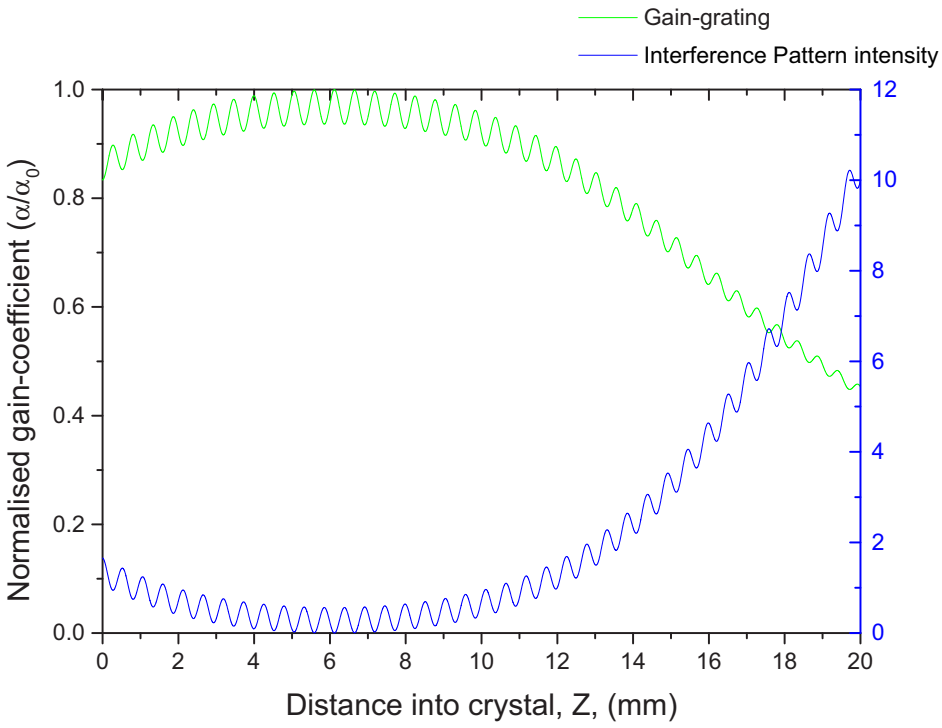

Figure 2.26: The interference pattern intensity and subsequent gain-grating formed at point A in figure 2.25

Figure 2.27 shows the effect of writing beam ratio on the diffraction efficiency of a single transmission grating. Again, as the ratio changes the efficiency of the grating falls significantly. The form of the transmission grating at point A in figure 2.27 is shown in figure 2.28. Now, instead of remaining equal along the length of the amplifier, the writing beams have different intensities at every point. The subsequent interference pattern now has some finite value at its minimum point (node) and hence contributes to spatial hole burning which can be seen as the gain decaying along the amplifier. The important point to note from this section is that to maximise the diffraction efficiency of a gain-grating (both reflection and transmission) the writing beams must be, ideally, of equal intensity. Any difference between the two writing beams will result in a grating with an efficiency lower than the optimum and so steps must be taken to ensure that at the point where the beams interfere within the amplifier they have equal or similar intensities.

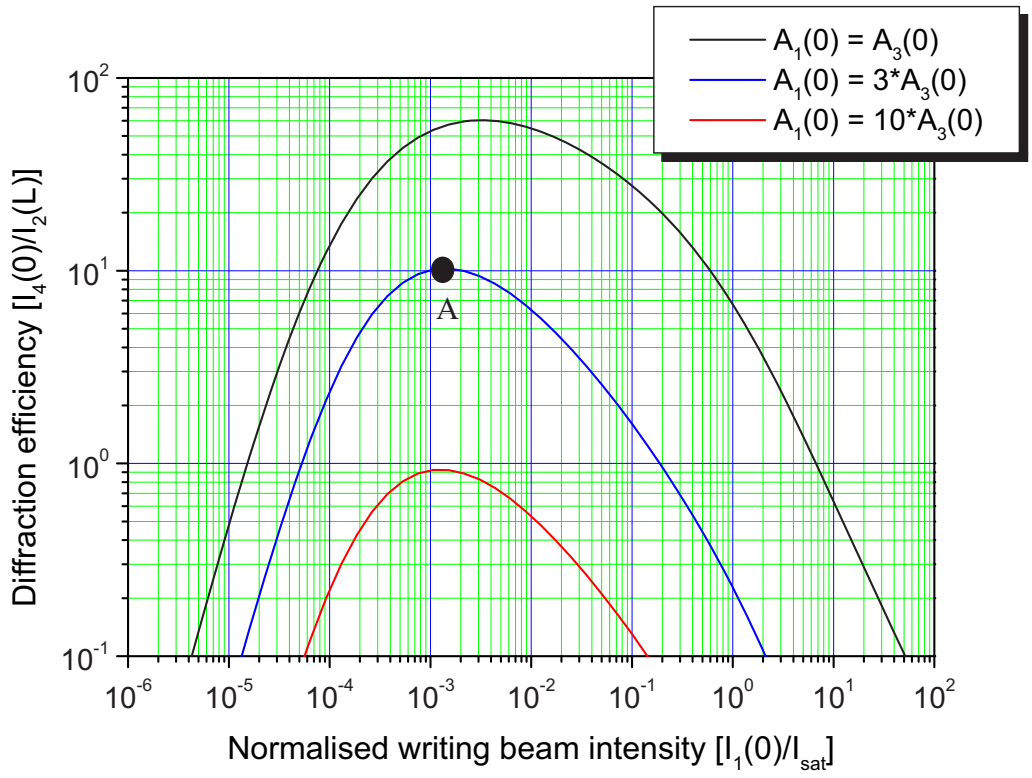

Figure 2.27: Diffraction efficiency characteristics of a single transmission grating for various writing beam ratios.

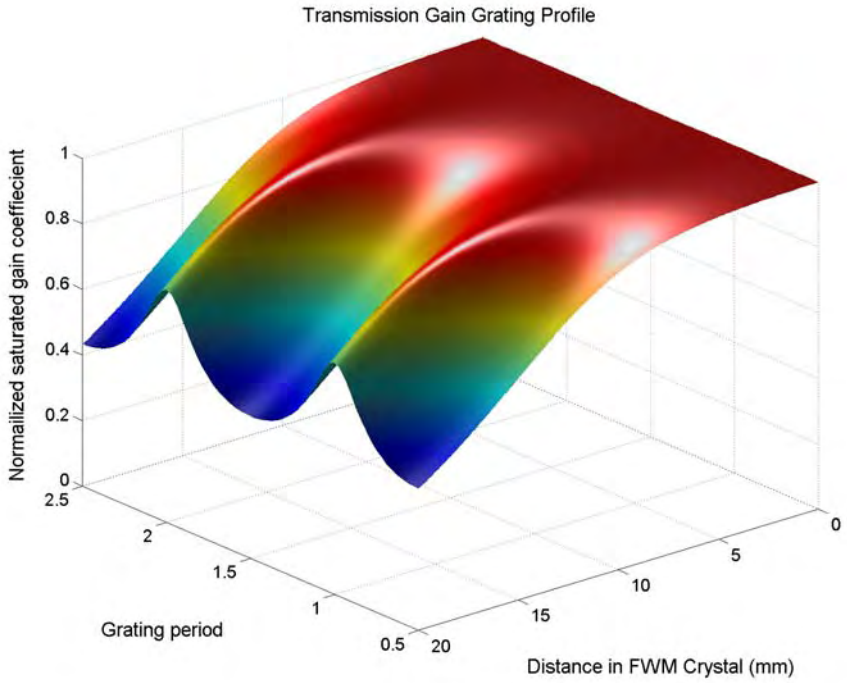

Figure 2.28: The interference pattern intensity and subsequent gain-grating formed at point A in figure 2.27

2.8 Four-wave mixing experimental

Saturable gain four-wave mixing was demonstrated experimentally using the scheme shown in figure 2.29. The FWM amplifier consisted of 1.1 at.% Nd-doped YVO_4 *a*-cut crystal of dimensions 20 mm x 3 mm x 5 mm, sided pumped by an 18 W fibre lensed laser-diode bar operating at 808 nm. The crystal was anti-reflection coated for the pumping wavelength on both *b* faces to reduce damaging back-reflections into the diode, and anti-reflection coated for 1064 nm on both *a* faces to reduce the likelihood of parasitic lasing occurring between these two faces. The output of the diode bar was focussed by a cylindrical lens of focal length f= 12.7 mm onto one of the *b* faces of the Nd:YVO_4 crystal, and the polarisation of the TE polarised pump beam was rotated by the use of a $\lambda/2$ wave plate to be parallel with the *c* axis of the crystal, thereby yielding maximum pump absorption ($\alpha = 31.4cm^{-1}$ at 808 nm) [11].

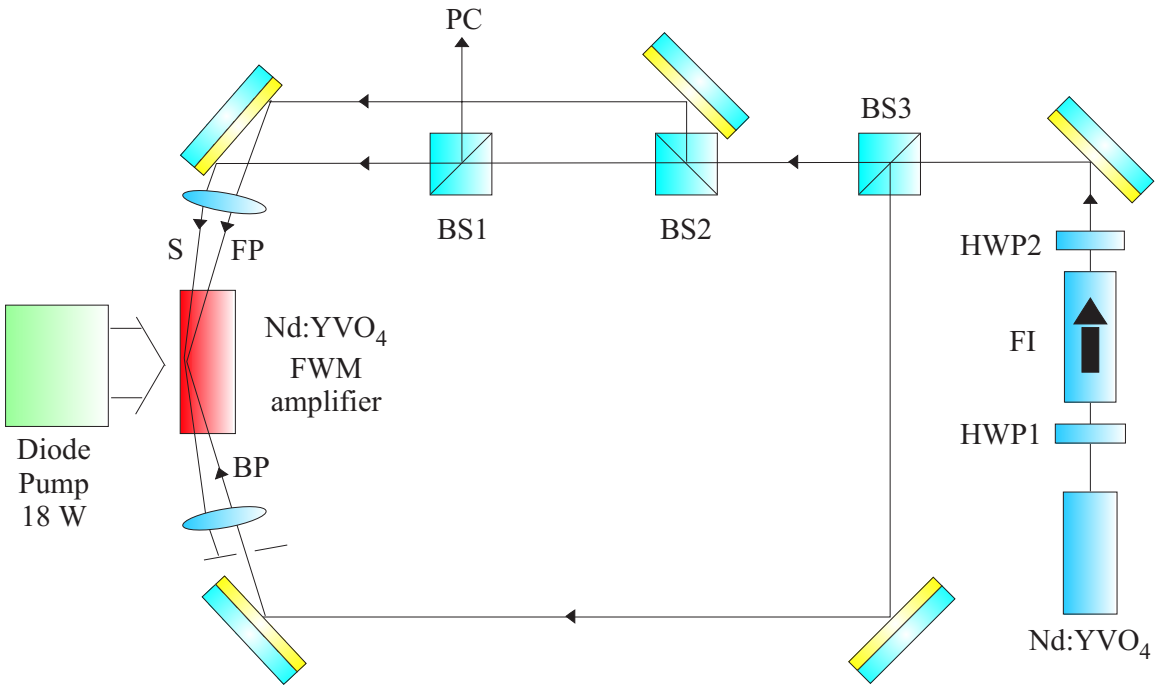

Figure 2.29: Schematic showing the experimental setup used to demonstrate gain saturation four-wave mixing in Nd:YVO_4 .

A single longitudinal mode Nd:YVO_4 laser that produced a diffraction-limited beam of 300 mW output power at 1064 nm was used to provide the forward pump (FP), the backward pump (BP) and the signal (S) beams

for the experiment. The three interacting beams were all focussed into the Nd:YVO_4 FWM amplifier using two 100mm focal length spherical lenses to a calculated spot size of 37 μm (slightly larger than the diode-pump spot-size of 36 μm). All beams were vertically polarised (parallel with the crystal *c*-axis). The crystal orientation and beam polarisations are shown in figure 2.30.

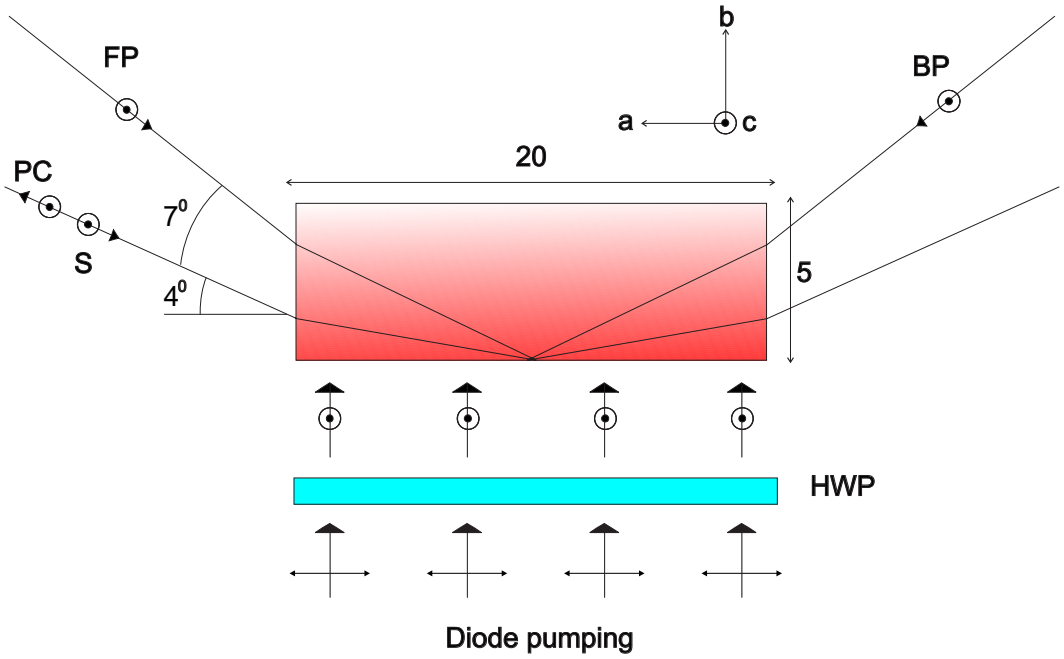

Figure 2.30: Schematic showing the interaction geometries and polarisation of the FWM beams.

The angle between the signal and the forward pump beams was around 7°, and the angle between the signal beam and the *a* axis was around 4°. The backward pump was arranged so that it counter-propagated with respect to the forward pump beam. This ensures that the backward pump was Bragg matched to the *transmission* gain-grating written by the interference between the forward pump and the signal beam. Similarly the forward pump will be Bragg matched to the *reflection* grating written by the backward pump and signal beam.

Because the signal and pump beams travel through the gain region at different angles, and hence have different path lengths in the population inverted region, the gain experienced by each of them was different. To

produce the largest modulated interference pattern, at the point where the beams intersect with the gain region, the grating writing beams had to be of similar intensities. The powers of the input beams were adjusted empirically to achieve maximum phase-conjugate reflectivity, the optimum power ratio between the interacting beams occurring with BP:FP:S = 17.6: 11:1. A point to note is that the S and FP beams shown in figure 2.30 are interchanged from the FWM cases discussed so-far in this thesis, with the S beam entering the crystal at a smaller angle than the FP. This helps in amplification of the PC output in two ways, firstly, The FP (and BP) enter the crystal at a larger angle than the S beam and so remove less of the gain - leaving more available for amplification of the PC. Secondly, the shallow angle at which the PC leaves the crystal (4^0) means it travels through more of the available gain region and accordingly sees a higher gain than had it left at a larger angle.

The phase-conjugate of the signal beam in this experiment has two components associated with it: the *reflection* and the *transmission* grating components which occur simultaneously. Figure 2.31 shows the two grating geometries.

In order to separate the two geometries, the grating readout beam, for instance the backward pump in the transmission grating case, would need to be prohibited from interfering with the grating writing beams (the forward pump and signal beam in this case). This could be achieved in two ways, firstly, the grating reading beam could be made incoherent with the writing beams. This could be achieved by sending the grating reading beam around a distance longer than the coherence length of the Nd:YVO_4 seed laser. This is impractical however, because of the very narrow bandwidth of the seed source ($\Delta\nu = 10\,kHz$ - product specification sheet) leading to a coherence length of $L = \frac{c}{\Delta\nu} = 30\,km$. Another method would be to use another 1064 nm Nd:YVO_4 laser for the grating reading beam removing any mutual coherence between itself and the grating writing beams. Secondly, the reading beam polarisation could be rotated orthogonally to the polarisation of the writing beams. This is also not without its problems since, as discussed in chapter 1, Nd:YVO_4 is a uniaxial tetragonal crystal

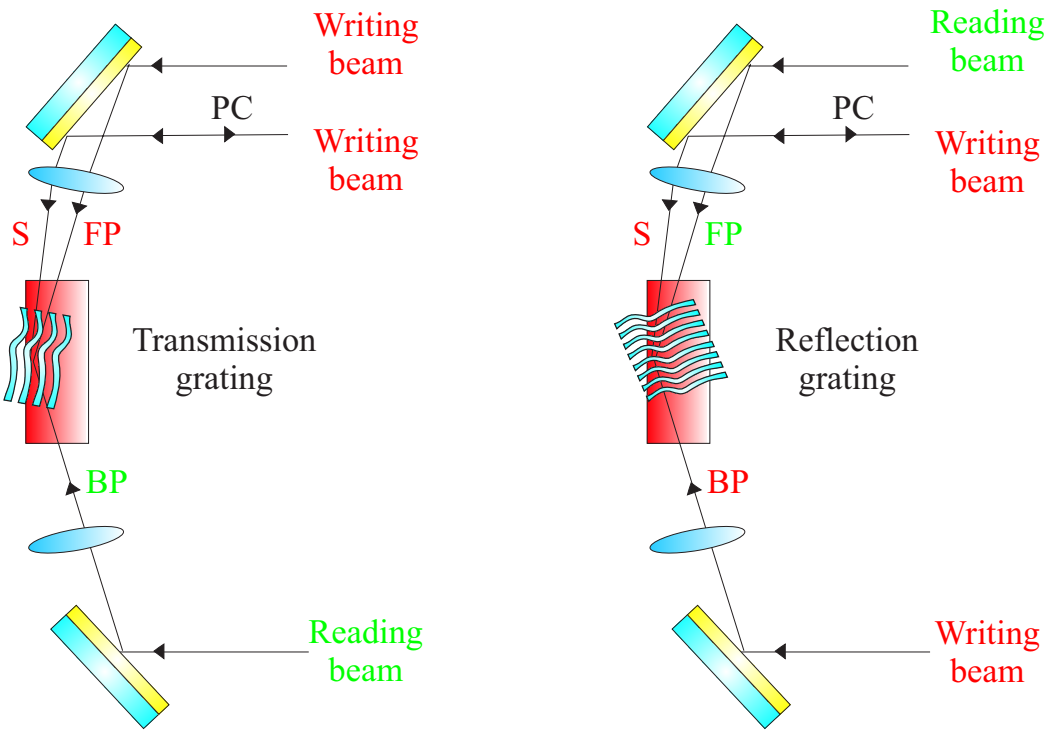

Figure 2.31: Schematic of the reflection and transmission geometries.

and as such suffers from a large natural birefringence. This would require the reading beam to enter the FWM amplifier at a different angle from the writing beams in order to Bragg match it to the gain-grating inside the crystal, and although this is quite possible to achieve it is experimentally undesirable.

The phase conjugate of the signal beam travels back along the signal where it is picked off by BS1 in figure 2.29. The whole setup can be viewed in a black box geometry whereby the forward and backwards pumps are seen as part of the entire system, in this case the signal beam is incident on a phase-conjugate mirror which has an associated phase-conjugate reflectivity, defined as

$$R_{pc} = \frac{PC\ output\ power}{Signal\ input\ power} \tag{2.48}$$

where, due to amplification of all four interacting beams within the gain medium, the reflectivity can have a value greater than unity.

2.8.1 Co-polarised four-wave mixing

Figure 2.32 shows the phase-conjugate reflectivity as a function of the forward pump input power for four different small-signal gains, which was varied by defocussing the pump diode focussing lens. A maximum reflectivity of 100 was observed for a small-signal gain (for the signal beam) of 3000. At each of the pumping levels the small-signal gain seen by the signal beam is higher than that of the pump beams due to the angular dependence of the gain.

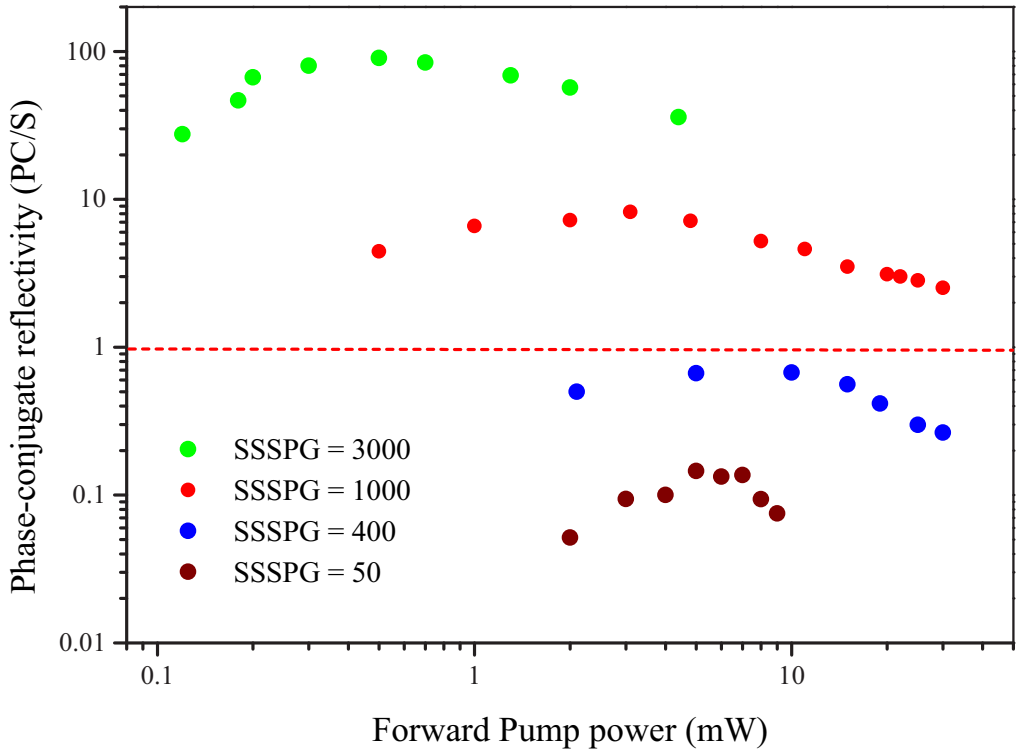

Figure 2.32: Graph of phase-conjugate reflectivities versus the forward pump input power.

From the graph it can be seen that when the small-signal single pass (SSSP) gain of the signal beam had values of 1000 and 3000 the peak reflectivity was greater than 1. The dashed red line shows where the phase-conjugate reflectivity is equal to 1, (i.e. all incident signal beam light is reflected); above this line the reflected phase-conjugate beam has a higher power

than the incident signal.

A point to note about this system that would reduce the reflectivity, is that for true FWM to occur and hence a true phase-conjugate of the signal beam to be produced the FP and BP need to be phase-conjugates of each other (see section 2.5.1). However, in this scheme the FP and BP are not *true* phase-conjugates of each other as they are just two individual Gaussian beams obtained via a beam-splitter placed in front of the seed laser. At the focus of the 100 mm spherical lenses the FP and BP have a plane phase-front while at all other points in the FWM crystal their phase-fronts are only approximately phase-conjugates of each-other and as such are not completely Bragg matched to the volume gain-grating. This mismatch in the phase-fronts would be expected to lead to a reduction in the measured diffraction efficiency and so for a true FWM system the efficiency is expected to increase.

With this in mind, the high phase-conjugate reflectivities achieved using the gain FWM scheme mentioned above are far greater than those achieved by a rival scheme also using a Nd:YVO_4 crystal as the FWM amplifier [18] but pumped with 12 W of diode power. In their scheme the FP and BP were derived from the forward and backward modes of a linear laser cavity and so *were* phase-conjugates of each other. The maximum phase-conjugate reflectivity reported however, was only 0.014. The reason for this low value of reflectivity was that optimisation of the FP and BP was hard to achieve since the power in the forward and backwards mode of the linear cavity is a function of the mirror reflectivities making any optimisation of the system difficult.

2.9 Conclusions

In this chapter it has been shown that a diode side pumped Nd:YVO_4 crystal set in a bounce geometry is capable of achieving high small-signal single pass gains (in excess of 15000) needed for gain saturation four-wave mixing. This amplifier was then configured into a four-wave mixing ge-

ometry in order to ascertain the maximum phase-conjugate reflectivities achievable with such a system. A maximum reflectivity of around 100 was achieved for the co-polarised case. A model of the FWM process was then presented and used to show the form of the gratings formed within the amplifier. It was shown that, in order to achieve maximum diffraction efficiency of a gain-grating, the two writing beams should have equal intensities. The next chapter deals with the integration of such a four-wave mixing scheme into a resonator geometry capable of sustained continues-wave phase-conjugate oscillation.

2.10 References

[1] A. E. Siegman. Lasers. pages 297–298. University Science Books, 1986.

[2] A. Yariv. Optical electronics in modern communications. pages 176–179. Oxford University Press, 1997.

[3] S. Mailis, J. Hendricks, D. P. Shepherd, A. C. Tropper, N. Moore, R. W. Eason, G. J. Crofts, M. Trew, and M. J. Damzen. High-phase-conjugate reflectivity ($>$ 800%) obtained by degenerate four-wave mixing in a continuous-wave diode-side- pumped Nd:YVO_4 amplifier. *Optics Letters*, 24(14):972–974, 1999.

[4] C. L. Tang, H. Stantz, and G. DeMars. Spectral output and spiking behavior of solid-state lasers. *Journal of Applied Physics*, 34(8):2289–2295, 1963.

[5] D. R. Hall and P. E. Jackson. The physics and technology of laser resonators. pages 65–67. Institute of Physics publishing, 1992.

[6] J. E. Bernard and A. J. Alcock. High-efficiency diode-pumped Nd:YVO_4 slab laser. *Optics Letters*, 18(12):968–970, 1993.

[7] W. A. Clarkson and D. C. Hanna. Two-mirror beam-shaping technique for high-power diode bars. *Optics Letters*, 21(6):375–377, 1996.

[8] P. B. Chapple. Beam waist and M^2 measurment using a finite slit. *Optical Engineering*, 33(7):2461–2466, 1994.

[9] A.E. Siegman. How to (maybe) measure laser beam quality. *in DPSS lasers: applications and issues (OSA TOPS)*, 17:184–199, 1998.

[10] C. L. Bonner. Multi-watt, diode-pumped planer waveguide lasers. *PhD thesis, University of Southampton*, pages 65–68, 2000.

[11] W. Koechner. Solid-state laser engineering. pages 63–65. Springer-Verlag, 1999.

[12] I. O. Musgrove. Personal communication, September 2001.

[13] J. E. Bernard, E. McCullough, and A. J. Alcock. High-gain, diode-pumped Nd:YVO_4 slab amplifier. *Optics Communications*, 109(1-2):109–114, 1994.

[14] M. J. Damzen, Y. Matsumoto, G. J. Crofts, and R. P. M. Green. Bragg-selectivity of a volume gain grating. *Optics Communications*, 123(1-3):182–188, 1996.

[15] H. J. Caulfield. Handbook of optical holography. pages 89–125. Academic Press, 1979.

[16] E. Hecht and A. Zajac. Optics. pages 45–46. Addison-Wesley publishing, 1974.

[17] G. J. Crofts and M. J. Damzen. Numerical modelling of continuous-wave holographic laser oscillators. *Optics Communications*, 175(4-6):397–408, 2000.

[18] A. Brignon, L. Loiseau, C. Larat, J. P. Huignard, and J. P. Pocholle. Phase conjugation in a continuous-wave diode-pumped Nd:YVO_4 laser. *Applied Physics B-Lasers and Optics*, 69(2):159–162, 1999.

Chapter 3

Adaptive holographic resonators

3.1 Overview

In chapter 2 it was shown that a saturable-gain phase-conjugate mirror is capable of achieving reflectivities of greater than unity. This allows the possibility of using the four-wave mixing geometry in a PC resonator scheme and achieving oscillation. This chapter looks at such resonator geometries and shows how the phase-conjugate nature of their modes allows for correction of phase distortions present within the resonator loop. The chapter begins with an overview of the operation of a so called 'self-pumped' phase-conjugate resonator whereby a PCM is produced using a FWM geometry with a single input beam. In section 3.4 a non-reciprocal transmission element (NRTE) is introduced as a means of optimising the output power of a phase-conjugate resonator and it is shown how such a device can correct for phase-shifts induced in the resonating mode due to the gain-grating. Experimental results from such adaptive resonators are presented in section 3.7 and it is shown that severe intra-cavity phase distortions can be corrected for via the phase-conjugate nature of the laser mode. Finally, in section 3.8 it is shown how such a phase-conjugate resonator can be produced that requires no external seed laser.

3.2 Phase-conjugate resonator operation

In this section the operation of a laser resonator is presented that is capable of adapting its internal mode structure thereby maintaining a single mode output. The process is broken down into two distinct steps. The first, the grating *writing* process, describes the formation of a gain-grating, in which is encoded any distortions seen by a reference beam as it travels around a resonator loop. With reference to figure 3.1, a plane wave at point A is directed into the gain region at point B. The plane-wave at point B will act as the forward pump (FP) for a four-wave mixing geometry. This wave then travels through the gain region, where it is amplified, and on to point C.

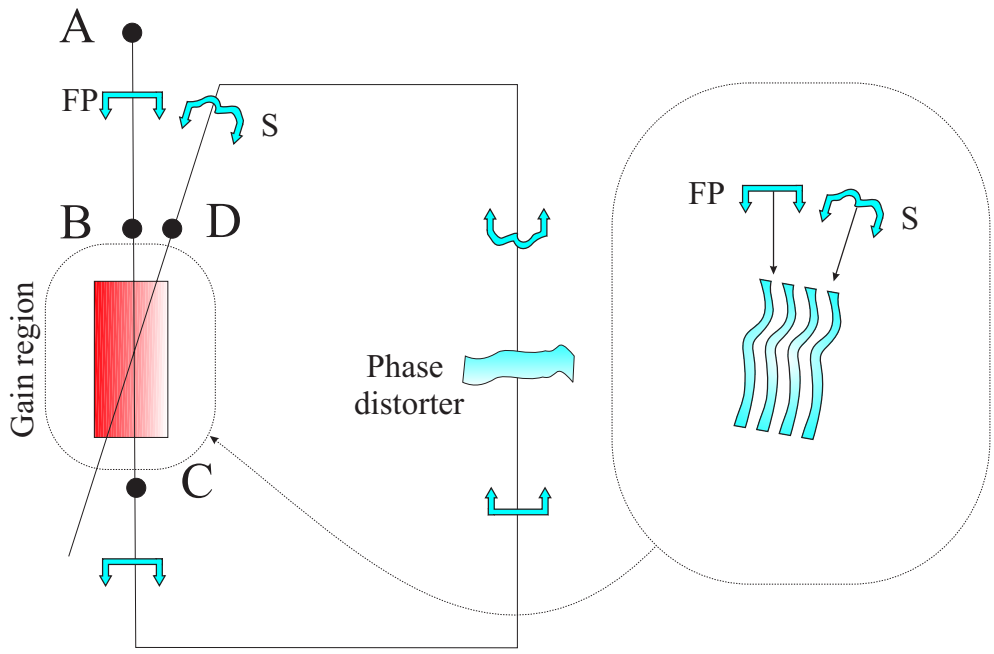

Figure 3.1: The grating writing process inside a phase-conjugate resonator with a transmission grating geometry

The amplified plane-wave then travels anti-clockwise around the resonator loop, where it is aberrated by any phase distortions within the loop, and on to point D, where it assumes the role of the signal beam (S) in a four-wave mixing geometry. It is important to note that the phase distortions described above are shown occurring outside the gain region. Experimen-

tally, however, the phase distortions will occur within the amplifier via thermal effects such as those discussed in section 1.1.1 but in this case the analysis remains unchanged (although easier to visualise).

The S beam now contains all the information on the form of the total phase distortion experienced by the FP as it travelled around the resonator. The S beam then travels into the gain region where it intersects the FP. At the point of intersection the FP and S interfere with each other (as long as the path length of the cavity is less than the coherence length of the laser). The interference pattern produced spatially hole burns a grating into the gain-region (see section 2.3) in which is stored all the phase information needed to reconstruct a PC beam.

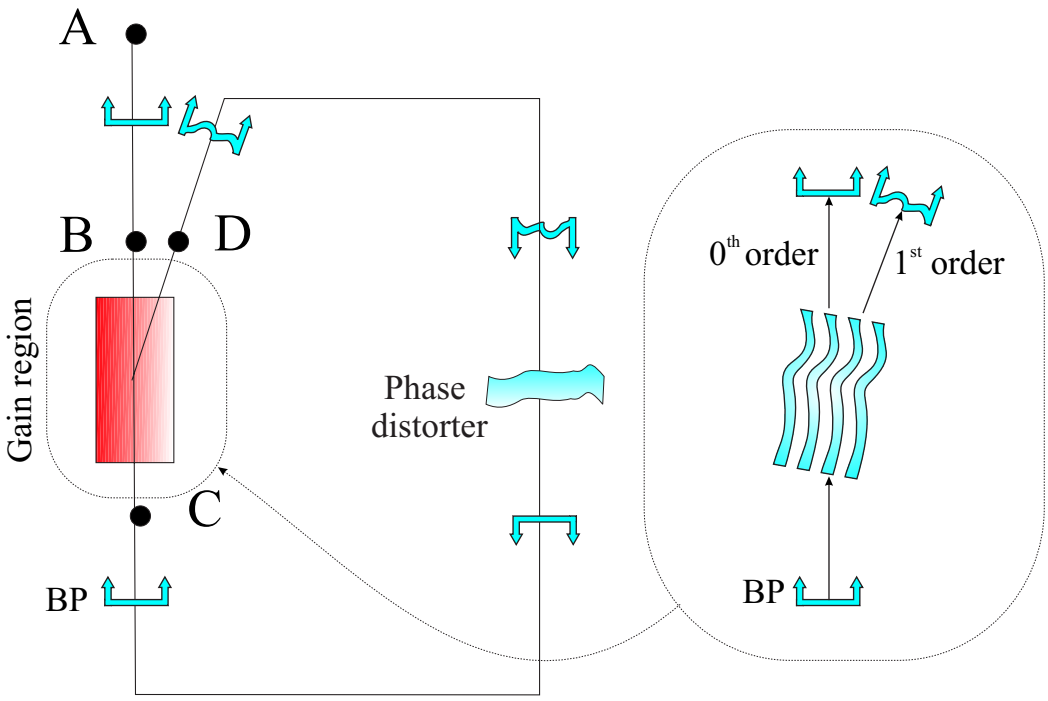

Figure 3.2: The grating reading process inside a phase-conjugate resonator with a transmission grating geometry

The second process, shown in figure 3.2, describes the *reading* of the gain-grating and the formation of a phase-conjugate mode in the clockwise direction. Within the high gain region amplified spontaneous emission (ASE) can scatter from the gain-grating formed by the writing process. This scattered radiation can then travel back along the S beam path back

through the distorter to become the backward-pump in the FWM geometry. The backward-pump can then scatter off the gain-grating (1^{st} order) and continue to oscillate around the loop in a clockwise direction. The gain-grating has essentially closed the loop in this direction. The undiffracted part of the BP (0^{th} order) passes through the gain region where it is amplified further and on to point A to become the output of the resonator.

In order for the ASE to be diffracted by the gain-grating with a high efficiency it must satisfy the Bragg and frequency conditions of the grating [1]. The Bragg condition ensures that the k-vector of the BP be exactly opposite to the k-vector of the FP i.e. if the BP is the phase-conjugate of the FP it is diffracted with the highest efficiency from the grating. The scattered wave is then, according to section 2.5 the phase-conjugate of the S wave which travels back through the phase distortions in the reverse direction and is therefore corrected for the aberrations, so that at point C the BP is once again the phase-conjugate of the FP, i.e. a self-consistent mode is formed. Since the phase-conjugate beam has the highest diffraction efficiency from the grating it must then have the lowest threshold of oscillation. The undiffracted part of the BP (the 0^{th} order of the gain-grating) still remains the phase-conjugate of the FP as it travels back through the gain region and on to point C ensuring that the resonator output is an amplified plane-wave. The frequency selectivity condition of the grating ensures that only those frequencies that fall within the narrow bandwidth of the gain-grating are diffracted with a high efficiency (and hence oscillate) [2], and this aspect is discussed further in section 3.5.

In the simple explanation above it is assumed that the input to the resonator, the FP, has a plane-wave phase front. More generally the input can be any arbitrary wavefront and the amplified output will still remain the phase-conjugate of the input field.

In section 2.8 the FWM process, when described in a black-box geometry, could be viewed as a PCM. The phase-conjugate resonator shown in figures 3.1 and 3.2 can also be viewed as a PCM whereby a single input to the system (FP) is amplified and phase-conjugated, the rest of the system be-

ing the PCM. It is because only a single input beam is required to achieve phase-conjugation within this self-intersecting scheme that the process has been termed self-pumped phase-conjugation [3].

3.2.1 Other resonator geometries

The above analysis corresponds to a phase-conjugate resonator with a loop closed via a *transmission* gain-grating. Figure 3.3 shows schematically how an adaptive resonator can be formed that is closed by a *reflection* gain-grating. As with the transmission case a plane phase-front, termed the FP is input into the system at point B in figure 3.3. This then travels anti-clockwise around the resonator loop on to point D where it is termed the signal (S) beam. Again, the interference between the FP and S is stored in the form of a gain-grating within the FWM amplifier.

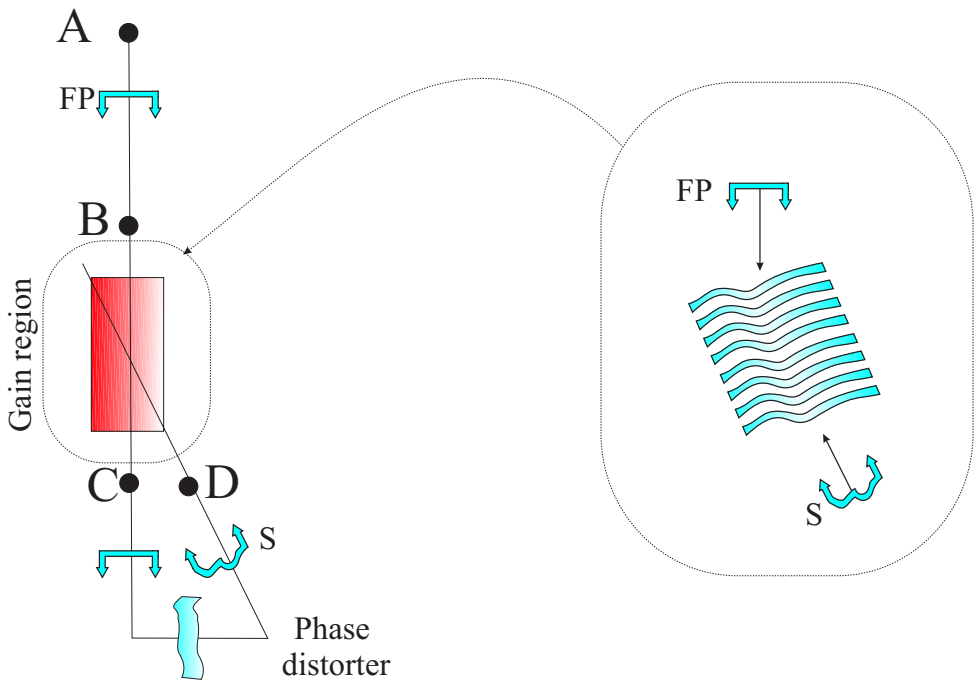

Figure 3.3: The grating writing process inside a phase-conjugate resonator with a reflection grating geometry

Figure 3.4 shows how this grating closes the resonator and forms a PC oscillating mode in the clockwise direction. ASE scattered from the grating

travels clockwise around the loop to point C. At this point any ASE that is Bragg matched (and is hence the PC of the FP) to the grating is diffracted into the first order of the grating and begins to oscillate. Again, the zeroth order of the grating becomes the PC output of the resonator.

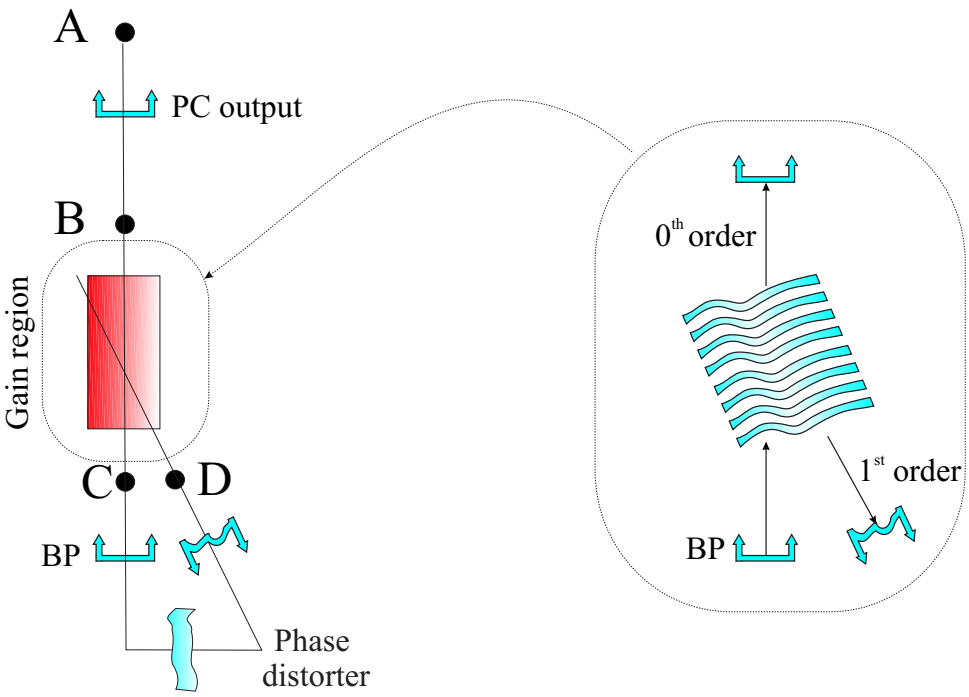

Figure 3.4: The grating reading process inside a phase-conjugate resonator with a reflection grating geometry

3.3 ABCD analysis of the resonator loop

In section 2.4 it was shown that the pump-diode could be focussed down to a spot size of around 36 μm inside the Nd:YVO_4 crystal. In this section an ABCD analysis [4] is used to show how the grating writing beams, produced by the input seed-laser, propagate around the phase-conjugate resonator. The primary aim of this section is to design a resonator such that the forward-pump and the signal beam are of comparable sizes with each other and with the gain region. This mode-matching ensures that full use of the gain region is achieved maximising the extracted power.

Table 3.1 shows the ray transfer matrices for four optical elements used in

Description	Transfer matrix
Free space of length d	$\begin{bmatrix} 1 & d \\ 0 & 1 \end{bmatrix}$
Thin lens with focal length f	$\begin{bmatrix} 1 & 0 \\ -\frac{1}{f} & 1 \end{bmatrix}$
Interface from n_1 to n_2	$\begin{bmatrix} 1 & 0 \\ 0 & \frac{n_1}{n_2} \end{bmatrix}$
Phase-conjugate mirror	$\begin{bmatrix} 1 & 0 \\ 0 & -1 \end{bmatrix}$

Table 3.1: Ray matrices used in resonator model

the ABCD analysis. Figure 3.5 shows the propagation of the input seed laser as it passes around the clockwise direction through the PC resonator. The seed input beam has a spot size of 0.9 mm at the output aperture of the seed laser (distance,z, = 0) and an M^2 of 1. This beam is then directed towards lens 1 which is placed 500 mm from the output of the seed-laser. Lens 1 has a focal length of 100 mm and focusses the forward-pump into the crystal (with refractive index n = 2.17) to a waist-size of 37 µm . This beam is then recollimated with the use of a second 100 mm focal length lens (lens 2), placed at 712 mm. This recollimated beam travels a distance of 1 m around the loop where it becomes the signal beam which is subsequently focussed back into the gain region by lens 1 to a waist-size of again 37 µm .

The FP and S beam now have a good overlap with each other and with the gain region. The phase-conjugation process now reverses the direction of the S beam and is described by the PCM element in table 3.1. The phase-conjugate mode produced within the amplifier travels back along the original beam all the time remaining the PC of the forward travelling beam. This means that the spot size of the PC mode is identical at all points to the forward travelling beam producing an output that is a true PC of

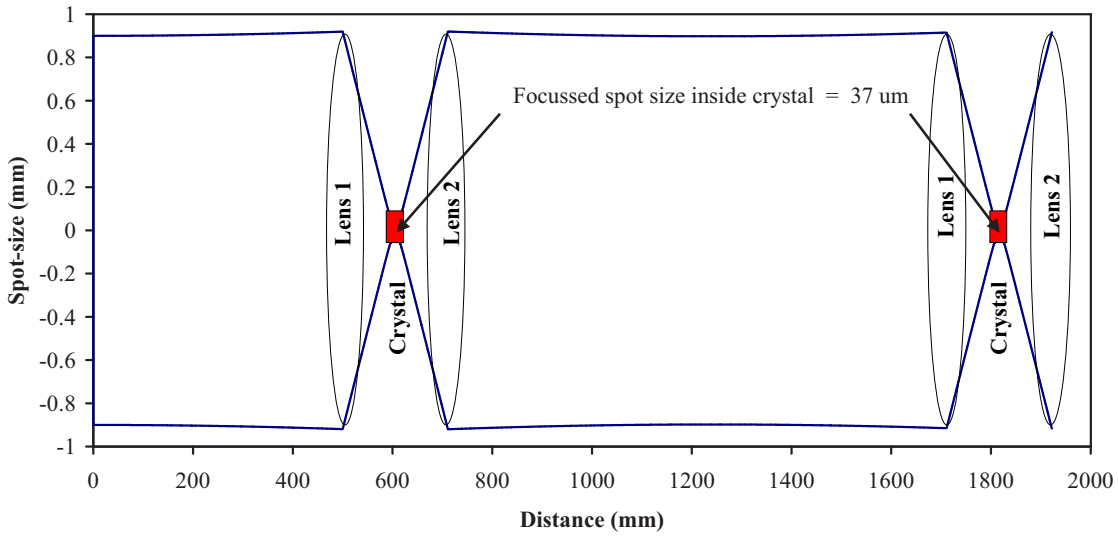

Figure 3.5: Spot-size of the grating writing beam as it travels around the phase-conjugate resonator.

the input beam ensuring that the oscillating mode also has good overlap with the amplifier gain region. The values given for the focal length for the lenses used in the above analysis will not be entirely correct for 1064 nm light, where the material dispersion of the lens will cause the focal length to change slightly for different wavelengths. In this case slight adjustments to the positioning of the lenses have to be made experimentally to produce the best overlap.

3.4 Non-reciprocal transmission element

In section 3.2 it was shown that a gain-grating is formed when the FP and S beam overlap within the inverted region of the FWM-amplifier. In order to maximise the output from the phase-conjugate resonator it is necessary to match the intensity of the two grating writing beams so that the interference pattern they write has the largest contrast ratio producing a high diffraction-efficiency grating (see section 2.7.1). With reference to figure 3.1, the intensity of the S beam is much greater than that of the FP

due to the high gain experienced by the signal as it passes through the FWM-amplifier. In the anti-clockwise direction a device is needed that attenuates the S beam so that its intensity matches that of the FP at the point at which they intersect within the gain region of the FWM amplifier. The attenuation factor in this case will be roughly equal to the single-pass gain experienced by the FP as it travels through the FWM-amplifier (up to 15000). It was also shown that phase-conjugate oscillation of the resonator occurs in the clockwise direction. In order for the loss in this direction, and hence the lasing threshold to be as small as possible, a high transmission is required.

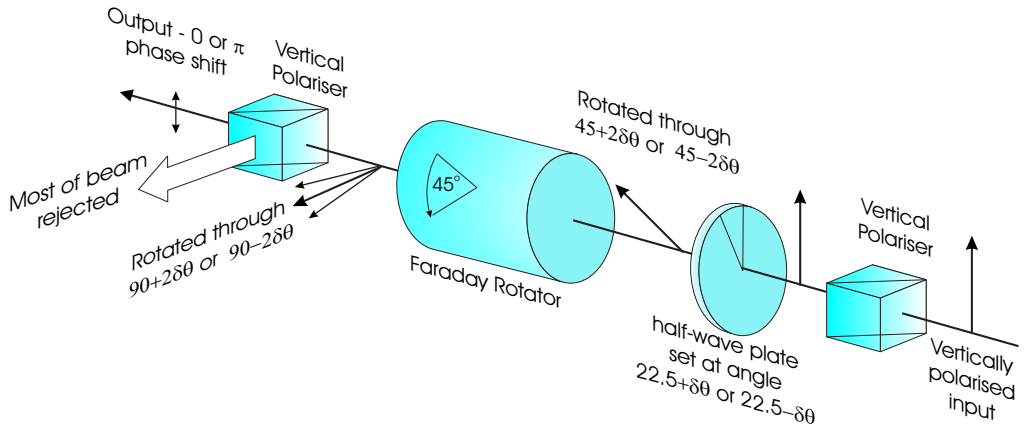

Figure 3.6: Non-reciprocal transmission element in the low transmission (anti-clockwise) direction.

One way of achieving this is to use a non-reciprocal transmission element (NRTE) as shown in figure 3.6. This device consists of two vertical polarisers with a Faraday rotator and half-wave plate inserted between them. Firstly, the beam that travels anti-clockwise through the resonator loop is considered. This is the direction which requires attenuation of the beam and is defined as the low transmission direction (t_-) through the NRTE. Figure 3.6 shows a vertically polarised beam travelling from right to left through the NRTE (low transmission direction). The half-wave plate is set to $22.5° \pm \delta\theta$ where $\delta\theta$ represents a small deviation either side of $22.5°$. The half-wave plate then produces a rotation in the polarisation of the vertically polarised input beam of $45° \pm 2\delta\theta$. This beam is subsequently rotated by a further $45°$ in the same direction as it passes through the Faraday

rotator. The beam, which is now horizontally ($\pm 2\delta\theta$) polarised, is then incident on a second polariser again oriented to pass vertically polarised light. It can be seen that if the output polarisation from the Faraday rotator is above the horizontal then the output from the second polariser has the same relative phase as the input beam, i.e. as the E-field component of the *input* beam increases (positive amplitude) the *output* E-field also increases (also a positive amplitude). If the output of the rotator is below the horizontal then the vertically polarised output will be π out of phase with the input i.e a positive value for *input* amplitude will give a negative value for *output* amplitude . This phase shift will turn out to have important consequences for the operation of the adaptive resonator and is studied further in section 3.6.

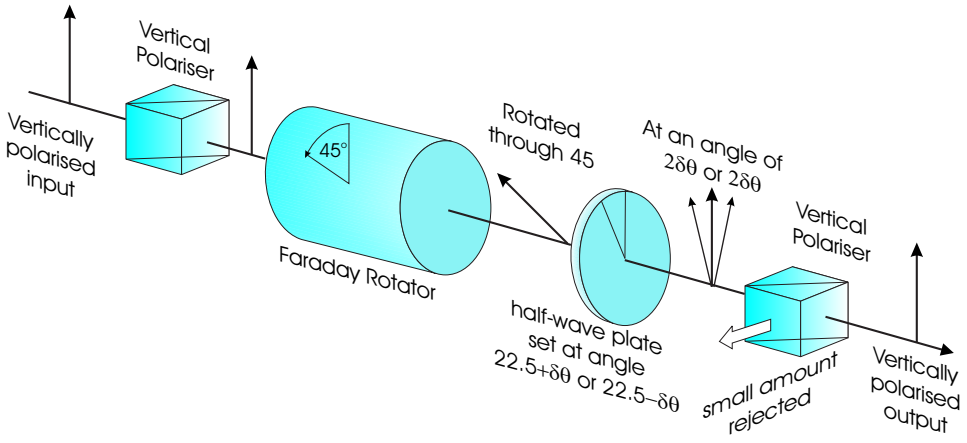

Figure 3.7: Non-reciprocal transmission element in the high transmission (clockwise) direction.

Figure 3.7 shows the clockwise, high transmission beam (t_+), which travels from left to right through the same NRTE. This time the beam is rotated by $45°$ in the *same* direction as the anti-clockwise beam by the Faraday rotator, but $45° \pm 2\delta\theta$ in the other direction by the half-wave plate. The output from the polariser in this direction has a large intensity, is vertically polarised and has the same relative phase as the input in this direction.

This NRTE can now be placed within the adaptive resonator loop in order to optimise the PC output intensity. The amplitude non-reciprocity ensures that the diffraction efficiency of the grating can be maximised, whilst the loss to the resonating PC mode is minimised.

3.4.1 NRTE modelling

The NRTE can be modelled using Jones matrix algebra [5]. The Jones matrix for a vertical polariser is

$$P_v = \begin{bmatrix} 0 & 0 \\ 0 & 1 \end{bmatrix} \tag{3.1}$$

The Jones matrix used to describe the rotation of the input beam by the half-wave plate is given as

$$HWP = i \begin{bmatrix} \cos(2\theta) & \sin(2\theta) \\ \sin(2\theta) & -\cos(2\theta) \end{bmatrix} \tag{3.2}$$

where θ is the half-wave plate angle. The 45° rotation produced by the Faraday rotator is given by the matrix

$$FR = \begin{bmatrix} \cos(45) & \sin(45) \\ -\sin(45) & \cos(45) \end{bmatrix} \tag{3.3}$$

Finally, the vertically polarised input field amplitude is given by

$$E_{input} = \begin{bmatrix} 0 \\ 1 \end{bmatrix} \tag{3.4}$$

The *amplitude* transmission of the NRTE in the low transmission (t_-) direction is then given by matrix multiplication of each optical element within the NRTE in reverse order in which they are first encountered by the input beam, giving

$$t_- = P_v \cdot FR \cdot HWP \cdot P_v \cdot E_{input} \tag{3.5}$$

and for an input field travelling through the NRTE in the high transmission (t_+) direction

$$t_+ = P_v \cdot HWP \cdot FR \cdot P_v \cdot E_{input} \tag{3.6}$$

The *intensity* transmission (T_-) in the t_- (and similarly for the t_+) direction can now be found using the formula

$$\begin{aligned} T_- &= t_-^\dagger t_- \\ T_- &= \begin{pmatrix} t_{-x}^* & t_{-y}^* \end{pmatrix} \begin{pmatrix} t_{-x} \\ t_{-y} \end{pmatrix} \end{aligned} \tag{3.7}$$

where t_{-x} and t_{-y} are the amplitude transmission components for the horizontal and vertical polarisations and t_{-x}^* and t_{-y}^* are their conjugates.

The top graph in figure 3.8 shows the amplitude transmission of the NRTE in both the low transmission (t_-) (green line) and high transmission (t_+) (blue line) directions. At point A (HWP angle = 67.5°) the amplitude transmission in the t_- is zero, whilst in the t_+ direction it is plus one, corresponding to an intensity transmission of one as shown in the bottom graph in figure 3.8. By moving the HWP angle slightly the transmission in the t_- direction can be made arbitrarily small allowing good attenuation of the amplified signal beam, whilst at the same time the transmission in the t_+ direction is almost unity allowing the PC mode to pass almost unattenuated. An ideal NRTE would allow one to vary the intensity in the t_- direction making it possible to match the writing beam intensities whilst having unity transmission in the t_+ direction for all HWP angles. The bottom graph in figure 3.8 shows the modelled intensity transmission through the NRTE in both directions and some experimental data for verification. The NRTE model can now be used within a model of the phase-conjugate resonator system using the HWP angle as an optimising parameter (see section 3.9).

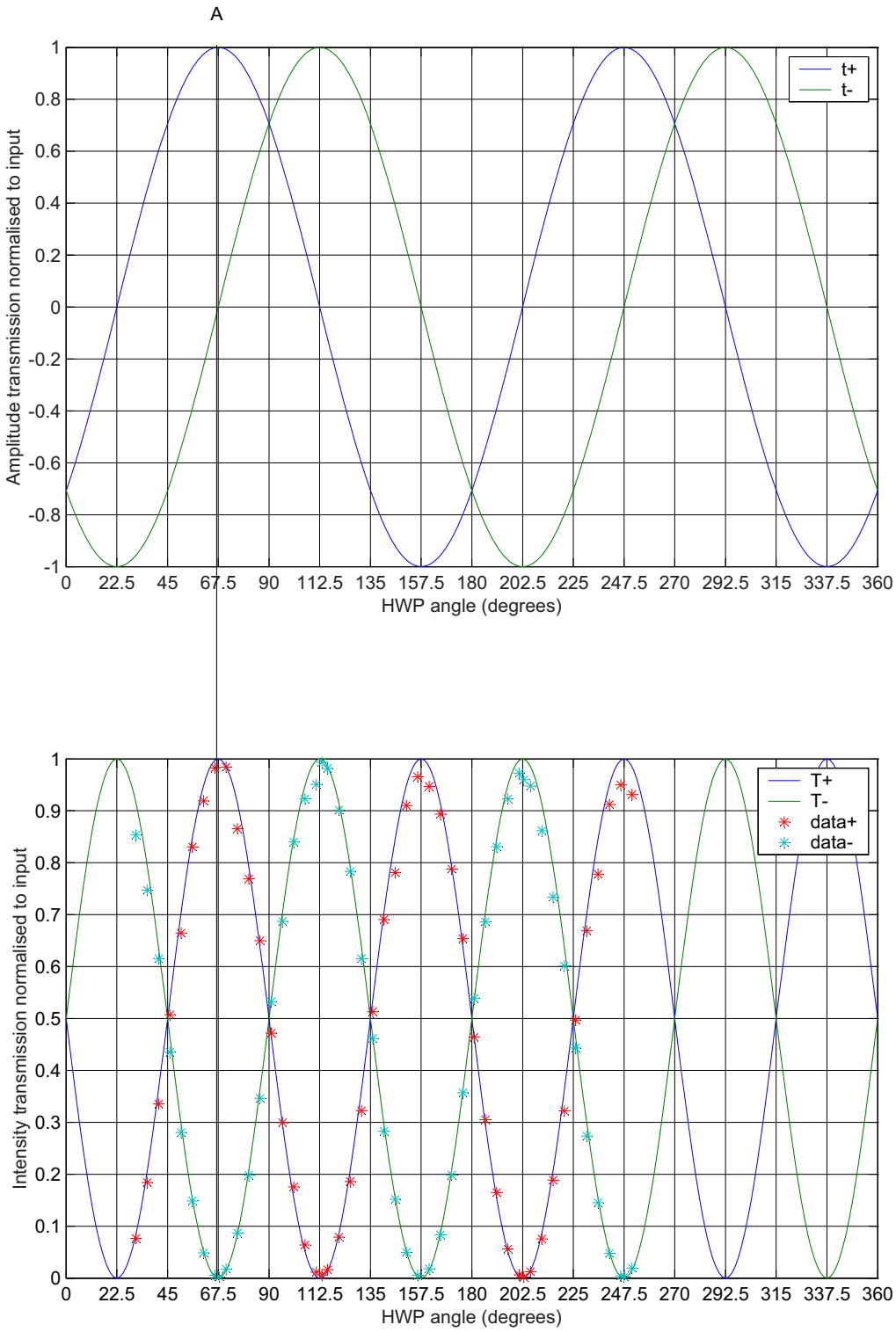

Figure 3.8: Modelling of the amplitude transmission (top) and intensity transmission (bottom) in both directions through the NRTE.

3.5 SLM operation - frequency selectivity

Diffraction gratings are often employed in laser resonators as a means of controlling the spectral distribution of the laser output. Single longitudinal mode operation of the phase-conjugate oscillator can be achieved due to the spectral selectivity of the volume gain-grating formed within the FWM crystal. It has been shown [1] that the diffraction efficiency, η, of a volume gain-grating with a k-vector $K = \frac{2\pi}{\Lambda}$ where Λ is the grating period can be given by

$$\eta = \exp\left(2\alpha_{ave}d\right)\left[\frac{\sinh\left(\phi^2 - \chi^2\right)^{1/2}}{\left(1 - \frac{\chi^2}{\phi^2}\right)^{1/2}}\right]^2 \tag{3.8}$$

and, for a FWM amplifier of length d and refractive index n, ϕ and χ are given by

$$\begin{aligned}\phi &= \alpha_{grating}\frac{d}{2} \\ \chi &= \frac{\Delta\lambda\ K^2 d}{8\pi n}\end{aligned} \tag{3.9}$$

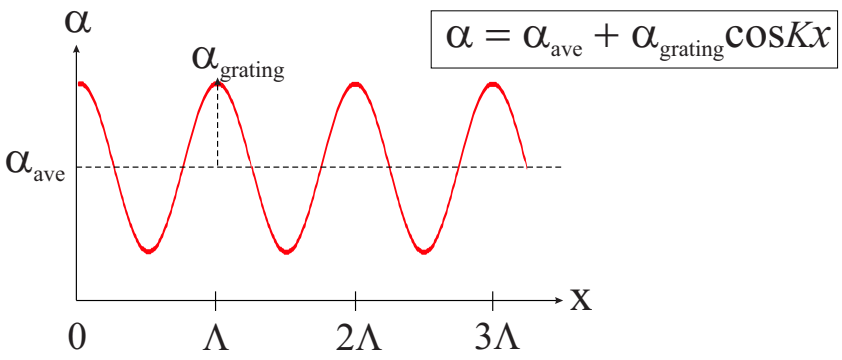

Figure 3.9: The form of the gain-grating used in the diffraction efficiency model.

where α_{ave} is the average value of the saturable amplitude gain coefficient and $\alpha_{grating}$ is the amplitude of the modulation of the grating as defined in figure 3.9. Any small deviation in the grating reading beam wavelength, $\Delta\lambda$, from the Bragg matched wavelength leads to a reduction in

the diffraction efficiency of the grating as shown in figure 3.10.

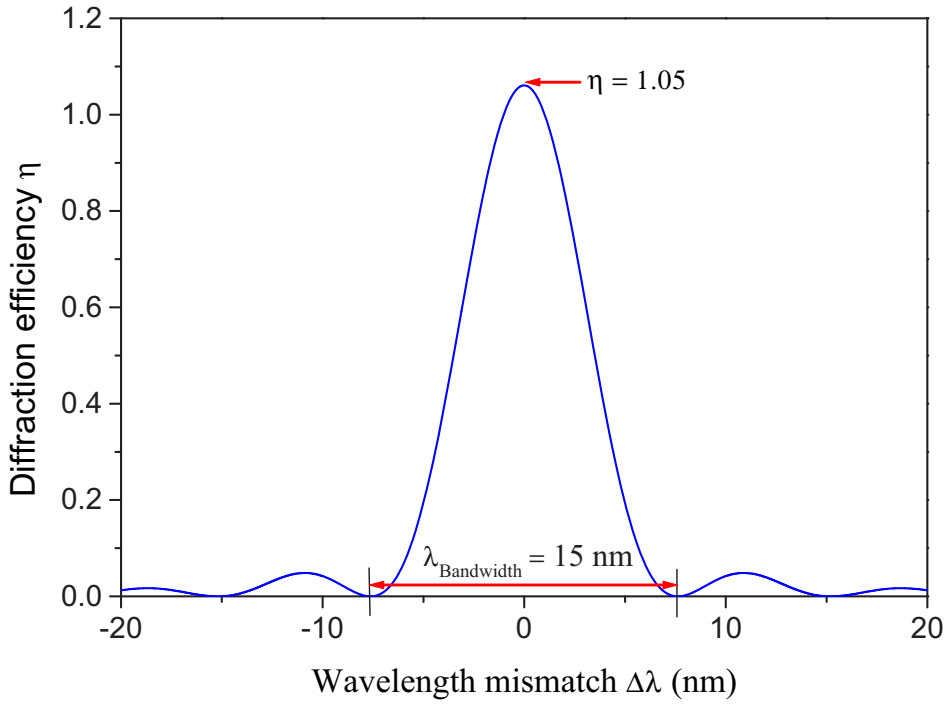

Figure 3.10: Diffraction efficiency of a gain-grating as a function of the reading beam wavelength mismatch.

The wavelength bandwidth of the grating, $\lambda_{bandwidth}$, was given in [1] as

$$\lambda_{bandwidth} = \frac{\lambda_0^2}{dn \sin^2 \theta} \tag{3.10}$$

For two 1064 nm writing beams, for example, incident within a 20 mm long Nd:YVO_4 gain region with an angle of $2\theta = 5^0$ between them (which is typical for a transmission grating) yields a grating bandwidth, $\lambda_{bandwidth}$, of about 15 nm. This is very large and by itself is not wavelength selective enough to account for SLM operation of the phase-conjugate resonator. The above description, however, looks at a gain-grating written in a standard FWM geometry with independent writing and reading beams saturating the gain of the amplifier.

In order to see how the gain-grating contributes to the SLM operation of the adaptive resonator it is necessary to study the threshold condition for

the phase-conjugate laser loop given by

$$\eta T_+ > 1 \tag{3.11}$$

where the diffraction efficiency, η, of the grating can be greater than unity because of the gain in the grating as described previously and T_+ is the transmission in the clockwise direction through the NRTE. When the resonator is oscillating under steady-state conditions the diffraction efficiency is

$$\eta_{ss} = \frac{1}{T_+} \tag{3.12}$$

that is the total backward loop gain and losses, are clamped to 1. To produce an optimum output of the resonator the NRTE transmission in the high transmission (T_+) direction is typically around 95% giving a diffraction efficiency at steady-state of 1.05. This is the point at which the loop gain in the clockwise direction i.e. the diffraction efficiency η of the grating (saturated to its steady-state value by the oscillating mode) is equal to the clockwise losses (such as the 5% removed by the NRTE).

So although the bandwidth of the grating is large enough to diffract a broad range of wavelengths into the first order of the grating the actual number of longitudinal modes that will then go on to produce a sustainable oscillation is in fact very small (see section 3.7.4). This occurs because all other modes (i.e. modes shifted from the Bragg wavelength) have a diffraction efficiency less than 1.05 (see figure 3.10) and so the total loop gain/losses is less than unity and so cannot sustain an oscillation.

3.6 Phase changes in the resonator loop

The non-reciprocal π phase-shift induced by the NRTE between the clockwise and anti-clockwise modes plays an important role in the build up of a sustainable resonator mode. To see this, first consider the case when

there is no relative phase-shift between the clockwise and anti-clockwise transmitted beams through the NRTE.

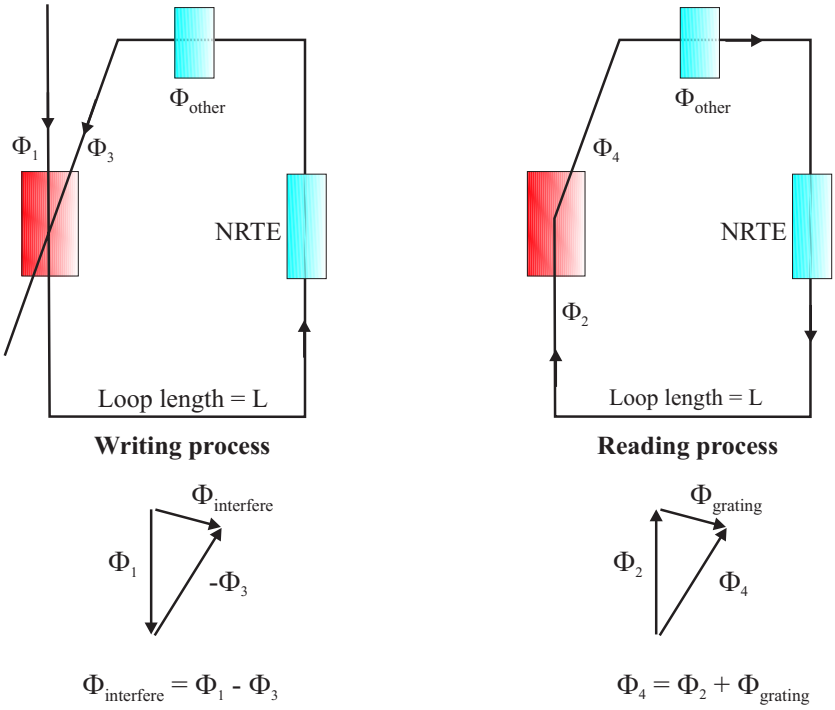

Figure 3.11: Round trip instantaneous phase of loop.

Referring to figure 3.11, the seed input beam (FP) into the adaptive resonator has an instantaneous phase at time t of ϕ_1, at the entrance to the FWM crystal and a wave-vector k_1. The signal beam's instantaneous phase ϕ_3, produced as the FP travels around the resonator loop, is then given by

$$\phi_3 = \phi_1 + k_1 L + \phi_{other} \tag{3.13}$$

where L is the loop length and ϕ_{other} describes any other phase shifts accumulated by the signal wave as it travels around the loop including any phase distortions within the loop. The interference between beam 1 and 3 (the FP and S beam respectively) creates an interference pattern whose phase, $\phi_{interfere}$, is given as

$$\begin{aligned}\phi_{interfere} &= \phi_1 - \phi_3 \\ \phi_{interfere} &= \phi_1 - \phi_1 - k_1 L - \phi_{other} \\ \phi_{interfere} &= -k_1 L - \phi_{other}\end{aligned} \tag{3.14}$$

In section 2.3 it was shown that the gain-grating has a π phase-shift relative to the interference pattern. The phase of the gain-grating, $\phi_{grating}$, taking into account the π phase-shift is given by

$$\begin{aligned}\phi_{grating} &= \phi_{interfere} + \pi \\ \phi_{grating} &= -k_1 L - \phi_{other} + \pi\end{aligned} \tag{3.15}$$

In the reading process beam 2 (the backward pump) with phase, ϕ_2, at the entrance to the FWM amplifier and with a wave-vector, k_2, is scattered into the first-order of the gain-grating to produce beam 4 (the PC reconstruction) with a phase, ϕ_4, given by

$$\begin{aligned}\phi_4 &= \phi_2 + \phi_{grating} \\ \phi_4 &= \phi_2 - k_1 L - \phi_{other} + \pi\end{aligned} \tag{3.16}$$

beam 4 then travels around the loop, through all other phase elements, ϕ_{other}, to once again become beam 2 whose new phase, ϕ_2^*, is given by

$$\begin{aligned}\phi_2^* &= \phi_4 + k_2 L + \phi_{other} \\ \phi_2^* &= \phi_2 + (k_2 - k_1) L + \pi\end{aligned} \tag{3.17}$$

If $k_1 = k_2$ i.e. the grating reading beam has the same frequency as the grating writing beams, then $\phi_2^* = \phi_2 + \pi$ and destructive interference occurs resulting in an unsustainable laser mode. To achieve a sustainable oscillation i.e. constructive interference between successive round trips of the laser-mode it is required that

$$(k_2 - k_1) L = (2n - 1)\pi \tag{3.18}$$

where n is any integer. substituting $k = \frac{2\pi\nu}{c}$ into this yields

$$\Delta\nu = \frac{\left(n - \frac{1}{2}\right) c}{L} \tag{3.19}$$

where $\Delta\nu$ is the difference in frequency of the clockwise and anti-clockwise mode. So a sustainable phase-conjugate mode can build up as long as equation 3.19 is met i.e. the anti-clockwise PC mode shifts slightly in frequency from that of the seed laser. As an example, for a seed input of 1064 nm around a phase-conjugate resonator with a round-trip length of 1 m the frequency shift needed to achieve oscillation is $\Delta\nu = 0.15$ GHz which is well within both the gain bandwidth of Nd:YVO_4 (254 GHz [6]) and the bandwidth of the gain-grating (see section 3.5).

When the NRTE is set such that there is a non-reciprocal π phase shift between the two directions, following the same procedure, ϕ_2^* is now given by

$$\phi_2^* = \phi_2 + (k_2 - k_1)L + 2\pi \tag{3.20}$$

in this case when the clockwise and anti-clockwise mode have the same wavelength, $k_1 = k_2$, constructive interference of the mode can occur and oscillations are sustained.

3.7 Seeded resonator results

Figure 3.12 shows the experimental phase-conjugate oscillator (PCO) in schematic form. The seed laser was capable of producing a 300 mW 1064 nm output in a single-longitudinal mode, diffraction limited beam. This was then sent through a Faraday isolator placed between two half wave plates. The first wave-plate allowed the seed input power to the resonator to be varied for optimisation of the phase-conjugate oscillator. The second wave-plate rotated the polarisation of the beam, coming from the Faraday isolator, to the vertical position ($\|$ to the crystal *c*-axis) thereby accessing the greatest emission cross section for the Nd:YVO_4 crystal. Any

phase-conjugate output from the PCO travelling back towards the seed laser would be removed by the isolator before it reached the seed laser.

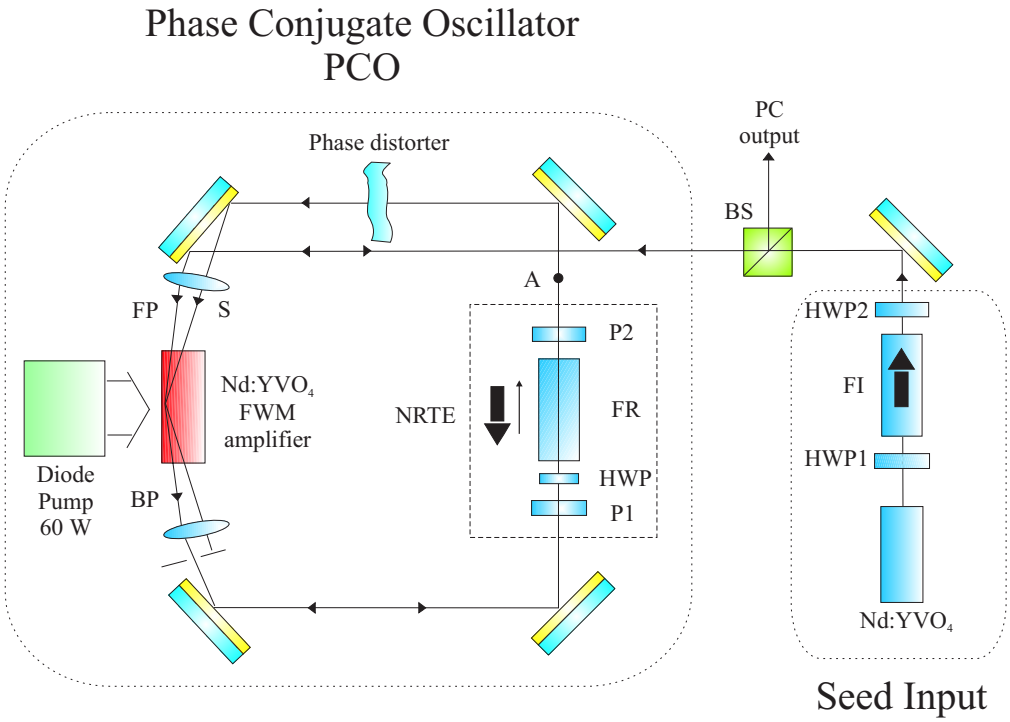

Figure 3.12: Schematic of the seeded phase-conjugate resonator.

The FWM amplifier used for the PCO was different from that used in the FWM experiments, described in section 2.8, in several aspects. Firstly, the crystal used consisted of a 1.1 at.% Nd-doped YVO_4 *a*-cut crystal of dimensions 20 mm x 1 mm x 5 mm, (see appendix C for diagram). The *a* faces of the crystal were angled at approximately 2° to reduce the effects of parasitic lasing. The crystal was anti-reflection coated for the pumping wavelength on both *b* faces and anti-reflection coated for 1064 nm on both *a* faces. The *c* faces (those in contact with the heat-sink) were inspection polished only. Secondly, the crystal was side pumped by a 60 W TM polarised laser-diode bar. This meant that the diode output was already vertically polarised and did not need an additional half-wave plate to access the maximum pump absorption coefficient (unlike the TE polarised diode used previously). Finally, the output of the diode bar was focussed by a cylindrical lens of focal length f = 6.35 mm onto one of the *b* faces of the Nd:YVO_4 crystal giving a calculated spot size in the crystal of 36 μm .

The gain of the FWM amplifier could be varied by moving the 6.35 mm focussing lens towards (or away) from the pumped *b* face of the crystal, decreasing the spot-size of the focussed diode pump beam on the face of the crystal and resulting in an increased inversion density and hence gain. All interacting beams (FP, BP and S) were focussed into the gain region by the use of 100 mm focal length spherical lenses. The beams were then re-collimated by the use of another identical lens placed roughly 200 mm from the first as described in section 3.3.

3.7.1 Input-Output characteristics

Figure 3.13 shows the measured phase-conjugate output power as a function of the seed laser input power for 5 values of measured small-signal single-pass gain of the FP beam.

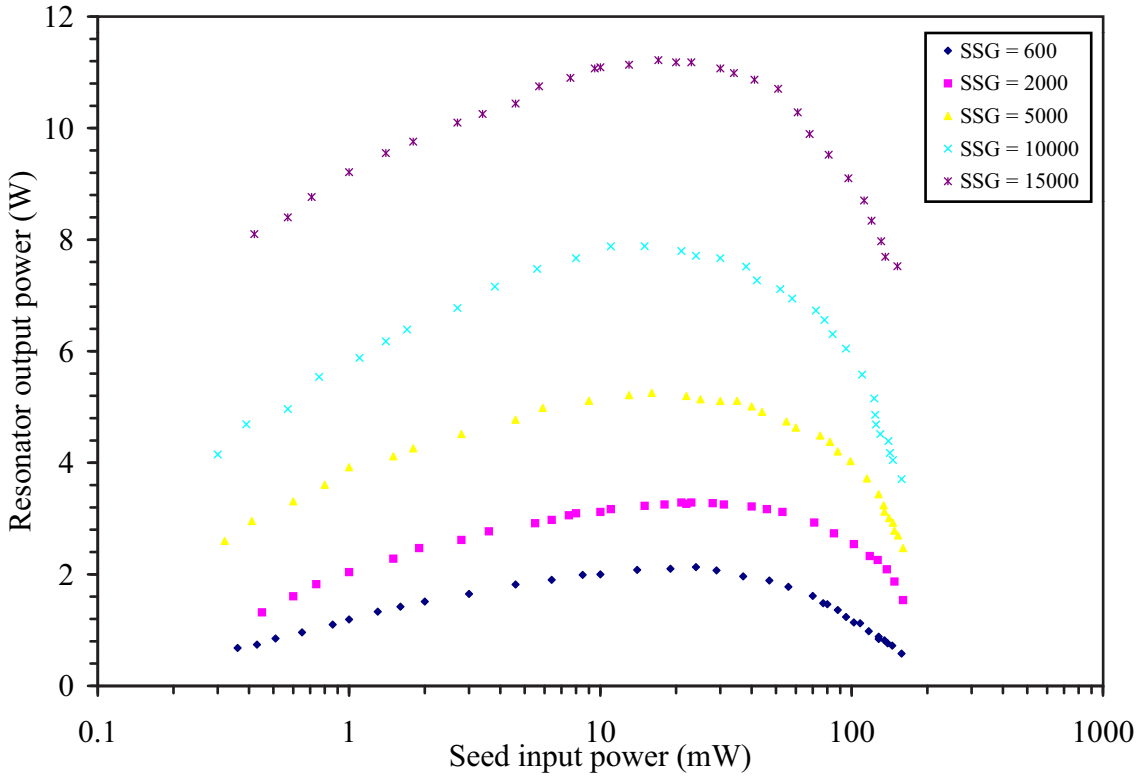

Figure 3.13: Measured seeded resonator output power versus seed input power for several values of measured small-signal single-pass gain.

A maximum output of around 11.6 W was achieved for a SSG of 15000. The peak output for all cases occurred for a seed input power of around 25 mW, which is fairly consistent with a theoretical prediction made by Brignon *et al* who calculated that the peak output of a phase-conjugate resonator was expected to occur for a seed input intensity of around $0.1 \times I_{sat}$ [7]. For Nd:YVO_4 with an $I_{sat} = 0.83\ kWcm^{-2}$ and a focussed spot size of 40 μm the peak output is predicted to occur at around 4.2 mW. Below this maximum value the output begins to fall as the diffraction efficiency of the grating formed within the FWM amplifier is decreased due to very low saturation of the gain (section 2.7). Above this value the output also falls as a result of over-saturation of the inversion density removing most of the available gain needed for the oscillating mode.

The resonator shows a well defined termination point for a seed input of around 200 mW at which lasing ceases for all gains. At this point the resonator fails to reach threshold due to the over-saturation of the gain by the grating writing beams producing a low diffraction efficiency grating, η. The complete round trip gain of the phase-conjugate resonator at this stage is then less than 1, $\eta T_+ < 1$, and so the PC mode no longer reaches threshold.

3.7.2 Intracavity oscillating power

Figure 3.14 shows the power circulating in the clockwise direction of the cavity (measured at point A in figure 3.12) as a function of the seed input power.

Taking the curve for a forward pump SSG of 15000 as an example the first thing to notice is that the peak of the intra-cavity power (around 380 mW) occurs for a seed input of 70 mW. This is 7 times higher than the seed input of 10 mW needed to give the maximum resonator output in figure 3.13. The peak in the intra-cavity power does not necessarily correspond to maximum output from the phase-conjugate oscillator. Secondly for the peak resonator output of 11.6 W the intra-cavity power is just 290 mW. This would suggest that most of the power in the phase-conjugate output

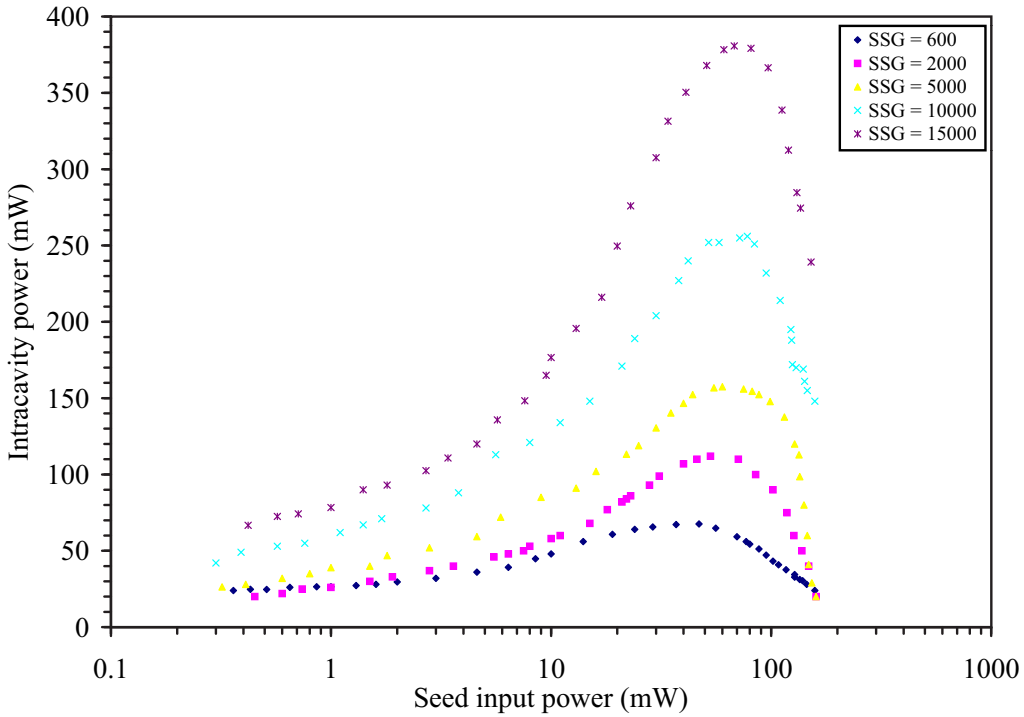

Figure 3.14: Clockwise intra-cavity oscillating power versus seed input power for several values of small signal single pass gain.

beam is picked up on its final pass through the FWM amplifier and that the diffraction efficiency of the gain-grating formed is small, diffracting only a small proportion of the output beam back into the loop to sustain steady-state oscillation.

3.7.3 NRTE HWP angle versus output

Figure 3.15 shows the phase-conjugate output power of the resonator as a function of the NRTE half-wave plate angle for each of the small-signal gains. The seed input power in each case was set to give the maximum resonator output. Also shown, is the transmission characteristics versus NRTE HWP angle (figure 3.16). For a small-signal gain of 15000 the maximum output of 11.6 W occurs for a HWP angle (i.e. the angle between the vertical polarisation of the signal beam and the HWP optic axis) of around 63°. The intensity transmission of the NRTE in the anti-clockwise

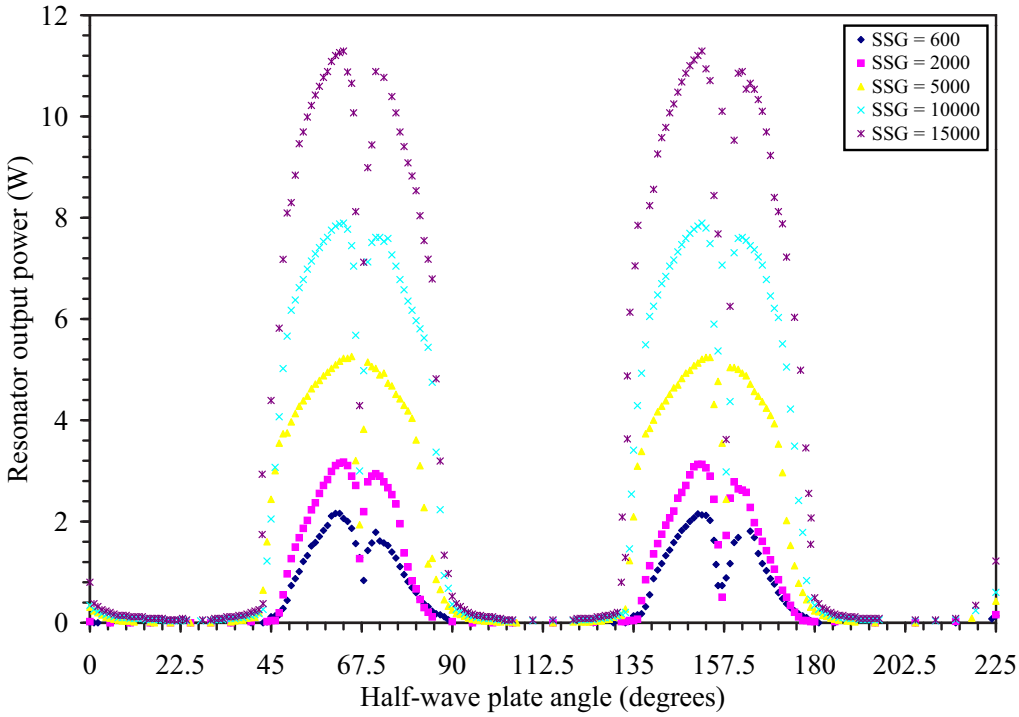

Figure 3.15: Seeded resonator output power versus NRTE HWP angle for several values of small-signal single-pass gain.

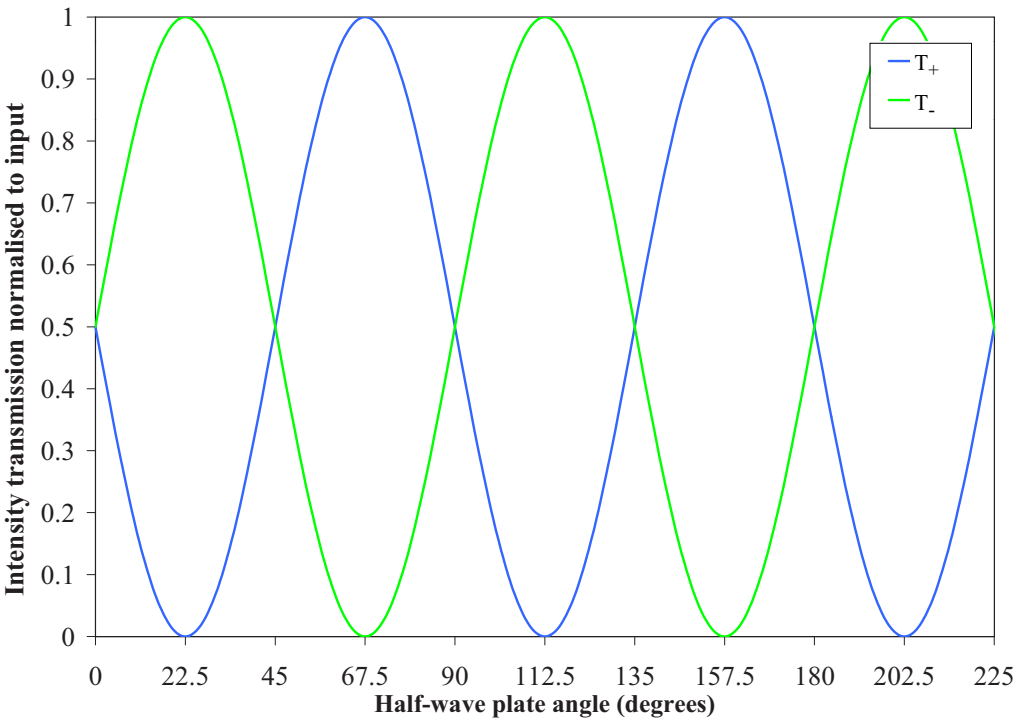

Figure 3.16: Intensity transmission in the clockwise and anti-clockwise directions through the NRTE as a function of NRTE HWP angle.

(T_-) direction at this point (shown in figure 3.16) is roughly 0.02 i.e. 2% of the incident power is transmitted in this direction. At an angle of 40° the output from the resonator is almost zero in all five cases. At this point the writing beam intensities are not well matched and hence the gain-grating has a low diffraction efficiency (see section 2.7.1), the resonator fails to reach threshold and the output is zero. At a HWP angle of around 45° the threshold of oscillation is reached and the resonator begins to produce a phase-conjugate output. As the HWP angle is increased further the output power increases until it reaches the maximum of 11.6 W at 63°. At this stage the NRTE is producing a non-reciprocal π phase shift between the clockwise and anti-clockwise modes as discussed in section 3.6 and can oscillate with the same wavelength as the seed laser. A further increase in the HWP angle to approximately 67.5° causes an abrupt drop in the output power, due to the anti-clockwise (T_-) transmission of the NRTE being almost zero, therefore the signal (S) beam is not present and hence no grating is formed resulting in zero output from the resonator.

With a further increase in the HWP angle the intensity transmission characteristics of the NRTE repeats itself (i.e. are symmetric), however, at this point the relative phase-shift induced by the NRTE between the clockwise and anti-clockwise beams in the resonator loop is zero i.e. the NRTE has a reciprocal phase-shift (see section 3.4.1). According to the discussion in section 3.6 if the wavelength of the PC mode is the same as the seed laser when the NRTE has a reciprocal phase-shift, then oscillation of the phase-conjugate resonator is expected to cease, however, the experimental results show otherwise, although the maximum output is lower for the same NRTE intensity transmission. An output is only expected to occur on the phase-reciprocal side of the NRTE HWP angle if the PC mode adjusts its frequency slightly from that of the seed laser. In section 3.6 it was shown that a shift in frequency of just 0.15 GHz was enough to compensate for the π phase-shift of the gain-grating, however, such a small shift in the frequency could not be detected experimentally due to limitations in the resolution (0.2 GHz) of measuring equipment (see next section).

3.7.4 Single longitudinal mode operation

Single longitudinal mode operation of the phase-conjugate resonator was confirmed using a plane-plane Fabry-Perot cavity with a distance of 15 mm between the two mirrors (yielding a free-spectral range of 10 GHz) the FWHM linewidth of the PC output, calculated from the Fabry-Perot trace, is around 0.2 GHz (instrument limited resolution). The output trace of the Fabry-Perot showing the single longitudinal mode operation of the resonator is shown in figure 3.17.

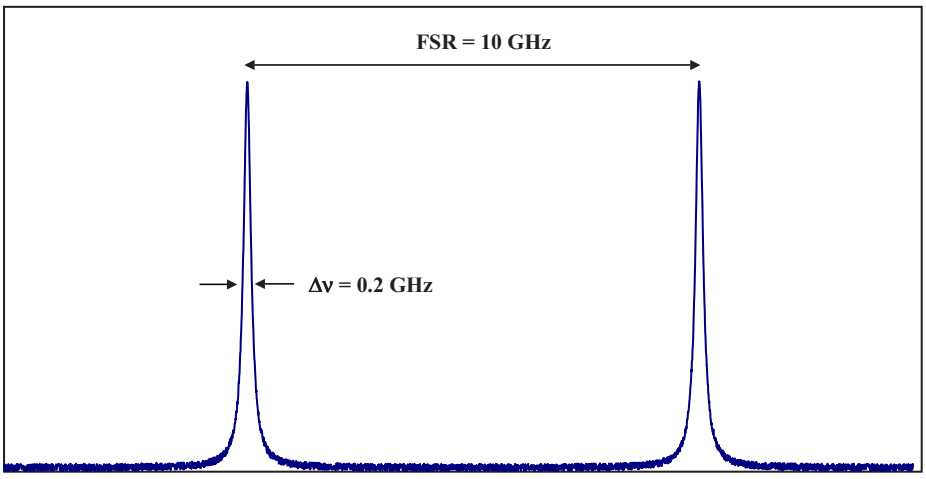

Figure 3.17: Fabry-Perot trace of the output of the seeded phase-conjugate resonator showing SLM operation.

3.7.5 Distortion correction and M^2

Figure 3.18 shows the spatial output from the resonator operating at an output of 11.6 W (SSG = 15000) a good Gaussian fit was obtained in both the vertical and horizontal axis of the beam. The M^2 of the output was measured using a Coherent mode-master and found to be 1.4 in the horizontal plane, $M_x^2 = 1.4$, and 1.3 in the vertical plane, $M_y^2 = 1.3$. It is immediately clear that the output is not the true phase-conjugate of the circular Gaussian input beam from the seed laser and is believed to be due

Figure 3.20: Spatial output from the PCO with a phase distortion present.

Figure 3.19: The form of the distortion ($M^2 > 30$) used to confirm the adaptive properties of the PCO.

Figure 3.18: Spatial output from the PCO with a SSG of 15000.

to the asymmetry of the gain region in the FWM amplifier reshaping the input beam as described in section 2.4.3.

To confirm the distortion correcting nature of the phase-conjugate mode a phase distortion, whose form is depicted in figure 3.19, was placed into the resonator loop at the position shown in figure 3.12. The phase-distorter used consisted of a 0.5 mm thick glass-slide etched in hydrofluoric acid producing a highly aberrated beam with $M^2 > 30$. Figure 3.20 shows the spatial output from the resonator with the distortion in the loop. The output was seen to improve in spatial quality with improved M^2 of $M_x^2 = 1.3$ and $M_x^2 = 1.2$ and slightly increased in power to 11.9 W. It would seem that the PC output from the adaptive laser can be improved slightly, both in spatial quality and power by adding phase distortions within the loop and this initially surprising result has a simple explanation.

When the adaptive resonator is running on a phase-conjugate mode the gain-grating closes the resonator loop and allows oscillation, a conventional laser mode cannot oscillate because the loop is not closed. However, a small proportion of the ASE from the amplifier is incident on the cavity mirrors and oscillates in a highly multimode beam producing a background noise which is output with the PC mode and can clearly be seen in figure 3.18. When the distortion is placed within the loop the phase-conjugate mode is able to compensate for the aberrations and continues to oscillate while the conventional multimode background noise, which is not able to adapt itself, suffers high losses and ceases to oscillate. This means the spatial quality of the PC mode increases and more gain is available for it hence increasing its power. This is analogous to such laser systems described in [8] whereby a hologram is designed, and placed inside a conventional laser cavity, which gives a higher divergence (and hence loss) for higher order modes, removing them from the cavity whilst leaving the fundamental mode unaffected.

3.8 Self-starting resonator results

The seeded phase-conjugate oscillator described in 3.2 can be made self-starting by removing the seed laser and replacing it with a wedged output coupler of the appropriate reflectivity. Figure 3.21 shows the *self-starting* PCO in schematic form. In this self-starting scheme the PC mode is initiated by ASE from the FWM amplifier travelling towards the output coupler (4% reflectivity) where a proportion is reflected back towards the amplifier to become the forward pump. This then travels around the loop to

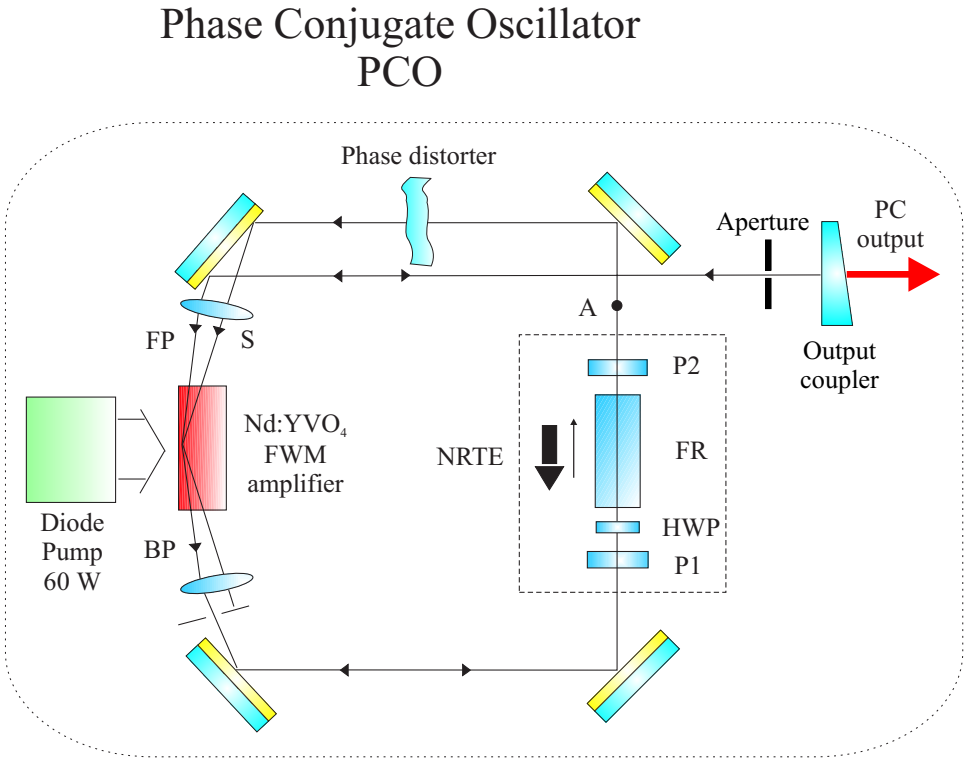

Figure 3.21: Self-starting phase-conjugate oscillator.

become the signal beam which forms the gain-grating when it intersects with the forward-pump. The process of phase-conjugate mode formation is then the same as that of the seeded case described in section 3.2. There are, however, two major differences for the self-starting case. The first concerns the transverse mode formation of the phase-conjugate mode. In the seeded case the gain-grating and hence the laser transverse mode is defined by the TEM_{00} seed input laser. In the self-starting case the transverse mode is defined by the ASE that is reflected from the output coupler

and as such has no well defined spatial profile and therefore some form of mode control needs to be employed to achieve single transverse mode oscillation. In this case transverse mode control was achieved by use of a 2 mm diameter aperture placed just in front of the output coupler within the cavity.

The second major difference concerns the frequency shift between the clockwise and anti-clockwise modes to compensate for the π phase shift of the gain-grating from the interference pattern (explained in section 3.6). In the self-starting case there can be no frequency shift between the clockwise and anti-clockwise modes since they are coupled together by the output coupler i.e. both the clockwise and anti-clockwise modes have to have the same wavelength. As mentioned in section 3.6, when the NRTE is set in such a way that it is phase non-reciprocal (i.e. a π phase shift between the two directions through the NRTE), the phase-conjugate resonator *can* produce an output when the clockwise and anti-clockwise beams have the same wavelength. However, if the NRTE is set such that there is zero phase-shift between the two directions then the PC mode cannot oscillate without shifting its wavelength slightly from that of the grating writing beams causing the *self-starting* resonator to cease output.

Figure 3.22 shows the PC output power of the *self-starting* resonator as a function of the NRTE HWP angle for SSG of 10000 and 15000. Also shown is the output versus HWP angle curve for a seeded resonator with a SSG of 15000. The maximum output power obtained for the single mode self-starting case was 8.2 W for a SSG of 15000 and 6 W for a SSG of 10000. As for the *seeded* case an output is obtained for the HWP values at which the NRTE is phase non-reciprocal. However, unlike the *seeded* case, phase-conjugate oscillation ceases when the NRTE displays phase reciprocity as the wavelength of the PC mode is not independent of the grating writing beams and hence cannot adjust its wavelength to compensate for the grating induced π phase shift.

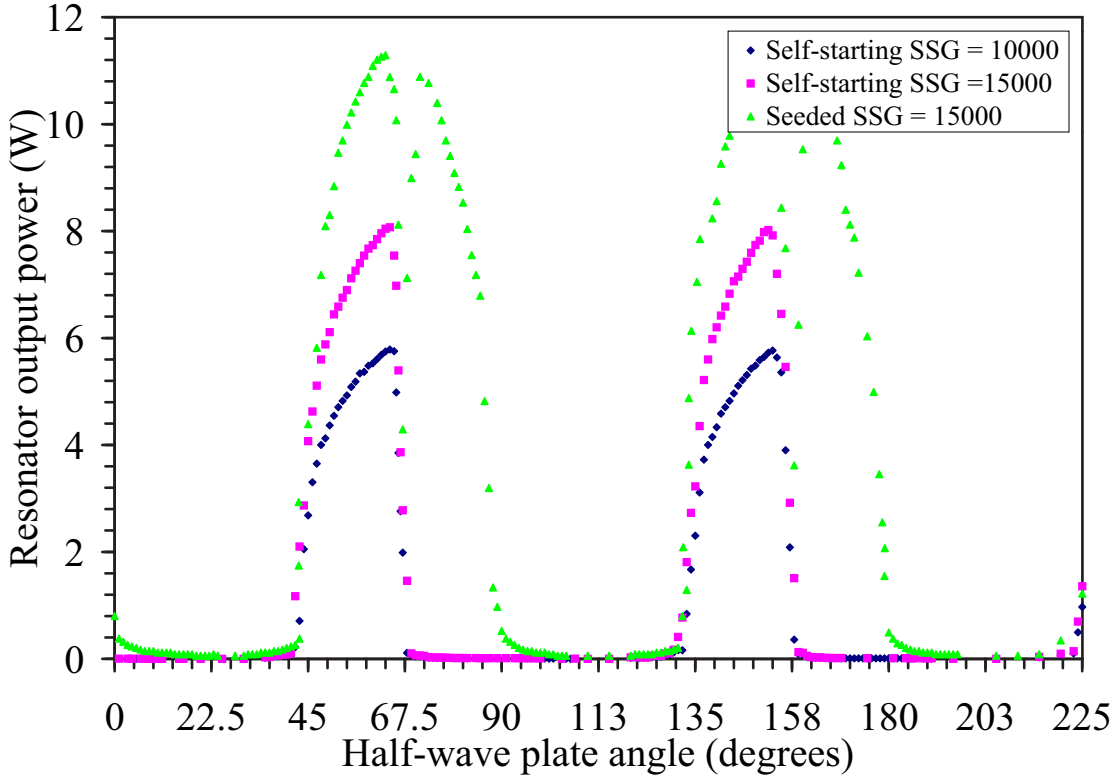

Figure 3.22: Self-staring resonator output for a 4% output coupler against NRTE HWP angle.

3.8.1 Distortion correction and M^2

The output from the self-starting phase-conjugate resonator with a SSSP gain of 15000 is shown in figure 3.23. When an aperture of around 2 mm diameter was placed at the position shown in figure 3.21 the resonator operated with an 8.2 W power output in a single longitudinal mode (see figure 3.26) with an $M_x^2 = 1.5$ and a $M_y^2 = 1.4$. Again, to confirm the phase-conjugate nature of the resonator mode a 0.5 mm thick etched glass slide (producing beams with M$^2 > 30$) was placed in the resonator loop at the position shown in figure 3.21. The output of the self-starting resonator with the added loop distortion is shown in figure 3.25 and while the output power in this case dropped to 7.6 W, the M^2 remained the same. The form of the distortion is shown in figure 3.24 by placing the glass-slide into the path of the output beam of the phase-conjugate resonator.

Figure 3.23: Self-starting output.

Figure 3.24: The spatial form of the phase distortion ($M^2 > 30$).

Figure 3.25: Self-starting output with intra-cavity phase distortion.

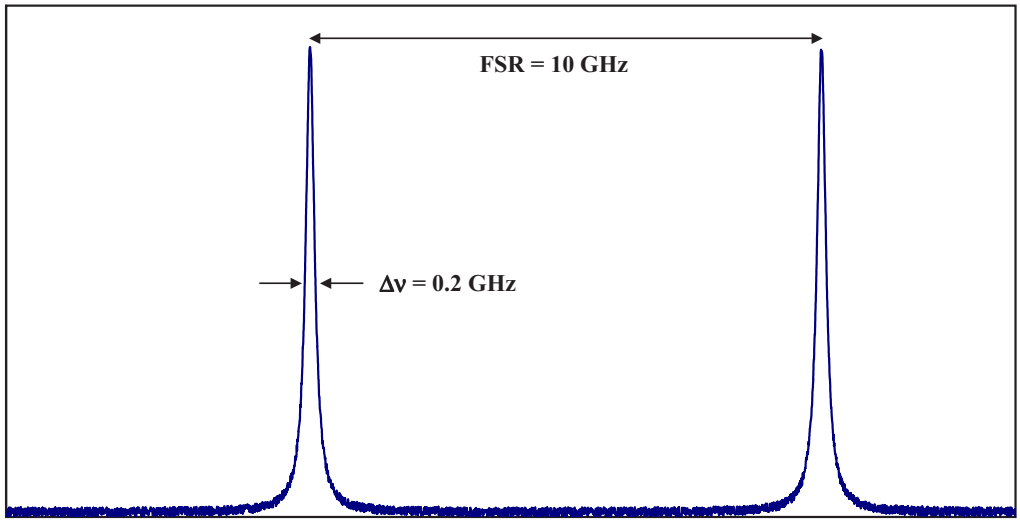

Figure 3.26: Fabry-Perot trace showing SLM operation of self-starting resonator with a 4% output coupler.

3.9 Phase-conjugate oscillator modelling

3.9.1 Seeded holographic resonator theory

In section 2.7 it was shown that a gain-grating formed by the intersection of two mutually coherent laser beams could give a diffraction efficiency of greater than 1 when probed with a third beam. These high efficiencies then allowed the realisation of a CW phase-conjugate resonator based around the FWM amplifier. Figure 3.27 shows, in schematic form, how the self-intersecting loop geometries studied in this chapter can be related to the forward pump, backward pump, signal and PC beams of the FWM model studied in section 2.7.

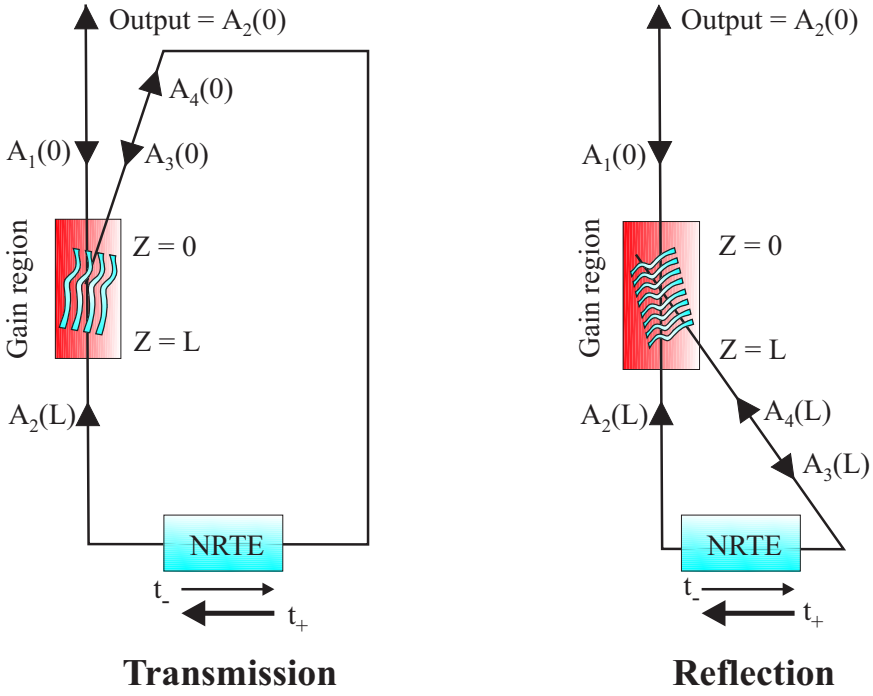

Figure 3.27: Seeded phase-conjugate oscillator running on a single transmission or a single reflection grating.

The steady-state interactions of both resonators can be modelled by solving the FWM coupled equations (equation 2.46 for the transmission grating and equation 2.45 for the reflection) with the appropriate boundary conditions and iterating the solution until a steady-state solution is reached. The boundary conditions for the transmission grating geometry shown in figure 3.27 are

$$\left.\begin{aligned} A_1(0) &= seed\,input \\ A_3(0) &= t_- A_1(L) \end{aligned}\right\} grating\,writing\,beams$$
$$A_2(L) = t_+ A_4(0) \qquad (3.21)$$
$$A_4(L) = 0$$

and for the reflection grating resonator are given by

$$\left.\begin{array}{l} A_1(0) = seed\,input \\ A_4(L) = t_- A_1(L) \end{array}\right\} grating\,writing\,beams$$
$$A_2(L) = t_+ A_3(L) \tag{3.22}$$
$$A_3(0) = 0$$

where the amplitude transmission coefficients through the NRTE (equations 3.5 and 3.6)in the low transmission, t_-, and the high transmission, t_+, directions as

$$t_- = P_v \cdot FR \cdot HWP \cdot P_v \cdot E_{input} \tag{3.23}$$

$$t_+ = P_v \cdot HWP \cdot FR \cdot P_v \cdot E_{input} \tag{3.24}$$

This model was then solved numerically for a given seed laser input field amplitude, $A_1(0)$, FWM amplifier SSSP gain-length product, $\alpha_0 L$, and NRTE HWP angle producing an amplitude transmission of t_+ and t_-. Figure 3.28 shows the seeded resonator output beam intensity (normalised to I_{sat}) against seed input intensity (also normalised to I_{sat}) for a transmission grating geometry resonator. The figure shows the input-output curves for three values of small-signal gain length products, $\alpha_0 L = 3$, $\alpha_0 L = 4$ and $\alpha_0 L = 5$, corresponding to SSSP intensity gains of 403, 2981 and 22026 respectively. The clockwise oscillating loop intensity as a function of normalised seed input for each gain coefficient above is shown in figure 3.29. From these two figures it can be seen that modelling predicts the same behavior seen experimentally (and shown in figures 3.13 and 3.14) where the maximum output from the phase-conjugate resonator does not necessarily occur for the maximum (clockwise) oscillating loop power.

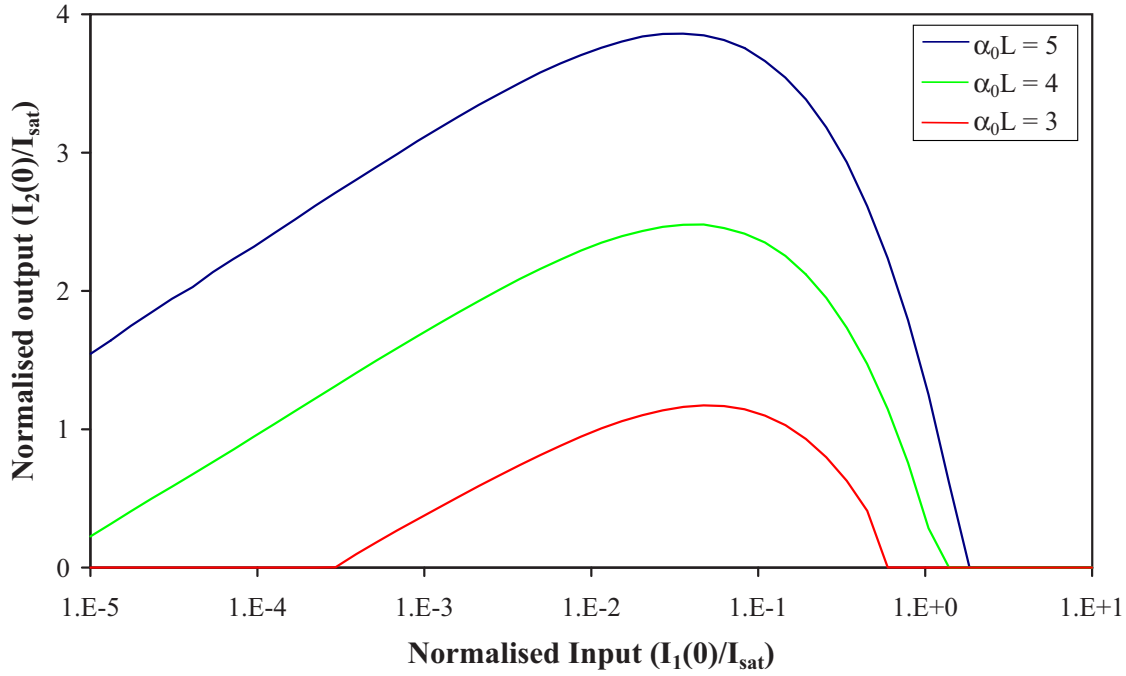

Figure 3.28: Modelled seeded phase-conjugate resonator output versus input intensity (all normalised to the saturation intensity).

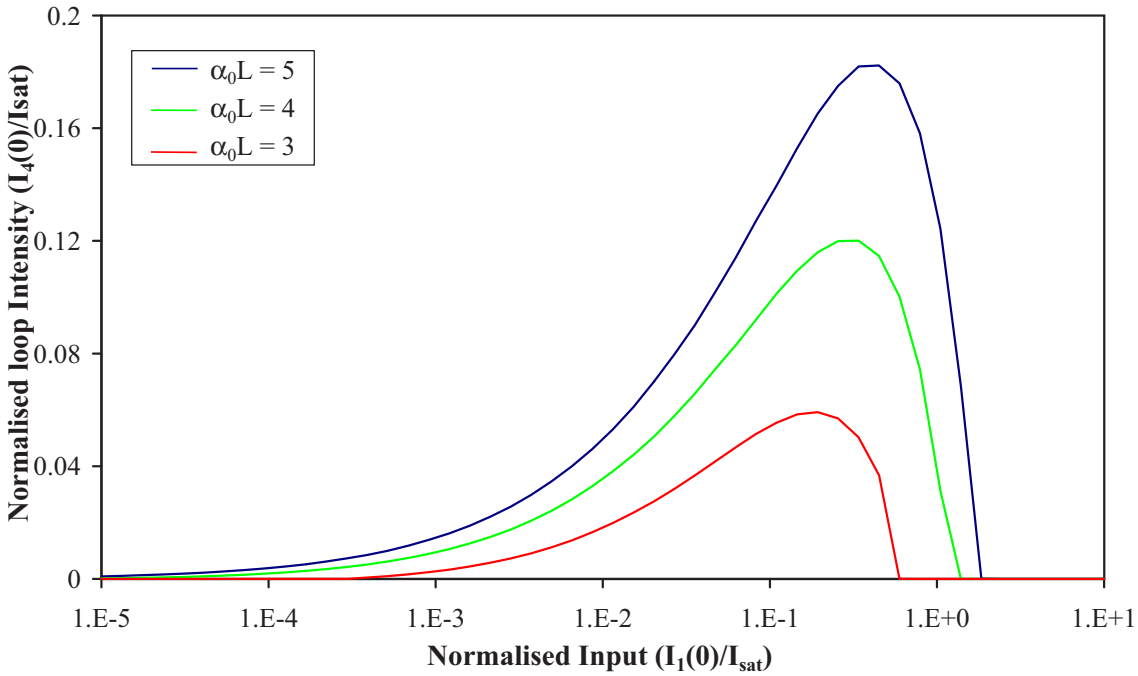

Figure 3.29: Modelled seeded phase-conjugate resonator loop intensity versus input intensity (all normalised to the saturation intensity).

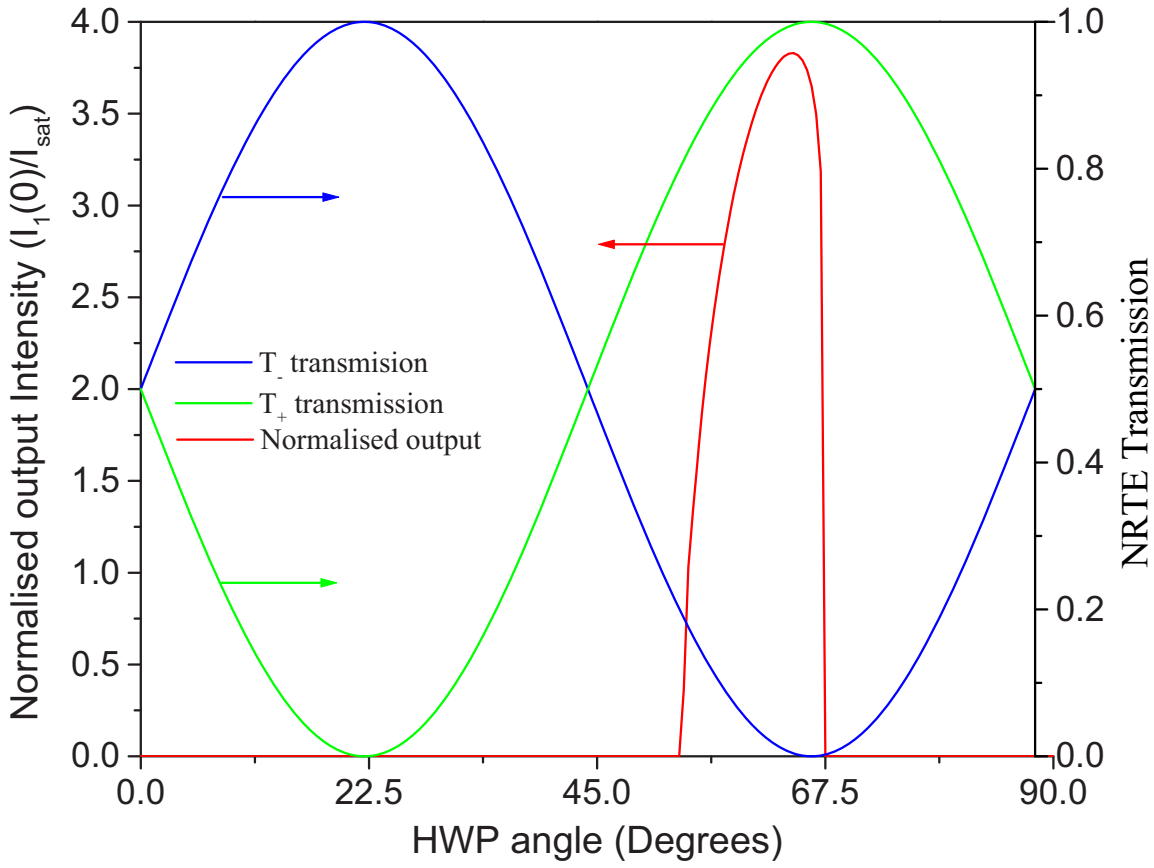

Figure 3.30: Seeded resonator output as a function of the NRTE HWP angle. The transmission characteristics of the NRTE in both directions are also shown.

The resonator output intensity as a function of the NRTE HWP angle for a given seed laser input was also modelled and is shown in figure 3.30. The FWM amplifier was given a small-signal amplitude gain length product of 5 ($\alpha_0 L = 5$) and the seed laser input set to correspond to the point of maximum output shown in figure 3.28. Also shown in figure 3.30 is the clockwise (T_+) and anti-clockwise (T_-) intensity transmission through the NRTE as a function of HWP angle. One point to note, however, is that the model does not predict the double peak behavior seen experimentally for a seeded resonator (see figure 3.15). The lack of a second peak (when the NRTE is acting in a *phase-reciprocal* manner) occurs because the model is frequency independent and cannot compensate for the grating π phase shift by adjusting its oscillating frequency as occurs experimentally (see section 3.6).

3.10 Conclusions

In this chapter it has been shown that saturable gain FWM can be used as a basis for phase-conjugate resonators capable of running in a seeded and self-starting mode of operation. In the seeded operation an output power of around 11.6 W in a single longitudinal and transverse mode was achieved using 60 W of diode pump power. The phase-conjugate nature of the resonator mode was verified by placing severe phase distortions within the resonator loop and observing the laser output. It was found that severe intra-cavity phase aberrations could be corrected for as long as the beam was not distorted to such an extent that it no longer overlapped with the gain region in the FWM amplifier. This now allows the possibility of placing additional power amplifiers, both within the arms or the loop of the adaptive resonator, so that the phase-conjugate output power can be scaled. Any new phase distortions introduced by the power amplifiers should be corrected for via the phase-conjugation process.

3.11 References

[1] M. J. Damzen, Y. Matsumoto, G. J. Crofts, and R. P. M. Green. Bragg-selectivity of a volume gain grating. *Optics Communications*, 123(1-3):182–188, 1996.

[2] M. J. Damzen, R. P. M. Green, and G. J. Crofts. Spatial characteristics of a laser-oscillator formed by optically-written holographic gain-grating. *Optics Communications*, 110(1-2):152–156, 1994.

[3] M. J. Damzen, R. P. M. Green, and G. J. Crofts. Reflectivity and oscillation conditions of a gain medium in a self-conjugating loop geometry. *Optics Letters*, 19(1):34–36, 1994.

[4] A. E. Siegman. Lasers. pages 782–785. University Science Books, 1986.

[5] A. Yariv. Optical electronics in modern communications. pages 17–30. Oxford University Press, 1997.

[6] Fujian JDSU Casix Inc. http://www.casix.com/products/crystals/ndyvo4.htm.

[7] A. Brignon and J. P. Huignard. Continuous-wave operation of saturable-gain degenerate 4-wave- mixing in a Nd:YVO_4 amplifier. *Optics Letters*, 20(20):2096–2098, 1995.

[8] J. R. Leger, D. Chen, and K. Dai. High modal discrimination in a Nd:YAG laser resonator with internal phase gratings. *Optics Letters*, 19(23):1976–1978, 1994.

Chapter 4

Power-scaling phase-conjugate resonators

4.1 Overview

In chapter 3 the operation was described of a phase-conjugate resonator that could correct for passive phase distortions present within the resonator loop. It was shown that the phase-conjugate nature of the resonator mode produced a SLM near diffraction-limited output even with the intra-cavity phase distortions present. In this chapter the possibility of scaling the output power of the phase-conjugate resonator is explored. The placement of additional power-amplifiers both within the resonator loop and the output arm is studied to determine where extraction of the stored power is maximised. The first section of this chapter deals with extending the phase-conjugate resonator model presented in section 3.9 to include the power-amplifier at various positions within the resonator and to determine how best to distribute the gain between the two amplifiers. In section 4.3 initial experimental results for power-scaling the PC resonator are presented and it is shown that the combined system is capable of up to 11.7 W near diffraction-limited SLM operation [1]. Finally, section 4.4 looks at the limitations for power-scaling the PC resonator in the current setup and describes why attempts to further increase the output power

caused the PCO to cease operation.

4.2 Resonator and amplifier modelling

In this section the placing of an additional power-amplifier (PA) within the existing seeded resonator setup is explored theoretically. Figure 4.1 shows the three different positions at which the PA could be placed around the phase-conjugate resonator. The first position (1) lies within the amplifier input-output arm, between the FWM amplifier and the seed laser. When placed at this position the PA has no effect on the phase-conjugate resonator apart from amplifying the initial seed input beam and the final PC output beam: in other words, the phase-conjugate resonator's input-output characteristics have not been changed by the addition of the PA into the arm. In this sense one could view the phase-conjugate resonator as a low power master oscillator whose well defined output is amplified by the PA stage.

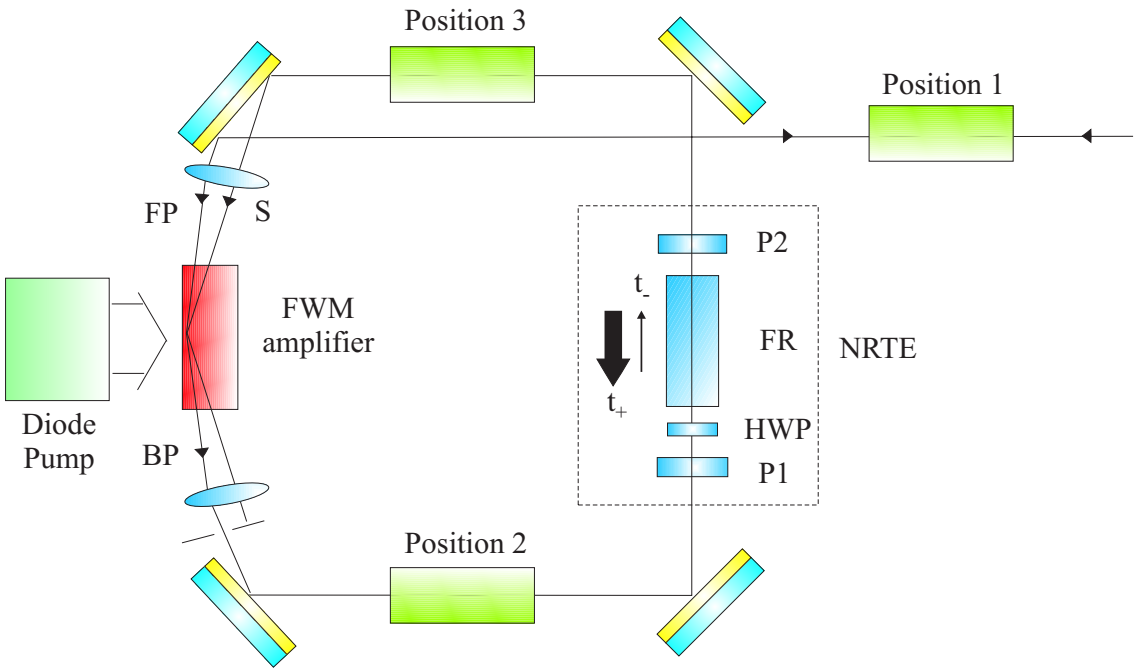

Figure 4.1: Schematic showing the three positions at which an additional power-amplifier could be placed within the seeded resonator setup.

The next position (2) lies between the FWM amplifier and the NRTE (going anti-clockwise around the resonator loop). The placement of a PA in this region can be ruled out instantly however for the following reason. As the seed input beam travels through the FWM amplifier its power is amplified from typically 20 mW to 7 W. If this amplified 7 W beam were then to travel through the PA at position 2 a large amount of the stored gain within the PA would be removed. As this beam then travelled anti-clockwise further around the loop it would pass through the NRTE in the low transmission direction where the vast majority of the power would be removed from the loop leaving very little stored power within the PA for the clockwise oscillating PC mode.

The last position (3) lies between the NRTE and the FWM amplifier (anti-clockwise around the loop). At this point the anti-clockwise oscillating power is typically a few mW so that the S beam and the FP are of comparable power, forming high efficiency gain-gratings and so the problems discussed for position 2 are not encountered. The disadvantage of placing the PA here, however, is the low oscillating power in the clockwise PC mode (see figure 3.14) leading to low extraction of the stored power in the PA. In the following sections the placement of a PA at position 1 and 3 is studied further to determine where maximum output power for a given PA gain occurs and how the available pump power is best distributed between the FWM amplifier and PA.

4.2.1 Power-amplifier at position 1

The phase-conjugate oscillator (PCO) model presented in section 3.9 can be further developed to incorporate a PA in the output arm of the cavity by modifying the boundary conditions used (see figures 4.2 and 4.3) to give

$$\begin{aligned} A_1(0) &= A_+(L) \\ A_3(0) &= t_- A_1(L) \\ A_2(L) &= t_+ A_4(0) \\ A_4(L) &= 0 \\ A_{output} &= A_-(0) \end{aligned} \tag{4.1}$$

where A_{output} is the output field amplitude of the entire PCO-PA system. $A_+(L)$ and $A_-(0)$ are the single-pass output field amplitudes from the power-amplifier in the forward and backward directions respectively (see figure 4.2) and can be obtained by solving the following coupled growth equations describing the saturation of the PA small-signal gain, g_0, by the input and output beams

$$\begin{aligned} \frac{dA_+}{dz} &= \frac{g_0 A_+}{1 + \left(\frac{|A_+|^2 + |A_-|^2}{|A_{sat}|^2}\right)} \\ \frac{dA_-}{dz} &= \frac{-g_0 A_-}{1 + \left(\frac{|A_+|^2 + |A_-|^2}{|A_{sat}|^2}\right)} \end{aligned} \tag{4.2}$$

with the boundary conditions

$$\begin{aligned} A_+(0) &= seed\ input \\ A_-(L) &= A_2(0) = output\ from\ FWM \end{aligned} \tag{4.3}$$

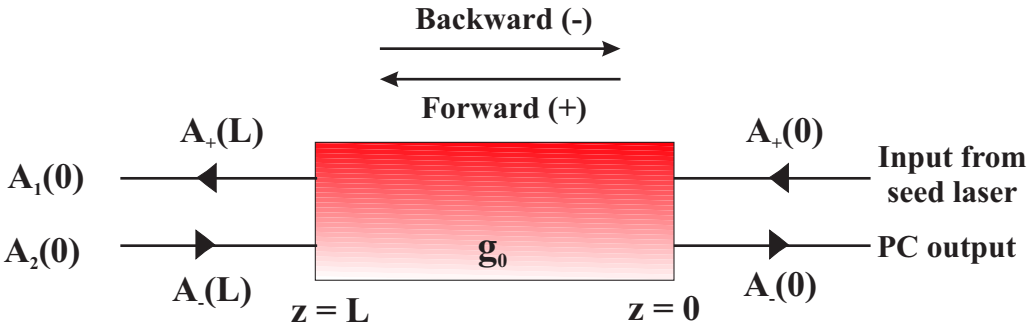

Figure 4.2: Exploded view of the power amplifier in figure 4.3. The forward and backward fields are shown separated here for clarity.

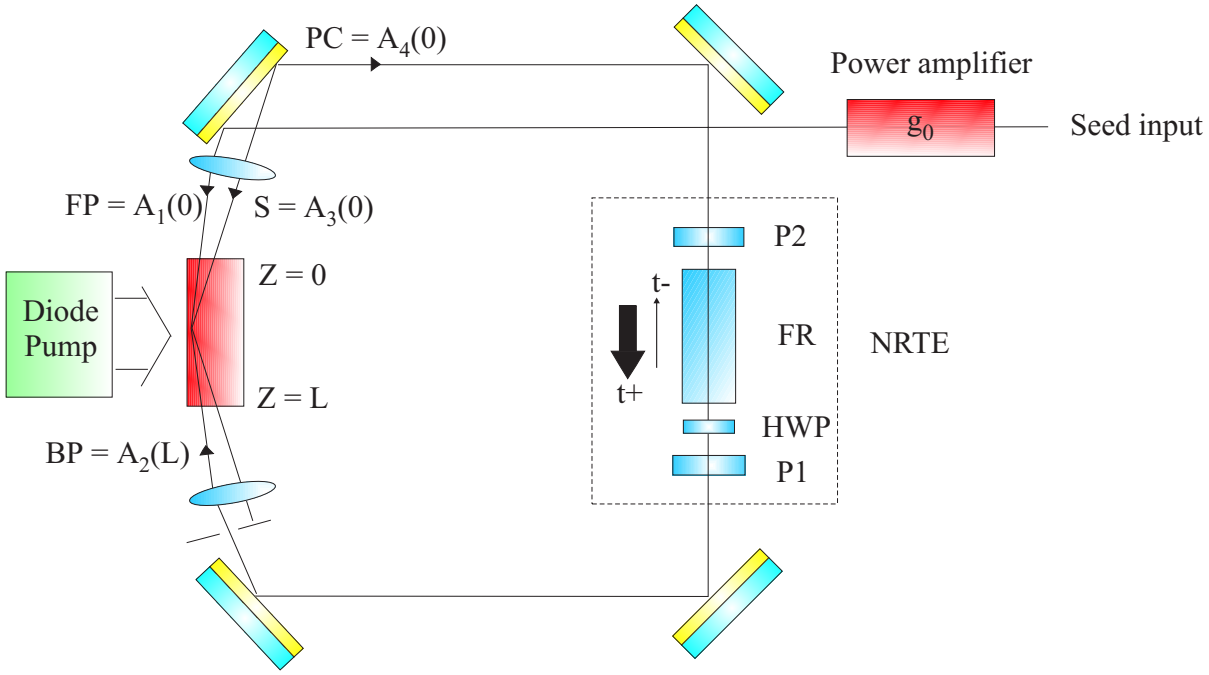

Figure 4.3: Schematic showing the boundary conditions used to solve the coupled growth equations of the input and phase-conjugate output of the power-amplifier.

Figure 4.4 shows the PCO-PA output intensity as a function of seed-laser input intensity (all normalised to saturation intensity, I_{sat}, of Nd:YVO_4) for amplifier amplitude gain length products g_0L = 0, 0.8, 1.2 and 2 corresponding to SSSP gains ($G_0 = \exp(2g_0L)$) in the PA of 1, 5 and 10 and 55 respectively. The FWM-amplifier in all four cases had an $\alpha_0 L$ product of 4.15 corresponding to an intensity gain of approximately 4000. As g_0 was increased the peak output intensity from the resonator also increased and occurred for a lower value of seed input intensity, a consequence of the fact that the seed laser passes through the PA before becoming the input to the PCO.

The model shows that by increasing the gain of the PA the PC output rises accordingly. Crofts *et al* [2] made the theoretical observation that by adding a PA *inside* the PCO loop the PC output power would likewise increase. They also made the observation that when the total gain of the loop was set to a constant value ($\alpha_0 L + g_0 L = const$) the highest output power was obtained when all the available loop gain was concentrated within the FWM amplifier. With an amplifier external to the loop, however, the situation is more complicated. In this model the total loop gain-length coefficient was set to $\alpha_0 L + g_0 L = 5$. Figure 4.5 shows the PCO-PA output against the seed laser input for a selection of ratios of $\alpha_0 L$ and $g_0 L$. It can be seen from the graph that although the gain of the FWM amplifier decreases, the total PC output intensity initially increases due to the compensating increase in the gain of the PA. As the FWM amplifier gain is reduced further and the PA gain is increased the output from the system starts to fall due to the gain of the FWM being so low thereby giving a very weak output. Further decreasing the FWM gain causes the PCO to fail to reach oscillation threshold ($\eta T_+ \geqslant 1$) and so no output is obtained. From this it can be seen that the distribution of gain between the FWM amplifier and the PA has some optimum value around which the output from the PCO-PA system starts to fall. Operation of the PCO-PA system around this optimum point will still produce a PC output (assuming the PCO has enough gain to reach threshold) but with reduced efficiency.

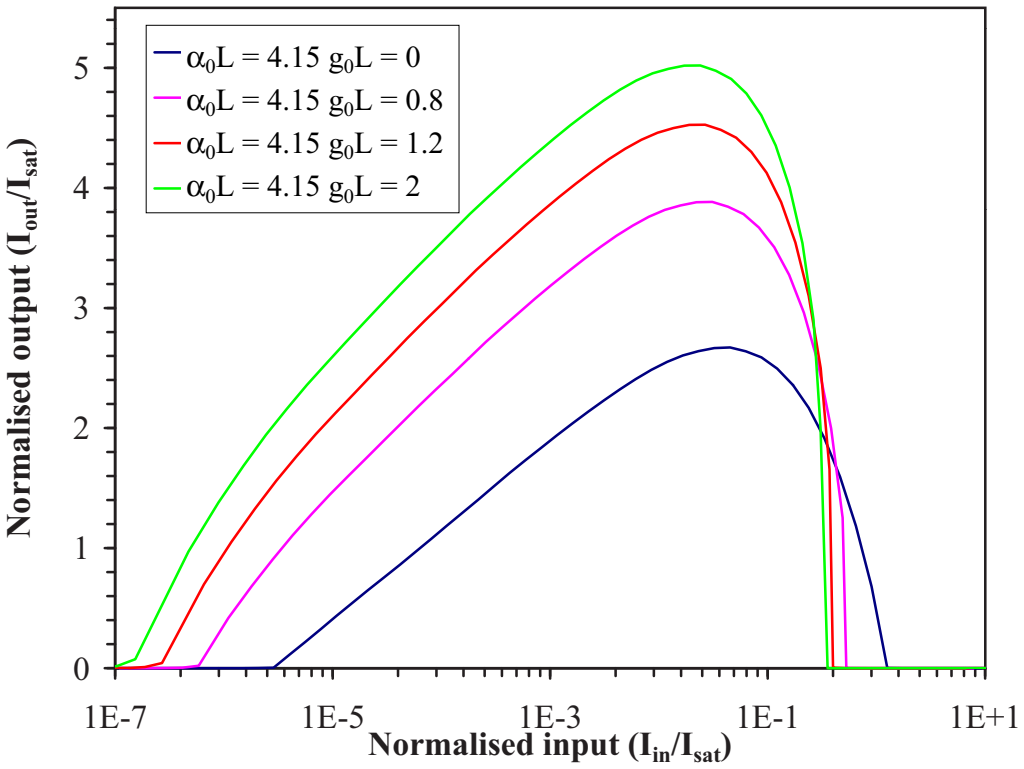

Figure 4.4: The modelled input-output curves of the combined phase-conjugate resonator power-amplifier system (PA in arm).

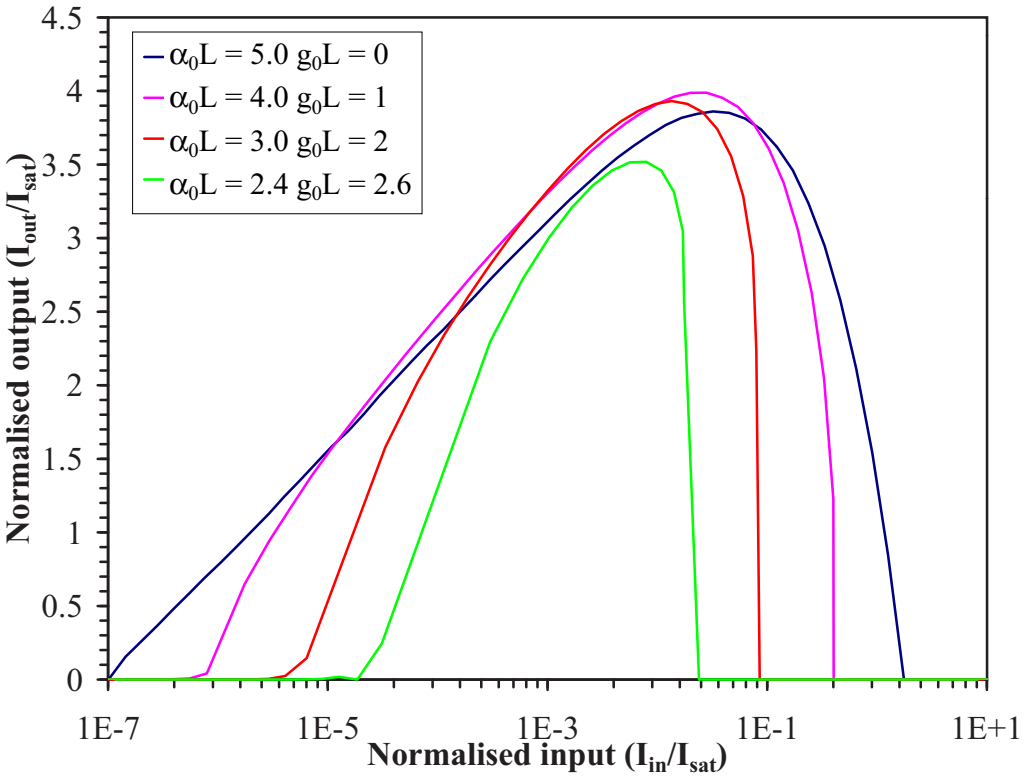

Figure 4.5: Input-output curves of the combined PCO-PA. The total gain of the two amplifiers is held constant and is distributed between them in various ratios (PA in arm).

4.2.2 Power-amplifier at position 3

Figures 4.6 and 4.7 show schematically the boundary conditions used to solve for the case of the power-amplifier placed at position 3 within the phase-conjugate resonator cavity. The new boundary conditions are

$$\begin{aligned} A_1(0) &= seed\ input \\ A_3(0) &= A_+(L) \\ A_2(L) &= t_+ A_-(0) \\ A_4(L) &= 0 \end{aligned} \tag{4.4}$$

where $A_+(L)$ and $A_-(0)$ are the single-pass output field amplitudes from the power-amplifier in the forward and backward directions respectively and can be obtained by solving the coupled equations of equation 4.2 with the following boundary conditions

$$\begin{aligned} A_+(0) &= t_- A_1(L) \\ A_-(L) &= A_4(0) \end{aligned} \tag{4.5}$$

Figure 4.8 shows the modelled output intensity versus seed input intensity for the phase-conjugate resonator with the PA placed at position 3. The threshold equation for this amplifier configuration is now $\eta G_{PA} T_+ \geqslant 1$ where η is the diffraction efficiency of the gain-grating, G_{PA} is the gain of the PA and T_+ is the transmission of the NRTE in the (high transmission) clockwise direction. Again, as for the case of the PA in the output arm, the maximum output from the combined PCO-PA system increased as the gain of the PA was increased. However, as the PA gain was increased, the maximum resonator output occurred for *increasing* values of seed input (for the PA in the *arm* the seed input required for maximum output *decreased* as the PA gain increased). In this sense the PA would be better placed in the output arm of the phase-conjugate resonator since a lower value of seed laser input would extract less power from the FWM in the anti-clockwise direction (figure 4.9) and hence leave more available power in the FWM gain region for amplification of the (useful) PC output.

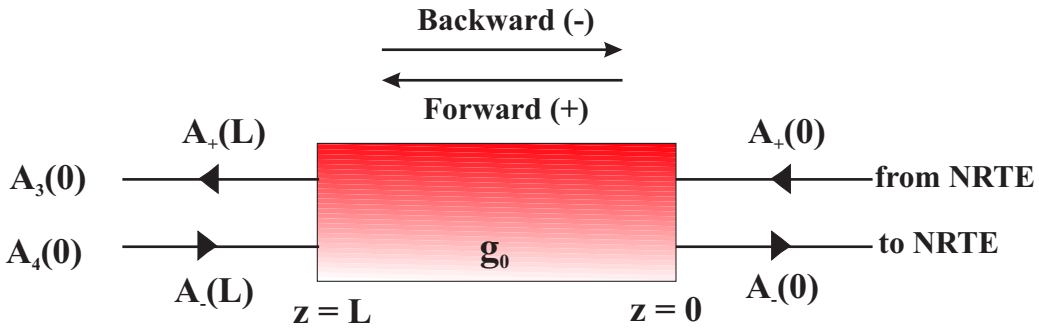

Figure 4.6: Exploded view of the power amplifier in figure 4.7. The clockwise and anti-clockwise fields are shown separated here for clarity.

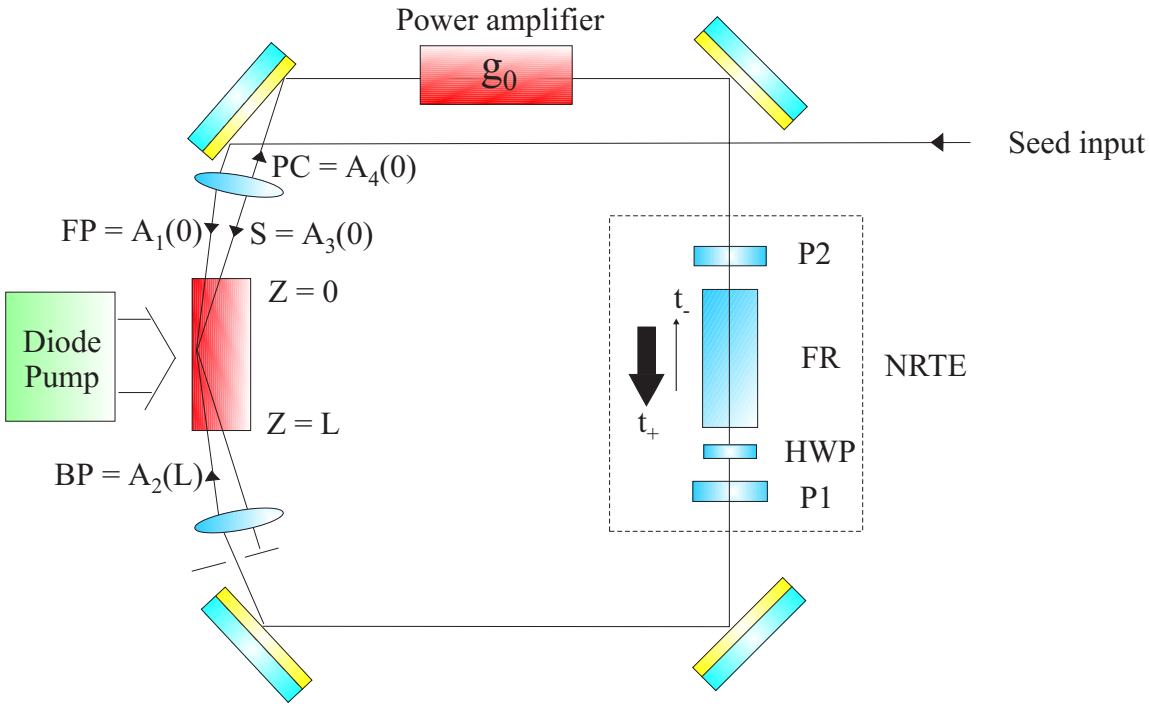

Figure 4.7: Schematic showing the boundary conditions used to solve the coupled growth equations of the phase-conjugate resonator fields.

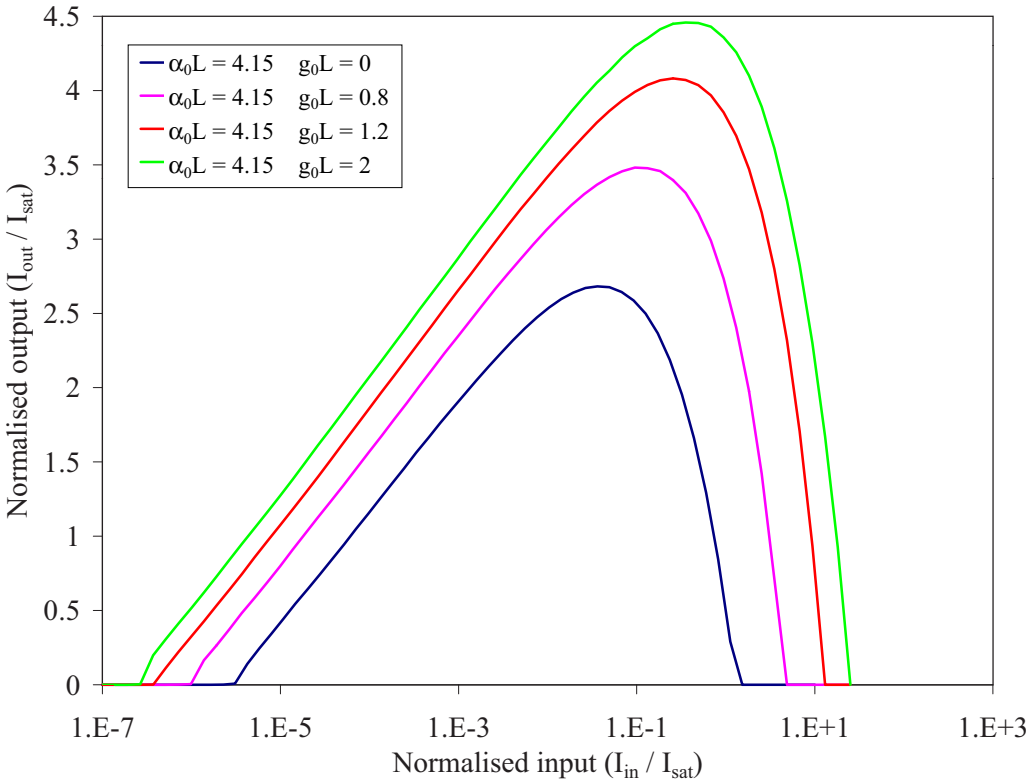

Figure 4.8: The modelled input-output curves of the combined phase-conjugate resonator power-amplifier system (PA in loop).

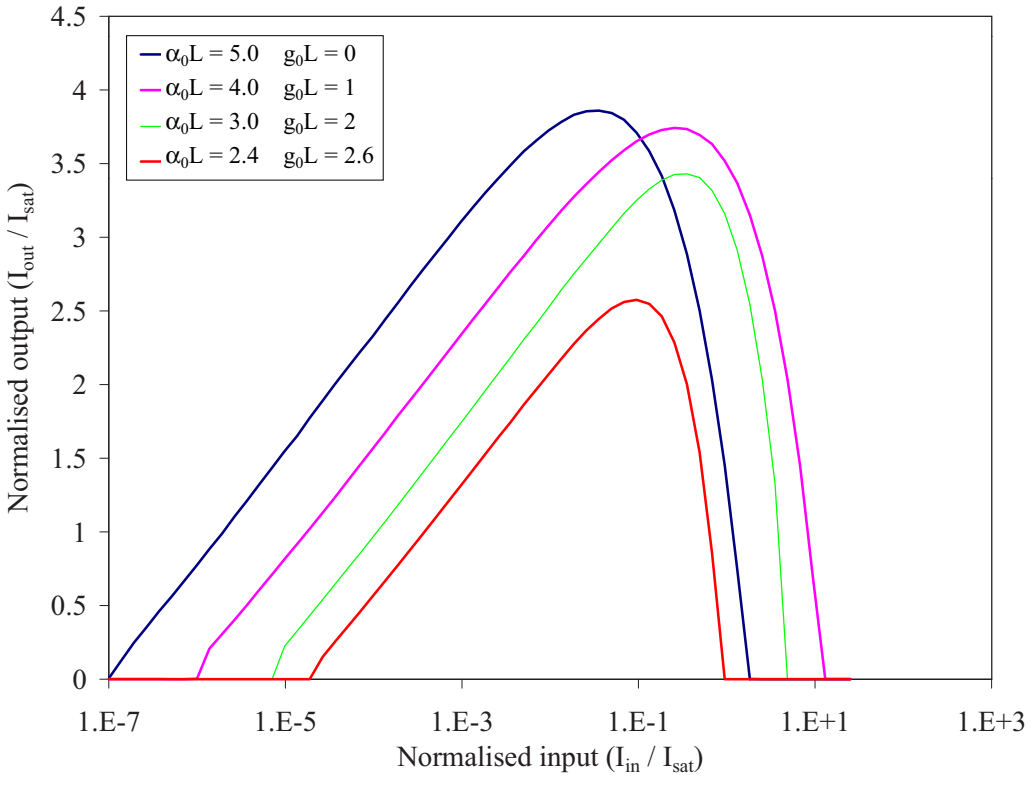

Figure 4.9: Input-output curves of the combined PCO-PA. The total gain of the two amplifiers is held constant and is distributed between them in various ratios (PA in loop).

Figure 4.9 shows the modelled input-output intensity characteristics for the phase-conjugate resonator with the intra-loop amplifier when the total gain shared between the FWM amplifier and PA is set to a constant value of $\alpha_0 L + g_0 L = 5$. Here it can be seen that as more of the total gain is situated within the PA and less in the FWM amplifier the maximum output from the system decreases i.e. maximum output is obtained when all the available gain is concentrated within the FWM amplifier. The problem with this is that as the gain of the FWM amplifier is increased (either by focussing the diode pump beams to smaller spot sizes or increasing the diode pump power) detrimental thermal effects within the amplifier are increased. It is therefore more desirable to *distribute* the available power between the PA and FWM amplifier thereby reducing the thermal loading of both.

4.3 Amplifier in arm - experimental

The setup used to demonstrate power-scaling of the phase-conjugate oscillator is shown in schematic form in figure 4.10. The power-amplifier (PA) consisted of 1.1 at.% Nd-doped YVO_4 *a*-cut crystal of dimensions 20 mm x 3 mm x 5 mm, sided pumped by a 32 W fibre lensed laser-diode bar operating at 808 nm. The crystal was anti-reflection coated for the pumping wavelength on both *b* faces and anti-reflection coated for 1064 nm on both *a* faces. The output of the diode bar was subsequently focussed by a cylindrical lens of focal length *f*= 12.7 mm onto one of the *b* faces of the Nd:YVO_4 crystal, and the TE polarised pump beam was rotated by the use of a $\lambda/2$ wave plate so that it was parallel with the *c* axis of the crystal, thereby yielding maximum pump absorption ($\alpha = 31.4cm^{-1}$). The PA was placed in the phase-conjugate output arm between the PCO and the Nd:YVO_4 seed laser. The output from the PCO was focussed into and then recollimated out of the PA by the use of two 100 mm focal length spherical lenses placed approximately 200 mm apart.

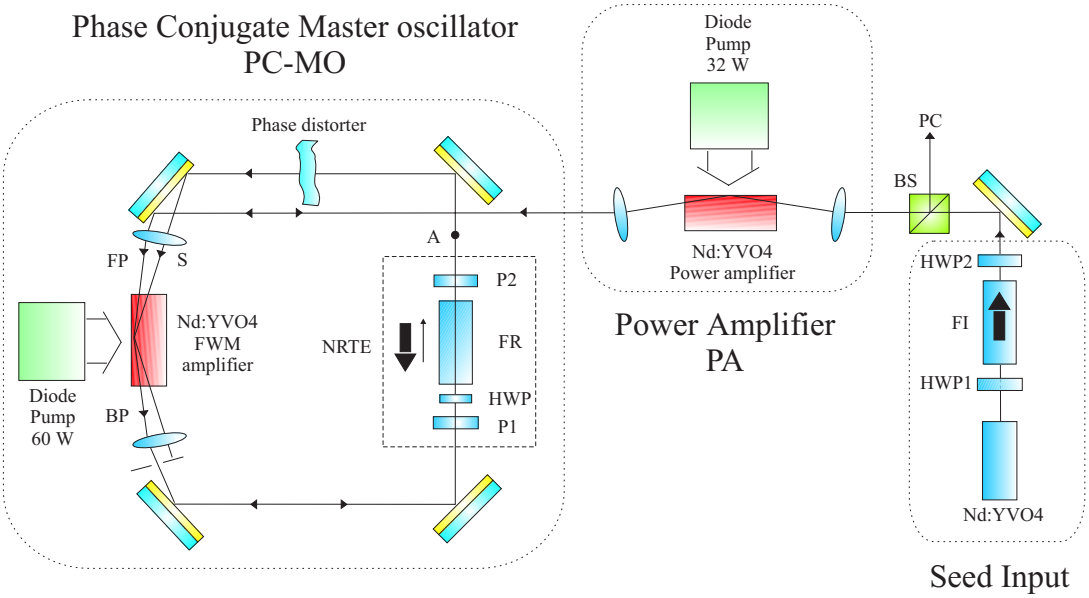

Figure 4.10: Schematic showing the PCO-PA setup. The power amplifier is placed in the output arm of the phase-conjugate resonator.

The PA gain could be varied by adjusting the position of the 12.7 mm cylindrical lens resulting in a larger or smaller diode pump beam spot size on the face of the Nd:YVO_4 crystal. The PCO could be optimised by switching the PA diodes off so that the output of the PCO was unamplified (gain of 1 - neglecting the small intrinsic loss of Nd:YVO_4 = 0.001 cm^{-1}) as it passed through the PA crystal. An image of the actual experimental setup used can be seen in figure 4.11 showing the relative positioning of the seed laser, PA and PCO.

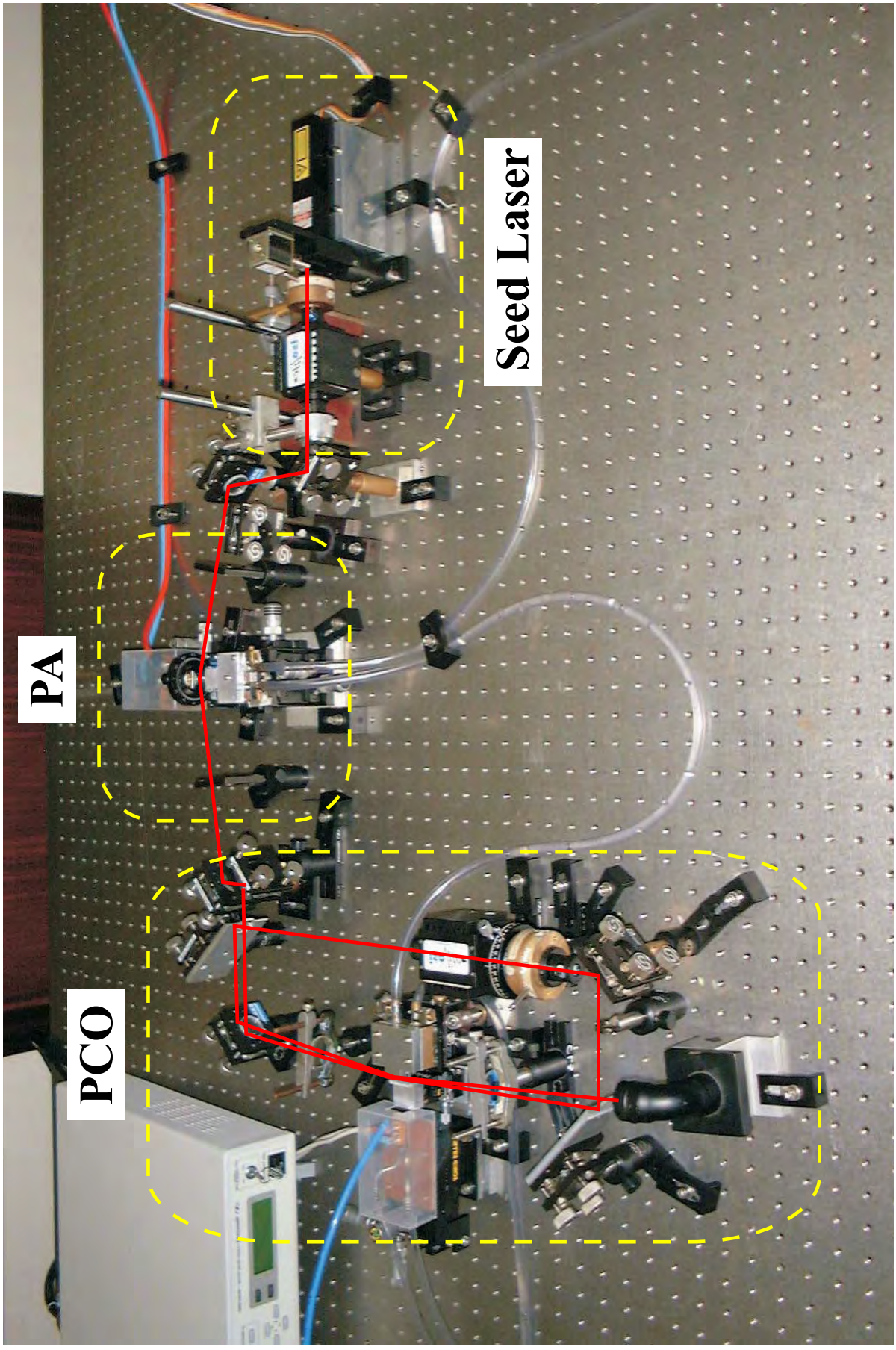

Figure 4.11: Setup of the phase-conjugate resonator with power amplifier in output arm.

4.3.1 Input-Output characteristics

Figure 4.12 shows the PC output power from the phase-conjugate resonator (with the power-amplifier in the arm), as a function of the seed laser input power. The first curve (diamonds) shows the output when the power-amplifier had a small-signal single-pass (SSSP) gain of 1 (amplifier un-pumped). As the seed input power is increased from a value of around 0.3 mW the PC output power also increases. In this region the saturation depth of the gain-grating in the FWM amplifier is increasing and so its diffraction efficiency increases with input power. The maximum output

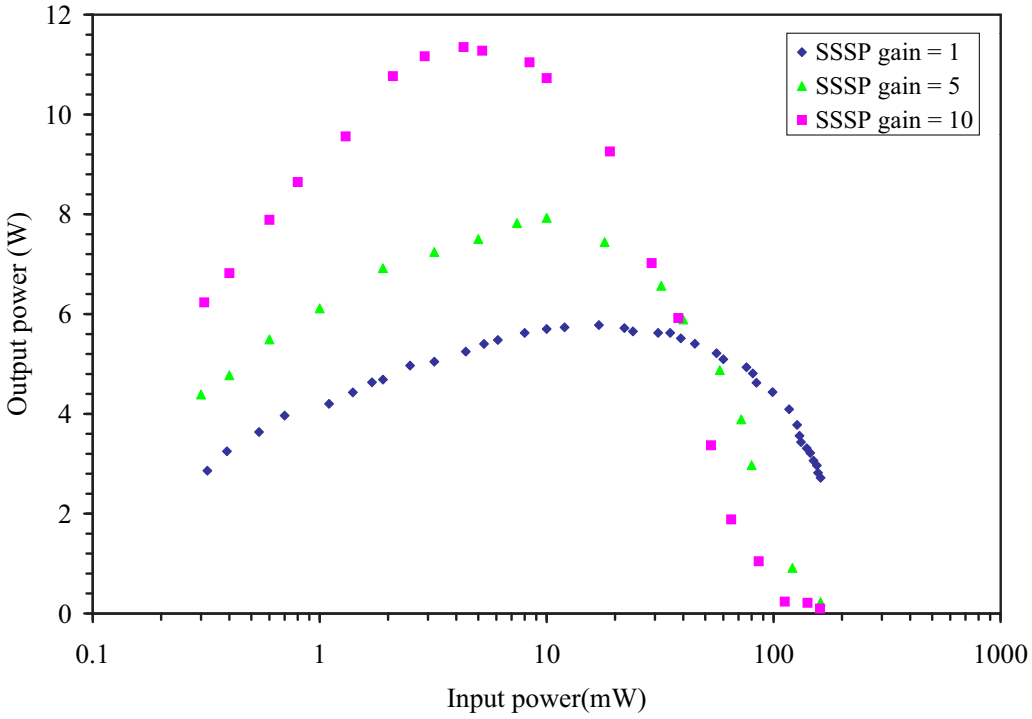

Figure 4.12: The phase-conjugate output power of the combined phase-conjugate resonator and power-amplifier as a function of seed-laser input power for various amplifier gains. Maximum PC output increases with amplifier gain and occurs for smaller values of input seed power.

of around 6 W from the resonator occurred at an input power of 20 mW. Beyond this value the PC output begins to fall as the gain of the FWM amplifier is oversaturated by the high value of seed input beam power causing the efficiency of the grating to fall (see section 2.7).

The PA was then turned on and its gain varied by defocussing the cylindrical lens used to focus the light from the pump diode into the crystal. In this arrangement the PCO was left in exactly the same configuration as for the first set of results (diamonds). This way it could then be shown how, for a set configuration of the PCO, and hence a known input-output curve (diamonds), the PA affected the results for the combined PCO-PA. It is important to note that, as shown in section 4.2.1, keeping the PCO gain constant whilst varying the PA gain will not necessarily produce the maximum power output from the combined PCO-PA system as it is likely that some optimum distribution of gain will occur between the FWM amplifier and the PA that maximises the power output.

The second curve in 4.12 (triangles) shows the PC output when the power-amplifier had a SSSP gain of around 5. Here the peak output occurred for around 10 mW of seed laser input giving a maximum power output of the combined PCO-PA system of around 8 W. The third curve (squares) shows the PC output when the PA had a SSSP gain of around 10. The seed input for maximum output occurred at around 4.3 mW giving a total power output from the combined PCO-PA system of 11.7 W.

4.3.2 NRTE HWP angle versus output

In section 3.7.3 it was shown that the output of the PCO was highly dependent on the transmission of the NRTE in the anti-clockwise (low transmission) direction. By rotating the half-wave plate angle (i.e. the angle between the vertical polarisation of the signal beam and the HWP optic axis) inside the NRTE the intensity of the two grating writing beams could then be matched and the resulting diffraction grating efficiency could be maximised (see section 2.7). Figure 4.13 shows the power output of the combined PCO-PA as a function of the NRTE HWP angle for the three values of the PA gain (SSSP gain of 1, 5 and 10).

In a similar manner to that for the seeded resonator geometry results presented in section 3.7.3 the seed input power was set to give a maximum resonator output. At a NRTE HWP angle of 22.5° the output from the

resonator was almost zero for all three cases of PA gain. At this point the writing beam intensities were not well matched and hence the gain-grating formed had a low diffraction efficiency (see section 2.7.1) causing the resonator to fail to reach threshold resulting in zero output.

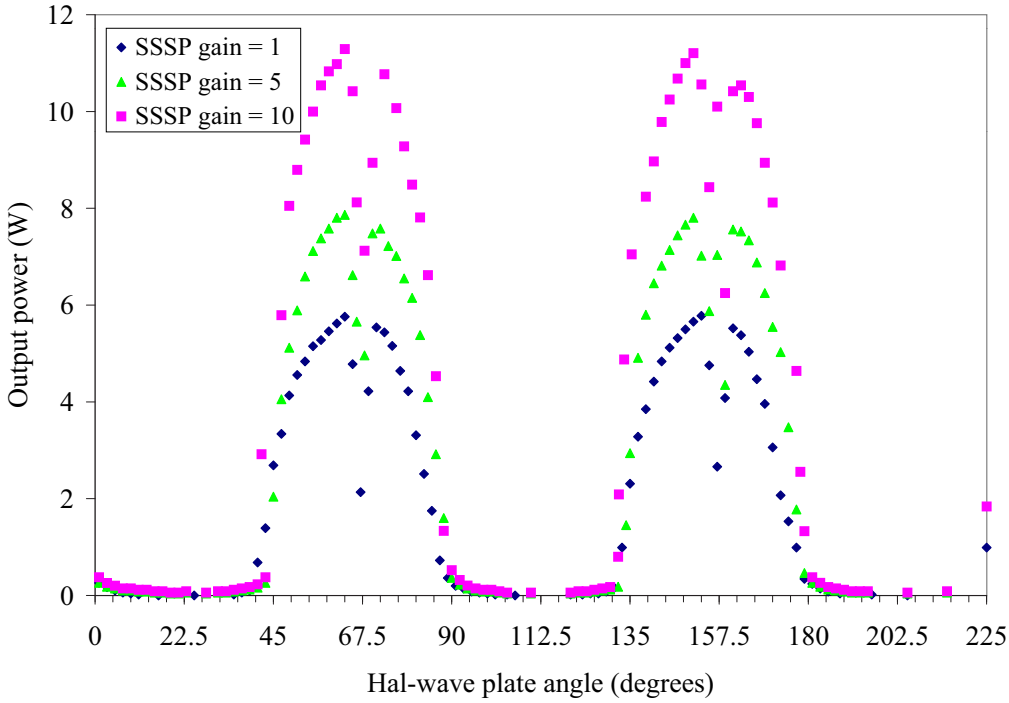

Figure 4.13: The phase-conjugate output power of the combined phase-conjugate resonator and power-amplifier as a function of the angle of the half-wave plate inside the NRTE.

At a HWP angle of around 40° the threshold of oscillation is reached and the resonator begins to produce a phase-conjugate output. As the HWP angle was increased further the output power increased until it reached the maximum value of 6 W (for PA SSSP gain = 1) and 11.7 W (for PA SSSP gain = 10) at 63°. The intensity transmission of the NRTE in the anti-clockwise (low transmission) direction for this HWP angle (shown in figure 3.16) was roughly 0.03 (i.e. 3% of the incident power was transmitted in this direction). A further increase in the HWP angle to approximately 67.5^0 caused an abrupt drop in the output power in all three cases, at this point the anti-clockwise ($t_{\_}$) transmission of the NRTE was almost zero resulting in a very low intensity signal (S) beam being transmitted, with which the gain-grating is formed with the FP. This causes the subsequent

gain-grating to have a low diffraction efficiency resulting in the resonator failing to reach threshold.

4.3.3 Intracavity oscillating power

To examine the effect of varying the gain of the PA on the PCO (which was not changed throughout the experiment) the power within the PCO was measured in the clockwise direction at point A in figure 4.10. Figure 4.14 shows the measured intracavity (clockwise) oscillating power at this point as a function of the seed-input power. It can be seen that for the three

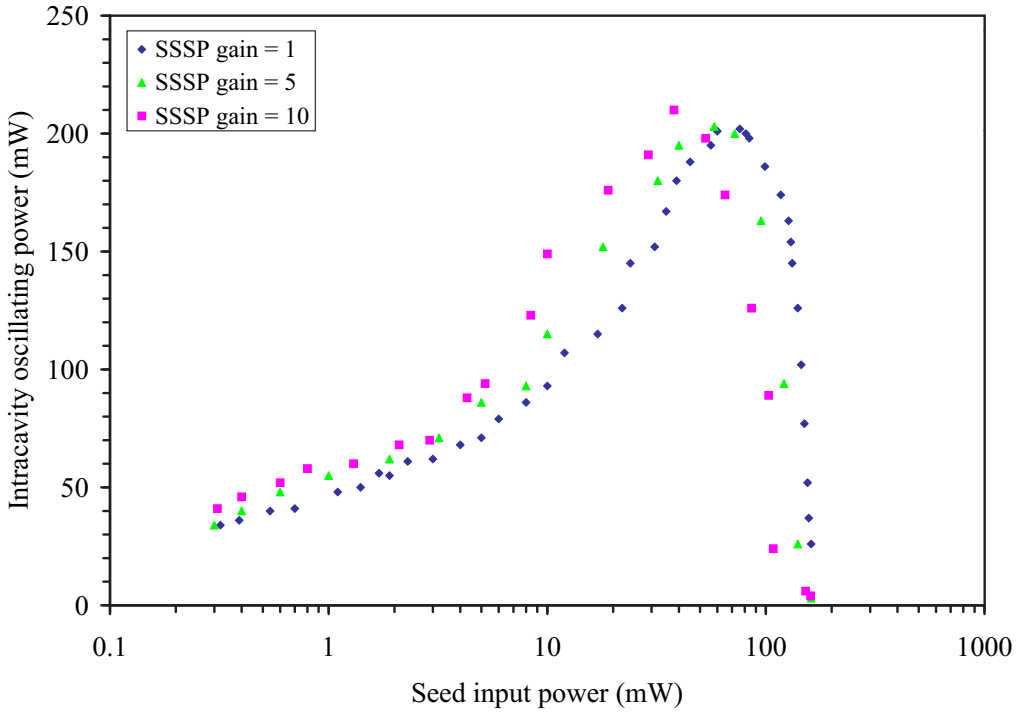

Figure 4.14: Intracavity power curves of the clockwise resonator beam (Measured at point A in figure 4.10) as a function of seed input power.

different SSSP gains of the PA the shape of the curves remained fairly constant but were progressively shifted towards lower values of seed input powers as the PA gain was increased. These results would suggest that for any given configuration of the PCO i.e. SSSP gain of the FWM amplifier, angle of the FWM beams, NRTE transmission etc. the input-output curves

for that PCO remain essentially constant regardless of the gain of the PA in the output arm.

4.3.4 Distortion correction and M^2

Figure 4.15 shows the spatial profile of the output (taken using a Coherent beam profiler) from the PCO when the PA pumping was turned off (SSSP gain = 1). The resonator operated with an output power of around 6 W with a near diffraction limited mode (M_x^2 = 1.3 and M_y^2 = 1.2). The beam was elliptical in geometry due to the asymmetry of the gain region in the FWM amplifier (a $1/e^2$ absorption depth of around 300 μm for Nd:YVO_4 and a $1/e^2$ height of around 36 μm for the diode focussed into the crystal). The spatial output from the system was further investigated with the PA pumping turned on and its gain varied by repositioning the 12.7 mm cylindrical diode focussing lens.

The second figure, figure 4.16, shows the spatial profile of the output beam with a power of around 8 W and the PA operating at a SSSP gain of around 5. The M^2 of the beam in both directions remained unchanged. The last figure, figure 4.17, shows the spatial profile of the output beam when the SSSP gain of the PA was increased to around 10 (output power of approximately 11.7 W). The M^2 of this beam increased slightly in the horizontal direction to give M_x^2 = 1.4 but remained unchanged in the vertical direction with a M_y^2 = 1.2.

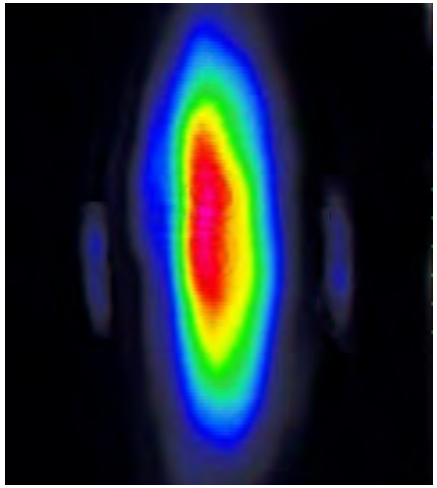

Figure 4.15: Spatial output of combined FWM and power amplifier system with SSSP gain = 1.

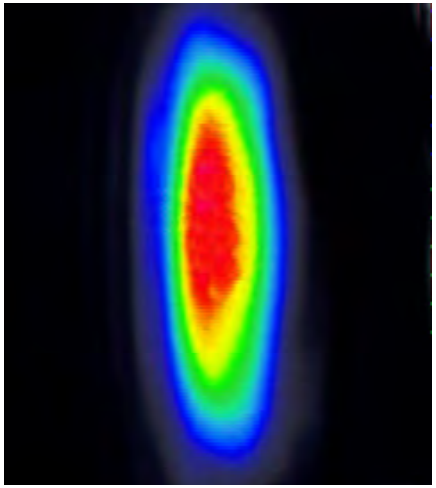

Figure 4.16: Spatial output of combined FWM and power amplifier system with SSSP gain = 5.

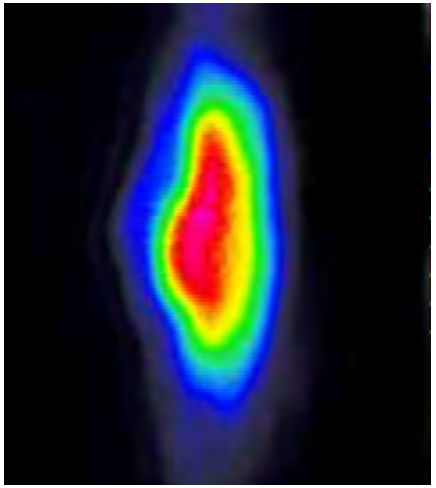

Figure 4.17: Spatial output of combined FWM and power amplifier system with SSSP gain = 10.

The output was examined with a plane-plane Fabry-Perot interferometer (figure 4.18) and was found to have a single-longitudinal mode at the same frequency as the seed-laser. The small increase of the M^2 in the horizontal direction was due, partly, to an increasing misalignment between the two interfering beams with the FWM gain region caused by small displacements of the seed input beam upon passing through the pumped PA. The resonator, however, was still operating on a PC mode, shown by the fact that the output spatial profile remained unchanged even when a severe phase distortion (HF etched glass slide) was placed into the resonator (at the position shown in figure 4.10). The plane-plane Fabry-Perot trace shown in figure 4.18 shows the SLM operation of the PCO-PA system for the 11.7 W output.

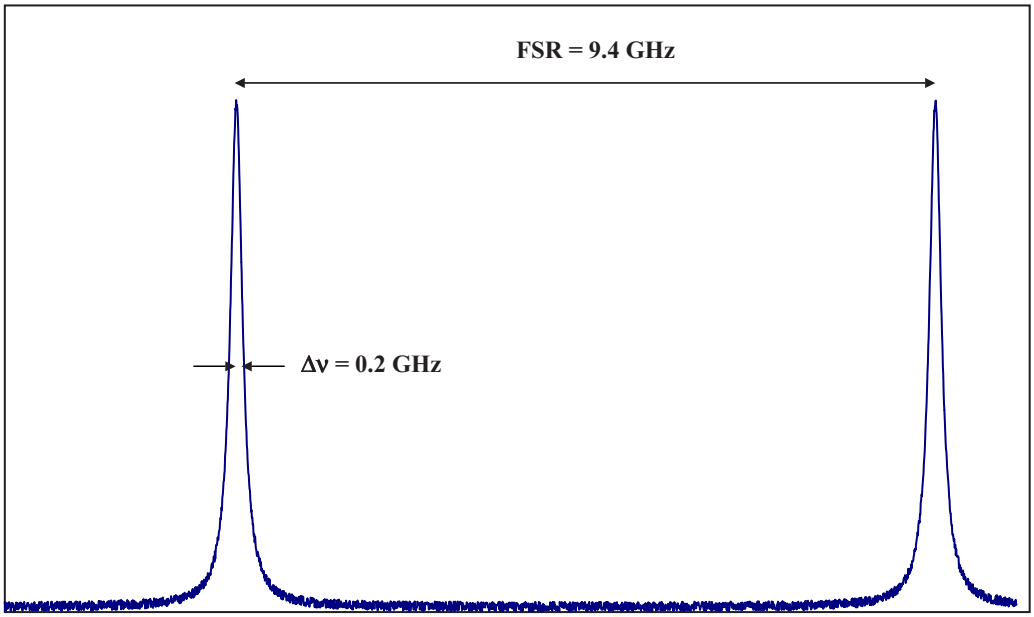

Figure 4.18: Fabry-Perot trace of the output of the seeded phase-conjugate resonator with power-amplifier in the output arm confirming SLM operation.

One important point that should be noted is that in order to see how the gain of the PA affected the output power from the PCO, the PCO was not re-optimised in obtaining the results shown in figures 4.12, 4.13 and 4.14. Any attempt to increase the combined PCO-PA output power by changing the PCO would then change the characteristics of that PCO meaning that no insight is gained into how *just* the PA affects a set configuration of the

PCO. It is expected that optimisation of both the PA and PCO in future implementations of the resonator will lead to increased power outputs.

4.4 Further power-scaling considerations

The results presented within this chapter describe initial investigations into the power-scaling of the phase-conjugate resonators described in chapter 3. When running the phase-conjugate resonator with the PA in the output arm the FWM amplifier gain was reduced (by increasing the diode pump focussed spot size) so that by itself the phase-conjugate resonator (PA turned off) operated with an output power of 6 W (in section 3.7.1 it was shown that the phase-conjugate resonator could produce a maximum output of up to approximately 11.6 W). The increased spot size of the FWM gain region meant that the system as a whole was less sensitive to displacement of any of the interacting beams, for instance, the movement of the seed input beam due to thermal lensing, as it passes through the PA (see section 4.3.4). As the gain of the FWM amplifier was increased (by increased focussing of the diode pump) in an effort to further increase the PCO-PA output the grating writing beams no longer overlapped with the (now smaller) gain region and hence lasing of the PCO would cease. This shows a limitation of the power-scaled phase-conjugate resonator - in order for the PCO to work the distortions introduced to the interacting beams by the PA have to be such that the grating writing beams will still overlap within the gain region.

Another avenue explored to try and increase the output power of the PCO-PA was to increase the gain of the PA by tighter focussing of the pump diode, but this too had its problems. As the gain of the PA increased, the ASE from the PA also increased, this ASE would then travel towards the high gain FWM amplifier, where it was amplified further, removing most of the available gain for the PC mode. This in turn would mean the PCO would fail to reach threshold and lasing would cease. Some possible solutions to these problems are discussed in section 6.2.1.

4.5 Conclusions

In this chapter it has been shown that a seeded phase-conjugate adaptive resonator operating with an output power of 6 W can be power-scaled by the inclusion of a separate power amplifier within the output arm of the phase-conjugate resonator. Initial results show that the output can be scaled up to 11.7 W before misalignment of the grating writing beams with each other and the FWM gain-region causes the phase-conjugate resonator to cease operation. The operation of a phase-conjugate oscillator with a power-amplifier in both the input-output arm and within the resonator loop was modelled, and it was shown that by increasing the gain of the PA in both arrangements an increase in the output power of the combined PCO-PA system was predicted. However when the total gain distributed between the FWM amplifier and PA was kept constant it was predicted that for a PA placed into the loop of the PCO a maximum output was obtained when all the gain was in the FWM amplifier. For the PA placed in the output arm of the PCO the model predicted that a maximum output of the combined PCO-PA system could be obtained for some optimum distribution of the gain between the two amplifiers.

4.6 References

[1] J. M. Hendricks, D. I. Hillier, S. J. Barrington, D. P. Shepherd, R .W. Eason, M. J. Damzen, A. Minnassian, and B. Thompson. Power scaling of continuous-wave adaptive gain-grating laser resonators. *Optics Communications*, accepted for publication, February 2002.

[2] G. J. Crofts and M. J. Damzen. Numerical modelling of continuous-wave holographic laser oscillators. *Optics Communications*, 175(4-6):397–408, 2000.

Chapter 5

Fibre phase-conjugation

5.1 Overview

In the previous chapter it was shown that the phase-conjugate output power from an adaptive resonator could be increased with the addition of further gain elements within the output arm of the resonator. In this chapter the initial groundwork is set for investigations into the use of a pumped multimode fibre as the active gain element within a gain FWM scheme. The chapter begins with an introduction into the use of phase-conjugation for correcting the distortions caused to a beam as it travels along the length of a step-index multimode fibre. These distortions, caused by polarisation and modal scrambling in the fibre, are corrected for upon a double-pass through the fibre after reflection from a PCM. It is shown that only a fraction of the multimode single pass output and that only one polarisation need be phase-conjugated to fully reconstruct the original input beam. Finally, in section 5.4 it is shown how these results can be exploited in the demonstration of a novel two-fibre device that displays intensity nonreciprocity when used in a PC arrangement and which has the potential to replace the bulk NRTE described in section 3.4 in an all-fibre phase-conjugate resonator.

5.2 Background

The study of phase-conjugate methods used for the correction of polarisation and modal scrambling of light transmitted through multimode optical fibres has received considerable attention in previous years. In the first demonstration of modal dispersion correction in a multimode fibre, using photorefractive four-wave mixing in $BaTiO_3$ as a PCM, it was shown that faithful reconstruction of an input beam could occur even when only half the polarisation information of the scrambled field was incident on the PCM [1]. The authors speculated that the information content of each polarisation component of the scrambled output field was assumed to be similar and therefore conjugation of one component only was sufficient to faithfully reproduce the original input beam. The $BaTiO_3$ PCM could only phase-conjugate the e-polarised component of the scrambled output field and was termed a non-polarisation preserving phase-conjugate mirror (NPPPCM). Later work showed how it was possible to correct (phase-conjugate) both components of the scrambled field by decomposing the unpolarised output from the multimode fibre into its two orthogonal states, followed by rotation of the o-polarised (w.r.t. the $BaTiO_3$) component, via a half-wave plate, to become e-polarised. The two e-polarised components could then be phase-conjugated by this polarisation preserving PCM (PPPCM) [2].

Subsequent experimental work [3] and theoretical analysis [4] explains the initially surprising results concerning the ability of a non-polarisation preserving PCM to correct for polarisation scrambling within a multimode fibre. Further work examined the quantitative differences between NPPPC and PPPC and concluded that high contrast image restoration was only possible via PPPC [5] and that NPPPC resulted in contrast degradation and reduced image resolution [6]. More recent work has examined the case of partial phase-conjugation in which only a fraction of the scrambled output from the multimode fibre is sent to the PCM to be phase-conjugated and it is shown that the original input beam can be reproduced even with phase-conjugation of only part of the scrambled field [7].

5.3 Phase-conjugation in multimode fibres

In this section phase-conjugate correction of modal distortion in a highly multimode step-index fibre is demonstrated and the experimental set-up used is shown schematically in figure 5.1. A 1.35 W 514.5 nm vertically polarised beam originating from an Ar ion laser was used as the input to the multimode fibre. This wavelength was chosen to achieve the optimum performance (response time and efficiency) for self-pumped phase-conjugation in the $BaTiO_3$ crystal used in the experiment [8]. The phase-conjugate output was measured via the tilted glass wedge at the input end of the fibre. The fibre was around 1 m in length, with a 300 μm diameter core and an $NA = (n_{core}^2 - n_{clad}^2)^{1/2}$ of 0.31. The total possible number of modes, *N*, that can be supported by such a step-index fibre is given by

$$\begin{aligned} N &= \frac{V^2}{2} \\ V &= \frac{2\pi a}{\lambda} NA \end{aligned} \tag{5.1}$$

where a is the radius of the fibre core and λ is the wavelength of the light travelling within it. As an example, for 514.5 nm light incident on a 300 μm diameter core fibre with an NA of 0.31 and refractive index of 1.5 (V = 852) the total number of supported modes that can exist is around 363000, although in practice this number is greatly reduced due to imperfections along the fibre length and mode stripping due to, for example, bending in the fibre. The light exiting the fibre was modally and polarisation scrambled, and was collimated by a x6.3 microscope objective lens. An aperture placed directly after this lens enabled selection of the whole beam, or on-axis/off-axis spatially restricted components for subsequent focussing into the $BaTiO_3$ self-pumped phase-conjugator, via the polarising beam splitter. Any vertically polarised (o-polarised) light was reflected by the polariser, and sent into a beam stop. Aperture sizes were set at either 7 mm (full size of the collimated output beam), 3 mm both on and off-axis, and finally 2 mm on-axis. Smaller aperture sizes could not be investigated due to the unacceptably long build-up time of the phase-conjugator at such low power levels. Following phase-conjugation, the e-polarised compo-

nent was relaunched into the fibre, and travelled back to the input end of the fibre. The fraction reflected from the wedge could then be measured or displayed via a CCD camera onto a beam profiler. As discussed in detail in reference [5], the light retracing its path back through the fibre is converted into two equal parts: a phase-conjugate component which shows spatial and polarisation correction fidelity, and a non-phase-conjugate background multimode output distributed amongst all spatial and polarisation modes of the fibre. In other words the horizontally polarised phase-

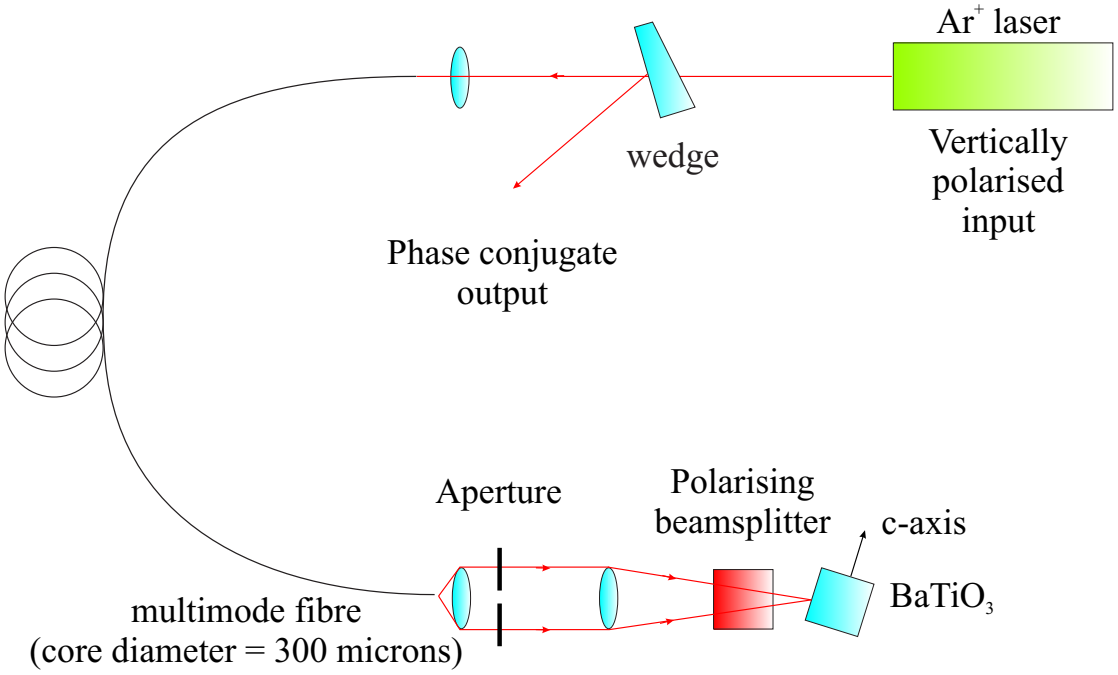

Figure 5.1: Schematic of set-up used to investigate phase-conjugate correction of modal distortion in a passive multimode fibre.

conjugate beam reflected from the NPPPCM upon being relaunched back into the multimode fibre is polarisation and modally scrambled in such a way that once the beam has travelled the length of the fibre the beam now consists of a 50% phase-conjugate component (reconstruction of the input beam with the same vertical polarisation) and 50% unpolarised scrambled output. It is therefore expected that $0.75 = 50\% + 0.5 * 50\%$ of the total output of fibre A in the phase-conjugate direction will have a vertical polarisation whilst the remaining $0.25 = 0.25 * 50\%$ will have a horizontal polarisation. Measurements of the power ratio between components po-

larised parallel to and perpendicular to the input beam yielded a value of 3:1 (vertical:horizontal), which is consistent with the theoretical values reported in reference [5].

Figure 5.2 shows the spatial profiles at the input and output ends of the fibre. Figure 5.2(a) was recorded at a distance of 10 mm from the output end of the fibre, and shows the highly multimode unpolarised output. Figures 5.2(b)-(e) show the phase-conjugate reconstruction of the Gaussian input beam, reflected off the wedge, at a distance of 1 m from the input end of the fibre. With no aperture present, figure 5.2(b), the fidelity appears very good, whereas with the on-axis 3 mm aperture, figure 5.2(c), or on axis 2 mm aperture, figure 5.2(d), the fidelity is seen to degrade, whilst the background noise increases. This is to be expected from both intuitive reasoning and also the results reported in reference [5]. With NPPPC only one half of the light returns to the input as a phase-conjugate. The remaining half appears as background noise as seen most clearly in figure 5.2(d). As the aperture is progressively reduced, the assumption that the fidelity is independent of the number of modes conjugated inevitably breaks down. The extreme case would be phase-conjugation of just one point in the multimode output beam (one lobe from a single high order mode). The information content in this case would be completely insufficient to permit any degree of phase-conjugate fidelity. As more modal content is included in the phase-conjugation process, the ratio of power in the phase-conjugate to power in the non-phase-conjugate noise increases, becoming true phase-conjugation only in the case of PPPC discussed earlier.

Figure 5.2(e) shows the last picture in this sequence, which was taken with a 3 mm aperture, positioned 2 mm off-axis. The phase-conjugate is again readily visible, but the level of the background noise is higher than for the on-axis case shown in figure 5.2(c).

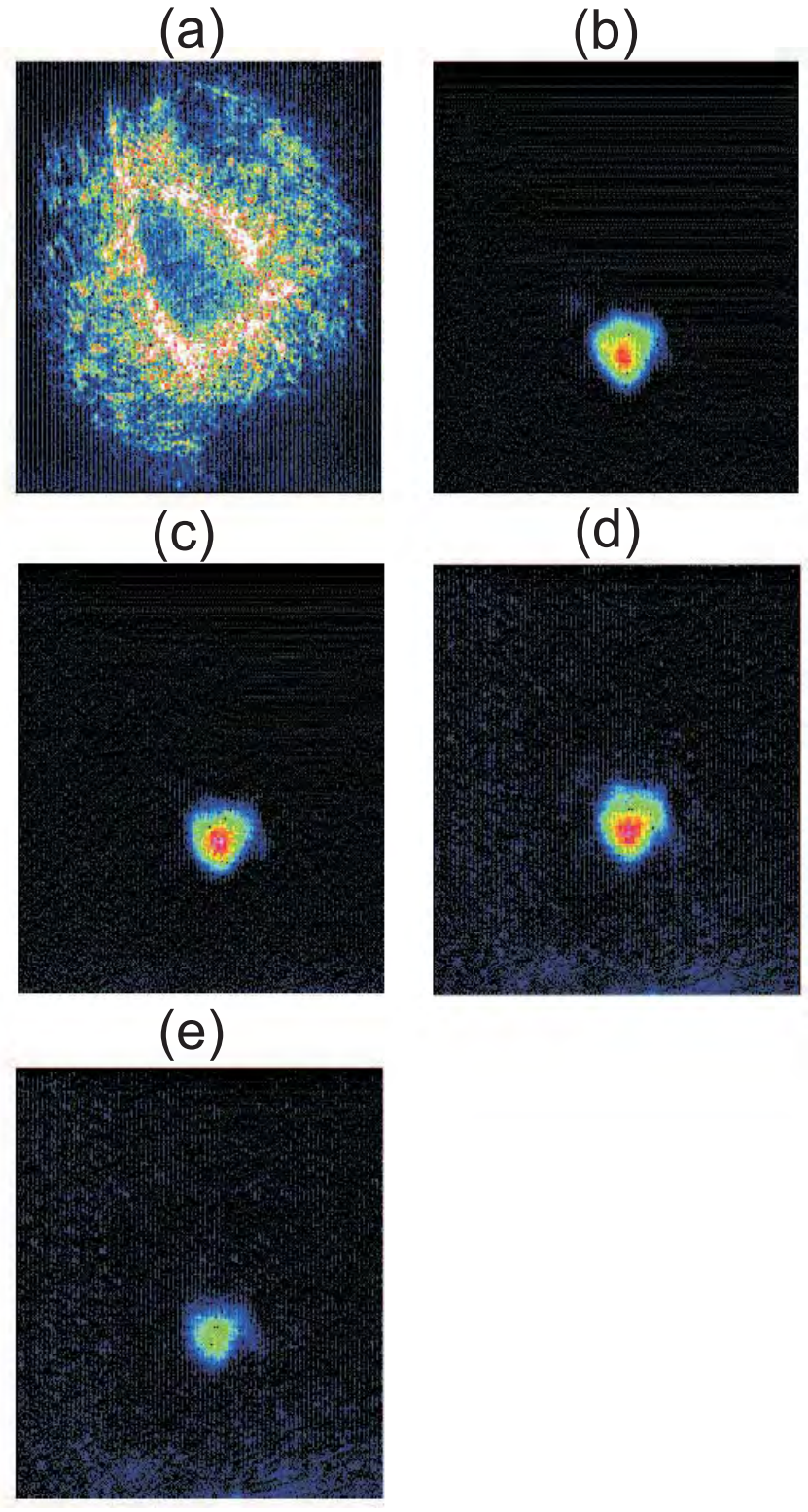

Figure 5.2: Spatial output from the multimode fibre: (a) the single-pass output 10 mm from the end of the fibre; (b-e)the phase-conjugate output recorded at the input end of the fibre after double-pass and modal correction after passing through an on-axis aperture of diameter 7 mm (b), 3 mm (c) and 2 mm (d); (e) the phase-conjugate after passing through an aperture of diameter 3 mm, centred 2 mm off-axis.

Figure 5.3 shows the modified set-up that was implemented for two separate Gaussian inputs. An additional beam splitter generated two roughly equal power inputs, which were phase-conjugated via NPPPC as before. Confirmation was needed that multiple inputs could be faithfully phase-conjugated and remain spatially separated for future implementation of gain-grating techniques in pumped doped fibres. Unlike the case for im-

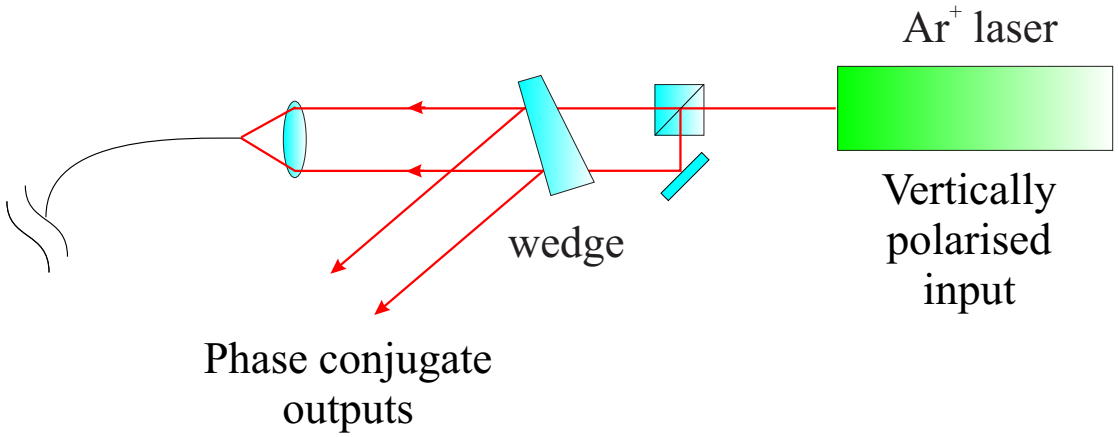

Figure 5.3: Modification to figure 5.1 to allow two simultaneous input beams.

plementation of gain-grating phase-conjugation in bulk laser crystals such as that described in chapter 2, where beams can overlap in the gain medium but remain spatially resolvable in the far-field through angular adjustment, the same degree of freedom does not exist in a fibre geometry. Two input beams become irretrievably mixed, via modal and polarisation scrambling, as they propagate down the length of fibre, and only phase-conjugation can reconstruct their initial spatial separation.

5.4 Non-reciprocal transmission in fibres

As stated earlier in section 5.1, there is a need to implement a non-reciprocal transmission element in an all-fibre gain-grating resonator design [9]. In section 2.7.1 it was shown that within the gain medium, optimized diffraction efficiency occurs for a large modulation depth in the interference pattern produced by overlap of the signal and pump beams. For high gain

media this will not occur without large attenuation of the amplified input seed laser or amplified spontaneous emission beam that travels around the phase-conjugate resonator loop once, to become the FWM signal beam. The phase-conjugate nature of the backwards-travelling wave in the multimode fibre can be exploited to produce just such a NRTE.

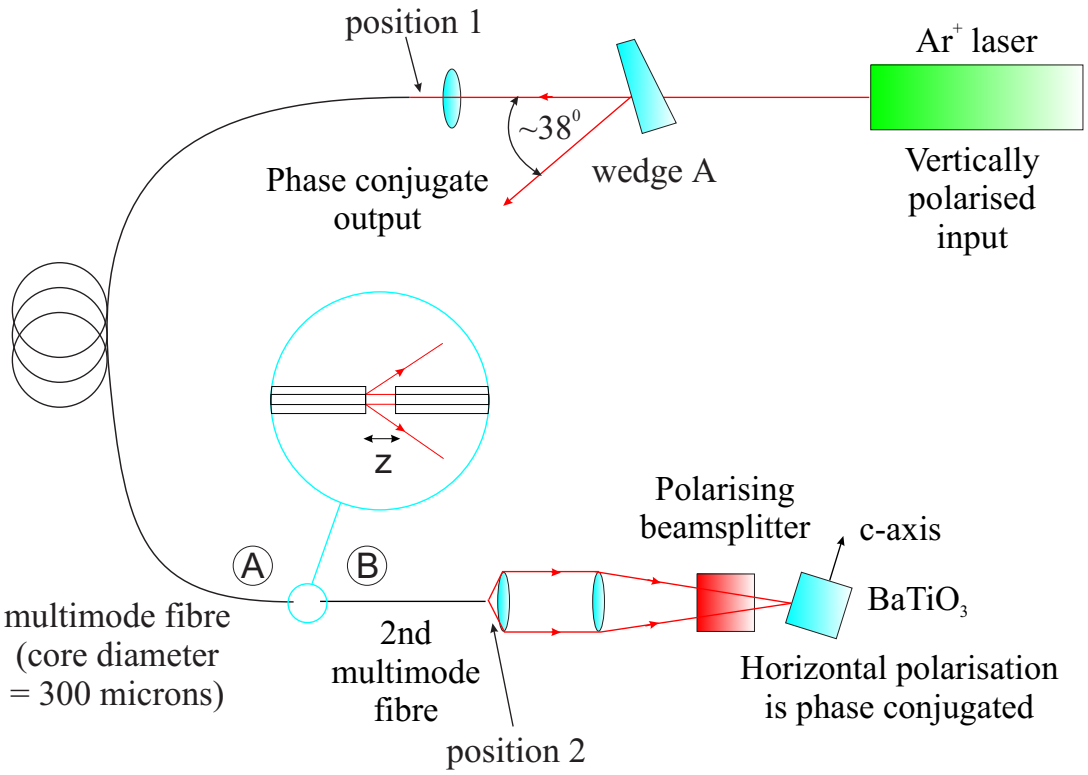

Figure 5.4: Use of two separate fibres to allow variation of modal content for subsequent phase-conjugation.

Figure 5.4 shows a modified version of the previous set-up, in which the fibre has been cut into two parts, A and B, and separated by a variable width gap, z, as shown in the inset. Fibre B can now be positioned to select specific regions from within the output modal content from fibre A, by variation of z, or adjustment of its lateral position. As z is increased, the forward transmission, T_-, (defined as power out of fibre B at position 2 divided by the power sent into fibre A at position 1) in the non-phase-conjugate direction decreases. With reference to figure 5.5, T_- is therefore defined as power at point 4 divided by power at point 1. The transmission through the two fibre system in the backwards (phase-conjugate) direction, T_+, is similarly defined as the ratio of the power out of fibre A at its

input end to that being relaunched by the phase-conjugator at the output end of fibre B (ratio of power at point 1 to that at point 4)

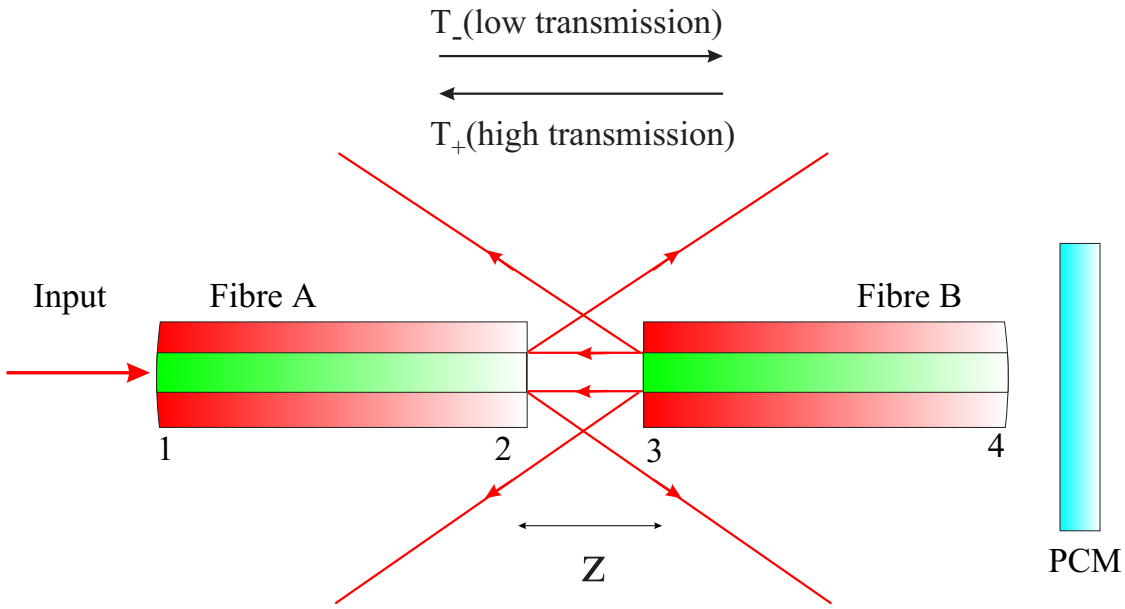

Figure 5.5: Schematic of two fibre geometry separated by a distance z, showing directions of low (T_-) and high (T_+) transmission.

These transmissions have been measured and are shown in figure 5.6, labelled as T_- and T_+ respectively, plotted as a function of distance z. The forward and backward transmissions are clearly different: of most importance is their very different limiting values as z is progressively increased. In the forward direction the transmission is essentially given by, neglecting all other losses, the ratio of the acceptance area of the core of fibre B to the area that the light exiting fibre A has spread out to at a particular value of z. In the backwards direction however, the field consists of a phase-conjugate part which will couple from fibre B back into fibre A, with a theoretical efficiency of 100% for any value of z, and a non phase-conjugate component which should have the same coupling characteristics exhibited by the forward travelling wave from point 2 to point 3. Given the measured values for T_- therefore, the values for T_+ can be predicted by the empirical formula

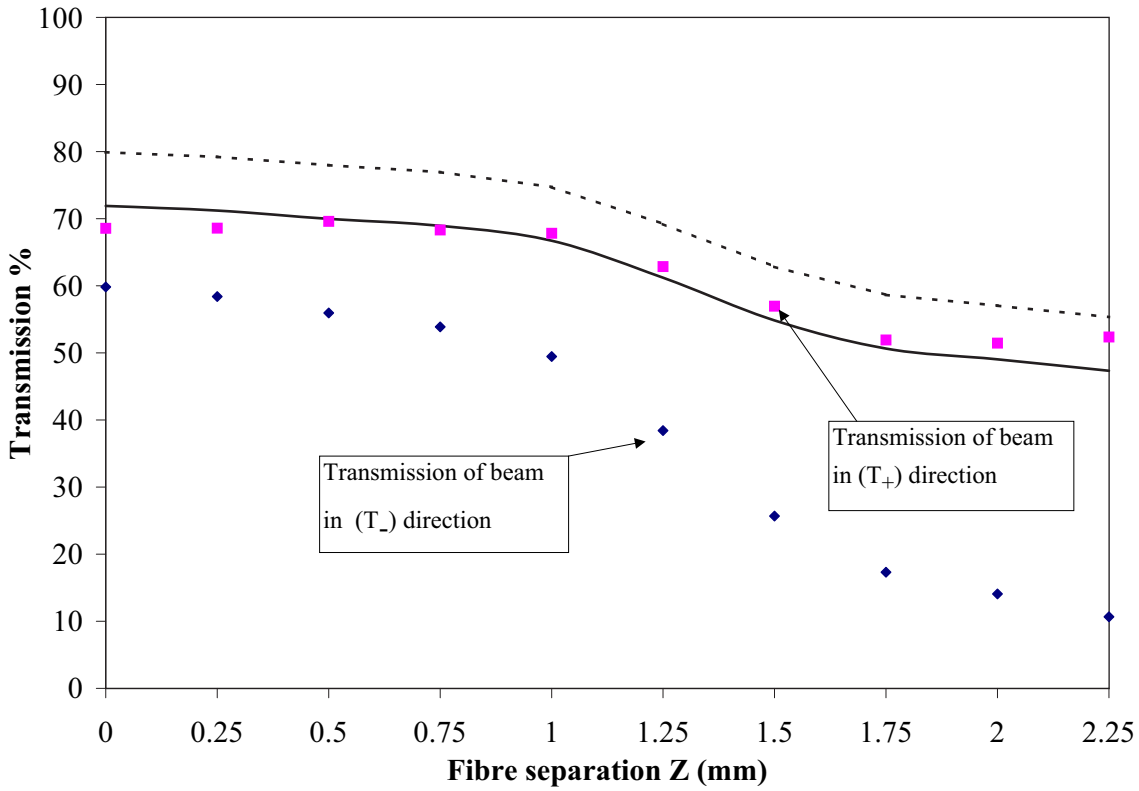

Figure 5.6: Measured values for T_+ and T_- as a function of separation, z.

$$T_+ = \underbrace{1/2}_{phase\ conjgate} + \underbrace{1/2 T_-}_{non-phase\ conjugate} \tag{5.2}$$

From figure 5.6 it can be seen that T_+ does indeed approach its limiting value of 50% at values of z of around 2mm. The power transmitted in the backward direction, P_+, was measured knowing the reflectivity at wedge A. The power out of fibre A at position 1 could then be found by taking into account the reflectivity of the glass wedge and the transmission of the objective lens. The wedge was at an angle of around 38° and so had different reflectivities for vertical and horizontal output polarisation components. The measured vertical reflectivity, R_v, was 7.5% whilst the horizontal reflectivity, R_h, was 1.9%. The effective reflectivity of the wedge, r_{eff}, is therefore given by

$$r_{eff} = 7.5 * \frac{V}{100} + 1.9 * \frac{H}{100} \tag{5.3}$$

where V and H are the percentage of the output field in the vertical and horizontal polarisations respectively. This had to be taken into account when measuring P_+, since the ratio between the two orthogonal polarisations varied as the distance between the fibers, z, was increased. When z = 0 the phase-conjugate reconstructed field is vertically polarised whilst the non-phase-conjugate part is split equally between the vertical and horizontal polarisations. Therefore 75% of the field is vertically polarised and 25% horizontally polarised. As the distance, z, increases the percentage of the vertical polarised field in P_+ increases, as less of the non-phase-conjugate (unpolarised) part is transmitted across the gap between the two fibres.

The dashed line shown in fig 5.6 is an empirical fit based on equation 5.2, knowing the measured values for T_-, which determines both the power launched into fibre B and the reciprocal relaunch of the non-phase-conjugate part into fibre A. This empirical fit does not pass through the measured T_+ data points because we are assuming an efficiency of 100% transmission of the phase-conjugate part of the field. Experimentally, however, the percentage of the phase-conjugate field that is transmitted through the two fibres is reduced due to absorption in the fibres and Fresnel losses at the fibre ends. This phase-conjugate transmission value was varied until a best fit for the measured data points was obtained (unbroken line) and is given by

$$T_+ = \underbrace{0.42}_{phase\ conjugate} + \underbrace{{}^1\!/_2 T_-}_{non-phase\ conjugate} \tag{5.4}$$

Only 84% (0.5*84% = 42%) of the phase-conjugate part is therefore transmitted in the backward direction rather than the theoretically predicted 100%. It is not possible to test the intriguing possibility of increasing the value of z to arbitrarily large values, as the power launched into fibre B (via T_-), which generates the self-pumped phase-conjugate signal, falls below the few mW threshold value required.

One other point to note is that when the distance between the fibres, z, is nominally zero the transmission in the forward and backward direc-

tions shown in figure 5.6 is different. This is a consequence of the fact that even with the fibres in close contact the non-phase-conjugate light can never achieve a 100% coupling efficiency between the two fibres. In the backwards direction however, the phase-conjugate part of the field has a higher coupling efficiency making the overall transmission in this direction higher. Only when we have 100% transmission in the forward direction will the values of T_- and T_+ agree at z = 0.

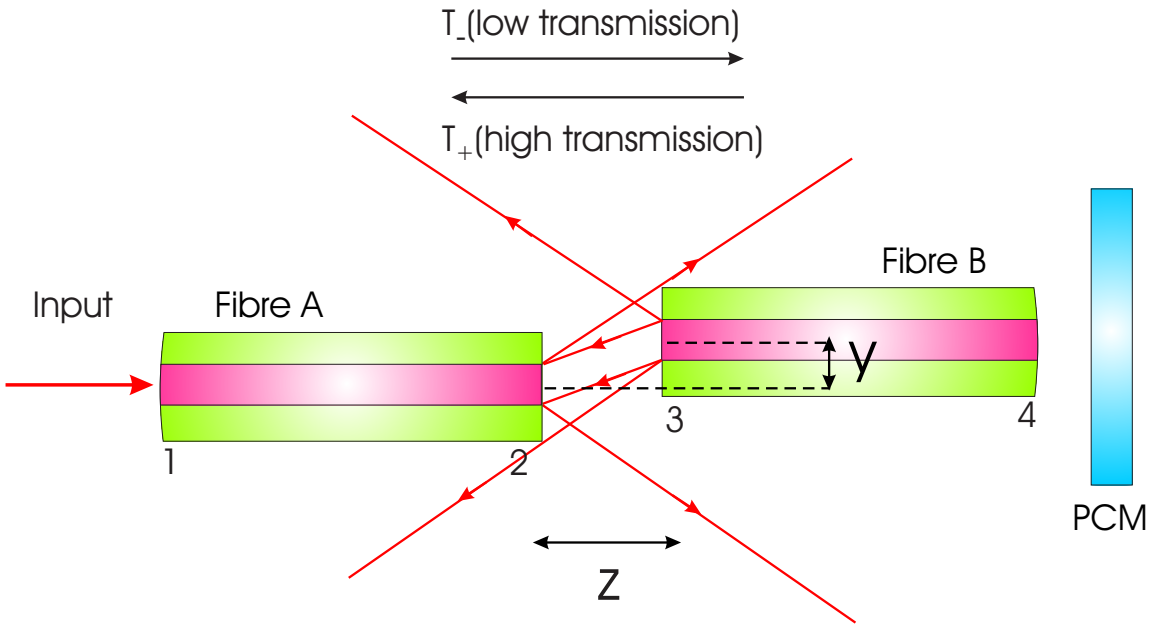

Figure 5.7: Lateral misalignment of the fibres, y, for an axial separation of z = 100 μm .

This two fibre system is also very insensitive to lateral misalignment between the multimode fibres. The same set-up was used as in figure 5.4, and the axial separation z was set to around 100 μm . The lateral displacement between the fibers, Y, was then varied as shown in figure 5.7 and the reconstructed output of the system recorded. Figure 5.8 shows the phase-conjugate output taken 1 m from the input end of the system for various values of lateral displacement, y, up to 115 μm .

From the above results and discussion, it is clear that an amplitude NRTE element in a multimode fibre setup can successfully be constructed when used in conjunction with a PCM. The present values of contrast ratio demonstrated, $\frac{T_+}{T_-}$, are only of order 5 for a PCM that only conjugates one po-

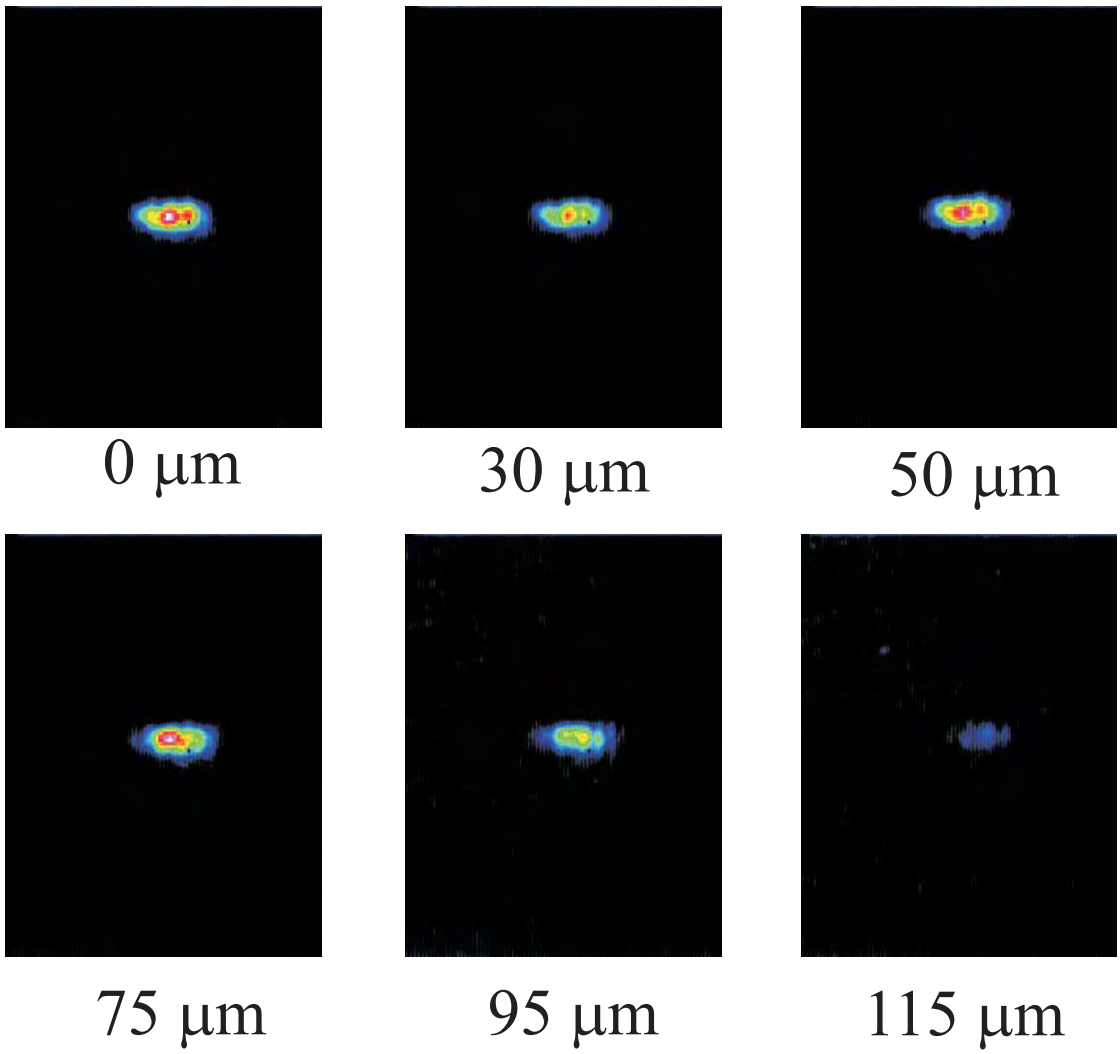

Figure 5.8: Phase-conjugate output for lateral misalignment between the two fibres.

larisation of the scrambled output field of the fibre. This contrast value, however, would be expected to increase when using a PCM that phase-conjugated both polarisation components of the fibre output. Using such a PPPCM it is predicted (theoretically) that the transmission in the phase-conjugate direction is 100% for all values of axial displacement, z, between the two fibres, since now the reflected field is the true PC of both polarisations of the scrambled output of the fibre, not just the horizontal polarisation as in the case of a NPPPCM. In the current implementation, the power levels required to achieve self-pumping for the $BaTiO_3$ are of order a few mW, and this effective threshold limits the values of z possible via T_{-}.

5.5 Conclusions

In this chapter it has been shown that correction for polarisation and modal scrambling within a passive highly multimode fiber can occur in a non-polarisation preserving phase-conjugate arrangement. Reconstruction of the original, undistorted, input beam and its polarisation was demonstrated for a large degree of both on-axis and off-axis undersampling of the total multimode output of the fibre. It was also shown how two separate fibre inputs could be reconstructed by use of phase-conjugation even after modal scrambling of the fields as they propagated along the multimode fibre. The properties of phase-conjugation were then further utilised in the demonstration of a useful non-reciprocal transmission device that will have immediate application in gain-grating resonators that use multimode fibres as the gain medium (see section 6.2.2 for a further discussion). Using this arrangement a contrast ratio for the fibre NRTE of around 5 has been shown for self-pumped photorefractive phase-conjugation.

5.6 References

[1] G. J. Dunning and R. C. Lind. Demonstration of image transmission through fibers by optical- phase conjugation. *Optics Letters*, 7(11):558–560, 1982.

[2] I. McMichael, M. Khoshnevisan, and P. Yeh. Polarization-preserving phase conjugator. *Optics Letters*, 11(8):525–527, 1986.

[3] K. Kyuma, A. Yariv, and S. K. Kwong. Polarization recovery in phase conjugation by modal dispersal. *Applied Physics Letters*, 49(11):617–619, 1986.

[4] A. Yariv, Y. Tomita, and K. Kyuma. Theoretical-model for modal dispersal of polarization information and its recovery by phase conjugation. *Optics Letters*, 11(12):809–811, 1986.

[5] I. McMichael, P. Yeh, and P. Beckwith. Correction of polarization and modal scrambling in multimode fibers by phase conjugation. *Optics Letters*, 12(7):507–509, 1987.

[6] P. H. Beckwith, I. McMichael, and P. Yeh. Image distortion in multimode fibers and restoration by polarization-preserving phase conjugation. *Optics Letters*, 12(7):510–512, 1987.

[7] S. Campbell, P. C. Yeh, C. Gu, and Q. B. He. Fidelity of image-restoration by partial phase-conjugation through multimode fibers. *Optics Communications*, 114(1-2):50–56, 1995.

[8] J. Feinberg. Self-pumped, continuous-wave phase conjugator using internal reflection. *Optics Letters*, 7(10):486–488, 1982.

[9] J. Hendricks, D. P. Shepherd, H.L. Offerhaus, M. Kaczmarek, R. W. Eason, and M. J. Damzen. Non-reciprocal transmission via phase conjugation in multimode optical fibres. *Optics Communications*, 190:357–365, 2001.

Chapter 6

Summary and future work

6.1 Summary

The work presented within this thesis has been concerned with the development and characterisation of a CW solid-state adaptive resonator that uses phase-conjugation to actively correct for phase distortions present within the resonator loop. The motivation for designing such a resonator lies with the power-scaling of solid-state lasers in a bid to increase the output power whilst maintaining SLM diffraction limited output, characteristic of low power operation. As the diodes used to pump laser amplifier crystals continue to increase in power so the thermal loading density within the crystal increases. This leads to undesirable thermal effects such as aberrated thermal lensing leading to distortions within the cavity modes decreasing the efficiency and brightness of the laser.

In Chapter 1 the fundamental background work used for the rest of the thesis was described. The chapter began with an introduction to the spectroscopic mechanisms responsible for the generation of thermal energy within the crystal lattice and a description of the negative effects this thermal loading caused was given. Some of the more successful schemes used to combat these effects within a solid-state laser were then described giving some insight into the methods used to not only minimise the effects of the thermal distortions but to minimise the thermal distortions in the first

instance. The chapter then went on to describe how a phase-conjugate wave could correct for phase distortions upon double passing the distorting medium. A mathematical description of this correction process was given showing that a distorted wavefront upon reflection from a PCM would always remain the phase-conjugate of the original wave (as long as the distortion did not vary at a rate faster than the time taken for the distorted wave to be phase-conjugated *and* travel back to the distortion). It was then described how, by replacing one of the mirrors within a laser cavity with a PCM, a resonator could be produced that could oscillate with a stable mode in what would appear to be a traditionally unstable cavity. Finally a review of some of the more popular methods used to produce the phase-conjugate of an incident wave was given stating the relative advantages and disadvantages when compared to phase-conjugation via gain saturation FWM.

In chapter 2 saturable gain FWM was introduced as a method of producing the phase-conjugate of a given wavefront. The chapter started with an introduction to gain saturation showing how a modulated intensity pattern could give rise to a modulation of the gain within a population inverted medium. This modulation of the gain could then be viewed in terms of a volume gain-grating which could diffract a Bragg matched readout beam with greater than unity efficiencies due to the stored population inversion. Among the many important features of such a volume gain-grating is its ability to store the phase information of the grating writing beams. A FWM geometry was then introduced and described in terms of real time holography that was capable of producing an amplified phase-conjugate of one of the three incident beams. It was shown that because of the mutually coherent nature of the four beams present in the FWM amplifier (three incident beams and one generated PC beam) six individual gain-gratings are formed simultaneously. Simplified modelling of this FWM interaction was then presented and used to show how the diffraction efficiency of the gain-gratings (both in a reflection and transmission grating geometry) varied as a function of the grating writing beam's intensities and the intensity ratio between them. This model gave an insight into the spatial profile of the gain-gratings formed within the gain of the amplifier and how this

profile affected the diffraction efficiency of the grating. Finally, a scheme was described that experimentally demonstrated gain saturation FWM in a Nd:YVO_4 crystal pumped with 18 W of diode power. It was shown that using this configuration a PCM could be produced with CW reflectivities of approximately 100 using grating writing beams of around 0.5 mW.

In chapter 3 the operation of a resonator based on the FWM geometry described in chapter 2 was described. It was shown that the high FWM reflectivities demonstrated make possible the sustained oscillation of an adaptive resonator with a phase-conjugate mode. The chapter began with an introduction to the operation of a simplified phase-conjugate resonator. In the standard FWM geometry presented in the last chapter strict Bragg matching of the reading beam to the gain-grating was required in order for the phase-conjugate to be produced with good efficiency. It was shown that the adaptive resonator was formed in a self-pumped phase-conjugate geometry eliminating the requirements for Bragg matching, since the phase-conjugate wave (and hence the BP) was formed from Bragg matched ASE producing a mode that was automatically matched to the grating. It was shown that two distinct processes occurred during the formation of the PC mode. The first involved the writing of a grating within the inverted amplifier that stored the phase information imprinted onto the single mode input beam as it travelled around the resonator cavity due to effects such as aberrated thermal lensing in the gain medium. It was shown that the grating efficiency could be maximised by use of an amplitude non-reciprocal element that would allow for the matching of the two writing beam's intensities thereby producing maximum contrast in the resulting interference pattern. The second of these processes involved the formation of the PC mode via the diffraction of ASE from the gain-grating. It was shown that a mode that was the PC of the input beam could oscillate in a self-consistent manner and was able to correct for phase distortions within the resonator loop (as long as the distortion was not so severe that it caused the writing beams to no longer overlap with each other *and* the gain region). The resonator FWM interactions were subsequently modelled and it was explained how a phase-conjugate resonator could lase using either a single *transmission* or a single *reflection* grating

although experimentally a mixture of both gratings were present simultaneously. An experimental resonator geometry was then presented that was capable of running in both a seeded and self-starting mode of operation. Using a Nd:YVO_4 crystal pumped with a 60 W laser diode it was shown that the seeded version of the resonator could produce a maximum output of 11.6 W in a SLM near-diffraction limited beam with a seed input of 25 mW. In the self-starting case the seed laser was replaced with a 4% reflectivity output coupler and the mode formation process was initiated from ASE reflected from the output coupler. Again with a 60 W pumping diode a maximum output of 8.2 W was achieved in an SLM near diffraction limited mode. The power was lower in the self-starting case due to the aperture placed within the resonator cavity needed to remove the higher order modes and maintain single mode oscillation.

In chapter 4 the seeded phase-conjugate resonator described in chapter 3 was modified to include an additional PA in an attempt to scale the output power of the phase-conjugate resonator. The additional thermal distortions introduced by the PA could then be corrected for via the distortion correcting nature of the phase-conjugate mode. The chapter began by considering the three possible regions at which the PA could be placed within the existing phase-conjugate resonator. The placement of the PA in the output arm of the resonator was considered and found to be the best option due to the large output power at that point, resulting in greatest power extraction from the PA. An adaptive resonator was then built using the existing PCO (pumped with a 60 W laser diode) with the incorporation of a PA in the output arm. The PA consisted of a Nd:YVO_4 crystal pumped with a 32 W diode setup in a bounce configuration described in chapter 2. Using this setup it was shown that the phase-conjugate output power of the PCO operating with an initial output of 6 W could be scaled to 11.7 W with the addition of the PA before misalignment of the cavity beams caused operation to cease. The phase-conjugate nature of the 11.7 W cavity mode was confirmed by the placement of distorting phase-plates within the cavity, for which, the spatial profile of the output remained unchanged.

In chapter 5 initial work was presented on the use of a multimode fibre in place of the FWM amplifier in an adaptive resonator geometry. It is hoped that if phase-conjugation via gain FWM can be achieved within the fibre then the modal and polarisation distortions introduced to the input beam by the fibre can be corrected for, producing an amplified single mode output. Multimode fibres are preferred over single mode fibres in terms of the larger core size, which is beneficial in several respects. Firstly, a larger core size makes launching of pump beams easier and more efficient. Secondly, larger core sizes increase the threshold of undesirable non-linear effects within the fibre and thirdly, in a larger core fibre the pump light is distributed over a larger cross section reducing thermal effects such as fracture within the fibre core. The chapter begins by describing an experimental setup used to demonstrate how phase-conjugation of only one polarisation and only a small portion of the scrambled output of a multimode fibre is needed to reconstruct the original input beam. It was then shown that two separate inputs into the fibre could also be reconstructed via phase-conjugation even when they become (what would seem) irretrievably mixed due to the effects of polarisation and modal scrambling as they travelled along the length of the multimode fibre. This partial phase-conjugation within the multimode fibre was then exploited in the construction of a two fibre device that displayed non-reciprocity in its intensity transmission when used in a phase-conjugate system. Such a device would be important in the construction of an all fibre adaptive resonator for the matching of the grating writing beam intensities thereby optimising the resonator performance.

6.2 Future work

In this section a brief look at current work in progress as well as future directions and ideas concerning the adaptive phase-conjugate resonator will be given. The section deals with two specific areas of the adaptive resonators namely further power scaling and enhancing of the performance of the resonators described throughout this thesis and future implemen-

tation of the resonator using multimode fibres and hybrid fibre/crystal systems.

6.2.1 Further power-scaling

The results presented in chapter 4 represented only initial work on power-scaling the phase-conjugate resonator. As explained in section 4.4 the main problem encountered when the PA was placed into the output arm of the phase-conjugate resonator was misalignment of the grating writing beams with the FWM gain region. The combined PCO-PA system was made less sensitive to this problem by increasing the spot-size of the gain regions in both the FWM amplifier and the PA at the cost of the subsequently lower gains. A possible avenue to overcome this problem is to decrease the distance between the FWM region and the PA resulting in a lower total displacement of the beam. The loop length could also be decreased (currently around 1 m) thereby further reducing the displacement of the writing beams - in other words miniaturisation of the phase-conjugate resonator. Figure 6.1 shows two possible routes to miniaturisation by placing the FWM region and the PA within the same Nd:YVO_4 crystal therefore decreasing the distance between them albeit with the increased risk of parasitic lasing within the combined FWM/PA crystal. This also has the added benefit of using only one crystal and hence only one heat sink and chiller arrangement. This method of solid-state pumping can be found in some commercial lasers [1] whereby the two diode pump lasers face each other and are offset by their width so that light from one diode cannot enter the facet of the other. The first resonator, figure 6.1(a), shows a reflection grating geometry resonator with the PA in its *output arm*. The analysis of such a loop is exactly the same as previously described in section 3.2.1. Figure 6.1(b) shows a reflection geometry resonator with an *intracavity* PA.

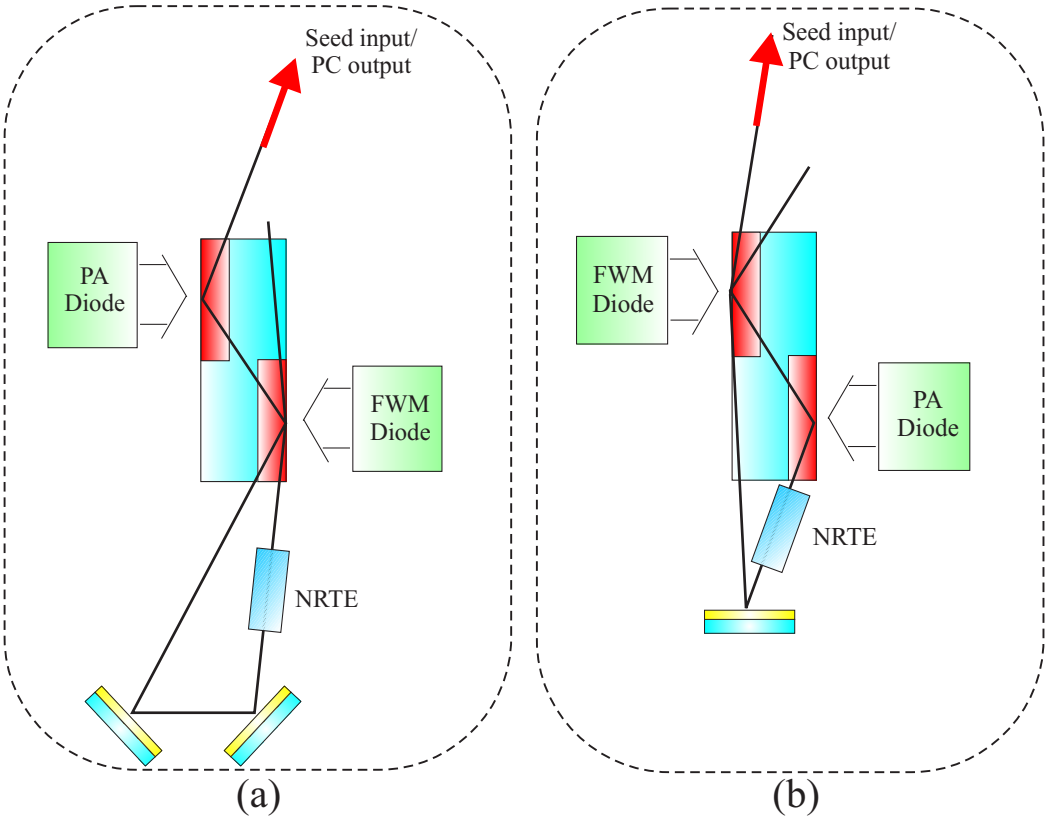

Figure 6.1: Possible implementation of FWM amplifier an PA into one Nd:YVO_4 crystal (a) resonator with PA in arm (b) resonator with PA in loop.

Another route under current investigation to increase the output power and efficiency of the power-scaled adaptive resonator is the use of cylindrical optics to better match the oscillating modes within the resonator to the asymmetrical gain region (see section 2.4.2). In a separate experiment conducted by collaborators on this project a conventional linear laser cavity (no PC techniques involved) was built [2] and the interactions modelled [3] based around the bounce geometry amplifier used in the phase-conjugate resonators discussed in this thesis. Pumping a Nd:YVO_4 crystal with 35 W of diode power at 808 nm and by using *spherical* mode matching optics inside the cavity it was shown that the resonator could operate with a 13.8 W near-diffraction limited SLM mode. However, when the spherical optics were replaced with *cylindrical* ones, so that the resonating mode could be optimised to the gain region in the horizontal and vertical directions independently, the output increased to 22 W near-diffraction limited SLM mode [4].

6.2.2 Fibre adaptive resonator

As stated in section 6.1 implementation of an adaptive resonator in a multimode fibre geometry would have several benefits including better power handling, less susceptibility to non-linear effects than single mode fibres and potentially cheaper to build than the bulk equivalent described in this thesis. The most important step towards the demonstration of a fibre resonator is to ascertain whether saturable gain FWM is possible within a multimode fibre and if so whether the subsequent production of a phase-conjugate wave will correct for polarisation and modal scrambling. Work currently under way includes investigations as to whether gain saturation FWM can be achieved within crystal fibres using the scheme shown in figure 6.2. The 6-200 mm long Nd:YAG crystal fibres, with typical core

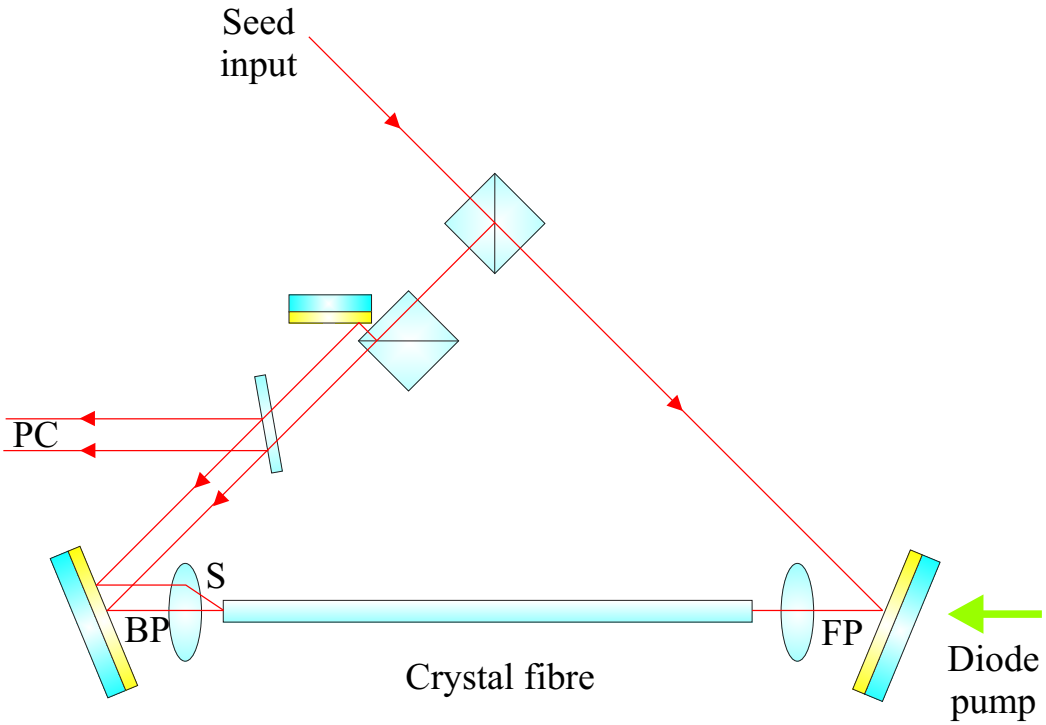

Figure 6.2: Gain saturation FWM within a crystal fibre.

diameters of between 40-100 μm , produce modal scrambling of the single mode input beam but allow a much shorter absorption length of the pump (typically 3-10 mm) [5]. Using this scheme it is hoped to show that modally scrambled fields can indeed write complicated volume gratings in the gain medium and that the modal scrambling can be corrected by the

subsequent production of a phase-conjugate wave.

It is not immediately clear what form the gain-gratings inside the fibre will take since the single mode input field will be distributed between all modes of the fibre. Unlike the bulk case, where the gain-grating forms at the point of overlap of the writing beams, it is now expected that the gain-grating will have some complicated form that is distributed throughout the pumped fibre core. To make matters worse different gratings are formed for the two interfering orthogonal polarisations within the fibre, whereas in the bulk case the polarisation state of the interfering beams can be controlled. On the plus side if FWM can be demonstrated then the different gratings could be used in a vector phase-conjugation scheme whereby the original polarisation of the input beam is restored as well as its spatial form [6].

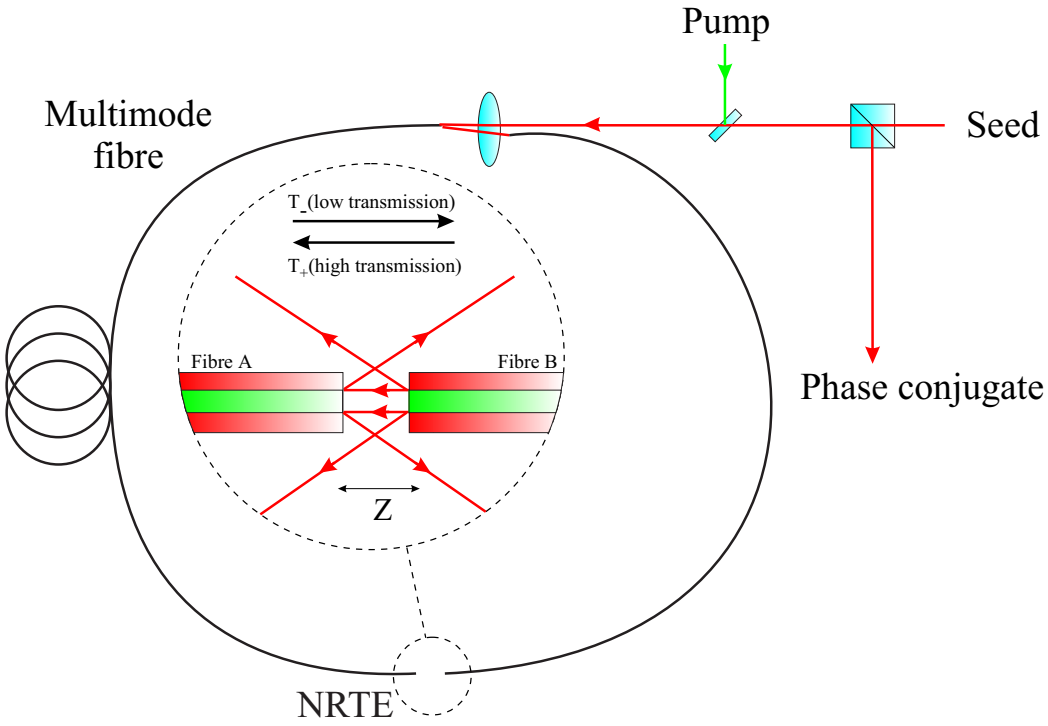

Figure 6.3: Schematic showing implementation of NRTE in a gain-grating fibre resonator geometry.

Figure 6.3 shows the intended scheme for a fibre NRTE (described in section 5.4) in an all-fibre gain-grating resonator. Such resonators routinely require a substantial reduction of the power in the forward propagating beam to compensate for the large round-trip gain. This ensures that the

grating that is written in the gain medium has large modulation depth. The backward propagating beam however needs to experience significant overall gain around the loop, and so similar attenuation is not desirable.

The inset in figure 6.3 shows the schematic diagram of the fibre NRTE in use. This scheme can prove very useful, given that an equivalent bulk NRTE (based around the Faraday isolator) cannot be used for polarisation scrambling multimode fibres.

6.3 References

[1] Q-peak laser systems. `http://www.qpeak.com/Products/gainmodule.htm`.

[2] M. J. Damzen, M. Trew, E. Rosas, and G. J. Crofts. Continuous-wave Nd:YVO_4 grazing-incidence laser with 22.5 W output power and 64% conversion efficiency. *Optics Communications*, 196(1-6):237–241, 2001.

[3] J. H. Garcia-Lopez, V. Aboites, A. V. Kiryanov, S. Holmgren, and M. J. Damzen. Experimental study and modelling of a diode-side-pumped Nd:YVO_4 laser. *Optics Communications*, 201(4-6):425–430, 2002.

[4] M. J. Damzen. Personal communication, February 2002.

[5] M. J. F. Digonnet, C.J. Gaeta, and H.J. Shaw. 1.064- and 1.32- μm Nd:YAG single crystal fiber lasers. *Journal of Lightwave Technology*, 4(4):454–460, 1986.

[6] R. P. M. Green, D. Udaiyan, G. J. Crofts, D. H. Kim, and M. J. Damzen. Holographic laser oscillator which adaptively corrects for polarization and phase distortions. *Physical Review Letters*, 77(17):3533–3536, 1996.

Appendix A

Second moments

The second moment of an intensity distribution $I(r)$ is given by

$$\sigma^2 = \frac{\int_{-\infty}^{\infty} (r - \bar{r})^2 I(r)\, dA}{\int_{-\infty}^{\infty} I(r)\, dA} \tag{A.1}$$

where A is the area over which the integral is taken and $\bar{r}$ is the centroid (first moment) of the intensity distribution and is defined as

$$\bar{r} = \frac{\int_{-\infty}^{\infty} rI(r)\, dA}{\int_{-\infty}^{\infty} I(r)\, dA} \tag{A.2}$$

for a non-circularly symmetric beam, for example the highly elliptical output of a laser diode, the second moment can be expressed in rectangular co-ordinates by

$$\sigma_y^2(z) = \frac{\int_{-\infty}^{\infty}\int_{-\infty}^{\infty} (y - \bar{y})^2 I(x,y)\, dxdy}{\int_{-\infty}^{\infty}\int_{-\infty}^{\infty} I(x,y)\, dxdy} \tag{A.3}$$

and similarly for $\sigma_x^2(z)$.

The diode output is assumed to have a Gaussian intensity profile in the y-axis given by

$$I(y,z) = \exp\left(-\frac{2y^2}{\omega_y(z)}\right) \tag{A.4}$$

where $\omega_y(z)$ is the spot-size of the diode beam in the y direction at a distance z along the propagation axis. The spot size of the diode beam can be obtained by substituting equation A.4 into equation A.3 and setting $\bar{y}$ to zero (since a Gaussian beam is symmetric about the origin and therefore the centroid lies at zero), we obtain

$$\sigma_y^2(z) = \frac{\int_{-\infty}^{\infty} y^2 \exp\left(-\frac{2y^2}{\omega_y(z)}\right) dy}{\int_{-\infty}^{\infty} \exp\left(-\frac{2y^2}{\omega_y(z)}\right) dy} \tag{A.5}$$

using the two standard integrals

$$\int_{-\infty}^{\infty} \exp\left(-ay^2\right) = \sqrt{\frac{\pi}{a}} \tag{A.6}$$

$$\int_{-\infty}^{\infty} y^2 \exp\left(-ay^2\right) = \frac{1}{2}\sqrt{\frac{\pi}{a^3}} \tag{A.7}$$

with $a = \frac{2}{\omega_y^2(z)}$ gives the second moment in the y direction as

$$\sigma_y^2(z) = \frac{\frac{1}{2}\sqrt{\frac{\pi}{a^3}}}{\sqrt{\frac{\pi}{a}}} = \frac{1}{2a} \tag{A.8}$$

and therefore the spot-size of the diode in the y direction can be related to the second moment by

$$\omega_y(z) = 2\sigma_y(z) \tag{A.9}$$

Appendix B

FWM theory

This appendix describes the modelling of a four-wave mixing interaction in a saturable gain medium previously described in the modelling paper by *Crofts and Damzen* [1] with whom we collaborated in the adaptive lasers project. The FWM model described here, although *not* my own work, forms the basis of the grating models in chapter 2 and the resonator models described in chapters 3 and 4 and so for completeness is included in this appendix.

Figure B.1 shows a schematic of the standard four-wave mixing geometry used throughout this thesis. Several sets of gain-gratings are written and simultaneously read by all the interacting beams. Each field has a complex slowly varying amplitude associated with it that describes both the amplitude and slowly varying phase of that field and is given by

$$\mathbf{A}_j = A_j \exp(i\phi) \tag{B.1}$$

Where j =1,2,3 or 4. The total complex electric field amplitude within the gain region due to the four wave mixing beams is given by

$$\begin{aligned} \mathbf{E}_{total} = \mathbf{A}_1 \exp(-i\mathbf{k}_1 \cdot \mathbf{r}) + \mathbf{A}_2 \exp(-i\mathbf{k}_2 \cdot \mathbf{r}) \\ + \mathbf{A}_3 \exp(-i\mathbf{k}_3 \cdot \mathbf{r}) + \mathbf{A}_4 \exp(-i\mathbf{k}_4 \cdot \mathbf{r}) \end{aligned} \tag{B.2}$$

where $\mathbf{k}_j$ is the wave vector of the jth field with magnitude

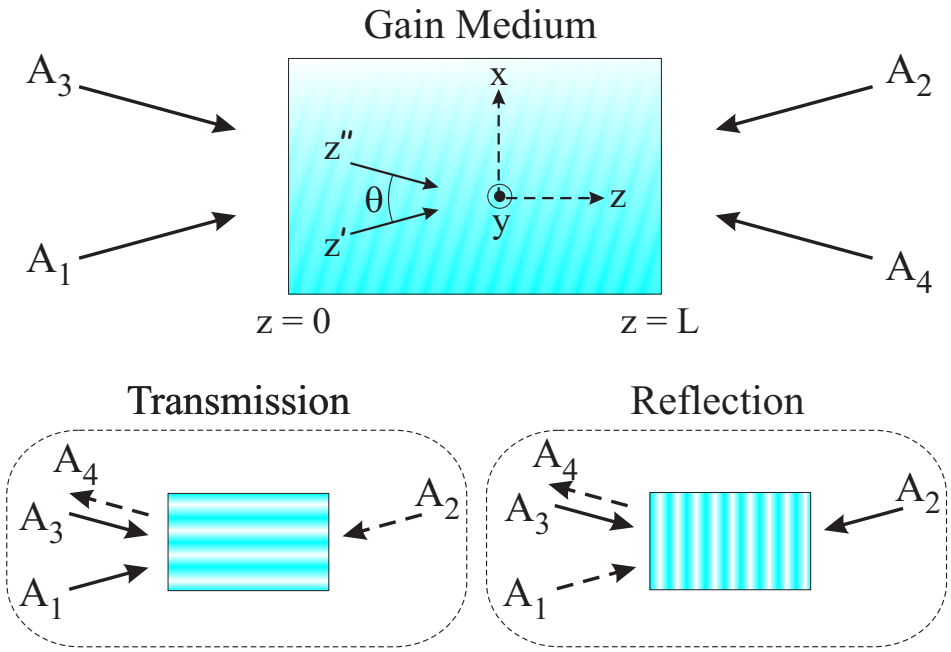

Figure B.1: Schematic of a gain four-wave mixing geometry showing the four interacting fields, the coordinate system and the two primary gratings of interest.

$$k = \frac{2\pi n}{\lambda_0} \tag{B.3}$$

where λ_0 is the free-space wavelength of the fields and n the refractive index of the gain medium. Fields $\mathbf{A}_1$ and $\mathbf{A}_2$ propagate in opposite senses along the z' axis whilst fields $\mathbf{A}_3$ and $\mathbf{A}_4$ propagate in opposite senses along the z'' axis. The two directions, z' and z'', subtend a small angle, θ, in the gain medium and thus the FWM fields have wave-vectors given by

$$\mathbf{k}_{1,2} = \pm k\hat{z'} = \pm k\left(+\hat{x}\sin\frac{\theta}{2} + \hat{z}\cos\frac{\theta}{2}\right) \tag{B.4}$$

$$\mathbf{k}_{3,4} = \pm k\hat{z''} = \pm k\left(-\hat{x}\sin\frac{\theta}{2} + \hat{z}\cos\frac{\theta}{2}\right) \tag{B.5}$$

where the $+$ and $-$ signs refer to indices 1,3 and 2,4 respectively and where $\hat{x}$ and $\hat{z}$ are the unit vectors along the two grating directions as shown in

figure B.1 and $\hat{z'}$ and $\hat{z''}$ are the unit vectors along the beam propagation directions.

The total electric field strength inside the gain medium due to the presence of the four waves has the form

$$\varepsilon_{total} = \tfrac{1}{2}\left(\mathbf{E}_{total}\exp\left(i\omega t\right) + \mathbf{E}^{*}_{total}\exp\left(-i\omega t\right)\right) \tag{B.6}$$

The total time averaged intensity produced within the medium is related to the total complex electric field amplitude by

$$I_{total} = \tfrac{1}{2}nc\varepsilon_0\mathbf{E}_{total}\cdot\mathbf{E}^{*}_{total} \tag{B.7}$$

Substituting equation B.2 into equation B.7 and multiplying out gives

$$\begin{aligned}\frac{I_{total}}{\frac{1}{2}nc\varepsilon_0} = {} & \mathbf{A}_1\cdot\mathbf{A}_1^{*} + \mathbf{A}_1\cdot\mathbf{A}_2^{*}e^{-(\mathbf{k}_1-\mathbf{k}_2)\cdot\mathbf{r}} + \mathbf{A}_1\cdot\mathbf{A}_3^{*}e^{-(\mathbf{k}_1-\mathbf{k}_3)\cdot\mathbf{r}} + \mathbf{A}_1\cdot\mathbf{A}_4^{*}e^{-(\mathbf{k}_1-\mathbf{k}_4)\cdot\mathbf{r}} \\ & + \mathbf{A}_2\cdot\mathbf{A}_2^{*} + \mathbf{A}_2\cdot\mathbf{A}_1^{*}e^{-(\mathbf{k}_2-\mathbf{k}_1)\cdot\mathbf{r}} + \mathbf{A}_2\cdot\mathbf{A}_3^{*}e^{-(\mathbf{k}_2-\mathbf{k}_3)\cdot\mathbf{r}} + \mathbf{A}_2\cdot\mathbf{A}_4^{*}e^{-(\mathbf{k}_2-\mathbf{k}_4)\cdot\mathbf{r}} \\ & + \mathbf{A}_3\cdot\mathbf{A}_3^{*} + \mathbf{A}_3\cdot\mathbf{A}_1^{*}e^{-(\mathbf{k}_3-\mathbf{k}_1)\cdot\mathbf{r}} + \mathbf{A}_3\cdot\mathbf{A}_2^{*}e^{-(\mathbf{k}_3-\mathbf{k}_2)\cdot\mathbf{r}} + \mathbf{A}_3\cdot\mathbf{A}_4^{*}e^{-(\mathbf{k}_3-\mathbf{k}_4)\cdot\mathbf{r}} \\ & + \mathbf{A}_4\cdot\mathbf{A}_4^{*} + \mathbf{A}_4\cdot\mathbf{A}_1^{*}e^{-(\mathbf{k}_4-\mathbf{k}_1)\cdot\mathbf{r}} + \mathbf{A}_4\cdot\mathbf{A}_2^{*}e^{-(\mathbf{k}_4-\mathbf{k}_2)\cdot\mathbf{r}} + \mathbf{A}_4\cdot\mathbf{A}_3^{*}e^{-(\mathbf{k}_4-\mathbf{k}_3)\cdot\mathbf{r}}\end{aligned} \tag{B.8}$$

These terms describe the six different gratings formed when then four mutually coherent waves interfere (see section 2.6 for a further discussion). Only the transmission and reflection gratings play a part in producing phase-conjugate waves in the FWM geometry so ignoring the other gratings (i.e. disregard the interference between $\mathbf{A}_1$ and $\mathbf{A}_2$ and also between $\mathbf{A}_3$ and $\mathbf{A}_4$) the total intensity pattern normalised to I_{sat} is given by

$$\begin{aligned}\frac{I_{total}}{I_{sat}} &= \sigma_i + \tfrac{1}{2}\left(\tau_i e^{-iK_\tau x} + \tau_i^{*}e^{+iK_\tau x}\right) + \tfrac{1}{2}\left(\rho_i e^{-iK_\rho z} + \rho_i^{*}e^{+iK_\rho z}\right) \\ &= \sigma_i + |\tau_i|\cos\left[K_\tau x - \phi_\tau\left(z\right)\right] + |\rho_i|\cos\left[K_\rho x - \phi_\rho\left(z\right)\right]\end{aligned} \tag{B.9}$$

where

$$\sigma_i = \frac{1}{A_{sat}^2} \sum_{j=1}^{4} \mathbf{A}_j \cdot \mathbf{A}_j^* \tag{B.10}$$

$$\tau_i = |\tau_i| \, e^{+i\phi_\tau} = \frac{2}{A_{sat}^2} \left[\mathbf{A}_1 \cdot \mathbf{A}_3^* + \mathbf{A}_4 \cdot \mathbf{A}_2^* \right] \tag{B.11}$$

$$\rho_i = |\rho_i| \, e^{+i\phi_\rho} = \frac{2}{A_{sat}^2} \left[\mathbf{A}_1 \cdot \mathbf{A}_4^* + \mathbf{A}_3 \cdot \mathbf{A}_2^* \right] \tag{B.12}$$

are the normalised mean intensity level, transmission grating amplitude and reflection grating amplitude respectively. $K_\tau x = k\,(z' - z'')$ and $K_\rho x = k\,(z' + z'')$ are the fast spatially varying phase components and $\phi_\tau(z)$, $\phi_\rho(z)$ are the slowly varying phase components of the transmission and reflection gratings respectively.

As the angle between the beams is small, the distinction between z, z' and z'' is neglected for the evolution of the slowly varying field amplitudes and are assumed to vary along z only. The gain-grating is formed when the interference pattern described by equation B.9 saturates the gain in the population inverted medium. The gain is then modulated according to

$$\begin{aligned} \alpha\,(x,z) &= \frac{\alpha_0}{1 + \frac{I_{total}}{I_{sat}}} \\ \alpha\,(x,z) &= \frac{\alpha_0}{1 + \sigma_i + |\tau_i| \cos\left[K_\tau x - \phi_\tau\,(z)\right] + |\rho_i| \cos\left[K_\rho x - \phi_\rho\,(z)\right]} \\ \alpha\,(x,z) &= \frac{\Gamma_0}{1 + M_\tau \cos\psi_\tau + M_\rho \cos\psi_\rho} \end{aligned} \tag{B.13}$$

where $\psi_\tau = K_\tau x - \phi_\tau\,(z)$ and $\psi_\rho = K_\rho z - \phi_\rho\,(z)$ are the spatially varying phases of the transmission and reflection grating components and

$$\Gamma_0 = \frac{\alpha_0}{1 + \sigma_i} \tag{B.14}$$

$$M_\tau = \frac{|\tau_i|}{1 + \sigma_i} \tag{B.15}$$

$$M_\rho = \frac{|\rho_i|}{1+\sigma_i} \tag{B.16}$$

When all the FWM beams are co-polarised both the reflection and transmissions gratings are present in the gain medium. This model separates the two orthogonal gratings to greatly simplify the theory. To produce a single transmission grating M_ρ is set to zero whereas a single reflection grating can be achieved by setting M_τ to zero. Using this simplification equation B.13 can be expanded in a Fourier cosine series as follows

$$\begin{aligned} \alpha &= \sum_{n=0}^{\infty} \alpha_g^{(n)}(z) \cos(n\psi_g) \\ \alpha &= \frac{1}{2} \sum_{n=0}^{\infty} \alpha_g^{(n)}(z) \exp(+in\psi_g) + c.c. \end{aligned} \tag{B.17}$$

with harmonic coefficients given by

$$\alpha_g^{(0)}(z) = \frac{\Gamma_0}{\sqrt{1-M_g^2}} \tag{B.18}$$

$$\alpha_g^{(n)}(z) = (-1)^n \frac{2\Gamma_0}{\sqrt{1-M_g^2}} \left(\frac{1-\sqrt{1-M_g^2}}{M_g} \right)^n \tag{B.19}$$

and where the subscript g can refer to either the transmission grating (g = τ) or the reflection grating (g = ρ).

The next stage in the FWM modelling process is to examine what effect the modulated gain of equation B.13 has on the FWM beams by placing the polarisation of the active laser ions into the non-linear Maxwell wave equation.

$$\nabla^2 \varepsilon_{total} - \frac{n^2}{c^2} \frac{\partial^2 \varepsilon_{total}}{\partial t^2} = \mu_0 \frac{\partial^2 \wp^{at}}{\partial t^2} \tag{B.20}$$

where the polarisation, $\wp^{at}$, for an active laser atom embedded in a solid-state crystal host is given by

$$\wp^{at} = \tfrac{1}{2} P^{at}_{total} \exp(i\omega t) + \mathbf{c.c.} \tag{B.21}$$

with a complex atomic polarisation amplitude, P^{at}_{tot}, given by

$$P^{at}_{total} = \varepsilon_0 \chi^{at} \mathbf{E}_{total} \tag{B.22}$$

where χ^{at} is the atomic susceptibility of the active ion and for a homogeneously broadened gain on resonance is given by

$$\chi^{at} = i\frac{2\alpha}{k} \tag{B.23}$$

inserting equations B.6 and B.21 into the non-linear wave equation and applying the SVEA [2]

$$\begin{aligned} \left|k^2 \mathbf{A}\right| &\gg \left|k\frac{\partial \mathbf{A}}{\partial z}\right| \gg \left|\frac{\partial^2 \mathbf{A}}{\partial z^2}\right| \\ \left|\omega^2 \mathbf{A}\right| &\gg \left|\omega\frac{\partial \mathbf{A}}{\partial t}\right| \gg \left|\frac{\partial^2 \mathbf{A}}{\partial t^2}\right| \end{aligned} \tag{B.24}$$

and plane wave (paraxial) approximation

$$\frac{\partial \varepsilon}{\partial x} = \frac{\partial \varepsilon}{\partial y} = 0 \tag{B.25}$$

the SVEA non-linear wave equation can now be expressed as

$$\left((-1)^{j+1}\frac{\partial}{\partial z} + \frac{n}{c}\frac{\partial}{\partial t}\right)\mathbf{A}_j = -i\frac{\mu_0 \omega^2}{2k} P^{at}_{total} \exp(+ik_j z) \tag{B.26}$$

this equation describes how the jth field is altered due to its interaction with the gain medium whose polarisation properties have been spatially modulated by the presence of the gain-grating. Equation B.26 can be solved for each FWM beam by choosing the appropriately phase matched components of the total polarisation (i.e. those polarisation components that are matched to the k-vector of the FWM field) producing a set of four steady-state coupled equations for a single transmission grating

$$
\begin{aligned}
+\frac{dA_1}{dz} &= \gamma_\tau A_1 + \kappa_\tau A_3 \\
-\frac{dA_2}{dz} &= \gamma_\tau A_2 + \kappa_\tau^* A_4 \\
+\frac{dA_3}{dz} &= \gamma_\tau A_3 + \kappa_\tau^* A_1 \\
-\frac{dA_4}{dz} &= \gamma_\tau A_4 + \kappa_\tau A_2
\end{aligned}
\tag{B.27}
$$

and for a single reflection grating

$$
\begin{aligned}
+\frac{dA_1}{dz} &= \gamma_\rho A_1 + \kappa_\rho A_4 \\
-\frac{dA_2}{dz} &= \gamma_\rho A_2 + \kappa_\rho^* A_3 \\
+\frac{dA_3}{dz} &= \gamma_\rho A_3 + \kappa_\rho^* A_2 \\
-\frac{dA_4}{dz} &= \gamma_\rho A_4 + \kappa_\rho A_1
\end{aligned}
\tag{B.28}
$$

where the coupling coefficients are related to the lowest order grating harmonics by

$$
\begin{aligned}
\gamma_g &= \alpha_g^{(0)} \\
\kappa_g &= \frac{1}{2}\alpha_g^{(1)} \exp\left(i\phi_g\right)
\end{aligned}
\tag{B.29}
$$

B.1 References

[1] G. J. Crofts and M. J. Damzen. Numerical modelling of continuous-wave holographic laser resonators. *Optics Communications*, 175(4-6):397-408,2000.

[2] R. A. Fisher. Optical phase-conjugation. pages 9-10, Academic press, 1983.

Appendix C

Crystal Geometry

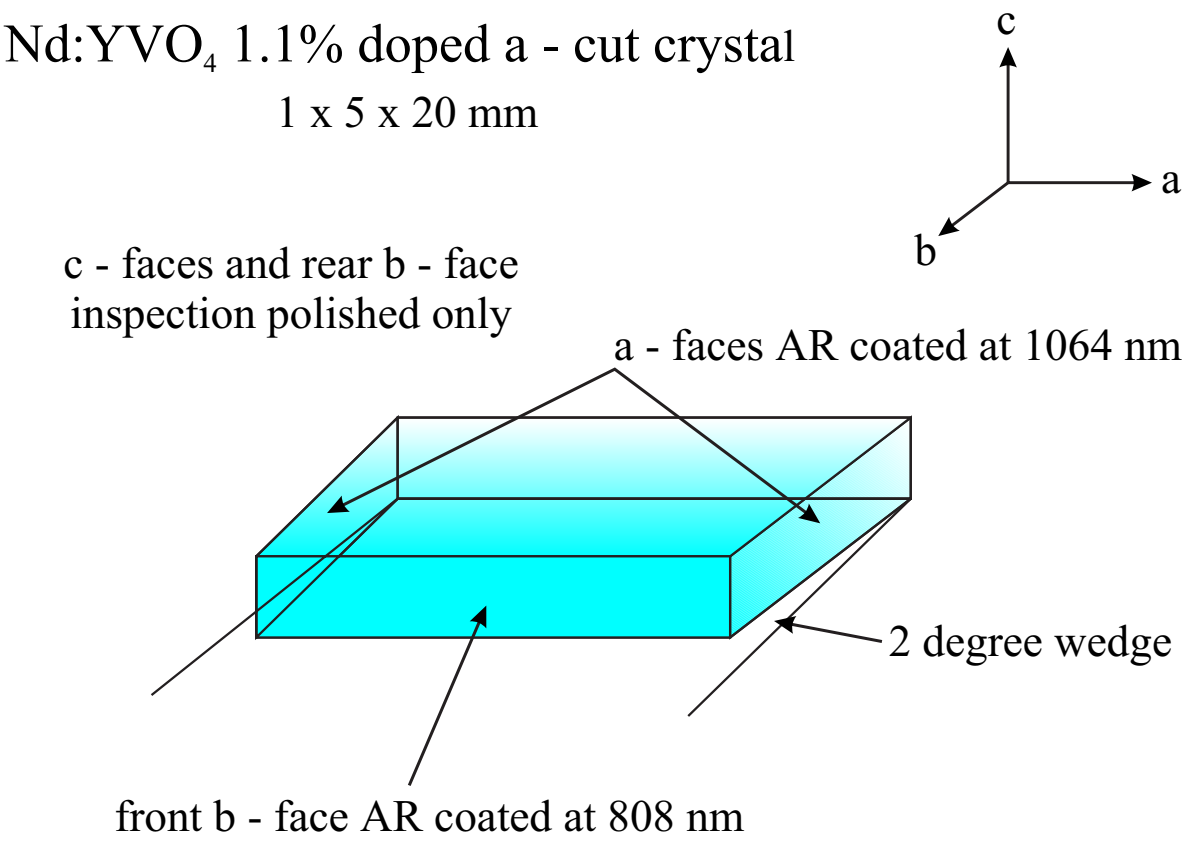

Appendix D

List of Publications

D.1 Journal Publications

S. Mailis, J.M. Hendricks, D.P. Shepherd, A.C. Tropper, N. Moore, R.W. Eason, G.J. Crofts, M. Trew and M.J. Damzen. High-phase-conjugate reflectivity (>800%) obtained by degenerate four-wave mixing in a continuous-wave diode-side-pumped Nd:YVO_4 amplifier. *Optics Letters*, 24(14):972–974, 1999.

M. Trew, G.J. Crofts, M.J. Damzen, J. Hendricks, S. Mailis, D.P. Shepherd, A.C. Tropper and R.W. Eason. Multiwatt continuous-wave adaptive laser resonator. *Optics Letters*, 25(18):1346–1348, 2000.

J.M. Hendricks, D.P. Shepherd, H.L. Offerhaus, M. Kaczmarek, R.W. Eason and M.J. Damzen. Non-reciprocal transmission via phase conjugation in multimode optical fibres. *Optics Communications*, 190:357–365, 2001.

J.M. Hendricks, D.I. Hillier, S.J. Barrington, D.P. Shepherd, R.W. Eason, M.J. Damzen, A. Minnassian and B. Thompson. Power scaling of continuous-wave adaptive gain-grating laser resonators. *Optics Communications*, accepted for publication, February 2002.

D.2 Conference Papers

M.J. Damzen, R.W. Eason, D.P. Shepherd, A.C. Tropper, G.J. Crofts, N. Moore, S. Mailis, M. Trew and J.M. Hendricks. High-reflectivity continuous-wave phase conjugation by four-wave mixing in a diode-pumped Nd:YVO_4 amplifier. In *CLEO 1999*, CF14, Baltimore, 1999.

J.M. Hendricks, S. Mailis, D.P. Shepherd, A.C. Tropper, N. Moore, R.W. Eason, G.J. Crofts, M. Trew and M.J. Damzen. Holographic laser resonators using degenerate four-wave mixing in a continuous wave diode side-pumped Nd:YVO_4 amplifier. In *CLEO/Europe-EQEC*, LtuD4, Munich, 1999.

J.M. Hendricks, S. Mailis, D.P. Shepherd, A.C. Tropper, G.J. Crofts, M. Trew, M.J. Damzen and R.W. Eason. Continuous wave adaptive laser resonators using degenerate four-wave mixing in a diode bar side-pumped Nd:YVO_4 amplifier. In *QE-14*, 1-17/135, Manchester, 1999.

J.M. Hendricks, S. Mailis, D.P. Shepherd, A.C. Tropper, G.J. Crofts, M. Trew, M.J. Damzen and R.W. Eason. Distortion-correcting holographic resonators. In *Solid-state lasers IX - Photonics west*, 3929:2–13, San Jose, 2000.

M. Trew, G.J. Crofts, M.J. Damzen, S. Mailis, J. Hendricks, D.P. Shepherd, A.C. Tropper, R.W. Eason. Multi-watt continuous-wave diode-pumped Nd:YVO_4 adaptive laser resonator. In *CLEO 2000*, CMJ7, San-Francisco, 2000.

J.M. Hendricks, D.P. Shepherd, H.L. Offerhaus, M. Kaczmarek, R.W. Eason, M.J. Damzen. Non-reciprocal transmission via phase conjugation in multimode optical fibres. In *CLEO 2001*, CWH4, Baltimore, 2001.

J.M. Hendricks, D.P. Shepherd, H.L. Offerhaus, M. Kaczmarek, R.W. Eason, M.J. Damzen. Phase conjugate non-reciprocal transmission in multimode optical fibres. In *CLEO/Europe-EQEC*, Munich, 2001.

D.I. Hillier, J.M. Hendricks, S.J. Barrington, D.P. Shepherd, R.W. Eason, M.J. Damzen, A. Minassian, B. Thompson. Power-scaling continuous-

wave adaptive laser resonators. In *CLEO 2002*, Long beach, 2002.

B.A. Thompson, A. Minassian, M.J. Damzen, J.M. Hendricks, D.I. Hillier, S.J. Barrington, D.P. Shepherd, R.W. Eason. Efficient adaptive self-starting Nd:YVO_4 gain grating laser oscillator. In *CLEO 2002*, Long beach, 2002.

D.3 Other Publications

This section includes a list of other publications arisen throughout the course of my Ph.D. but not related to the work presented in this thesis.

A.J. Boyland, S. Mailis, J.M. Hendricks, P.G.R. Smith, R.W. Eason. Electro-optically controlled beam switching via total internal reflection at a domain-engineered interface in $LiNbO_3$. *Optics Communications*, 197:193–200, 2001.

A.J. Boyland, S. Mailis, J.M. Hendricks, P.G.R. Smith, R.W. Eason. Beam deflection and T.I.R switching in domain-engineered $LiNbO_3$. In *IOP - Optics and Nonlinear Optics of Micro-structured and Nanostructured materials*, London, 2001.

A.J. Boyland, S. Mailis, J.M. Hendricks, P.G.R. Smith, R.W. Eason. Electro-optically controlled beam deflection and switching via total internal reflection at a domain-engineered interface in $LiNbO_3$. In *International Workshop on Periodic Microstructured Nonlinear Optical Materials*, Madrid, 2001.

R.W. Eason, A.J. Boyland, S. Mailis, J.M. Hendricks, P.G.R. Smith. Electro-optically controlled beam deflection and switching in domain-engineered $LiNbO_3$. In *IOP-MOEMS*, London, 2001.